HOMOGENIZED BEHAVIOR FROM INCREASINGLY HETEROGENEOUS SYSTEMS: URANIUM TRANSPORT EXPERIMENTS AT THE INTERMEDIATE SCALE

by

Andrew Miller

A thesis submitted to the Faculty and Board of Trustees of the Colorado School of Mines in partial fulfillment of the requirements for the degree of Doctor of Philosophy (Environmental Science and Engineering).

Golden, Colorado

Date:_____

Signed:_____
Andrew Miller

Approved:_____
Bruce Honeyman
Thesis Advisor

Approved:_____
Derrick Rodriguez
Thesis Advisor

Golden, Colorado

Date:_____

_____
Robert Siegrist
Professor and Director
Division of Environmental Science and Engineering

ABSTRACT

Environmental systems exhibit a range of complexities which exist at a range of length and mass scales. Within the realm of radionuclide fate and transport, much work has been focused on understanding pore scale processes where complexity can be reduced to a simplified system. In describing larger scale behavior, the results from these simplified systems must be combined to create a theory of the whole. This process can be quite complex, and lead to models which lack transparency. The underlying assumption of this approach is that complex systems will exhibit complex behavior, requiring a complex system of equations to describe behavior. This assumption has never been tested. The goal of the experiments presented is to ask the question: Do increasingly complex systems show increasingly complex behavior?

Three experimental tanks at the intermediate scale (Tank #1: 2.4m x 1.2m x 7.6cm, Tank #2: 2.4m x 0.61m x 7.6cm, Tank #3: 2.4m x 0.61m x 0.61m (LxHxW)) have been completed. These tanks were packed with both homogenous and heterogeneous physical orientations of 1, 2, or 5 different particle sizes of a uranium contaminated sediment from a former uranium mill near Naturita, Colorado. The masses of sediment used were: Tank #1- 280kg, Tank #2- 163kg, and Tank #3- 1160kg. Steady state water flow was induced across the tanks using constant head boundaries. Pore water was removed from within the flow domain through sampling ports/wells; effluent samples were also taken. Each sample was analyzed for a variety of analytes relating to the solubility and transport of uranium. Flow fields were characterized using inert tracers and direct measurements of pressure head.

The results show that although there is a wide range of chemical variability within the flow domain of the tank, the effluent uranium behavior resembles breakthrough curves from much smaller scale experiments. Thus, although there is a wide range in variability caused by pore scale behaviors, these behaviors appear to be smoothed out as uranium is transported through the tank. This smoothing of uranium transport behavior

transcends many of the physical and chemical heterogeneities added to the tank experiments.

TABLE OF CONTENTS

ABSTRACT III

LIST OF FIGURES IX

LIST OF TABLES XV

DEDICATION XVII

CHAPTER 1 1

1.1 Introduction 1

1.2 Background 3

1.3 Processes Relating to the Scaling of RTM 5
1.3.1 Chemical Controls on Metal/Radionuclide Behavior 7
1.3.1.1 High Energy Surface/Solution Characterization 7
1.3.1.2 Bench Scale/Wet Chemical Methods for Characterization 9
1.3.1.3 Surface Complexation Models and Chemical Heterogeneity 10
1.3.2 Physical Controls on Metal/Radionuclide Behavior 14
1.3.3 Combined Physical/Chemical Effects 15

1.4 Extension of Bench Data to Field Conditions 17
1.4.1 Scaling from Batch to Column Scales 18
1.4.2 Scaling from Batch to Field Scales 22
1.4.3 Empirical and Stochastic Techniques 27

1.5 Scales of Measurement and Scales of Application 28
1.5.1 Characterization in Spatial Dimensions 28
1.5.2 Characterization in Time 32

1.6 Discussion 34

1.7 References 36

CHAPTER 2 47

2.1 Introduction 47

2.2 Tank Experiment #1 47
2.2.1 Tank Construction 47

2.2.2 Tank Packing 53
2.2.3 Tank Sampling/Water Flow 57
2.2.4 Tracer Test 58

2.3 Tank Experiment #2 59
2.3.1 Tank Construction 59
2.3.2 Tank Packing 62
2.3.3 Tank Sampling/Water Flow 63
2.3.4 Tracer Test 65
2.3.5 Core Removal 65

2.4 Tank Experiment #3 66
2.4.1 Tank Construction 66
2.4.2 Tank Packing 68
2.4.3 Tank Sampling/Water Flow 75
2.4.4 Tracer Test 76

2.5 Uranium Desorption Experiments 76

2.6 Analytical/Instrumental Methods 77

2.7 References 79

CHAPTER 3 81

3.1 Introduction 81

3.2 Methods 87
3.2.1 Tank Construction 87
3.2.2 Tank Packing 90
3.2.3 Experimental Procedures 92

3.3 Results 96
3.3.1 Uranium Data 96
3.3.2 Uranium and Alkalinity Relationships 101
3.3.3 Bromide Data 102

3.4 Discussion 102
3.4.1 Major Ion Solubility Controls 108
3.4.2 Mineral-Uranium Surface Interactions 110

3.5 Conclusions 118

3.6 References 119

CHAPTER 4 125

4.1 Introduction 125

4.2 Methods 128
4.2.1 Tank Construction 128
4.2.2 Sediment Separation 129
4.2.3 Sediment Packing 130
4.2.4 Water flow, Tracer Injection, Sampling and Analysis 134

4.3 Results 136
4.3.1 Water Chemistry Results 136
4.3.2 Flow Calibrated Results 144

4.4 Discussion 150

4.5 Conclusions 156

4.6 References 158

CHAPTER 5 163

5.1 Introduction 163

5.2 Methods 166

5.3 Results 167

5.4 Discussion 176

5.5 References 180

CHAPTER 6 185

CHAPTER 7 197

APPENDIX A ..... CD/Pocket

APPENDIX B ..... CD/Pocket

APPENDIX C ..... CD/Pocket

APPENDIX D ..... CD/Pocket

APPENDIX E ..... CD/Pocket

APPENDIX F ..... CD/Pocket

APPENDIX G.....CD/Pocket

LIST OF FIGURES

Figure 1.1 Representative scale of physical and chemical processes relating to metal/radionuclide transport. Points on plot represent relationship between number of grid cells and the size of one grid cell assuming a regular discretization comprised of cubes. 6

Figure 1.2 Relative amount of characterization possible as a function of aquifer volume. Bench scale references: Kohler et al. [1996], Neiss et al. [2007], Kantar and Honeyman [2006]. Field scale references: Stollenwerk [1998], Boggs et al. [1992], Curtis et al. [2006]..... 29

Figure 2.1 Photos of tank #1: A- Tank approximately half full of sediment, B- Tank packed and connected to pressure array, note sample port spatial relationships, C- Tank connected to sampler array and saturated, D- 3-way valve in sampling port, E- Constant head boundaries, F- Endplate of tank, outflow port barely visible at the bottom of the tank. 51

Figure 2.2 Pictures from the 'Big Dig' 2006, A- The backhoe breaks ground, B- The groundwater table is reached, the metal box maintains vertical wall integrity while digging below the water table, C- The <2mm composite was sieved directly into the drums, D- Larger size fractions were separated in wheel barrows, E- Groundwater sediments drying in the sun, F- Once full, the drums were shipped in a moving truck back to Colorado School of Mines 54

Figure 2.3 Construction and packing of tank #2, A- Fully constructed tank #2, gasket material clearly visible in black, B- Tank #2 fully packed, saturated and connected to pressure array, C- Opposite view as B, head boundaries in background, D- 3-way valve in sampling port connected to pressure array, E- Taking a core of the core for microbial analysis, F- Taking a core from the tank..... 61

Figure 2.4 Packing orientation in tank #2, red cross hatch is the >0.250mm fraction, yellow cross hatch is the <0.250mm, the upgradient end is on the left and downgradient end is on the right, top and bottom are no-flow boundaries. Picture created by Derrick Rodriguez. 63

Figure 2.5 Schematic of tank #3 construction, all dimensions in centimeters. Drawing completed by Jason Peterson. 69

Figure 2.6 Tank construction and packing of tank #3, A- Wet sieving of 4-12mm size fraction, B- Tank #3 fully constructed underneath tank #2, C- Aluminum grid in place creating ~11cm cubes, D- Packing of the various size fraction in the aluminum grid with several sampling wells in place, E- The screened end of

the sampling wells, F- Packing of the various size fractions, G- The tank is fully packed, and the lid is in place and caulked, H- Sample tubing and three way valves connected to the sampling wells. 71

Figure 2.7 Vertical cross section of tank #3 packing, upgradient end on the left, downgradient end on the right, y-dimension (into plane of page) ~5.6cm (~11.2cm thick)..... 72

Figure 2.8 Vertical cross section of tank #3 packing, upgradient end on the left, downgradient end on the right, y-dimension (into the plane of the page) ~16.8cm (~11.2cm thick)..... 72

Figure 2.9 Vertical cross section of tank #3, upgradient end on the left, downgradient end on the right, y-dimension (into the plane of the page) ~28.0cm (~11.2cm thick) 73

Figure 2.10 Vertical cross section of tank #3, upgradient end on the left, downgradient end on the right, y-dimension (into the plane of the page) ~39.1cm (~11.2cm thick) 73

Figure 2.11 Vertical cross section of tank #3, upgradient end on the left, downgradient end on the right, y-dimension (into the place of the page) ~39.1cm (~11.2cm thick) 74

Figure 3.1 Relative heterogeneities of experimental systems, Top line: Experimental Methods, Middle line: Scale of increasing heterogeneity of different experimental methods in the literature, Bottom line: Characteristic length scales. 82

Figure 3.2 Field sieving and tank construction photos, A- Sieving sediments in the field, B- Tank #2 constructed but prior to packing, C- Tank #1 packed and connected to the pressure system, D- Tank #2 packed and connected to the pressure system, E- Head boundaries used to control flow through the tanks, F- Three way valve for sampling and pressure measurements. 89

Figure 3.3 Tank #2 packing orientation, red cross hatch is the >0.250mm size fraction; the yellow cross-hatch is the <0.250mm size fraction; upgradient end is on the left, downgradient end is on the right. 93

Figure 3.4 Uranium breakthrough curves for both tank #1 (solid symbols) and tank #2 (open symbols). Total uranium determined from tank effluent samples. 97

Figure 3.5 Normalized uranium flux as a function of pore volume in both tanks. Tank #1 is the closed symbols, tank #2 is the open symbols. Black arrows are stop flow events with the elapsed time (in hours) labeled next to the arrow. The

area between the red arrows for tank #2 is the time of the AGW-2% injection.....98

Figure 3.6 Kriged uranium spatial distributions from three different time points representing the beginning, middle and end of the experimental timeframe. Upgradient end is on the left, down gradient end is on the right. 99

Figure 3.7 Kriged uranium spatial distributions for tank #2. Note the changing uranium scales. Upgradient end is on the left, downgradient end is on the right. 100

Figure 3.8 Uranium vs. alkalinity concentrations over time in tank #1. Each point represents the analysis from a single spatial sample. Lines of best fit are shown for each sampling point in time. 103

Figure 3.9 Uranium vs. alkalinity concentrations over time in tank #2. Each point represents the analysis from a single spatial sample..... 104

Figure 3.10 Normalized bromide breakthrough curves for tank #1 (closed symbols) and tank #2 (open symbols). 105

Figure 3.11 Kriged plots of bromide spatial distributions as a function of time in tank #1. Upgradient end on the left, downgradient end on the right. 106

Figure 3.12 Kriged bromide plots as a function of time for tank #2. Upgradient end is on the left, downgradient end is on the right. Note the changing concentration scales. 107

Figure 3.13 Calcium concentrations as a function of pH. Calcite solubility curves are the solid lines shown for the range of PCO2 found in tanks #1 and #2. Gypsum equilibrium is shown by the dashed lines for the range of SO42- found in tanks #1 and #2. x's are data from tank #1, while + symbols are data from tank #2.....109

Figure 3.14 Uranium concentration as a function of pH. Uranophane equilibrium is shown by the two solid lines for the range of PCO_2 found in tanks #1 and #2 while holding calcium and silicon constant. x's are results from spatial samples for tank #1, while the + symbols are data for tank #2.....111

Figure 3.15 Calculated vs. Measured uranium values for tanks #1 and #2. The x symbols are for tank #1 and the + symbols are for tank #2. The heavy black line is the 1:1 line. The error bars represent 37% error for tank #1 points, and 31% error for tank #2 points. Although they are not shown, they apply to all the plotted points.....116

Figure 4.1 Vertical cross section (y = 0-11.7cm) through the tank showing packing orientation of the size fractions as well as the location of the sampling wells;

upgradient end is on the left, downgradient end is on the right. The dimensions of each cell are 11.2cm x 11.7cm x 11.2cm (x, y, z). Square symbols are wells present in the middle of this cross section; triangles are wells which are on the boundary between cross sections. The number next to the well is the well number.....132

Figure 4.2 Vertical cross section (y = 11.7-23.4cm) through the tank showing packing orientation of the size fractions as well as the location of the sampling wells; upgradient end is on the left, downgradient end is on the right. The dimensions of each cell are 11.2cm x 11.7cm x 11.2cm (x, y, z). Square symbols are wells present in the middle of this cross section; triangles are wells which are on the boundary between cross sections. The number next to the well is the well number.....132

Figure 4.3 Vertical cross section (y = 23.4-35.1cm) through the tank showing packing orientation of the size fractions as well as the location of the sampling wells; upgradient end is on the left, downgradient end is on the right. The dimensions of each cell are 11.2cm x 11.7cm x 11.2cm (x, y, z). Square symbols are wells present in the middle of this cross section; triangles are wells which are on the boundary between cross sections. The number next to the well is the well number.....133

Figure 4.4 Vertical cross section (y = 35.1- 46.8cm) through the tank showing packing orientation of the size fractions as well as the location of the sampling wells; upgradient end is on the left, downgradient end is on the right. The dimensions of each cell are 11.2cm x 11.7cm x 11.2cm (x, y, z). Square symbols are wells present in the middle of this cross section; triangles are wells which are on the boundary between cross sections. The number next to the well is the well number.....133

Figure 4.5 Vertical cross section (y = 0-11.7cm) through the tank showing packing orientation of the size fractions as well as the location of the sampling wells; upgradient end is on the left, downgradient end is on the right. The dimensions of each cell are 11.2cm x 11.7cm x 11.2cm (x, y, z). Square symbols are wells present in the middle of this cross section; triangles are wells which are on the boundary between cross sections. The number next to the well is the well number.....134

Figure 4.6 Spatial profiles for pH and uranium after 94 days of water flow. Each plot corresponds to the vertical cross sections in Figures 4.1 through 4.5.....137

Figure 4.7 Spatial profiles for pH and uranium after 192 days of water flow. Each plot corresponds to the vertical cross sections in Figures 4.1 through 4.5.....138

Figure 4.8 Spatial profiles for pH and uranium after 290 days of water flow. Each plot corresponds to the vertical cross sections in Figures 4.1 through 4.5.....139

Figure 4.9 Correlation plot between uranium and pH. Each point represents the analysis from a single sampling well for the date shown. The dates shown encompass the majority of the experimental timeframe.....141

Figure 4.10 Correlation plot between calcium and pH. Each point represents the analysis from a single sampling well for the date shown. The dates shown encompass the majority of the experimental timeframe. Influent calcium concentration is 5.65mM 142

Figure 4.11 Correlation plot between uranium and calcium. Each point represents the analysis from a single sampling well for the date shown. The dates shown encompass the majority of the experimental timeframe 143

Figure 4.12 Correlation plot of silicon as a function of pH. Each point represents the results from a single well for the day indicated. Also shown are the influent concentrations before and after 4-20-09, as well as the solubility limit for silicon assuming equilibrium with chlorite.....145

Figure 4.13 pH as a function of local ground water velocity. Each individual column of points represents the analysis from a single well.....147

Figure 4.14 Uranium concentration as a function of ground water velocity. Each individual column of points represents the analysis from a single well..... 148

Figure 4.15 Uranium concentration as a function of local pore volumes eluted for a selected set of wells. The wells selected are all surrounded by <2mm composite material, and have local ground water velocities between 0.21-1.2cm/day.....149

Figure 4.16 Uranium breakthrough curve as a function of pore volumes 151

Figure 5.1 Bromide spatial distributions 46 days (0.73PV) after injection. The upgradient end is on the upper left, downgradient end is on the lower right. The number of wells with detectable bromide to create this plot is 38. Black points in plot represent well locations 168

Figure 5.2 Bromide spatial distributions 109 days (1.65PV) since injection. Upgradient end is on the upper left, downgradient end is on the lower right. The number of wells with detectable bromide was 12.....169

Figure 5.3 Bromide spatial distributions 137 days (2.10PV) after injection. Upgradient end is on the upper left, downgradient end is on the lower right. The number of wells with detectable bromide in this plots is 9.....170

Figure 5.4 Bromide breakthrough curve and model fit, points are data from the tank, and the line is the model output. Model values are in Table 5.1 171

Figure 5.5 Bromide breakthrough curves for three wells, plotted as a function of local pore volumes eluted. The number of pore volumes for well #19 has been scaled down by a factor of 25; the number of pore volumes for well #32 has been scaled down by a factor of 40.....174

Figure 6.1 Uranium breakthrough curves for all three tanks. Samples removed from the effluent line of each individual tank 186

Figure 6.2 Normalized uranium fluxes from all three tanks. The black arrows denote stop flow events in tanks 1 and 2; there was no stop flow event in tank 3. The red arrows denote the time when AGW-2% was being injected into tank 2 188

Figure 6.3 Normalized bromide breakthrough curves for all three tanks as a function of pore volumes since the bromide was injected. Samples removed from effluent line of the individual tanks.....189

Figure 6.4 Uranium versus pH results from spatial samples for all three tanks. The samples were taken from within the flow domain. Dates shown include: Tank 1: 3-6-07, 4-28-07, 6-12-07, 7-11-07, Tank 2: 3-8-08, 5-8-08, 7-11-08, 9-2-08, 12-22-08, Tank 3: 3-9-09, 5-11-09, 7-13-09, 9-21-09.....192

Figure 6.5 Alkalinity versus pH results from spatial samples for all three tanks. The samples were taken from within the flow domain. Dates shown include: Tank 1: 3-6-07, 4-28-07, 6-12-07, 7-11-07, Tank 2: 3-8-08, 5-8-08, 7-11-08, 9-2-08, 12-22-08, Tank 3: 3-9-09, 5-11-09, 7-13-09, 9-21-09.....193

Figure 6.6 Calcium versus pH results from spatial samples for all three tanks. The samples were taken from within the flow domain. Dates shown include: Tank 1: 3-6-07, 4-28-07, 6-12-07, 7-11-07, Tank 2: 3-8-08, 5-8-08, 7-11-08, 9-2-08, 12-22-08, Tank 3: 3-9-09, 5-11-09, 7-13-09, 9-21-09.....194

Figure 6.7 Silicon versus pH results from spatial samples for all three tanks. The samples were taken from within the flow domain. Dates shown include: Tank 1: 3-6-07, 4-28-07, 6-12-07, 7-11-07, Tank 2: 3-8-08, 5-8-08, 7-11-08, 9-2-08, 12-22-08, Tank 3: 3-9-09, 5-11-09, 7-13-09, 9-21-09.....196

LIST OF TABLES

Table 1.1 Summary of bench and column scale work discussed in the text. Note: IX = ion exchange. 19

Table 1.2 Summary of up-scaling studies from the bench to the field and field simulations. 23

Table 2.1 Summary of experimental conditions for the tank experiments..... 48

Table 2.2 Compositions of the artificial groundwaters used in all three tanks, concentrations for ions are in molar, pH is in standard pH units, and saturation index is unitless.....56

Table 3.1 Artificial ground water compositions used in tanks #1 and #2. Ion concentrations are in molar, pH in standard pH units, and alkalinity is in meq/L 93

Table 3.2 Aqueous uranium reactions and constants used in the speciation modeling. Unless otherwise specified all values are from the NEA thermodynamic database (*Guillamont et al.* [2003]) 113

Table 3.3 Surface reactions used in the speciation calculations. All reactions were determined by *Davis and Curtis* [2003]. SS is a very strong surface site, S is a strong surface site, and W is a weak surface site.....114

Table 3.4 Summary of calculations for chemical conditions around a single sampling point 114

Table 4.1 Composition of the artificial groundwater; concentrations for ions are in molar, pH is in standard pH units, and saturation index is unitless 135

Table 5.1 Model values used to create breakthrough curve in Figure 5.4 173

Table 5.2 Well classifications based on tracer response. The numbers in the table denote well ID numbers.....175

Table 5.3 Well classifications based on uranium response. The numbers in the table denote well ID numbers. The small, medium, large change refer to uranium concentration changes, while 1 and 2-stage refer to the breakthrough curve. See text for details.....175

Table 6.1 Minimum, maximum, and the range of values for master variables within all three tanks. Data from the following dates was used: Tank 1: 3-6-07, 4-28-07, 6-12-07, 7-11-07, Tank 2: 3-8-08, 5-8-08, 7-11-08, 9-2-08, 12-22-08, Tank 3: 3-9-09, 5-11-09, 7-13-09, 9-21-09. This table corresponds to the data shown in Figures 6.4 to 6.7 191

DEDICATION

Computers are worthless. They can only give answers.

-Pablo Picasso

This one is dedicated to those uninterested in answers.

CHAPTER 1

CRITICAL REVIEW OF SCALING IN METAL/RADIONUCLIDE TRANSPORT IN GROUNDWATER SYSTEMS

1.1 Introduction

When scaling of reactive transport models is considered, a common method is to create a hierarchy of heterogeneities which are clustered as a function of scale. Thus the effects of physical and chemical heterogeneities at a small scale are explicitly calculated and incorporated into the physical and chemical heterogeneities at the next higher scale. These models are mathematically complex (e.g. see *Qunitard and Whitaker* [1998]). These attempts at upscaling are reductionist in scope; they break a complex system into smaller fundamental or measurable parts and rely on constitutive relationships to relate the smaller parts into a cohesive whole.

There are two problems with this approach for large scale contaminated field systems. The first is that models need transparency and as such a certain amount of simplicity is required. In the *Quintard and Whitaker* [1998] paper mentioned above, there are 90 variables and 104 equations (not including appendices) describing the mathematical relationships of the system they define. With the possible exception of the authors, there are few who will understand the full implications of that model to the extent that a mental estimation of output can be made based on the altering of a single variable; model transparency has been lost. The second major problem with this approach to describe field scale sites is the range of scales that must be transcended. Recent work has related calcite dissolution chemistry from the pore scale up to a flow field of approximately $1mm^2$ (*Li et al.* [2006] and [2007]). These studies show different upscaled rates of dissolution based on the physical orientation of reactive pores. Thus, not only does the upscaling of this model need to extend from mm to km, but the field scale system must be characterized at the pore scale for these types of upscaling attempts

to be applicable. Both of these tasks may be impossible based on current computing and measurement techniques.

The fundamental assumption with these scaling techniques is that a complex system requires a complex system of equations to describe it. This assumption has never been tested experimentally. Thus the question is asked: Does increased system complexity cause complex transport behavior? The results from the experiments described herein will show that increasing system complexity does not necessarily yield complex behavior. This occurs despite the fact that there is a large amount of observed local variations in behavior, consistent with localized chemical reactions and flow variations. The implications of these results are that the complex model formulations to describe chemical reactions as a function of scale may not be necessary, models may not need to explicitly account for pore scale processes and heterogeneities, and methods should be derivable to maintain model transparency as well as account for heterogeneities as a function of scale.

These results are presented in the following manner. Chapter 1 is a critical review of how upscaling of ion transport is considered in both chemically active and chemically inert systems. A special focus in this review is how surface complexation models describing ion sorption to mineral surfaces have been used at a variety of scales. Chapter 2 describes the experimental methods in explicit detail. Chapters 3-5 are written as independent chapters. Each has an introduction to the experiments being covered and why, a brief synopsis of methods, results from the experiments and discussions of the results. Chapter 3 covers the first two tank experiments. These experiments are both 2-D tank experiments; the first was packed with a single size fraction (‘homogenous’), the second was packed with known macroscopic physical heterogeneities by splitting the single size fraction into two. All of the data for these two tanks is shown including uranium and other chemical constituents, as well as bromide tracer results. Chapter 4 describes the reactive chemistry within a 3-D tank packed with five different particle sizes of sediment. Chapter 5 discusses the inert transport in the 3-D tank, and compares the inert transport of bromide to the reactive transport of uranium. Chapter 6 is simply a summary of the results, and ideas for future directions.

1.2 Background

Traditionally contaminant/porous media sorption has been described with a K_D value, as defined in equation (1.1).

$$K_D = \frac{C_{ads}}{C_{aq}} \tag{1.1}$$

Here, C_{ads} is the concentration of the contaminant adsorbed to the porous media, and C_{aq} is the concentration of the contaminant in the solution phase. The use of the K_D value in the advective-dispersive equation (ADE, equation 1.2) is attractive due to the ability to solve for analytical solutions, and hence relatively easy solutions to a transport problem.

$$\frac{\partial C}{\partial t}(1+\frac{\rho}{\theta}K_D) = D_L \frac{\partial^2 C}{\partial x^2} - v_x \frac{\partial C}{\partial x} \tag{1.2}$$

Here, C is the contaminant concentration, t is time, ρ is bulk density, θ is porosity, D_L is the dispersion coefficient parallel to flow, x is distance, and v is water velocity. However, most metals and radionuclide sorption behavior is poorly described by K_D based models, and many have raised questions as to the validity of such an approach (*Bethke and Brady* [2000], *Reardon* [1981]).

To circumvent this problem, reactive transport models (RTM) have been developed and widely applied (*Steefel et al.* [2005]). These models are capable of defining a system in terms of the many possible chemical reactions and combining the reactions with a more simplified version of the ADE to describe transport. The reactive sub-model of the RTM is composed of a series of mass action equations describing reactions in solution as well as at mineral surfaces (i.e. sorption through the use of a surface complexation model (SCM)), dissolution/precipitation, and redox transformations (e.g. *de Windt et al.* [2003], *Zhu et al.* [2001], *Maher et al.* [2006]). Through simultaneous solution of a large set of mass action equations, chemical speciation as a function of conditions can be calculated. Using a RTM is computationally expensive, but with the advent of better computing technologies, the use of RTM has become widespread, and has led to success in describing data at both the lab and field scales. But the link between bench scale knowledge and field scale application is still somewhat tenuous (*Steefel et al.* [2005], *Bryant and Thompson* [2001], *van der Lee and de Windt*

[2001]). Current stumbling blocks preventing the up-scaling of bench-scale knowledge to field-scale application of RTM are a lack of understanding in: 1) how the interactions between physical and chemical processes affect observed system behavior, and 2) how physical and chemical heterogeneities in space and time will affect observed system behavior.

In previous reviews of RTM, specific aspects were considered such as model formulation and numerical methods used (*Yeh and Tripathi* [1989]), general advantages and disadvantages to RTM (*van der Lee and De Windt* [2001]), a short review of non-classical behavior and general hydrologic scaling effects (*Bryant and Thompson* [2001]), and the application of RTM to diverse earth systems and directions for new research (*Steefel et al.* [2005]). *Van der Lee and De Windt* [2001] raise the role of heterogeneity in describing real world systems, and both *Bryant and Thompson* [2001] and *Steefel et al.* [2005] raise the issue of scaling as being critical to understanding and mathematically describing earth systems. *Steefel et al.* [2005] even summarize current methods of scaling used in reactive transport modeling of contaminated systems including continuum, pore-scale, and multiple continuum models. However, to date no one has reviewed available literature to assess how issues related to scale are currently being considered for metal/radionuclide transport in saturated groundwater systems. Through this review process several aspects will be covered including: how physical and chemical heterogeneities affect observed behavior of metals/radionuclides, how data from the bench scale is applied in field scale simulations, the relationship between the scale of measurement and the scale of application (both spatially and temporally), and finally a discussion of a list of challenges to overcome in scaling of RTM. The overarching theme between these topics is to examine the connections that have been made between bench scale behavior and characterization with field scale behavior and characterization and to evaluate the validity and efficacy of such approaches.

1.3 Processes Relating to the Scaling of RTM

By analogy, in an attempt to comprehend scale in RTM, one can consider neuroscience. Extensive characterization of how two neurons communicate will not give any insight, and may not even hint at the presence of, a cognizant mind. Likewise, the study of a mind does not say anything definitive with respect to the complex bio-chemistry at the neuron interface. The scales of knowing are simply too disparate. The same is true in metal/radionuclide transport: molecular scale behaviors have been well characterized, but difficulties arise in prediction of large-scale contaminant behavior. The reason is that chemical reactions and physical processes of water flow can negate, have no effect on, or promote each other. These interactions complicate determination of scaling relationships. Also, as can be seen in Figure 1.1, the scaling of fundamental behavior is further complicated by the range of scales involved.

Figure 1.1 shows the relationship between the required number of grid cells in an aquifer as a function of the grid dimensions. On the plot, the points represent a regular discretization of cubes in a 125,000m^3 aquifer. Thus for a 1m^3 grid cell, 125,000 cells are required. As the volume of the cube changes, so does the total number of cells required. Also on the plot are representative scales for the different processes which can exert some control on metal/radionuclide transport behavior. These are not intended to be exact representations; for many of these processes the exact range of possible scales will depend on specific conditions at any given field site. However, it is important to note that the physical processes related to transport are generally larger in scale relative to the chemical processes. The explicit inclusion of chemical reactions to a transport simulation effectively doubles the range of length scales involved relative to inert transport where chemical behavior can be ignored. Independent of size range is the presence of physical and chemical heterogeneities. These heterogeneities complicate scaling procedures considerably and the role of chemical and physical heterogeneity in metal/radionuclide transport behavior is discussed in detail below. Finally, highlighted in red on the plot is an approximation for common numbers of grid cells used in the literature. Again, the

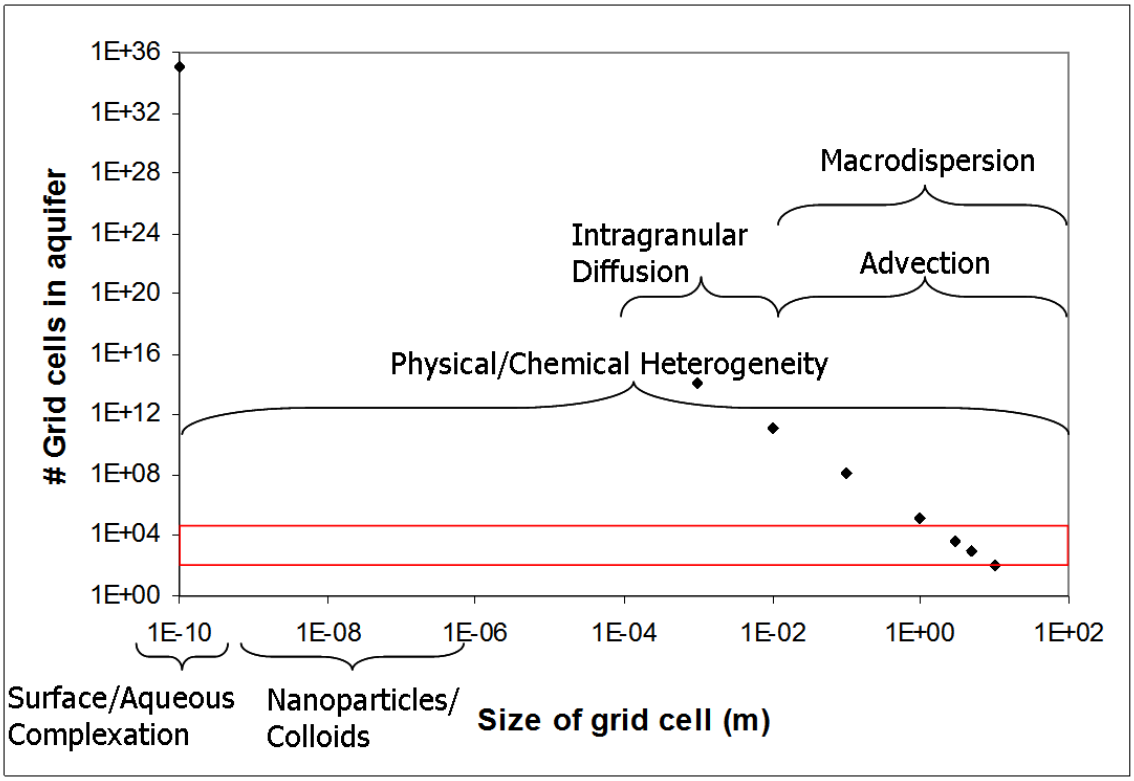

Figure 1.1 Representative scale of physical and chemical processes relating to metal/radionuclide transport. Points on plot represent relationship between number of grid cells and the size of one grid cell assuming a regular discretization comprised of cubes.

exact number that is used will often be a function of time, money, and modeling goals, but the range is relatively finite ranging from several hundred up to tens of thousands (A notable exception is *Scheibe and Yabusaki* [1998] where 16 million grid cells were used for a flow and transport simulation. This simulation required massively parallel, supercomputing capabilities.). When considering scale relationships in RTM simulations, it is noteworthy that all of the chemical processes involved, and many of the physical processes involved occur at a scale that is considerably smaller than the size of a representative grid cell (*Li et al.* [2006], *Liu et al.*[2006]). And yet, these sub-grid processes are often the controlling factors of observed behavior.

Using Figure 1.1 as a starting point, I will summarize the chemical and physical processes controlling metal/radionuclide behavior as a function of scale. I will then discuss how chemical and physical processes interact despite the large difference in effective scales and examine how both physical and chemical heterogeneities affect these interactions. And finally, I will relate these interactions to model formulations.

1.3.1 Chemical Controls on Metal/Radionuclide Behavior

There are two major threads of knowledge relating to chemistry dependent transport of metals. The first is through spectroscopic, synchrotron and other high energy based characterization technologies. The second is through modeling of observed macroscopic (though still at the bench scale) behavior.

1.3.1.1 High Energy Surface/Solution Characterization

The knowledge gained from the first thread of experimental inquiry is molecular scale interactions between relatively small numbers of atoms in solution and mineral surfaces. It also opens the molecular world to a better characterization of the processes

that can occur at mineral interfaces. For example, *Wersin et al.* [1994] uses several spectroscopic techniques (auger electron spectroscopy [AES], X-ray photoelectron spectroscopy [XPS], and Fourier transformed infrared analysis [FTIR]) to determine uranium(VI) behavior near sulfidic mineral interfaces. With the combination of these techniques they were able to measure uranium(VI) reduction to uranium(IV) or other uranium species with mixed valencies (IV)-(VI). The authors suggest that this newfound surface behavior may explain precipitates formed in anoxic ground water, and may control uranium solubility. Furthermore, *Waychunas et al.* [2002] found a discrete zinc bearing precipitate for high surface loadings of ferrihydrite with no Fe-Zn solid solution phase using x-ray absorption fine edge spectroscopy (EXAFS). This precipitate was forming despite the fact that the solution was undersaturated by two or more orders of magnitude. Similar discrete precipitates from an undersaturated solution were found by *Towle et al.* [1997] for a Co(II)-Al_2O_3 system using transmission electron microscopy (TEM), EXAFS and XPS. Besides surface information, a soluble ternary species, $Ca_2UO_2(CO_3)_3^0$, was discovered by fluorescence spectroscopy (*Kalmykov and Choppin* [2000]) and later confirmed by time-resolved laser-induced spectroscopy (TRLFS, *Bernhard et al.* [2001]). Both of these studies calculated that the ternary species would dominate most oxic groundwaters around former uranium mills and mines. Later it was found that this species is largely surface in-active, and can lead to enhanced uranium migration (*Zheng et al.* [2003], *Dong et al.* [2005], *Fox et al.* [2006]).

There are many other studies where spectroscopy has allowed for characterization of atom-atom interactions at mineral interfaces or in solution. The relevance to this review, however, is that the majority of these interactions is being measured at approximately the angstrom scale and represents an average signal for a relatively small total number of atoms. Using Figure 1.1, to explicitly account for all of these atom-atom interactions, 10^{36} grid cells would be required for the hypothetical aquifer, which is well beyond current computing abilities. A better use of this information is to anchor conceptual models for surface and aqueous complexation in a measurable reality. In other words the known and quantifiable existence of specific surface and aqueous complexes gives credence to some of the more simplified chemical models discussed below.

1.3.1.2 Bench Scale/Wet Chemical Methods for Characterization

The second major thread follows a more traditional surface chemical approach where macroscopic behavior is described through chemically plausible, but not necessarily real, surface interactions. The chemical controls on metal/radionuclide mobility are largely divisible into inorganic and organic interactions.

The uranyl ion is well known for forming strong complexes with inorganic constituents in solution. The ternary $Ca_2UO_2(CO_3)_3^0$ species mentioned above is one, phosphate and fluoride complexes are examples of others. In *Kohler et al.* [1996], the authors use a combination of batch and column data to explore the complexation and transport of the uranyl-fluoride ion. The important implication with respect to chemical controls on transport is that injection of fluoride, a strong uranium complexing agent, led to increased uranium mobility. Also the authors were able to *predict* uranium mobility through the use of an RTM determined from batch parameters.

Another, less obvious, inorganic control on metal/radionuclide mobility is related to the presence of anions which change sorption behavior. Decreased uranium adsorption was observed for increasing CO_3^{2-} and SO_4^{2-} concentrations (*Morrison et al.* [1995a] and [1995]b). Increasing PCO_2 at elevated pH decreases neptunium sorption to several different mineral surfaces (*Kohler et al.* [1999]). Also, sorption edges of chromate were found to shift to lower pH as a function of increasing PCO_2; i.e., for a given pH less sorption was observed with increasing PCO_2 (*Zachara et al.* [1987]). The implication is that the presence of carbonate species would lead to less chromate sorption, and faster chromate migration. The mechanisms for this behavior change depending on which metal-anion pair is being considered. In the case of oxy-anions, the mechanism is most likely competition for available surface sites. For cations, the mechanism is more likely to be altered aqueous complexation or altered surface properties, such as charge, caused by anion sorption (*VanGeen et al.* [1994]). Thus, inorganic ions present can enhance or retard metal migration depending on the ions involved, and the relative affinities for the ions in solution and the ions at the mineral surface.

Just as with the inorganic controls, introduced organic chemicals or natural organic matter (NOM) can have both enhancing and retarding effects on metal migration.

In one study comparing the ternary system of uranium and humic acid sorption to hematite, the humic acid was found to enhance uranium sorption at low pH values, and decrease sorption at higher pH values (*Lenhart and Honeyman* [1999]). In a similar study sorption behavior was found to vary as a function of pH in the presence and absence of humic acid, but was also found to be mineral specific (*Schmeide et al.* [2000]). A conceptual model to interpret these results can be found in *Honeyman and Ranville* [2002], but as with the inorganic chemicals it relates to the relative affinities of the metal and the organic matter both for each other as well as the mineral surface.

All of the above interactions can be modeled with the use of an aqueous and surface complexation model assuming that the experiments were completed under no-flow (batch) conditions. These SCM formulations are critical to describing the transport of metals/radionuclides in RTM.

1.3.1.3 Surface Complexation Models and Chemical Heterogeneity

The development of SCM has largely been driven by the chemical complexity described in the preceding sections. The goal of SCM is to explicitly account for variable surface complexes that form as a function of solution chemistry. Most SCM stem from the consideration of a mineral surface as an amphoteric functional group where cation sorption is a function of pH (*Hohl and Stumm* [1975]). Since the application of SCM formulations to environmental systems, conceptual models have grown in complexity as larger numbers of fundamental behaviors are experimentally determined (e.g. *Farley et al.* [1985] and *Wersin et al.* [1989] for surface precipitation). Notable additions to the amphoteric model relevant to this review are the triple layer model (TLM, *Davis et al.* [1978]a, *Davis et al.* [1978]b, *Davis et al.* [1980]) and the CD-MUSIC model (*Hiemstra and Van Riemsdijk* [1996]). These two models differ mostly in how they account for surface charge. The TLM distributes the charge into the solution phase in three distinct planes moving away from the surface where each plane is physically interpreted as being boundaries between inner/outer sphere coordination. The CD-MUSIC model distributes

some of the surface charge into the mineral phase itself as well as accounts for physical structure of bound ions at the surface. Both of these models have been extensively used to describe bench scale data in single mineral phase systems. And both have been used in connecting high-energy characterization techniques to observed behavior in batch reactors.

Arai et al. [2006] considered U sorption to imogolite and used the triple layer model to fit the data. Batch sorption envelopes were created for a range of chemical conditions, and surface speciation was measured using XAS. The model parameters were fit using the spectroscopically determined surface stoichiometry and macroscopic observed data from the batch reactors. *Ponthieu et al.* [2006] used the CD-MUSIC model to describe Cd, Co, Cu, Ni, Pb, and Zn sorption to both goethite and ferrihydrite (HFO). Again they fit the surface complexation constants of these species around the measured stoichiometries of surface complexes. The important outcome from this paper is that using the CD-MUSIC model, the coordination of protons and a single metal to these two different solid phases were accomplished using the same set of model parameters.

These studies raise intriguing points in the scaling of surface complexation models. Although they do range in scale from approximately the angstrom level (tens of atoms, synchrotron characterization) to tens of grams (~10^{22} atoms, batch reactors), the more important implication is that they are scaling through different levels of surface heterogeneity. The use of the TLM in *Arai et al.* [2006] represents an arguably simpler model than the CD-MUSIC model in terms of number of fitting parameters and conceptual model simplicity. Despite its relative simplicity, it is still capable of describing specific stoichiometric surface coordination on a single mineral type. In other words, the TLM conceptual model can explicitly account for the underlying surface site heterogeneity, which causes the observed sorption behavior (batch sorption experiments) and different coordination environments at the surface (observed using high energy characterization). In *Ponthieu et al.* [2006] this ability was extended to encompass metal behavior between Fe-O minerals of variable crystallinity. Because of the varying level of crystallinity the surface environment between these two minerals is even more heterogeneous than that of the single mineral phase of *Arai et al.* [2006], and yet the same model values described metal sorption between these two distinct solid phases.

Admittedly both of these studies fit their models to the observed data, and extrapolation beyond the heterogeneity in their respective systems is probably not warranted, but the fact remains that the models as presented explicitly account for surface site heterogeneity and reactivity based on known surface complexes.

Another attempt at scaling surface chemical heterogeneity from the atom scale up to batch scale behavior is to use distributed reactivity models (*Weber et al.* [1992], *Chen and Wagenet* [1995]). Instead of specific surface reactions, assumed by both the CD-MUSIC and TLM model formulations, distributed reactivity models define surface reactions with a set of parameters to describe reactivity. These models are typically restricted to organic sorption to soils/sediments where spectroscopic data is not available; they also tend to be based on K_D values. Thus the extension of this modeling construct to metal/radionuclide behavior ignores any advances that have been made based on spectroscopic data, and may or may not be able to describe metal-surface interactions which are poorly described by K_D based interpretations. However, distributed reactivity models may intersect with RTM in distributed rate models to describe kinetic formulations (*Haggerty and Gorelick* [1995]). This is discussed below in more detail in the section relating to scaling through time.

To move up on the scale of heterogeneity, and to apply SCM to transport scenarios, both the TLM and CD-MUSIC model are one point too simple, and on another, too complex. Both models are too simple in the sense that neither model would be able to account for the surface and mineral heterogeneity associated with a natural mineral matrix while simultaneously limiting the number of fitting parameters. They are both too complex in that the inclusion of a chemical speciation calculation at that level within the framework of a RTM code, would exhaust computing resources. Thus different conceptual models have been created to extend the SCM concept to mixed mineral systems.

The Generalized Composite (GC) and the Component Additivity (CA) approaches are two competing ideas to apply SCM to RTM (*Davis et al.* [1998]). The GC approach assumes that a natural mineral matrix is too complex to be understood, and fits hypothetical reactions to measured sorption behavior. The CA approach uses sorption behavior determined through sorption experiments on single mineral phases, and

then mathematically combines the behavior based on the proportions of the single minerals present in the matrix (for fuller discussions and some applications to real data see *Honeyman* [1984], *Davis et al.* [1998], *Payne et al.* [2006], and *Waite et al.* [2000]). Neither of these models explicitly includes electrostatic terms, which up to this point has often been the major difference between SCM formulations. This exclusion of surface charge has been critically examined in *Turner et al.* [2006]. Two different models, one which included electrostatic terms (three fitting parameters) and one which did not (four fitting parameters) were applied to the data of *Kohler et al.* [1999]. Both models were able to fit the data; however, they did require different total numbers of chemical reactions and surface site types. As opposed to the work of *Arai et al.* [2006] and *Ponthieu et al.* [2006] the point of the hypothetical reactions in *Turner et al.* [2006] is not to make an explicit link between known surface complexes and observed behavior. Instead the goals are more pragmatic, in that sorption data collected from a range of chemical conditions is to be described with the simplest model possible. This more pragmatic goal of linking SCM theory with chemical transport is necessary because of computing limitations and model transparency. Currently the GC approach is more common in transport simulations (*Curtis et al.* [2006], *Stollenwerk* [1995] and [1998], *Kent et al.* [2000] and [1995], *Davis et al.* [2000]). The CA approach, though more rigorous in nature, is difficult to implement because of the difficulty in determining surface areas of individual minerals in mineral matrices, as well as difficulty in determining both the chemical behavior and presence of mineral coatings and poorly crystalline material (*Davis et al.* [2004).

Despite the fact that the GC models are often applied at the same experimental scale as the more complex TLM and CD-MUSIC models, the GC approach is capable of describing sorption data on a far more heterogeneous sample with a limited number of fitting parameters. Thus, the GC approach is an up-scaled version of the TLM and CD-MUSIC models where the scale is of increasing surface reactivity heterogeneity. This is an important distinction: in order to up-scale a SCM in terms of heterogeneity, a new, somewhat simplified conceptual model was necessary. Even with the required simplifications of the GC approach, good agreement to data has been observed (*Davis et al.* [1998], *Payne et al.* [2006], and *Waite et al.* [2000]). Furthermore, the added

simplicity of the GC approach, allows for a semi-mechanistic inclusion of metal sorption as a function of solution chemistry into transport scenarios which has lead to better descriptions of metal/radionuclide transport compared to more empirical models. There are more limitations to the GC models in terms of extrapolation beyond a set of experimental conditions, but for the most part many field systems are bound to certain ranges of chemical compositions. If the GC model is formulated from experiments containing that range, then it will most likely represent the conditions found in the field. Also, as with any model, decisions made by the modeler often introduce as much error as the simplified conceptual model (*Payne et al.* [2006]).

1.3.2 Physical Controls on Metal/Radionuclide Behavior

In this review, physical controls are defined as controls on transport that are largely related to the flow of the water through porous media. Many of the effects will be shown to be closely related to the chemical effects mentioned above. These physical controls will be separated by the scales at which they have been shown to occur: pore scale diffusion and macrodispersion.

Under increasingly powerful microscopes, minerals and porous media have been found to be quite fractured. Indeed, the oft invoked conceptual model divides the water filled domain into mobile water zones between grains of porous media, and immobile zones of stagnant water within the interior of the mineral grain (*Brusseau et al.* [1992], *Neville et al.* [2000], *Li et al.* [1994], *Griffioen et al.* [1998]). Within the mineral grain, diffusion is assumed to be the major process determining contaminant concentrations, while in the mobile phase reaction kinetics and advective mixing are often in control. The transfer of contaminant mass from the immobile (diffusive) zone to the mobile (advective) zone is often a controlling factor in contaminant tailing behavior (see *Li et al.* [1994], *Haggerty and Gorelick* [1995], *Brusseau* [1992], *Griffioen et al.* [1998]).

In the mobile domain, advective mixing is often controlled by porous media heterogeneities both at the pore scale and as a function of heterogeneities at the aquifer

scale (i.e. larger scale variations in hydraulic conductivity). These pore scale and field scale heterogeneities in water flow are commonly modeled by fitting a dispersion coefficient to the data; longitudinal dispersion coefficients have been shown to be scale dependent (*Gelhar et al.* [1992]). Interestingly, however, as numerical models have become increasingly sophisticated and modeling grids have become increasingly more detailed, dispersion caused by pore scale heterogeneity can be explicitly accounted for (*Beckie* [1998]).

Overall, the physical processes for metal/radionuclide behavior are not particularly different from physical processes controlling any other contaminant migration. And as shown in Figure 1.1, these processes tend to occur at the 0.1 mm scale up to the kilometer scale. The major difference between metals/radionuclides and organic contaminants is how the physical processes interact with chemical processes, and how RTM compute both.

1.3.3 Combined Physical/Chemical Effects

As can be seen in Figure 1.1, the physical and chemical processes typically occur at different scales. However, in a contaminated aquifer setting of any scale (columns or field), the physical and chemical effects occur simultaneously and despite the scale discrepancy have the ability to affect each other. Many of the studies cited above either simplify the flow domain (by using batch reactors or homogenous porous media) to understand the basic chemistry controlling metal transport or they simplify the chemistry to understand the physical aspects of transport. These simplifications are made at both the bench and field scales, and may often confuse the "real" reason for observed macro-scale behavior. The presence of these simplifications is also evidence for the absence of scaling methods. This section will highlight several studies where physical and chemical heterogeneities are considered together at a variety of scales and the outcomes of such experiments.

In *Brusseau and Zachara* [1993] the authors pack a column with two sands of different hydraulic conductivities and two different chemical reactivities. A pulse input of radio-labeled Co was injected into the column. The breakthrough curve (BTC) of the Co was fairly traditional in that it had a steep rising edge and displayed tailing behavior that lasted for about 10 pore volumes. In modeling the BTC the dual domain model previously discussed was used. Many of the parameters in the model were fit from either batch sorption data or through the use of the non-reactive tracer tritiated water. The best simulation of the data explicitly included terms for the physical heterogeneity, sorption heterogeneity, rate limited mass transfer between mobile and immobile zones and rate limited sorption.

In the above study, rate limited mass transfer and sorption kinetics were found to have an impact on a bench scale column study. In *Liu et al.* [2006] a combined experimental and modeling study was completed to explore chemical reactivity and intra-granular diffusion. Through extensive characterization of micro-scale chemical heterogeneities (*Liu et al.* [2004]) a conceptual model was created to explain the slow release of uranium from micro-precipitates present in fractures deep within the porous media. The major outcome of the modeling effort was that coupled dissolution and diffusion within a fracture was slower than either process alone. It was found that the diffusion of reactants into the fracture, dissolution, and diffusion of products out, leads to a slower observed release than can be attributed to either dissolution or diffusion. This understanding may help to explain variations in kinetic data between lab and field data, or, in the scaling of kinetic parameters (e.g. *White and Brantley* [2003], *Maher et al.* [2006]). In contrast to the 1-D study of *Liu et al.*[2006], 2-D pore scale modeling efforts (*Li et al.* [2007], *Li et al.* [2006]) found that spatial distributions of reactivity under advective conditions can lead to different observed macroscopic rate behavior even though the total reactivity between simulations was the same. In column experiments pore scale water velocities caused by particle scale heterogeneities have been linked with observed reaction rates (*Pang et al.* [2002]), although the cause of this link has yet to be delineated (*Zhang et al.* [2008], *Chen and Wagenet* [1995], *Haggerty et al.* [2004]).

However, the question still remains what, if any, effect do these pore scale processes have at the field scale. In a 3-D field scale modeling effort *Burr et al.* [1994]

simulated tetrachloroethane in a hypothetical field setting similar to that of the Borden site. Linear sorption behavior and local chemical equilibrium were invoked, and a stochastic approach to hydraulic conductivity and K_D values were adopted. Despite the simplifications to the chemistry involved, "pseudokinetic" behavior was observed in plume displacement and dispersion. The cause of this behavior was only due to macroscopic heterogeneities in the flow field caused by the variations in hydraulic conductivity. In other words pore-scale chemical processes were of limited importance. "Pseudokinetic" behavior is also cited by *Espinoza and Valocchi* [1997], but their hypothetical aquifer was physically homogenous and chemically heterogeneous. In other words pore-scale reactions are controlling contaminant behavior. In a different study, *Harvey and Gorelick* [2000] offer an alternative hypothesis to explain the observed macro-dispersion at the Macrodispersion (MADE) site. The model that they used to describe the field data of an inert tracer did not include dispersion, but with the use of the two domain conceptual model, the same observed dispersion was produced. Thus confusion remains in comparing field and bench scale data, and in determining methodologies to use bench data for field applications.

1.4 Extension of Bench Data to Field Conditions

Steefel et al. [2005] discuss in a generalized fashion specific model formulations to scale fundamental knowledge. Here, I will focus on scaling studies characterized by contaminants whose observed behavior is largely caused by sorption reactions alone, which also include data at: 1) batch to column scales, 2) bench (batch or column scales) to field scales, and 3) simulated data using empirical and stochastic techniques.

1.4.1 Scaling from Batch to Column Scales

Table 1.1 summarizes many studies, most of which contain both batch data, used to create a SCM of some type, and column data where the SCM can be applied to transport data. To scale between these two experimental techniques, reactive surface area of the mineral is often used, although some variations in surface reactivity are sometimes made. What makes each of these studies unique is the choice of SCM, the mineral phase used, and metal of concern. *Barnett et al.* [2000], *Brusseau and Zachara* [1993] and *Gabriel et al.* [1998] all use an empirical approach (sorption isotherms) to describe surface interactions between the contaminant and sediment used. When applied to transport data in the column experiments, the isotherm based models are not good predictors of contaminant breakthrough. Model fits improve when kinetic terms are included in the models. In *Barnett et al.* [2000] and *Gabriel et al.* [1998], this is completed through adding kinetic terms related to chemical reaction; whereas in *Brusseau and Zachara* [1993] mass transfer limitations are also included. Furthermore, in *Gabriel et al.* [1998] lowering the flow rate in a column experiment allowed the kinetic formulation to be omitted (i.e. the local equilibrium assumption was valid).

Szecsody et al. [1998] and *Kohler et al.* [1996] both use a non-electrostatic surface complexation model to describe Co and U transport, respectively, and *Stollenwerk* [1995] uses a diffuse double layer model to describe Mo transport. Just as in the above studies, *Szecsody et al.* [1998] fit kinetic parameters in the RTM in order to fill discrepancies between observed transport behavior and observed batch reactor behavior. Neither *Stollenwerk* [1995] nor *Kohler et al.* [1996] use a kinetic formulation in descriptions of transport behavior. The model formulation used by *Stollenwerk* [1995] is incapable of including kinetically controlled behaviors. Since there is a clear indication of mass transfer limitations of some sort in the breakthrough curves, the simulation of column data based on batch reactor behavior does not accurately capture Mo breakthrough or late time tailing behavior. *Kohler et al.* [1996] explore the explicit omission of kinetic formulations by plotting sorption isotherms derived from batch and

Table 1.1 Summary of bench and column scale work discussed in the text. Note: IX = ion exchange.

Reference	Batch or Column	Solid Phase Type (idealized vs. field material)	Mass of Solid Phase Used (g)	Solid:Sol'n Ratio (g/L, batch only)	Average fluid residence time (hours, column only)	Sorbate	Surface Complexation Model (y/n)	Experimental Duration (batch, days)	Experimental Duration (column, days)	Experimental Length (column, cm)
Barnett et al 2000	Batch	Field	0.1	3.3		U	N	2		
	Column	Field	2		0.18	U	N		55-150	1.7
Brusseau and Zachara 1993	Column	Idealized	1992		3.8	Co	N		3.2	30.5
Gabriel et al. 1998	Batch	Idealized	2	200		U	N	12		
	Column	Idealized	100		1.2 and 12.1	U	N		0.25-25	14.6 and 14.8
Kohler et al. 1996	Batch	Idealized	unspecified	100		U	Y	unspecified		
	Column	Idealized	122		4.01 and 16.0	U	Y		0.94 and 3.74	21.1
Stollenwerk 1995	Batch	Field	10-50	333-1000		Mo	Y	3		
	Column	Field	253-266		18	Mo	Y		9-75	30
Szecsody et al. 1998	Batch	Both	unspecified	unspecified		Co	Y	12.5-42		
	Column	Both	23-204		2.03-7.6	Co	Y		4.1-14.5	14.4-35.6
Zachara et al. 2002	Batch	Field	unspecified	2-250		Cs	IX	0.67		
Steefel et al. 2003	Column	Field	31.5		0.79 and 3.9	Cs	IX		8.2-45	15

column data, and for similar pH the isotherms from the two scales of inquiry are coincident. In contrast *Gabriel et al.* [1998] performed a similar analysis, and found significant differences between column derived sorption and batch derived sorption behavior. Thus it appears that the local equilibrium assumption is valid in *Kohler et al.* [1996] and not in *Gabriel et al.* [1998]. This difference is reflected in the RTM formulations as *Kohler et al.* [1996] did not make any kinetic corrections from batch to column data; however, note the similar column retention times in Table 1.1. *Kohler et al.* [1996] did consider several equilibrium SCM formulations to describe both batch and column data. The SCM parameters that were derived from column studies were capable of predicting both behavior under different chemical conditions in another experimental column and predicting the behavior in batch reactors when using the solid:solution ratio to scale surface interactions. However, the batch derived SCM, did not give good predictions in column studies. The stated reason for this is that batch conditions are less sensitive to strong binding surface site density than are columns. Thus when batch data is plotted as an adsorption edge the error between model and data appears small; when that same SCM is applied to transport scenarios, the change in retardation factors becomes considerable.

Another type of metal/radionuclide interaction with mineral surfaces is ion exchange. Ion exchange models describe positively charged ions interaction with the fixed negative charge present in many types of clay minerals. Largely speaking, these interactions are more prevalent with mono- and divalent species (e.g. Cs^+, Sr^{2+}, I^-, Na^+, Ca^{2+}). In a pair of studies, *Zachara et al.* [2002] completed sediment characterization and batch scale studies of Cs^+ ion exchange with Hanford sediments, while column studies were completed using the same sediments by *Steefel et al.* [2003]. Ion exchange models were fit to batch data based on the cation exchange capacity (CEC) and the specific ion that was being exchanged for Cs^+ (Na^+, K^+, or Ca^{2+}). Depending on the exchanging ions, different numbers of surface sites with variable affinities for each of the ions were included. In the case of Ca^{2+}, five discrete exchange sites were required for description of batch behavior. The use of these batch scale exchange parameters to describe transport data under predicts Cs^+ retardation in column experiments. However, the extent of the discrepancy depends on the specific ion pairings in the column

experiments (Cs^+-Na^+, vs. Cs^+-Ca^{2+}). To circumvent this problem, and to create a global ion exchange model where all of the ions are present in a single transport experiment, the batch data was re-fit using three exchange sites, and is augmented with data from column experiments. As in *Kohler et al.* [1996], the model fits from column data were able to describe both column and the batch data, whereas the batch data did not describe column data particularly well.

In scaling information from the batch to the column scale, there is a significant jump in terms of the amount of heterogeneity. This is reflected in the total mass of sediments used between the two experimental methods, and also between the elapsed experimental times in both methods (Table 1.1). When given by the referenced sources, the mass of sediment used in batch experiments was one to two orders of magnitude smaller than that used in columns. Using the longest experimental times, the ratio of column:batch experimental time ranges from 0.3-75.

How the authors dealt with this heterogeneity discrepancy divides into two groups: kinetic responses and changes in equilibrium surface models. Both *Steefel et al.* [2003] and *Kohler et al.* [1996] change the surface equilibrium models to account for observed changes in reactivity between batch and column scale data. In both of these cases the cause of this discrepancy is attributed to unnoticeable errors in fitting batch data which becomes noticeable error in describing transport. Also in both of these cases, SCM fit from the more heterogeneous column systems can also describe data in the less heterogeneous batch systems. In comparing average hydraulic retention times for *Kohler et al.* [1996] and *Gabriel et al.* [1998] it is interesting to note that they are almost equal in magnitude and range. Despite this, using a clean quartz sand *Kohler et al*. [1996] saw no kinetic hindrances, while *Gabriel et al.* [1998] using a goethite coated sand observed kinetic hindrances. Some of these discrepancies may be attributable to the pH ranges studied (3-5 in *Kohler et al.* and 7-9 in *Gabriel et al.*), but the effective increase in chemical heterogeneity significantly changed U behavior and the necessary scaling response. *Gabriel et al.* [1998], *Brusseau and Zachara* [1993] and *Barnett et al.* [2000] use kinetic formulations to close the gap between batch and column behavior. Part of this approach stems from experimental protocol where local equilibrium assumptions were not valid; the other part of this approach is related to the limitations imposed by the

empirical surface models. When *Barnett et al.* [2000], *Brusseau and Zachara* [1993] and *Gabriel et al.* [1998] determined isotherm parameters from batch data, these parameters are assumed to be constant in the transport scenarios. Whether or not this is true is not explored by the authors. It should also be pointed out that when isotherm parameters were estimated from independent column experiments, they did much better in describing a different column's behavior. So at the same level of total heterogeneity (column scale), and for relatively restricted aqueous phase chemical heterogeneities, the isotherm based transport approach can describe transport behavior.

1.4.2 Scaling from Batch to Field Scales

A common approach to modeling field scale systems contaminated with metals/radionuclides is to collect an aquifer sample, perform batch scale studies for characterization and development of a SCM, and then use this SCM directly in field simulations or in interpreting field data scaling the total surface reactivity to measured values of mineral surface area (*Curtis et al.* [2006], *Stollenwerk* [1998], *Kent et al.* [2000] and [1995], *Davis et al.* [2000]). Of these studies, all but one occurred at the Cape Cod site in Massachusetts. The exception is *Curtis et al.* [2006] which took place at the Naturita site in southwestern Colorado. Relevant characteristics of these studies can be found in Table 1.2.

Stollenwerk [1998] is an extension of the work previously presented at the bench scale. Here, the SCM is extended to a field test in the Cape Cod aquifer. Besides the difference in scales, a major difference between the two works is that in *Stollenwerk* [1998] the SCM has been augmented. In *Stollenwerk* [1995] the SCM consisted of one surface site type, and two Mo-surface reactions. In *Stollenwerk* [1998] the field data is modeled with both the single site type (identical to *Stollenwerk* [1995]) and a two site model with four total Mo-surface reactions, i.e. more surface chemical heterogeneities are being explicitly included. The new site is considered a 'strong' site which has a high affinity for Mo sorption. Relatively good fits to the field data are achieved with both the

Table 1.2 Summary of up-scaling studies from the bench to the field and field simulations.

Reference	Site	Metal(s) of concern	SCM (y/n)	Number of sampling events	Number of sampling wells (including MLS)	Experimental duration	Contaminant Travel Distance (m)	Assumed Dimensionality
Kent et al. 1995	Cape Cod	Cr, Se	Y	28	4	64 days	2	1
Davis et al. 2000	Cape Cod	Cr, Pb, Zn, Cu, Ni	N	11 (for spatial distributions), ~225 (for BTC)	undeterminable	15 months	37, 52	2
Kent et al. 2000	Cape Cod	Zn	Y	1	>>18	~50 yrs (of contaminant migration), 75 year simulation	400	2
Stollenwerk 1998	Cape Cod	Mo	Y	19	656	2.1 yrs	250	2
Curtis et al. 2006	Naturita	U	Y	unspecified	12 (for 11yrs of monitoring), 52 (for 3yrs of monitoring)	~59 yrs (of contaminant migration), 15 yrs (active monitoring)	~1000	2

Field scale simulations with no supporting data

Reference	Site	Metal(s) of concern	SCM (y/n)	Number of nodes	Time steps	Simulation duration	Length of model domain (m)	Assumed Dimensionality
Morrison et al. 1995	Uranium mill remediation	U	Y	720	10 days	216 yrs	914	2
Zhu et al. 2001	Uranium mill remediation	none	N	200	29.2 days	200 yrs	800	1

one and two site SCM; however the two-site model is a closer match over longer periods of time. In model simulations, the addition of the second surface site limits lateral dispersion relative to the one site model. Similar limitations on dispersion were seen for Zn sorption to Cape Cod sediments where two surface sites of two different strengths limited dispersion over a 59 year simulation (*Kent et al.* [2000]). From these bench to field studies it appears that the SCM can be scaled through mineral surface area. The intriguing counter point to this method is that the one surface site model fits of column data in *Stollenwerk* [1995] did not capture the breakthrough or tailing observed in the column. Although this appears to be related to mass transfer limitations, as the model also did not capture the small amount of non-idealities in the Br^- breakthrough curve. The role of second surface site in field applications may be analogous to the re-calculation of SCM formulation that was required by *Steefel et al.* [2003] and *Kohler et al.* [1996] to scale from batch to column systems. Small, unnoticeable errors in fitting SCM at the bench scale may exhibit themselves as the scale of transport increases. The cause of this is most likely due to reactive chemical heterogeneities of the mineral surfaces involved and not physical heterogeneities. Thus the methods used to determine SCM parameters (batch vs. column), and decisions made by SCM developers (one surface site vs. two surface sties, how many reactions to include, etc.) appear to be critical in understanding reactive transport behavior as a function of scale.

In another series of work, uranium sorption to natural sediments has been explored as function of scale. The work of *Davis et al.* [2004], *Davis and Curtis* [2003], and *Curtis et al.* [2006] examine uranium sorption at both bench (batch and column) and field scales. The distinction between this work and the work of *Stollenwerk* [1995] and *Stollenwerk* [1998] is that U aqueous and surface chemistry is far more complex than that of Mo. To describe aqueous U complexation, 23 reactions are included in *Davis et al.* [2004]; whereas *Stollenwerk* [1995] includes only 11 for Mo. Also, the fitted SCM for U at the batch scale is described using six complexation reactions and three surface site types; where as for Mo at most two surface sites and four total reactions were used. From this a hypothesis can be drawn that due to the complexity of U chemistry, it will be more difficult to scale data due to local chemical heterogeneities as a function of scale. However, despite this added level of complexity, similar results were found compared to

Stollenwerk [1998]. The SCM developed from batch scale data using a GC, nonelectrostatic approach (*Davis et al.* [2004]) gives marginally good fits to column data (*Davis and Curtis* 2003), and fairly good fits to field data (*Curtis et al.* [2006]). The discrepancies between model output and column data appeared to be related to chemical conditions in the column experiment; columns with a pH of 7.0 and 0.02 atm of CO_2 had smaller discrepancies than columns at pH of 7.4 or 7.9 with PCO_2 of 0.0028 atm and 373 ppm, respectively. The authors cite kinetic variation as a function of chemical concentrations as a possible reason for the discrepancies. At the field scale, the fits of U to the field data are very good. Hydrologic characterization of the field site showed that hydraulic conductivity did not vary spatially, and several other estimates and assumptions related to precipitative inputs, source term estimates, and other hydrologic terms such as porosity and dispersivity were required. All of these assumptions were tested against the non-reactive transport of Cl^-, which was present at the site as part of the ore roasting process. These fits are somewhat dubious as the simulations occurred over ~50 years, but only about ten years of data were available. And, since chemical and physical processes are connected, it is unclear how these assumptions related to physical characterization helped to influence the modeled U distribution. Nevertheless, the same behavior where column data is marginally well described by a SCM and field data is very well described is evident. A final point from *Curtis et al*. [2006] is that for the model formulation used, the scaled sensitivity of the SCM terms was equal to zero for length scales up to 500m. In other words, in this case, below 500m of length there is little to no model sensitivity to chemical reactivity terms.

In these batch to column to field scale studies, the major scaling method is through surface area of the mineral phase. Since the transport behavior of the ions is controlled through surface reactions, scaling to surface area seems reasonable. However, there is evidence that the important value is not total surface area, but instead reactive surface area. *Fuller et al.* [1995] found good correlations between Pb/Zn sorbed concentrations and Fe/Al phases extracted in a selective extraction, and only weak correlations between Pb/Zn sorbed concentrations and particle size, a proxy for surface area. Separating reactive and total surface areas is a fairly complicated procedure as total surface area determinations (N_2 BET, Hg porosimetery, etc.) are not without their

artifacts, and reactive surface area determinations are complicated by poorly formed crystalline phases, and surface coatings (*Arnold et al.* [1998], *Arnold et al.* [2001]). Obtaining the reactive surface area often requires either potentiometric titrations of the mineral surface, or saturation of the surface with the contaminant of interest, or both. However, even then there are limitations to this practice with both ideal and natural sediments (*Lutzenkirchen et al.* [2002]). As SCM are usually fit to macroscopic batch data, the determined binding constants represent an averaging of contaminant sorption behavior over both the reactive and non-reactive areas on the surface. Scaling SCM through total surface area assumes that: 1) the degree of surface heterogeneity/reactivity of sediment material used in SCM formulation experiments is similar to that found in the field, and 2) that the water-rock interactions and reactivity will be similar in field conditions compared to batch conditions. This latter assumption has been tested by *Payne et al.* [2001] and *Curtis et al.* [2004]. In both of these studies favorable comparisons are made between SCM predictions based on batch scale determinations and *in-situ* determined K_D values. However, both of these studies use similar masses of sediment material (tens of grams) for both the *in-situ* and batch determinations. The first assumption is more difficult to test, but it can be argued that the deviation between simulations based on batch experiments and column scale behavior is evidence that the surface reactivity is not constant as a function of scale.

Despite these considerations, from the data presented here, it appears that extrapolating from batch to field scale heterogeneity via surface area appears to be an approach that gives satisfactory results. This same technique has been used to scale sorption behavior at the same experimental scale but with different minerals (i.e. scaling through increasing levels of chemical heterogeneity, *Prikryl et al.* [2001], *Bertetti et al.* [1998]). The question still remains as to why this procedure does not appear to work at extrapolating from the batch to the column scale. One possibility is that the fitting of field data smoothes any error caused by local chemical heterogeneity. In columns, where a transport model can be more accurately constrained the variability in surface behavior as a function of scale is more apparent.

1.4.3 Empirical and Stochastic Techniques

An alternative to using surface area as a scaling technique is to use empirical surface complexation descriptions (i.e. K_D based models), and then use a stochastic treatment through Monte Carlo simulations. The stochastic approach stems from physical hydrology where the assumption can be made that traditional flow and transport equations (ADE) are valid and that the method or scale of measurement does not match that of the equations (*Cushman* [1986], *Dagan* [1986]). Thus much work has been dedicated to creating a single hydraulic conductivity measurement at the critical scale from many point measurements at the sub-critical scale. This single measurement is given a statistical distribution about a mean (often log-normal), and then Monte Carlo simulations are completed for values within the distribution. The output of the simulations are averaged (ensemble averaging) to get a final output (e.g. *Neuman and di Federico* [1998], *Selroos and Cvetkovic* [1992], *Rajaram* [1997]). Stochastic techniques have been largely relegated to scaling flow and transport parameters, although there are several examples where stochastic techniques have also been used to describe surface reactions (*Burr et al.* [1994], *Rajaram* [1997]). However, many assumptions were made in these studies that are not generally true for inorganic transport, most notably the assumptions of linear sorption behavior and an inverse relationship between log hydraulic conductivity and log K_D values (*Fuller et al.* [1996]). So, the translation of the knowledge gained from these studies to upscaling metal transport behavior may be limited. Furthermore, this upscaling technique has never been applied to field data, organic or inorganic. It has been suggested by *Turner et al.* [2006] that the stochastic approach is best for systems where bounding calculations are more important than specific predictions, such as in the siting of a nuclear waste repository. The use of such an approach is bolstered by the fact that empirical sorption parameters of several metals/radionuclides have been found to be log normal in distribution (*Turner et al.* [2006], *Payne et al.* [2001]).

1.5 Scales of Measurement and Scales of Application

Philosophically, the need for a model becomes increasingly irrelevant as the amount of characterization increases. Models are meant to be meaningful representations; however, as the amount of characterization increases the model becomes less of a general representation and instead becomes an explicit description of the system being modeled. One source of the need for scaling in transport models stems from the fact that characterization of most earth systems can only be partially accomplished. Also there is no way to know the extent of our characterization without characterizing the entire system, at which point the model loses its relevance. Thus, the amount of characterization plays a critical role in model formulation and it divides between spatial characterization and temporal characterization.

1.5.1 Characterization in Spatial Dimensions

Figure 1.2 compares the relative amount of characterization possible as a function of the water volume in an aquifer. The y-axis represents the total sample volume of a single sampling event in time divided by the total water volume of the aquifer presented as a percent. For the bench scale work of *Kohler et al.* [1996], and *Kantar and Honeyman* [2006], the sample volume was comprised of what had eluted from the effluent end of the column in between sampling events. The work of *Neiss et al.* [2007] included ports located as a function of distance along the column length. For the field scale sites and the two studies which are not grouped, a few approximations were necessary. First, when not given, porosity of the aquifers was assumed to be 0.3. Second, the well purge volume was included as part of the sample volume, and when not given a total sample volume of 1L was assumed for field sites. And finally, the total aquifer volume is the volume of water which was contaminated at the time of the study

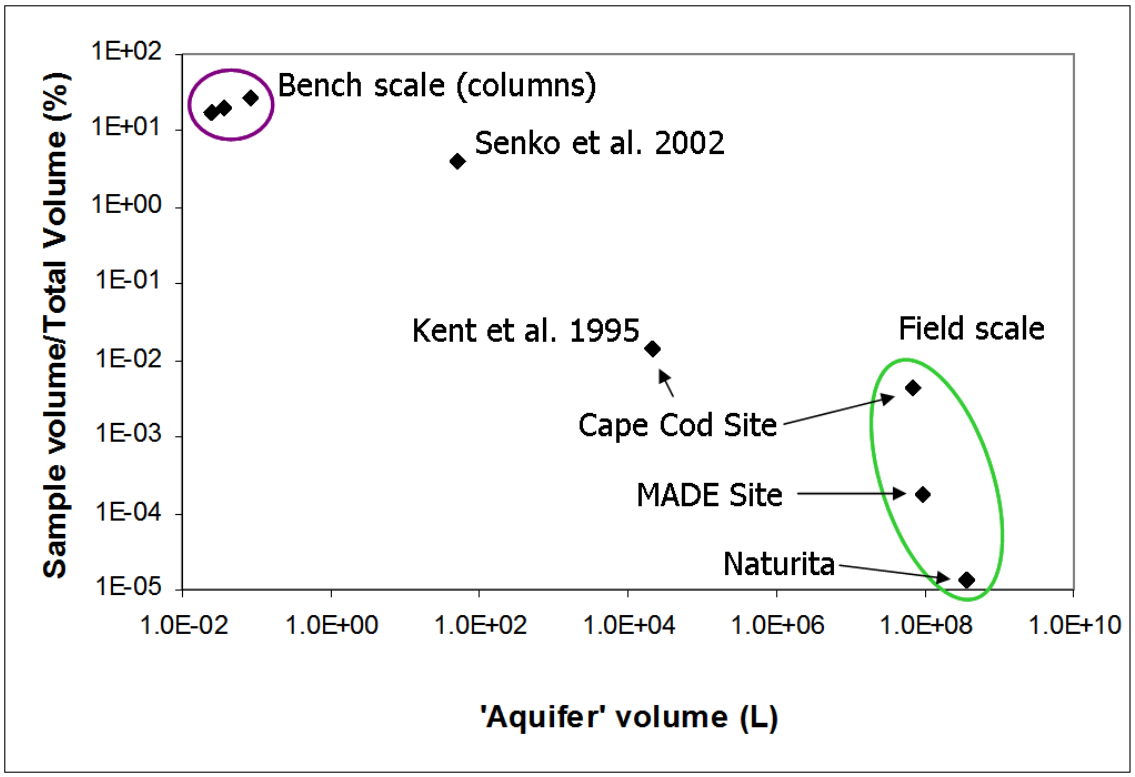

Figure 1.2 Relative amount of characterization possible as a function of aquifer volume. Bench scale references: Kohler et al. [1996], Neiss et al. [2007], Kantar and Honeyman [2006]. Field scale references: Stollenwerk [1998], Boggs et al. [1992], Curtis et al. [2006].

(*Kent et al.* [1995] was a 2-dimensional study and so a width of 1m was assumed.).

The most striking feature of this plot is the bimodality for traditional experimental scales. The bench scale work is characterized by having a very small aquifer volume, and a high percent of characterization. The field sites are characterized by large total volumes, and considerably smaller levels of characterization. The two intermediate points are included to show how certain experimental techniques can be used to help connect bench scale characterization with field scale behavior. The work of *Senko et al.* [2002] included 'push-pull' tests to study the amount of uranium immobilization that can be expected in an in-situ system. This is not a metal transport study per se, in that the transport involved was dominated by injection of electron donor and acceptor, and then removing sample volumes after a period of incubation. However, it is included here to emphasize that new experimental techniques may be required to help solve the scaling issues associated with RTM. The *Kent et al.* [1995] study was a reactive tracer test where chromium and selenium were injected into the Cape Cod aquifer. The major difference between this work and others is that the scale of chromium and selenium transport was only 2.0m. Thus the total volume is substantially smaller than other field sites. The discrepancy in levels of characterization between experimental methods limits the total number of variables that can be accurately determined in field scale systems compared to bench scale systems, and also obviates the need for scaling methodologies.

Another point relating to Figure 1.2 is that if a plot could be constructed comparing the total number of variables that can be controlled in an experimental system vs. the scale of the experimental system, the same type of relationship would hold. At smaller scales, a much higher number of variables can be controlled including sediment type, influent used, flow rates, etc. In the field, the controllable variables are severely limited. This raises a theoretical concern about solely using field scale systems to elucidate scaling methods. There are many variables that cannot be determined, and many others that cannot be controlled. Some have even raised the point that delineation of fundamental transport processes from field scale experiments may be impossible (*Bryant and Thompson* [2001]). Indeed, in many model formulations, similar output behavior can be created from drastically different conceptual models (*Espinoza and Valocchi* [1997] and *Burr et al.* [1994] mentioned earlier, and Figure 5 in *Kent et al.*

[1995] where similar changes in breakthrough curve shape can be created by changing the SCM or the amount of lateral dispersion).

Figure 1.2 is focused on the characterization of the aqueous phase, however a similar relationship would be found between experimental scale and characterization of the solid phase material. As part of a field experiment, sediment cores are often removed for characterization of physical and chemical properties. These sediments are often characterized by both simpler methods, such as XRD, sequential chemical extractions, N_2 BET measurements, etc., and more extravagant methods such as SEM, TEM, and synchrotron based technologies. Using all of these techniques the core as removed from the ground can be characterized in terms of almost any physical or chemical parameters necessary for RTM conceptual models. However, the upscaling of core characterization to a model grid scale is complicated by physical heterogeneities at the field scale. Returning to Figure 1.2, the issue is then how to meaningfully relate the level of possible bench scale characterization of a single core (high degree of characterization, low total volume/mass) to the level of field scale application (low degree of characterization, high total volume/mass).

Because of this limited level of characterization, new experimental methods are necessary. Ideally, these new experiments would: 1. plot in the area of *Senko et al.* [2002], and *Kent et al.* [1995] in Figure 1.2, and 2. allow for explicit control of physical and chemical heterogeneities. Indeed, there are several reports of experiments that are taking place at this 'intermediate' scale. However, many of these experiments are concerned only with upscaling of flow parameters (*Fernandez-Garcia et al.* [2002], *Chao et al.* [2000], *Barth et al.* [2001]a) or inert transport (*Barth et al.* [2001]b, *Levy and Berkowitz* [2003]), while others are focused on multi-phase and organic contaminant transport (e.g. *Illangasekere et al.* [1995]). In order to help determine scaling methods for RTM, these same types of experiments need to be completed with inorganic contaminants where local chemical and physical heterogeneities can be quantified and controlled.

1.5.2 Characterization in Time

Tables 1.1 and 1.2 give a summary of experimental protocol with respect to the timing of both bench and field scale experiments, respectively. There is a very large discrepancy between an average column experiment (~45 days as presented in Table 1.1) and the timescale of an average field simulation (~decades-centuries). With respect to RTM, this represents a significant barrier to scaling kinetic information. Ideally, rate laws relating to mineral precipitation/dissolution, adsorption/desorption, and redox transformations can be extended through time and connected to the descriptions of mechanistic chemistry in RTM.

There are several problems with this idea. The first is related to use of the semi-mechanistic SCM described above. Because of the semi-mechanistic approaches to modeling which have heretofore been applied in transport scenarios, fundamental rate laws with respect to adsorption reactions are not applicable. The second problem is related to mineral dissolution/precipitation reactions. There is a well discussed discrepancy between mineral dissolution rates as measured in laboratories compared to those estimated from field data. This discrepancy can be attributed to several reasons including: coupled chemical reactions (*Maher et al.* [2006]), changes in surface reactivity (*White and Brantley* [2003], *VanCappellen* [1996]), heterogeneous grain size distributions (*Lichtner and Tartakovsky* [2003]), coupled physical and chemical processes (*Liu et al.* [2006]), as well as pore scale heterogeneities (*Li et al.* [2007], *Meile and Tuncay* [2006]). With respect to metal/radionuclide transport, the dissolution/precipitation of minerals can affect transport through: solubility controls, dissolution by-product complexation (e.g., pH or carbonate dependent aqueous complexation), and metal/radionuclide incorporation into a precipitating mineral (i.e. solid solution formation). Without the ability to describe these rate limited reactions in a meaningful way, spatial distributions of reactive products cannot be predicted. And finally, reaction rates are often controlled by physical processes occurring at much larger scales. For example, advective mixing at larger length scales can control the local chemical concentration profile near a reactive surface. This physical control on concentration can create spatial gradients in reactive rates. Thus, explicit consideration

of rate-limited processes has largely been limited to more empirical applications (see *Li et al.* [2006] and *Liu et al.* [2006]).

As mentioned earlier, the distributed rate laws may be the best conceptual model to describe such complex systems where both physical and chemical heterogeneities contribute to spatially and temporally variable observed rates of reaction (*Rajaram* [1997], *Haggerty et al.* [2004]). This method is somewhat analogous to the GC SCM approach, where the system is deemed too complex to really understand, so a hypothetical and not particularly physically meaningful representation is used instead. If this analogy holds true, the wide scale application of a single rate distribution relationship is probably not warranted (i.e., this approach will not be scale independent through heterogeneity found at different field sites). This approach at describing rate controlled processes has been applied to metal/radionuclide transport by *Qafoku et al.* [2005]. The authors apply a distributed rate model to several column experiments with favorable results, but only a single groundwater composition was used. Since these distributed rate models are based on K_D descriptions of contaminant sorption, the use of a single set of kinetic parameters for different ground water compositions may or may not describe observed data. Put another way, the distributed rate model may be able to describe reactive rate limited reactions caused by surface heterogeneities, but it may not be able to describe variations in reaction paths as a function of solution phase heterogeneities. Also, most RTM codes are not currently capable of including distributed reactivity formulations. It has also been untested as to whether a single distributed rate function can describe data over field relevant portions of time.

In considering which kinetic formulation to use in transport scenarios we must return to Figures 1.1, 1.2, and Tables 1.1 and 1.2. In transport scenarios we are fundamentally limited in the amount of characterization that can occur at the field scale; this is true for physical/chemical characteristics as well as temporal characteristics. In Table 1.2, it is remarkable that the number of sampling events for field sites range from one to several hundred over the course of, at longest, 15 years of monitoring. Despite this, the simulations range from 64 days to 216 years. If there is a very slow rate limited process, would the limited characterization that is possible in field settings be able to detect it over the time ranges used for sampling? And, if it were, how would that

knowledge be included in a RTM where the chemical processes are occurring at a scale well below a standard grid cell? Extrapolation of bench data is even more complex, as the longer column experiments last about 150 days, and by their very nature solid phase cores represent a point measurement in time. In all of the field site studies presented here, kinetic formulations were not necessary to fit the observed data. It is unclear as to whether this is related to the assumptions made by the modelers, that the field sites all had conditions consistent with the local equilibrium assumption, or whether kinetic effects, if any, were below an effective 'detection limit' for field scale characterization.

1.6 Discussion

Most of the attempts to describe scale effects in porous media fall into three categories: mathematical, empirical relationships and alterations to a conceptual model. In physical hydrology literature, the observation of scale dependence has led to many mathematical methods that either scale a specific parameter based on certain conditions (*Renard and de Marsily* [1997], *Gasda and Celia* [2005], *Wood et al.* [2003]) or scale field measurable parameters to a calculated 'ensemble' measurement that can be used in transport codes (*Cushman* [1986], *Dagan* [1986], *Neuman and di Federico* [1998], *Selroos and Cvetkovic* [1992], *Rajaram* [1997]). It has also been noted that the best scaling methodologies for determining bulk flow may not be the best scaling method for mass transport (*Scheibe and Yabusaki* [1998]). Thus, to follow this line of reasoning, each parameter in a transport code may need an independent scaling calculation. This process would be daunting to carry out, and would require scaling relationships for all of the variables used in both space and time. In simulations where chemical reactions are considered, the numerical formulation is considerably more complex (*Quintard and Whitaker* [1998], *Rubin* [1983]). The state of general knowledge on scaling relationships is far too limited to derive scaling equations for the multitude of variables that occur in RTM. Furthermore, many of the numerical attempts at up-scaling chemical reactions in porous media are so complex that model transparency is lost; the ability to discern cause

and effect relating to transport is impossible to critically evaluate (*Konikow and Bredehoeft* [1992], *Oreskes* [1994], [2000] and [2001]). This runs counter to the goal of RTM which is to act as "an important set of interpretive tools for unraveling complex interactions between coupled processes and the effects of multiple space and time scales in the Earth" (*Steefel et al.* [2005]).

Though they are important to critically evaluate experimental systems and to help determine the best experimental path, mathematical attempts at scaling are probably not the answer to the scaling problem. As has been pointed out, the processes involved in RTM are many and the scale over which they occur are too small to be explicitly included in RTM. So, either scaling of measurements and fundamental processes up to a model grid cell or a different conceptual model is needed for RTM to be widely applied to contaminant transport scenarios independent of scale. In order to achieve this, new experiments are needed at the 'intermediate' scale where physical and chemical heterogeneities can be controlled and/or quantified. This will allow for a 'bridge' between bench and field data, and may allow for the creation of a new conceptual model for RTM where scale can be explicitly accounted for.

Fundamentally, the scaling relationship is scaling as a function of the heterogeneities inherent to a system at different length scales: surface site reactive heterogeneity of a single mineral, spatial heterogeneity of mineral types, flow heterogeneity caused by physical heterogeneity, and rate heterogeneity caused by spatial and temporal variations in chemical/physical heterogeneity. Since there is no direct measure of heterogeneity, we rely on measurable proxies such as length and time scales to represent heterogeneity. Currently, data is limited to only two levels of heterogeneity. To test scaling methods and new conceptual models which inherently account for system heterogeneity, more data is needed at different levels of heterogeneity. Before this occurs, codes may be written and simulations may be performed, but whether these models are representations of real systems remains untestable.

1.7 References

Arai, Yuji, M. McBeath, J.R. Bargar, J. Joye, and J.A. Davis. 2006. Uranyl adsorption and surface speciation at the imogolite-water interface: Self-consistent spectroscopic and surface complexation models. *Geochimica et Cosmochimica Acta* 70:2492-2509.

Arnold, T., T. Zorn, G. Bernhard, and H. Nitsche. 1998. Sorption of uranium(VI) onto phyllite. *Chemical Geology* 151:129-141.

Arnold, T., T. Zorn, H. Zanker, G. Bernhard, and H. Nitsche. 2001. Sorption behavior of U(VI) of phyllite: experiments and modeling. *Journal of Contaminant Hydrology* 47:219-231.

Barnett, M.O., P.M. Jardine, S.C. Brooks, and H.M. Selim. 2000. Adsorption and Transport of Uranium(VI) in Subsurface Media. *Soil Science Society of America Journal* 64:908-917.

Barth, Gilbert R., Mary C. Hill, Tissa H. Illangasekare, and Harihar Rajaram. 2001a. Predictive modeling of flow and transport in a two-dimensional intermediate-scale, heterogeneous porous medium. *Water Resources Research* 37 (10):2503-2512.

Barth, Gilbert R., Tissa H. Illangasekare, Mary C. Hill, and Harihar Rajaram. 2001b. A new tracer-density criterion for heterogeneous porous media. *Water Resources Research* 37 (1):21-31.

Beckie, Roger. 1998. Chapter 11 Analysis of Scale Effects in Large-Scale Solute-Transport Models. In *Scale Dependence and Scale Invariance in Hydrology*, edited by G. Sposito. Cambridge, UK: Cambridge University Press.

Bernhard, G., G. Geipel, T. Reich, V. Brendler, S. Amayri, and H. Nitsche. 2001. Uranyl(VI) carbonate complex formation: Validation of the $Ca_2UO_2(CO_3)_{3(aq)}$ species. *Radiochimica Acta* 89:511-518.

Bertetti, F.P., Roberto T. Pabalan, and Michael G. Almendarez. 1998. Studies of Neptunium(V) Sorption on Quartz, Clinoptilolite, Montmorillonite, and alpha-Alumina. In *Adsorption of Metals by Geomedia*, edited by E. A. Jenne. San Diego: Academic Press.

Bethke, Craig M., and Patrick V. Brady. 2000. How the K_D Approach Undermines Ground Water Cleanup. *Ground Water* 38 (3):435-443.

Boggs, J. Mark, Steven C. Young, Lisa M. Beard, Lynn W. Gelhar, Kenneth Rehfeldt, and E. Eric Adams. 1992. Field Study of Dispersion in a Heterogeneous Aquifer 1. Overview and Site Description. *Water Resources Research* 28 (12):3281-3291.

Brusseau, Mark L., Ron E. Jessup, and P. Suresh C. Rao. 1992. Modeling Solute Transport Influenced by Multiprocess Nonequillibrium and Transformation Reactions. *Water Resources Research* 28 (1):175-182.

Brusseau, Mark L. 1992. Transport of Rate-Limited Sorbing Solutes in Heterogeneous Porous Media: Application of a One-Dimensional Multifactor Nonideality Model to Field Data. *Water Resources Research* 28 (9):2485-2497.

Brusseau, Mark L., and John M. Zachara. 1993. Tranport of Co^{2+} in a Physically and Chemically Heterogeneous Porous Medium. *Environmental Science and Technology* 27 (9):1937-1939.

Bryant, Steven L., and Karsten E. Thompson. 2001. Theory, modeling and experiment and reactive transport in porous media. *Current Opinion in Colloid and Interface Science* 6:217-222.

Burr, D.T., Edward A. Sudicky, and R.L. Naff. 1994. Nonreactive and reactive solute transport in three-dimensional heterogeneous porous media: Mean displacement, plume spreading, and uncertainty. *Water Resources Research* 30 (3):791-815.

Chao, Hsin-Chia, Harihar Rajaram, and Tissa H. Illangasekare. 2000. Intermediate-scale experiments and numerical simulations of transport under radial flow in a two-dimensional heterogeneous porous media. *Water Resources Research* 36 (10):2869-2884.

Chen, Wenlin, and Robert J. Wagenet. 1995. Solute Transport in Porous Media with Sorption-Site Heterogeneity. *Environmental Science and Technology* 29 (11):2725-2734.

Curtis, Gary P., Patricia Fox, Matthias Kohler, and James A. Davis. 2004. Comparison of in situ K_D values with a laboratory determined surface complexation model. *Applied Geochemistry* 19:1643-1653.

Curtis, Gary P., J.A. Davis, and David L. Naftz. 2006. Simulation of reactive transport of uranium(VI) in groundwater with variable chemical conditions. *Water Resources Research* 42: W04404, doi:10.1029/2005WR003979.

Cushman, John H. 1986. On Measurement, Scale, and Scaling. *Water Resources Research* 22 (2):129-134.

Dagan, Gedeon. 1986. Statistical Theory of Groundwater Flow and Transport: Pore to Laboratory, Laboratory to Formation, Formation to Regional Scale. *Water Resources Research* 22 (9):120S-134S.

Davis, J.A., Robert O. James, and James O. Leckie. 1978. Surface Ionization and Complexation at the Oxide/Water Interface I. Computation of Electrical Double

Layer Properties in Simple Electrolytes. *Journal of Colloid and Interface Science* 63 (3):480-499.

Davis, J.A., and James O. Leckie. 1978a. Surface Ionization and Complexation at the Oxide/Water Interface II. Surface Properties of Amorphous Iron Oxyhydroxide and Adsorption of Metal Ions. *Journal of Colloid and Interface Science* 67 (1):90-107.

Davis, J.A., and James O. Leckie. 1978b. Effect of Adsorbed Complexing Ligands on Trace Metal Uptake by Hydrous Oxides. *Environmental Science and Technology* 12 (12):1309-1315.

Davis, J.A., and James O. Leckie. 1980. Surface Ionization and Complexation at the Oxide/Water Interface III. Adsorption of Anions. *Journal of Colloid and Interface Science* 74 (1):32-43.

Davis, J.A., Jennifer A. Coston, D.B. Kent, and Christopher C. Fuller. 1998. Application of the Surface Complexation Concept to Complex Mineral Assemblages. *Environmental Science and Technology* 32 (19):2820-2828.

Davis, J.A., D.B. Kent, Jennifer A. Coston, K.M. Hess, and J.L. Joye. 2000. Multispecies reactive tracer test in an aquifer with spatially variable chemical conditions. *Water Resources Research* 36 (1):119-134.

Davis, J.A., and Gary P. Curtis. 2003. Application of Surface Complexation Modeling to Describe Uranium(VI) Adsorption and Retardation at the Uranium Mill Tailings Site at Naturita, Colorado. Washington D.C.: U.S. Nuclear Regulatory Commission.

Davis, J.A., David E. Meece, Matthias Kohler, and Gary P. Curtis. 2004. Approaches to surface complexation modeling of uranium(VI) adsorption on aquifer sediments. *Geochimica et Cosmochimica Acta* 68 (18):3621-3641.

De Windt, L., A. Burnol, P. Montarnal, and J. van der Lee. 2003. Intercomparison of reactive transport models applied to UO_2 oxidative dissolution and uranium migration. *Journal of Contaminant Hydrology* 61:303-312.

Espinoza, Carlos, and Albert J. Valocchi. 1997. Stochastic analysis of one-dimensional transport of kinetically adsobing solutes in chemically heterogeneous aquifers. *Water Resources Research* 33 (11):2429-2445.

Farley, Kevin J., David A. Dzombak, and Francois M. M. Morel. 1985. A Surface Precipitation Model for the Sorption of Cations on Metal Oxides. *Journal of Colloid and Interface Science* 106 (1):226-242.

Fernandez-Garcia, Daniel, Xavier Sanchez-Vila, and Tissa H. Illangasekare. 2002.

Convergent-flow tracer tests in heterogeneous media: combined experimental-numerical analysis for determination of equivalent transport parameters. *Journal of Contaminant Hydrology* 57:129-145.

Fox, Patricia, J.A. Davis, and John M. Zachara. 2006. The effect of calcium on aqueous uranium(VI) speciation and adsorption to ferrihydrite and quartz. *Geochimica et Cosmochimica Acta* 70:1379-1387.

Fuller, Christopher C., J.A. Davis, Jennifer A. Coston, and Eleanor Dixon. 1996. Characterization of metal adsorption variability in a sand and gravel aquifer, Cape Cod, Massachusetts, U.S.A. *Journal of Contaminant Hydrology* 22:165-187.

Gabriel, U., J.-P. Gaudet, L. Spadini, and Laurent Charlet. 1998. Reactive transport of uranyl in a goethite column: an experimental and modeling study. *Chemical Geology* 151:107-128.

Gasda, S.E., and M.A. Celia. 2005. Upscaling relative permeabilities in a structured porous medium. *Advances in Water Resources* 28:493-506.

Gelhar, Lynn W., Claire Welty, and Kenneth R. Rehfeldt. 1992. A Critical Review of Data on Field-Scale Dispersion in Aquifers. *Water Resources Research* 28 (7):1955-1974.

Haggerty, Roy, and Steven M. Gorelick. 1995. Multiple-rate mass transfer for modeling diffusion and surface reactions in media with pore-scale heterogeneity. *Water Resources Research* 31 (10):2383-2400.

Haggerty, Roy, Charles Harvey, Claudius Freiherr von Schwerin, and Lucy C. Meigs. 2004. What controls the apparent time-scale of solute mass transfer in aquifers and soils? A comparison of experimental results. *Water Resources Research* 40.

Harvey, Charles, and Steven M. Gorelick. 2000. Rate-limited mass transfer or macrodispersion: Which dominates plume evolution at the Macrodispersion Experiment (MADE) site? *Water Resources Research* 36 (3):637-650.

Hiemstra, T., and W.H. van Riemsdijk. 1996. A Surface Structural Approach to Ion Adsorption: The Charge Distribution (CD) Model. *Journal of Colloid and Interface Science* 179:488-508.

Hohl, Herbert, and Werner Stumm. 1976. Interaction of Pb^{2+} with Hydrous gamma-Al2O3. *Journal of Colloid and Interface Science* 55 (2):281-288.

Honeyman, Bruce D. 1984. Ph.D. Thesis. Cation and Anion Adsorption in Binary Mixtures of Adsorbents: An Investigation of the Concept of Adsorptive Additivity. Stanford University, Stanford, CA.

Honeyman, Bruce D., and James F. Ranville. 2002. Colloid Properties and Their Effects on Radionuclide Transport through Soils and Groundwaters. In *Geochemistry of Soil Radionuclides*, edited by P.-C. Zhang and M. V. Brady. Madison: Soil Science Society of America.

Illangasekare, Tissa H., James L. Ramsey Jr., Karsten H. Jensen, and Michael B. Butts. 1995. Experimental study of movement and distribution of dense organic contaminants in heterogeneous aquifers. *Journal of Contaminant Hydrology* 20:1-25.

Kalmykov, Stepan N., and Gregory R. Choppin. 2000. Mixed $Ca^{2+}/UO^{2+}/CO_3^{2-}$ complex formation at different ionic strengths. *Radiochimica Acta* 88:603-606.

Kantar, Cetin, and Bruce D. Honeyman. 2006. Citric Acid Enhanced Remediation of Solids Contaminated with Uranium by Soil Flushing and Soil Washing. *Journal of Environmental Engineering* 132 (2):247-255.

Kent, D.B., J.A. Davis, C.D. Anderson, and B.A. Rea. 1995. Transport of chromium and selenium in a pristine sand and gravel aquifer: Role of adsorption processes. *Water Resources Research* 31 (4):1041-1050.

Kent, D.B., R.H. Abrams, J.A. Davis, Jennifer A. Coston, and D.R LeBlanc. 2000. Modeling the influence of variable pH on the transport of zinc in a contaminated aquifer using semiempirical surface complexation models. *Water Resources Research* 36 (12):3411-3425.

Kohler, Matthias, Gary P. Curtis, D.B. Kent, and J.A. Davis. 1996. Experimental investigation and modeling of uranium(VI) transport under variable chemical conditions. *Water Resources Research* 32 (12):3539-3551.

Kohler, Matthias, Bruce D. Honeyman, and James O. Leckie. 1999. Neptunium(V) Sorption on Hematite (alpha-Fe_2O_3) in aqueous suspension: The Effect of CO_2. *Radiochimica Acta* 85:33-48.

Kohler, Matthias, Gary P. Curtis, David E. Meece, and James A. Davis. 2004. Methods for Estimating Adsorbed Uranium(VI) and Distribution Coefficients of Contaminated Sediments. *Environmental Science and Technology* 38:240-247.

Konikow, Leonard F., and John D. Bredehoeft. 1992. Ground-water models cannot be validated. *Advances in Water Resources* 15:75-83.

Lenhart, John J., and Bruce D. Honeyman. 1999. Uranium(VI) sorption to hematite in the presence of humic acid. *Geochimica et Cosmochimica Acta* 63 (19/20):2891-2901.

Levy, Melissa, and Brian Berkowitz. 2003. Measurement and analysis of non-Fickian dispersion in heterogeneous porous media. *Journal of Contaminant Hydrology*

64:203-226.

Li, L., D.A. Barry, P.J. Culligan-Hensley, and K. Bajracharya. 1994. Mass transfer in soils with local stratification of hydraulic conductivity. *Water Resources Research* 30 (11):2891-2900.

Li, L., C.A. Peters, and M.A. Celia. 2006. Upscaling geochemical reaction rates using pore-scale network modeling. *Advances in Water Resources* 29:1351-1370.

Li, L., C.A. Peters, and M.A. Celia. 2007. Effects of mineral spatial distribution on reaction rates in porous media. *Water Resources Research* 43 (Online (W01419)):17.

Lichtner, Peter C., and D.M. Tartakovsky. 2003. Stochastic analysis of effective rate constant for heterogeneous reactions. *Stochastic Environmental Research and Risk Assessment* 17:419-429.

Liu, Chongxuan, John M. Zachara, Odeta S. Qafoku, James P. McKinley, Steve M. Heald, and Zheming Wang. 2004. Dissolution of uranyl microprecipitates in subsurface sediments at Hanford Site, USA. *Geochimica et Cosmochimica Acta* 68 (22):4519-4537.

Liu, Chongxuan, John M. Zachara, Wassana Yantasee, Paul D. Majors, and James P. McKinley. 2006. Microscopic reactive diffusion of uranium in the contaminated sediments at Hanford, United States. *Water Resources Research* 42.

Lutzenkirchen, Johannes, Jean-Francois Boily, Lars Lovgren, and Staffan Sjoberg. 2002. Limitations of the potentiometric titration technique in determining the proton active site density of goethite surfaces. *Geochimica et Cosmochimica Acta* 66 (19):3389-3396.

Maher, Kate, Carl I. Steefel, Donald J. DePaolo, and Brian E. Viani. 2006. The mineral dissolution rate conundrum: Insights from reactive transport modeling of U isotopes and pore fluid chemistry in marine sediments. *Geochimica et Cosmochimica Acta* 70:337-363.

Meile, Christof, and Kagan Tuncay. 2006. Scale dependence of reaction rates in porous media. *Advances in Water Resources* 29:62-71.

Morrison, Stan J., Robert R. Spangler, and Vijay S. Tripathi. 1995a. Adsorption of uranium(VI) on amorphous ferric oxyhydroxide at high concentrations of dissolved carbon(VI) and sulfur(VI). *Journal of Contaminant Hydrology* 17:333-346.

Morrison, Stan J., Vijay S. Tripathi, and Robert R. Spangler. 1995b. Coupled reaction/transport modeling of a chemical barrier for controlling uranium(VI)

contamination in groundwater. *Journal of Contaminant Hydrology* 17:347-363.

Neiss, Jim, Brandy D. Stewart, Peter S. Nico, and Scott Fendorf. 2007. Speciation-Dependant Microbial Reduction of Uranium within Iron-Coated Sands. *Environmental Science and Technology* 41 (21):7343-7348.

Neuman, Shlomo P., and Vittorio di Federico. 1998. Chapter 13 Correlation, Flow, and Transport in Multiscale Permeability Fields. In *Scale Dependence and Scale Invariance in Hydrology*, edited by G. Sposito. Cambridge: Cambridge University Press.

Oreskes, Naomi, Kristin Shrader-Frechette, and Kenneth Belitz. 1994. Verification, Validation, and Confirmation of Numerical Models in the Earth Sciences. *Science* 263:641-646.

Oreskes, Naomi. 2000. Why Believe a Computer? Models, Measures, and Meaning in the Natural World. In *The Earth Around Us: Maintaining a Livable Planet*, edited by J. S. Schneiderman. San Francisco: W.H. Freeman and Co.

Oreskes, Naomi, and Kenneth Belitz. 2001. Philosophical Issues in Model Assessment. In *Model Validation: Perspectives in Hydrological Science*: John WIley and Sons, Ltd.

Pang, Lipang, Murray Close, Daniela Schneider, and Greg Stanton. 2002. Effect of pore-water velocity on chemical nonequilibrium transport of Cd, Zn, and Pb. *Journal of Contaminant Hydrology* 57:241-258.

Payne, T.E., R. Edis, B.R. Fenton, and T.D. Waite. 2001. Comparison of laboratory uranium sorption data with 'in situ distribution coefficients' at the Koongarra uranium deposit, Northern Australia. *Journal of Environmental Radioactivity* 57:35-55.

Payne, T.E., and Peter L. Airey. 2006. Radionuclide migration at the Koongarra uranium deposit, Northern Australia- Lessons from the Alligator Rivers analogue project. *Physics and Chemistry of the Earth* 31:572-286.

Payne, T.E., J.A. Davis, M. Ochs, M. Olin, C.J. Tweed, S. Altmann, and M.M. Askarieh. 2006. Comparative evaluation of surface complexation models for radionuclide sorption by diverse geologic material. In *Surface Complexation Modeling*, edited by J. Lutzenkirchen. Amsterdam: Elsevier Ltd.

Ponthieu, M., F. Juillot, T. Hiemstra, W.H. van Riemsdijk, and M.F. Benedetti. 2006. Metal ion binding to iron oxides. *Geochimica et Cosmochimica Acta* 70:2679-2698.

Prikryl, James D., ALka Jain, David R. Turner, and Roberto T. Pabalan. 2001. Uranium^{VI}

sorption behavior on silicate mineral mixtures. *Journal of Contaminant Hydrology* 47:241-253.

Qafoku, Nikolla, P., John M. Zachara, Chongxuan Liu, Paul L. Gassman, Odeta S. Qafoku, and Steven C. Smith. 2005. Kinetic Desorption and Sorption of U(VI) during Reactive Transport in a Contaminated Hanford Sediment. *Environmental Science and Technology* 39 (9):3157-3165.

Quintard, Michel, and Stephen Whitaker. 1998. Transport in chemically and mechanically heterogeneous porous media IV: large-scale mass equilibrium for solute transport with adsorption. *Advances in Water Resources* 22 (1):33-57.

Rajaram, Harihar. 1997. Time and scale dependent effective retardation factors in heterogeneous systems. *Advances in Water Resources* 20 (4):217-230.

Reardon, E.J. 1981. K_D's - Can They Be Used to Describe Reversible Ion Sorption Reactions in Contaminant Migration? *Ground Water* 19 (3):279-286.

Renard, Ph., and G. de Marsily. 1997. Calculating equivalent permeability: a review. *Advances in Water Resources* 20 (5-6):253-278.

Rubin, James. 1983. Transport of Reacting Solutes in Porous Media: Relation Between Mathematical Nature of Problem Formulation and Chemical Nature of Reactions. *Water Resources Research* 19 (5):1231-1252.

Scheibe, Timothy D., and Steven Yabusaki. 1998. Scaling of flow and transport behavior in heterogeneous groundwater systems. *Advances in Water Resources* 22 (3):223-238.

Schmeide, K., S. Pompe, M. Bubner, K.H. Heise, G. Bernhard, and H. Nitsche. 2000. Uranium(VI) sorption onto phyllite and selected minerals in the presence of humic acid. *Radiochimica Acta* 88:723-728.

Selroos, Jan-Olaf, and Vladimir Cvetkovic. 1992. Modeling Solute Advection Coupled With Sorption Kinetics in Heterogeneous Formations. *Water Resources Research* 28 (5):1271-1278.

Senko, John M., Jonathan D. Istok, Joseph M. Suflita, and Lee R. Krumholz. 2002. In-Situ Evidence for Uranium Immobilization and Remobilization. *Environmental Science and Technology* 36 (7):1491-1496.

Steefel, Carl I., Susan Carroll, Pihong Zhao, and Sarah Roberts. 2003. Cesium migration in Hanford sediment: a mulitsite cation exchange model based on laboratory experiments. *Journal of Contaminant Hydrology* 67:219-246.

Steefel, Carl I., Donald J. DePaolo, and Peter C. Lichtner. 2005. Reactive transport

modeling: An essential tool and a new research approach for the Earth sciences. *Earth and Planetary Science Letters* 240:539-558.

Stollenwerk, Kenneth G. 1995. Modeling the effects of variable groundwater chemistry in adsorption of molybdate. *Water Resources Research* 31 (2):347-357.

Stollenwerk, Kenneth G. 1998. Molybdate transport in a chemically complex aquifer: Field measurements compared with solute-transport model predictions. *Water Resources Research* 34 (10):2727-2740.

Szecsody, James E., John M. Zachara, Ashokkumar Chilakapati, P.M. Jardine, and Alan S. Ferrency. 1998. Importance of flow and particle-scale heterogeneity on Co(II/III) EDTA reactive transport. *Journal of Hydrology* 209:112-136.

Towle, Steven N., J.R. Bargar, Gordon E. Brown Jr., and George A. Parks. 1997. Surface Precipitation of $Co(II)_{(aq)}$ on Al_2O_3. *Journal of Colloid and Interface Science* 187:62-82.

Turner, David R., F.P. Bertetti, and Roberto T. Pabalan. 2006. Applying Surface Complexation Modeling to Radionuclide Sorption. In *Surface Complexation Modeling*, edited by J. Lutzenkirchen. Amsterdam: Elsevier Ltd.

Van Cappellen, Phillippe. 1996. Reactive surface area control of the dissolution kinetics of biogenic silica in deep-sea sediments. *Chemical Geology* 132:125-130.

van der Lee, J., and L. De Windt. 2001. Present state and future directions of modeling of geochemistry in hydrogeological systems. *Journal of Contaminant Hydrology* 47:265-282.

Van Geen, Alexander, Alexander P. Robertson, and James O. Leckie. 1994. Complexation of carbonate species at the goethite surface: Implications for adsorption of metal ions in natural waters. *Geochimica et Cosmochimica Acta* 58 (9):2073-2086.

Waite, T.D., J.A. Davis, B.R. Fenton, and T.E. Payne. 2000. Approaches to modeling uranium(VI) adsorption on natural mineral assemblages. *Radiochimica Acta* 88:687-693.

Waychunas, G.A., Christopher C. Fuller, and J.A. Davis. 2002. Surface complexation and precipitate geometry for aqueous Zn(II) sorption on ferrihydrite I. X-ray absorption extended fine structure spectroscopy analysis. *Geochimica et Cosmochimica Acta* 66 (7):1119-1137.

Weber Jr., Walter J., Paul M. McGinley, and Lynn E. Katz. 1992. A Distributed Reactivity Model for Sorption by Soils and Sediments 1. Conceptual Basis and Equilibrium Assessments. *Environmental Science and Technology* 26 (10):1955-

1962.

Wersin, Paul, Laurent Charlet, Rainer Karthein, and Werner Stumm. 1989. From adsorption to precipitation: Sorption of Mn^{2+} on $FeCO_{3(s)}$. *Geochimica et Cosmochimica Acta* 53:2787-2796.

Wersin, Paul, Michael F. Hochella Jr., Per Perrson, George Redden, James O. Leckie, and David W. Harris. 1994. Interaction between aqueous uranium(VI) and sulfide minerals: Spectroscopic evidence for sorption and reduction. *Geochimica et Cosmochimica Acta* 58 (13):2829-2843.

White, A.F., and Susan L. Brantley. 2003. The effect of time weathering of silicate minerals: why do weathering rates differ in the laboratory and the field. *Chemical Geology* 202:479-506.

Wood, Brian D., Fabien Cherblanc, Michel Quintard, and Stephen Whitaker. 2003. Volume averaging for determining the effective dispersion tensor: Closure using periodic unit cells and comparison with ensemble averaging. *Water Resources Research* 39 (8):1210.

Yeh, Gour-Tsyh, and Vijay S. Tripathi. 1989. A Critical Evaluation of Recent Developments in Hydrogeochemical Transport Models of Reactive Multichemical Components. *Water Resources Research* 25 (1):93-108.

Zachara, John M., Donald C. Girvin, Ronald L. Schmidt, and C. Thomas Resch. 1987. Chromate Adsorption on Amorphous Iron Oxyhydroxide in the Presence of Major Groundwater Ions. *Environmental Science and Technology* 21 (6):589-594.

Zachara, John M., Steven C. Smith, Chongxuan Liu, James P. McKinley, R. Jeffrey Serne, and Paul L. Gassman. 2002. Sorption of Cs^{+} to micaceous subsurface sediments from the Hanford site, USA. *Geochimica et Cosmochimica Acta* 66 (2):193-211.

Zhang, Xiaoxian, John W. Crawford, and Iain M. Young. 2008. Does pore water velocity affect the reaction rates of adsorptive solute transport in soils? Demonstration with pore-scale modeling. *Advances in Water Resources* 31:425-437.

Zheng, Zuoping, Tetsu K. Tokunaga, and Jiamin Wan. 2003. Influence of Calcium Carbonate on U(VI) Sorption to Soils. *Environmental Science and Technology* 37 (24):5603-5608.

Zhu, Chen, Fang Q. Hu, and David S. Burden. 2001. Multi-component reactive transport modeling of natural attenuation of an acid groundwater plume at a uranium mill tailings site. *Journal of Contaminant Hydrology* 52:85-108.

CHAPTER 2

EXPERIMENTAL METHODS

2.1 Introduction

In subsequent chapters, methods relevant to each experimental apparatus and to the results and conclusions made will be presented. This chapter is a more in-depth synopsis of the procedures used, as well as a centralized location for all the methods used. The following sections are divided by each intermediate scale experiment, followed by batch desorption experiments, and ends with analytical methods used. A summary table of the tank experiments is presented in Table 2.1.

2.2 Tank Experiment #1

Tank #1 represents the 'base-case' in terms of heterogeneity. The goal of the experiment was to create the simplest flow field possible in two dimensions at the intermediate scale to analyze the effects of chemical heterogeneity. The methods will cover: tank construction, tank packing, sampling procedures, and the tracer test.

2.2.1 Tank Construction

The materials needed to construct the tank were:

- Aluminum framing, 0.5 in. (1.27cm) thick, 3 in. (7.62cm) wide

Table 2.1 Summary of experimental conditions for the tank experiments.

Tank Exp.	Dimensionality	Particle Sizes	Total Sediment Mass (kg)	AGW used	Tracer Used	Average Flow Rate (ml/day)	Pore Volume (L)	Porosity	Average Retention Time (days)
1	2-D	<2mm Comp.	280 (est.)	AGW- Atmospheric, No Si	Bromide	2600	80	0.42	31
2	2-D	1. <0.250mm 2. >0.250mm	163	1. AGW- Atmospheric, No Si 2. AGW- 2% CO_2	Bromide	850	48	0.42	56
3	3-D	1. <2mm Comp. 2. <0.250mm 3. >0.250mm 4. 0.125-0.250mm 5. 4-12mm	1160	AGW- Atmospheric, with Si	Bromide	3950	270	0.37	68

- 2 Aluminum end plates, 0.5 in. (1.27cm) thick, 12 in. (30.5 cm) wide, 49 in. (124.5cm) tall
- Aluminum bottom plate, 0.5 in. (1.27cm) thick, 12 in. (30.5 cm) wide, 8 ft. (2.44m) long
- 2 Plexiglas sheets, 0.5 in. (1.27cm) thick, 4 ft. (1.22m) wide, 8 ft (2.44m) long
- Gasket material, 0.5 in. (1.27cm) thick, approximately 16 linear feet (4.88m)
- 0.5 in. (1.27cm) aluminum channeling, approximately 48 linear feet (14.6m)
- Commercial air filter material, approximately 4 $ft.^2$ ($0.37m^2$)
- Aluminum screening material, approximately 8 $ft.^2$ ($0.74m^2$)
- 2 in. (5.08cm) x 3/8 in. (0.95cm) nuts, bolts, and washers
- 2.5 in. (6.35cm) x 1/16 in. (0.16cm) screws and nuts
- 1 in. (2.54cm) x 1/16 in. (0.16cm) countersunk, flathead screws
- 3/8 in. (0.95cm) copper tubing, approximately 1 ft. (30.5cm)
- 3/8 in. (0.95cm) brass valves
- 3/8 in. (0.95cm) ID tubing, approximately 50 linear feet (15.25m)
- 1/4 in. x 1/8 in. (0.64cm x 0.32cm) jam screws
- 1/4 in. (0.64cm) Puresep septa

The first step in constructing the tank was to weld together the aluminum framing to create load bearing, exterior supports for the Plexiglas walls. The outer dimensions were 4 ft. x 8 ft. (1.22m x 2.44m), and vertical supports were welded in place every 12 in. (0.3m). The Plexiglas walls were connected to this exterior support. The Plexiglas was placed on top of the exterior support, and 1/16 in. (0.16cm) holes were drilled through the Plexiglas and into the aluminum support structure. These holes were tapped, and the 1 in. (2.54cm) x 1/16 in. (0.16cm) countersunk, flathead screws were used to hold the Plexiglas in place. Bathroom caulking was used to cover the screw head, to prevent any weathering of the steel that might occur, and to create as smooth a surface as possible

along the interior walls of the tank. These screws were placed in 1 ft. (30.5cm) increments.

The next major step was to connect all the walls of the tank. The bottom plate was placed on a laser leveled, welded steel structure that was bolted to the floor. The 3/8 in. (0.95cm) bolts had already been put in place, and the threaded ends were sticking up through the bottom plate. The gasket material was placed on the bottom plate with small holes being created to go over the protruding bolts, and gasket lubricant was used to prevent tearing during wall placement. Enough gasket material was used to go up the walls of the tank on the up- and down-gradient ends as well. The Plexiglas/aluminum walls were placed on the bolts, and the nuts and washers were used to bolt the walls in place. The major load bearing connections in this tank are all from aluminum plating to aluminum plating (see Figure 2.1).

Next the end plates were added. The gasket material was positioned vertically on the up- and down- gradient ends of the tank to ensure a water tight seal. The endplates were then bolted to the aluminum exterior structure through pre-drilled holes. Three inches (7.6cm) from the bottom of each endplate, a 3/8 in. (0.95cm) hole was drilled and tapped. A hole was gouged through the gasket material at each end, and the copper tubing was screwed in to create influent and effluent ports. To each copper tube a brass valve was added to allow for flow control within the tank. The 3/8 in. (0.95cm) tubing was connected to the valve using a brass nipple. All hosing and tubing connections were made water tight with hose clamps and Teflon tape. The final internal dimensions of the tank are 8 ft. x 4 ft. x 3 in. (2.44m x 1.22m x 7.62cm, LxHxW).

The tank was now mostly constructed, but there are several added pieces and steps required to perform the experiments. The first is the addition of end filters. These filters were installed inside of the tank to maintain the constant head boundaries, and to keep the sediment within the flow domain. The end filters were constructed from the aluminum channeling, air filter material, and screening. The aluminum channeling was cut into 4 ft. (1.22m) sections, and several of them were bolted together to a final approximate width of 3 in. (7.6cm). Several hundred holes (1/4 in., 0.64cm) were drilled through all of this channeling to allow for free water flow through the aluminum channeling. The screen material was screwed to the channeling, and the air filter material

Figure 2.1 Photos of tank #1: A- Tank approximately half full of sediment, B- Tank packed and connected to pressure array, note sample port spatial relationships, C- Tank connected to sampler array and saturated, D- 3-way valve in sampling port, E- Constant head boundaries, F- Endplate of tank, outflow port barely visible at the bottom of the tank.

was encased in the supporting screen. The screen was then screwed shut to the aluminum channeling. Two of these end filters were needed, and once constructed they were simply slid into place at either end of the tank; they were held in place by the sediment that was added. The screen was pliable enough to allow for molding of the filters to maintain contact with the walls of the tank. The next added step was the addition of sampling ports. A total of 56 were installed on this tank, in a series of vertical lines. The first vertical line of ports was placed 6 in. (15.2cm) from the influent end of the tank. The subsequent lines were in one foot (30.4cm) increments giving eight total vertical lines of ports. On each vertical line, the ports were placed every 6 in. (15.2cm) starting from the bottom of the tank, giving seven total per vertical line. The ports themselves were constructed by drilling a 1/4 in. (0.64cm) hole halfway through the Plexiglas. In the very center of this hole, a 1/16 in. hole (0.16cm) was drilled all the way through the Plexiglas. The 1/4 in. (0.64cm) septa were placed in the hole, and held in place by the addition of the jam screws. This created a leak proof hole, were a needle could be installed to withdraw aqueous samples. The final ancillary equipment to be added was the constant head boundaries. These were constructed from 3.5 in. OD (8.9cm) and 3 in. ID (7.6cm) pipe that was glued to a 7 in. (17.8cm) PVC end cap. The end cap was sealed with caulking, and two holes were drilled, one inside of the 3 in. (7.6cm) pipe, and one in the space between the 3 in. (7.6cm) pipe and the 7 in. (17.8cm) PVC end cap. Brass nipples were screwed into these holes to allow for connection of the tubing. Hose clamps were used to keep the tubing in place and free of leaks. Two head boundaries were required, one on the influent end and one on the effluent end.

Prior to the addition of sediments, the tank was filled with water and allowed to sit for a couple of weeks to ensure that there were no leaks.

2.2.2 Tank Packing

As previously mentioned this tank was packed in a homogeneous fashion. This was completed by using only the <2mm size fraction. This size fraction was created in the field during the 'Big Dig' in the summer of 2006. During this time, twelve 55 gallon drums, and several additional five gallon buckets of sediment were collected and returned to the Colorado School of Mines. The sediment was collected from the Naturita field site (*Davis and Curtis* [2003]) using a backhoe and a dump truck. The backhoe dug from the surface down to the water table. Once at the water table, approximately 1m depth of sediments were collected. As they were collected, they were placed in the back of the dump truck where the majority of the water was allowed to drain. The then wet sediments were placed on large tarps from which sieving could take place. The sediments were sieved by hand into three size fractions: 4-12mm, 2-4mm, and <2mm. The >12mm fraction was discarded. It required about six days of sieving to create the necessary volumes and, as time continued, the sediments became increasingly drier. As the sediment dried, small balls of clay minerals were created that affected sieving efficiency. These 'clay balls' were often found masquerading as larger particles. This does not particularly affect the <2mm fraction, but they become important when using the 4-12mm material, which is done in tank #3. Eleven drums of <2mm composite material was created in the field, and one drum of 4-12mm. Only 3 five gallon buckets of the 2-4mm material was collected (see Figure 2.2).

Before packing the sediment was allowed to air dry to simplify packing procedures. For the masses required to fill the tank (~250kg), this had to be completed in batches. Fifty to one hundred kilograms were placed on a tarp in the lab, taking several shovelfuls of material from each of the 11 drums containing the <2mm composite. They were mixed regularly (~twice a day) to facilitate drying and to ensure sufficient mixing of the material from all 11 drums. As the sediment dried agglomerations of clay minerals were formed, and broken apart by hand when found. The color of the sediments was used as an indicator of dryness; the drier the sediment was the lighter brown it became. The sediments were allowed to dry for a few more days after a uniform light brown was achieved to ensure complete dryness. Once dry, they were placed in another 55 gallon

Figure 2.2 Pictures from the 'Big Dig' 2006, A- The backhoe breaks ground, B- The groundwater table is reached, the metal box maintains vertical wall integrity while digging below the water table, C- The <2mm composite was sieved directly into the drums, D- Larger size fractions were separated in wheel barrows, E- Groundwater sediments drying in the sun, F- Once full, the drums were shipped in a moving truck back to Colorado School of Mines

drum to await packing.

The dried sediment was packed into the tank in approximately 10cm lifts. Enough sediment was added to make about 10cm of depth, and that lift was then compacted by hand using an approximately 0.5 in. (1.3cm) diameter aluminum rod. This was completed by repeatedly stabbing the sediment with the rod until it became difficult for the rod to penetrate deeply. Once that lift was compacted, 10cm more of sediment was added, and the process was repeated until 7cm of space was left in the tank. As the tank was being packed, care was taken that the sediment was pushing the end filters into place and that no sediment was leaking around the filters. Also, due to the hazards associated with inhaling uranium contaminated sediment, a snorkel hood was placed such that the dust created from packing was removed. On top of the packed sediment, a layer of parafilm was put in place as a chemical barrier. On top of the parafilm, hydrated bentonite clay was compacted into the remaining space. It is assumed that this clay acted as a barrier between atmospheric gases and the water and sediment in the tank. On the top of the clay, a layer of plastic wrap was added to maintain the hydration of the clay. The exact mass of sediment that was required to fill the tank was not measured, but assuming a bulk density of 1.5 g/ml, and the internal volume of the tank, a good estimate is 286kg.

Once the tank was packed, water flow was commenced through the tank. The artificial ground water (AGW) that was used was designed to mimic the composition that is found at the field site; the composition can be seen in Table 2.2. The water is at saturation with respect to calcite and lab air was constantly sparged through the solution to maintain equilibrium with atmospheric PCO_2. Complete saturation of the tank through the head boundaries required about nine hours. The void volume of the tank was approximately 80L. As the tank was saturating there was a significant amount of subsidence in the center of the tank. This led to a slight bow in the sediment level moving from the influent end, to the middle, to the effluent end of the tank. The clay was pushed down to maintain contact with the parafilm. The total amount of subsidence was approximately 7cm, meaning that the total space at the top of the tank that did not have sediment (clay and air) was 15cm.

Table 2.2 Compositions of the artificial groundwaters used in all three tanks, concentrations for ions are in molar, pH is in standard pH units, and saturation index is unitless

Constituent	AGW-atmospheric	AGW-2%	AGW Tank #3
Na^+	$2.43x10^{-2}$	$2.11x10^{-2}$	$2.47x10^{-2}$
K^+	$2.50x10^{-4}$	$2.50x10^{-4}$	$2.42x10^{-4}$
Mg^{2+}	$2.67x10^{-3}$	$2.67x10^{-3}$	$2.46x10^{-3}$
Ca^{2+}	$5.73x10^{-3}$	$7.30x10^{-3}$	$5.65x10^{-3}$
SiO_2	0	0	$2.18x10^{-4}$
Cl^-	$1.65x10^{-2}$	$1.33x10^{-2}$	$1.44x10^{-2}$
SO_4^{2-}	$1.21x10^{-2}$	$1.21x10^{-2}$	$1.34x10^{-2}$
Ionic Strength	$5.11x10^{-2}$	$6.54x10^{-2}$	$5.13x10^{-2}$
pH	7.85	7.15	7.85
Alkalinity (meq/L)	0.61	3.85	0.61
Equilibrium Gas	Atmospheric	2%CO_2, 20%O_2, 78%N_2	Atmospheric
Calcite Saturation Index	0.09	0.08	0.06

2.2.3 Tank Sampling/Water Flow

Monitoring the tank required quantification of: local pressure head, both spatial and influent/effluent aqueous samples, and flow rates.

Into each of the sampling ports discussed earlier, a stainless steel 18 gauge needle was inserted. This needle was left in place unless the needle clogged with sediment, at which point it was replaced with a new one. Connected to the needle was a 3-way Luer lock valve. The other two directions allowed for aqueous sample removal, and the connection of a digital sensor array (DSA 3207, Scanivalve Corp.) to measure local pressure head. Sufficient characterization of the flow field was completed with only 25 of the ports being connected to the array. They were connected through 1/16 in. (0.16cm) ID tubing that was filled with water to maintain hydraulic connectivity. Readings were logged onto a computer that was attached to the array. For the ports that were not connected to the pressure system, the third direction on the Luer valve was not used.

Aqueous samples were removed from each of the ports that were located within the flow domain. Because of the soil subsidence, many of the sampling ports were in the hydrated clay layer and were thus not used. In order to limit the total number of samples, only half of the usable ports were sampled on any given day. Every other port in a row or a column was sampled. At the next sampling event, the ports that had not been previously sampled were sampled. Thus the ports sampled alternated between sampling events, and 24 or 25 total samples were taken per sampling event. Sampling events occurred every 4-5 days. To remove a sample, a syringe was connected to the 3-way valve, the valve was turned so that the needle could withdraw liquid from the tank, and 5-7mls of solution were removed. Measurements from the digital array showed that removing this volume did not significantly affect the flow field. The major constituents of concern were: pH, alkalinity, uranium, calcium, sodium, magnesium, potassium. Other ions were also quantified including: silicon, total sulfur, iron, manganese and strontium. Once the sample had been withdrawn, it was filtered through a 0.45μm PVDF syringe filter, and pH was immediately measured with a standard pH probe calibrated at pH 4, 7, and 10. The sample was subsequently split for alkalinity titrations (~3ml), and metals analysis (~2ml). Alkalinity samples were refrigerated until shipment to

collaborators at Lawrence Berkeley National Lab (LBNL) where an automatic titrator was used. Metals samples were acidified with 50µl of 1M nitric acid to a pH<2. Influent samples were removed directly from the influent head boundary, and effluent samples were removed from a t-joint installed in the effluent line. The t-joint was purged, and the solution was allowed to flow directly into the syringe. Thus, effluent samples represent flux averaged values. Other than how the samples were taken, the influent and effluent samples were treated in the same manner as the spatial samples.

The effluent of the tank was directed to a 5-gallon bucket, and was periodically measured using a graduated cylinder. This with elapsed time between events allowed for the calculation of flow rates.

Three stop flow events were completed to test the role of kinetic hindrances to desorption. They were completed by closing the brass valves at both the influent and effluent ends of the tank. The events occurred at 4.06, 4.52, and 5.95 pore volumes (PV) and lasted for 97 hours, 354.5 hours, and 500.5 hours, respectively. All sampling was suspended during this time. Flow was re-started by opening the valves, and sampling immediately began again.

2.2.4 Tracer Test

A pulse injection of the inert tracer bromide was used to delineate major flow paths. The concentration used was 2.02×10^{-3}M KBr spiked into AGW-atmospheric; at this concentration density induced sinking can be ignored (*Barth et al.* [2001]). The tracer was injected through a parallel head boundary connected through a t-joint in the influent line. This allowed for an instantaneous switch between AGW with and without bromide. A calculated minimum mass of 200mg Br^- was needed to ensure detection of the tracer spatially within the tank. The injection lasted 13.25 hours; 1.25 liters of tracer solution were injected for a total mass of 201mg Br^- (2.52×10^{-3}mols). Samples were removed both spatially and from the effluent as described above and refrigerated until

analysis. Monitoring continued until the effluent values were non-detectable (~1.5 months).

2.3 Tank Experiment #2

The goal of tank experiment #2 was to introduce physical heterogeneities by splitting the <2mm composite sediment into two size fractions. Thus the sediments added to tank #2 were identical to those of tank #1, but the physical orientation of the two size fractions was different. Also, two different compositions of AGW were used to test the effects of temporal chemical heterogeneities in the aqueous phase.

2.3.1 Tank Construction

The materials needed for tank #2 construction were:

- Plexiglas slats, 0.5 in. (1.27cm) thick, 3 in. (7.62cm) wide
- 2 Aluminum end plates, 0.5 in. (1.27cm) thick, 12 in. (30.5 cm) wide, 25 in. (63.5cm) tall
- Aluminum bottom plate, 0.5 in. (1.27cm) thick, 12 in. (30.5 cm) wide, 8 ft. (2.44m) long
- 2 Plexiglas sheets, 0.5 in. (1.27cm) thick, 2 ft. (0.61m) wide, 8 ft (2.44m) long
- Gasket material, 0.5 in. (1.27cm) thick, approximately 12 linear feet (3.7m)
- 0.5 in. (1.27cm) aluminum channeling, approximately 24 linear feet (7.3m)
- Commercial air filter material, approximately 2 $ft.^2$ ($0.18m^2$)
- Aluminum screening material, approximately 4 $ft.^2$ ($0.37m^2$)

- 2 in. (5.08cm) x 3/8 in. (0.95cm) nuts, bolts, and washers
- 2.5 in. (6.35cm) x 1/16 in. (0.16cm) screws and nuts
- Industrial strength epoxy (E6000)
- 3/8 in. (0.95cm) copper tubing, approximately 1 ft. (30.5cm)
- 3/8 in. (0.95cm) brass valves
- 3/8 in. (0.95cm) ID tubing, approximately 50 linear feet (15.25m)
- 1/4 in. x 1/8 in. (0.64cm x 0.32cm) jam screws
- 1/4 in. (0.64cm) Puresep septa

Tank #2 was similar but not identical to tank #1. The major difference between the two tanks are the dimensions; tank #2 had internal dimensions of 8 ft. x 2 ft. x 3 in. (2.44m x 0.61m x 7.6cm, LxHxW) making it half as tall as tank #1. Due to the smaller size and lower total mass of sediment and water that would be in the tank, the exterior aluminum framing was not needed. Instead the exterior supports were made out of the Plexiglas slats. These slats were connected to the exterior of the Plexiglas walls with industrial strength epoxy. The epoxy was allowed to cure for several days before construction proceeded. Once the walls and exterior supports were together, construction proceeded much like tank #1. The walls were set on bolts placed through the bottom aluminum plate separated by the gasket material. The endplates were added and bolted to the Plexiglas framing. In leak testing, the exterior Plexiglas supports were weaker than expected, so two additional braces were added across the top of the Plexiglas framing, one at 3 ft. (91cm) and one at 5.5 ft. (167cm). In the end plates, 3 in. (7.6cm) from the bottom, holes were drilled and tapped for the influent and effluent copper pipes. The brass valves were connected to these pipes, with brass nipples connected to the valves. The tubing was connected to the nipples with hose clamps (see Figure 2.3).

Constant head boundaries identical to those constructed for tank #1 were made for tank #2. End filters were also constructed similar to those of tank #1, but they were only 2 ft. (0.61m) tall. Sampling port construction was identical to that of tank #1; however, the spacing was not. Again, eight vertical lines of ports were created at 1 ft. (30.5cm) intervals starting at 6 in. (15.3cm) from the end of the tank. These ports were placed 1 in. (2.5cm) apart vertically giving a total of 176 sampling ports. Not all of these ports were

Figure 2.3 Construction and packing of tank #2, A- Fully constructed tank #2, gasket material clearly visible in black, B- Tank #2 fully packed, saturated and connected to pressure array, C- Opposite view as B, head boundaries in background, D- 3-way valve in sampling port connected to pressure array, E- Taking a core of the core for microbial analysis, F- Taking a core from the tank

sampled. The excessive number of ports allowed for greater flexibility in deciding where to sample, as well as providing flexibility for future experiments that might be performed in this tank.

2.3.2 Tank Packing

As previously mentioned, this tank was macroscopically heterogeneously packed with two size fractions. These size fractions were created by splitting the <2mm composite sediments into <0.250mm and >0.250mm. Prior to sieving the field derived <2mm sediments were allowed to air dry as before. The <2mm material was then separated by hand using a 0.250mm sieve of in house construction. The relative mass percent of the <2mm composite was 43.1% <0.250mm, and 56.9% >0.250mm. A total of 163.2kg of sediment were placed in tank #2. This consisted of 69.8kg of <0.250mm and 93.4kg of >0.250mm material. Thus the packing distribution was 42.8% <0.250mm, and 57.2% >0.250mm.

The packing orientation of the sediments can be seen in Figure 2.4. The packing orientation of the sediments was drawn onto the sides of the tank to facilitate packing. The sediments for tank #2 were added in whole layers not in 10cm lifts. Because of the subsidence observed in tank #1, sediments in tank #2 were mechanically compacted using a concrete vibrator. Thus, the first step was to add approximately enough >0.250mm sediment to fill the first layer of the tank. Then the concrete vibrator was used to compact the sediments. More sediment was added to level the layer, and the vibrator was again used to compact the sediments. This process was repeated for each subsequent level. On higher levels of packing (moving toward the top of the tank) marks were made on the concrete vibrator to ensure that only the layer being packed was being compacted. In other words, the vibrator was not extended through layers of different size fractions of material. To create the ‘block’ at the upgradient end of the tank, a 1/4 in. (0.64cm) aluminum slat was inserted to allow for a sharp juxtaposition of two different size fractions. Both sides of the slat were packed simultaneously with the necessary size

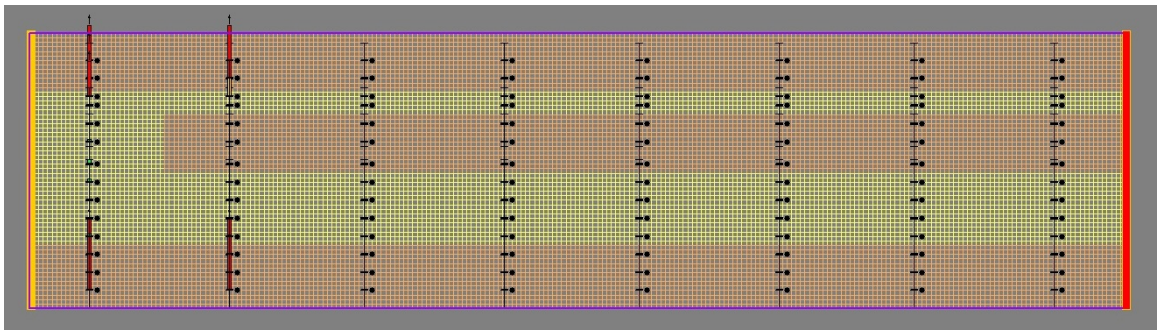

Figure 2.4 Packing orientation in tank #2, red cross hatch is the >0.250mm fraction, yellow cross hatch is the <0.250mm, the upgradient end is on the left and downgradient end is on the right, top and bottom are no-flow boundaries. Picture created by Derrick Rodriguez.

fractions. Before the final, topmost layer of >0.250mm sediment was added the aluminum slat was removed. As in tank #1, a layer of parafilm was placed on top of the sediment, and a hydrated clay layer (7cm thick) was placed on top of the parafilm.

Plastic wrap was placed on top of the hydrated clay to ensure continued hydration of the clay.

2.3.3 Tank Sampling/Water Flow

Initial flow and saturation was commenced with AGW-atmospheric (Table 2.2). The tank required approximately 48 hours to saturate. The long saturation time relative to tank #1 was caused by a small bubble in the effluent line that was impeding outflow. Once the bubble was cleared, the tank fully saturated. The total void volume of the tank was 48L. Sampling procedures for influent/effluent samples, spatial samples, and pressure head measurements were all identical to those in tank #1. Influent/effluent samples were taken every 2-4 days. Spatial samples were taken from 23 ports, on a

weekly basis. The density of spatial samples was slightly higher at the upgradient end of the tank where pre-modeling had shown that the block would cause the largest deviations from lateral flow. Effluent from the tank was directed to a 5-gallon bucket on a tared 50kg balance. Flow rates were measured by mass difference.

Only one stop flow event was performed. To accomplish this, as in tank #1, both the influent and effluent valves were closed. It occurred at 1.28 PV of flow, and lasted for 650 hours. Again, sampling was suspended during the stop flow event and was re-commenced when flow was re-started.

With the exception of during the stop flow event AGW-atmospheric was allowed to flow through the tank for the first 2.42 PV. At 2.42 PV, the influent was changed to AGW-2% (Table 2.2). This water is similar in ionic composition to AGW-atmospheric, but is in equilibrium with 2% CO_2 gas. To maintain near equilibrium with calcite the calcium concentration was increased slightly, and to minimize ionic strength differences the sodium concentration was decreased slightly. The water was made in a separate influent basin. Gas from cylinders with a composition of 2% CO_2, 20% O_2, and balance N_2 was sparged through the water at a rate greater than or equal to the sparge rate of atmospheric air through AGW-atmospheric. The pH of the solution was monitored until stability was achieved (several days). Once the pH had stabilized, samples were removed for analysis, and the flow was switched through a t-joint installed in the influent line. 1.3 PV of AGW-2% were injected into the tank; sampling continued unabated. pH of the influent was closely monitored to ensure continued equilibration with the 2% CO_2. Also, since the head boundaries were open to the atmosphere, plastic bags were placed over the influent head boundary to minimize exsolvation of CO_2. After 1.3 PV of solution were injected, the influent was reverted to AGW-atmospheric. AGW-atmospheric was used for the remainder of the experiment including during the bromide tracer test.

2.3.4 Tracer Test

Most of the procedures for bromide injection in tank #2 are identical to tank #1. The major difference is that due to the smaller size of tank #2, a smaller bromide mass was required. The minimum mass for detection was calculated to be 121mg Br^-. The same concentration, $2.02x10^{-3}$M KBr, spiked into AGW-atmospheric was used. The injection was completed over a period of 18.25 hours through a parallel head boundary, and a total mass of 153mg Br^- was injected. Sampling continued unabated, with identical procedures to that found in tank #1. Monitoring continued until the effluent values were non-detectable, a period of approximately 6 months.

2.3.5 Core Removal

To perform mass balance calculations and to take samples for microbial analysis, four cores were removed from tank #2. Before the cores could be taken, the tank was drained of all pore water and allowed to air dry for approximately a week. After this time, the sediment was dry enough to be compacted into a coherent core. Cores were removed at 6, 24, 54, and 84 in. (15.2, 61, 137, and 213cm) from the upgradient end of the tank, and samples were removed from each packed layer of the tank. Since the location of the layers was known, cores could be removed containing only one layer. The exception is the top two layers which are the thinnest. Here, both layers were taken in one core, and the different particle sizes were separated visually. To take a core, the coring device was hammered in to the desired depth. Then much of the sediment surrounding the core was removed by hand. This allowed for the 'breaking' and removal of the core material (see Figure 2.3). The core was laid on a sheet of plastic wrap, and pulled apart to expose a surface that had not been touched by the coring device or human hands. A core of the core was taken with a 50ml sterile centrifuge tube upon this fresh face. Microbial samples were frozen in a traditional freezer (T = 0°C) for several weeks before being moved to a -80°C freezer to await characterization. The remaining core

material was collected and allowed to air dry for chemical characterization including labile uranium determinations (*Kohler et al.* [2004]) and total organic and inorganic carbon determinations. Upon air drying clay balls had again formed and were broken apart by hand before any further work was done.

2.4 Tank Experiment #3

The goal of tank #3 was to create a physically and chemically heterogeneous flow domain in three dimensions. This was completed using five different size fractions of the Naturita sediment, and a tank that was significantly different in construction compared to tanks #1 and #2.

2.4.1 Tank Construction

The materials needed for tank #3 were:

- 1 Plexiglas bottom plate, 1 in. (2.5cm) thick, 24 in. (61cm) wide and 8 ft. (2.44m) long
- 2 walls of 1 in. (2.5cm) thick Plexiglas, cut to 94 in. (2.39m) length and 23 in. (58.4cm) in height
- 2 Plexiglas endplates, 1 in. (2.5cm) thick, 24 in. (61cm) wide and 23 in. (58.4cm) high
- 1 Plexiglas lid, 0.5 in. (1.27cm) thick, 8 ft. (2.44m) long and 24 in. (61cm) wide
- Plastic framing for end filters, 0.5 in. (1.27cm) thick, 3 in. (7.6cm) wide, cut to length, approximately 24 linear feet (7.3m) total

- Screen material for end filters mesh size = 750, approximately 4 ft.^{2} (0.37m^2)
- Perforated aluminum panel, support for screen material on end filters, approximately 4 ft.^{2} (0.37m^2)
- 1/16 in. (0.16cm) OD, 1/32 in. (0.08cm) ID aluminum tubing for well construction, approximately 50 linear feet (15.2m)
- Industrial strength epoxy (E6000)
- Bathroom caulking
- Copper tubing, 3/8 in. (0.95cm) diameter, approximately 1 linear foot (30.5cm)
- 2 brass valves

Tank #3 was placed within a welded metal frame that was constructed to hold tank #2; tank #3 was physically below tank #2. Thus the load bearing structures for tank #3 consisted of this external welded steel construction. The connections between the Plexiglas bottom, walls, and endplates only needed to be water tight not load bearing. The first step in construction was to place the Plexiglas bottom plate on the floor of the welded frame. A large bead of epoxy was run along the edge of the bottom plate, and the Plexiglas walls of the tank were put into place allowing 1 in. (2.5cm) of space at either end for the end plates. The walls of the tank were clamped to the exterior steel supports to allow the epoxy to cure. The next step was to add the end plates. A large bead of epoxy was run along the vertical edge of both walls at one end of the tank as well as along the edge of the bottom plate. The end plate was then put into place, and an exterior load bearing support was bolted to the welded frame to hold the end plate in place. This process was repeated at the other end of the tank. Once all the walls and endplates were in place, another bead of epoxy was run along the inside seam between all of the pieces to ensure a water tight seal. The final internal dimensions were 8 ft. x 2 ft. x 2 ft. (2.44m x 61cm x 61cm, LxHxW, see Figure 2.5).

The end filters were constructed out of the 3 in. (7.6cm) plastic slats. These were cut to length, and a frame was constructed with the same internal dimensions of the tank. The aluminum panel was screwed to the plastic frame, and the screen material was

epoxied to the aluminum panel. To ensure that no sediment leaked around the end filters, aluminum screen and air filter material used in previous tanks was wedged into the small space between the end filters and the wall of the tank.

After packing the sediments (described below) a 0.5 in. (1.27cm) Plexiglas lid was added to seal the tank from the atmosphere. Holes had been pre-drilled in the lid to allow the sampling wells to protrude up from the sediments. A bead of caulk was run all the way around the seam between the lid and the walls and endplates of the tank. The caulk was also used to seal the pre-drilled well holes.

Constant head boundaries from tank #1 were used for tank #3.

2.4.2 Tank Packing

As previously mentioned, five different particle sizes were used. These include the <2mm composite, <0.250mm, and >0.250mm fractions used in previous experiments, as well as the 4-12mm and 125-250μm fractions created for this experiment alone. The procedures to collect the <2mm composite, <0.250mm, and >0.250mm fractions were all the same as described previously. Approximately half of the total amount of produced <0.250mm material was re-sieved at 125μm. The procedure for this was identical to that used to create the <0.250mm and >0.250mm fractions, but the screen size was different. The sediment that was retained on the screen was used as the 125-250μm fraction. The <125μm fraction was set aside, and not used in this tank.

The 4-12mm fraction was created during the 'Big Dig'. The 'clay ball' effect was the worst in this size fraction. Because of the clay balls, and the fact that much of the smaller size fractions had adhered to the actual 4-12mm size fraction, this particle size was wet-sieved. This was completed with the use of a portable cement mixer, a 4mm screen, and water collection vessels. First, a massed amount of sediment was put into the cement mixer with approximately 3-5 gallons of water (12-20L). The cement mixer was then turned on, and the sediment and water was allowed to mix for 5-10 minutes. As soon as the mixer was turned off, the solution and sediment was dumped onto a 4mm screen. The

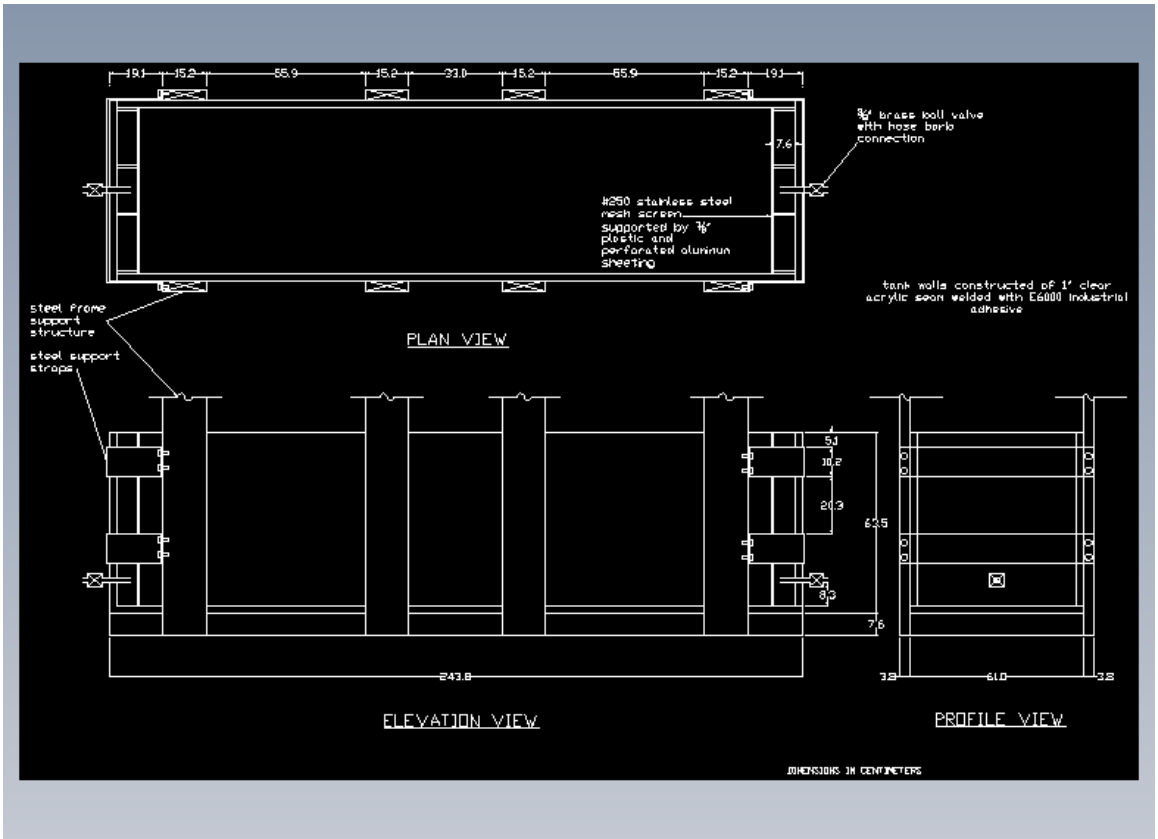

Figure 2.5 Schematic of tank #3 construction, all dimensions in centimeters. Drawing completed by Jason Peterson.

material that was retained on the screen was washed with a small volume (~500ml) of water to remove any remaining particles. The sediment was then allowed to air dry. The water (which passed through the screen, and had some particles removed via sedimentation) was recycled to clean the next batch of sediment (see Figure 2.6). This process was repeated until all of the sediments had been cleaned. New wash water was used when approximately half of the sediment had been cleaned. Once the sediments were dry, they were re-massed and placed in a drum until packing. The total amount of clay that was washed from the sediments was about 30% of the original mass; the total amount of washed 4-12mm material was 196kg.

The total amount of each sediment that was placed in the tank was as follows: 179kg of 4-12mm, 601kg of <2mm composite, 231kg of >0.250mm, 83kg of <0.250mm, and 62kg of 125-250μm. The total mass was 1159kg. Because of the complexities within this tank, pre-modeling of an inert tracer flowing through various packing orientations was completed with GMS 4.0. Details are in Appendix E. Of the orientations considered, the one that gave the least ideal tracer behavior (early breakthrough, long tailing, and in this case a shoulder peak) was implemented in the tank. It is assumed that the less ideal tracer behavior will lead to sharper concentration gradients for more reactive constituents. The packing orientations of the different size fractions can be seen in Figures 2.7 through 2.11. Due to the 3-D nature of the tank as well as the use of 5 different particle sizes, the packing procedures were considerably different in this tank than in the previous two.

An aluminum grid was constructed that divided the tank into five grid cells wide and twenty-two grid cells long (see Figure 2.6). Five layers were packed in the tank, and the aluminum grid was the same height as one layer. This gave each cell dimensions of approximately 11cm on a side, which is exactly how the flow domain was constructed in the GMS simulations. The grid was first placed on the bottom of the tank, and each size fraction was poured into the correct grid cell. When two different particle sizes were in adjacent cells, the cells were packed simultaneously to avoid the potential mixing of the particle size through imperfections in the aluminum grid. The concrete vibrator was used to compact the sediments, and each cell was topped off to be level with the top of the grid. When the first layer was full, the grid was pulled vertically out of the sediments and

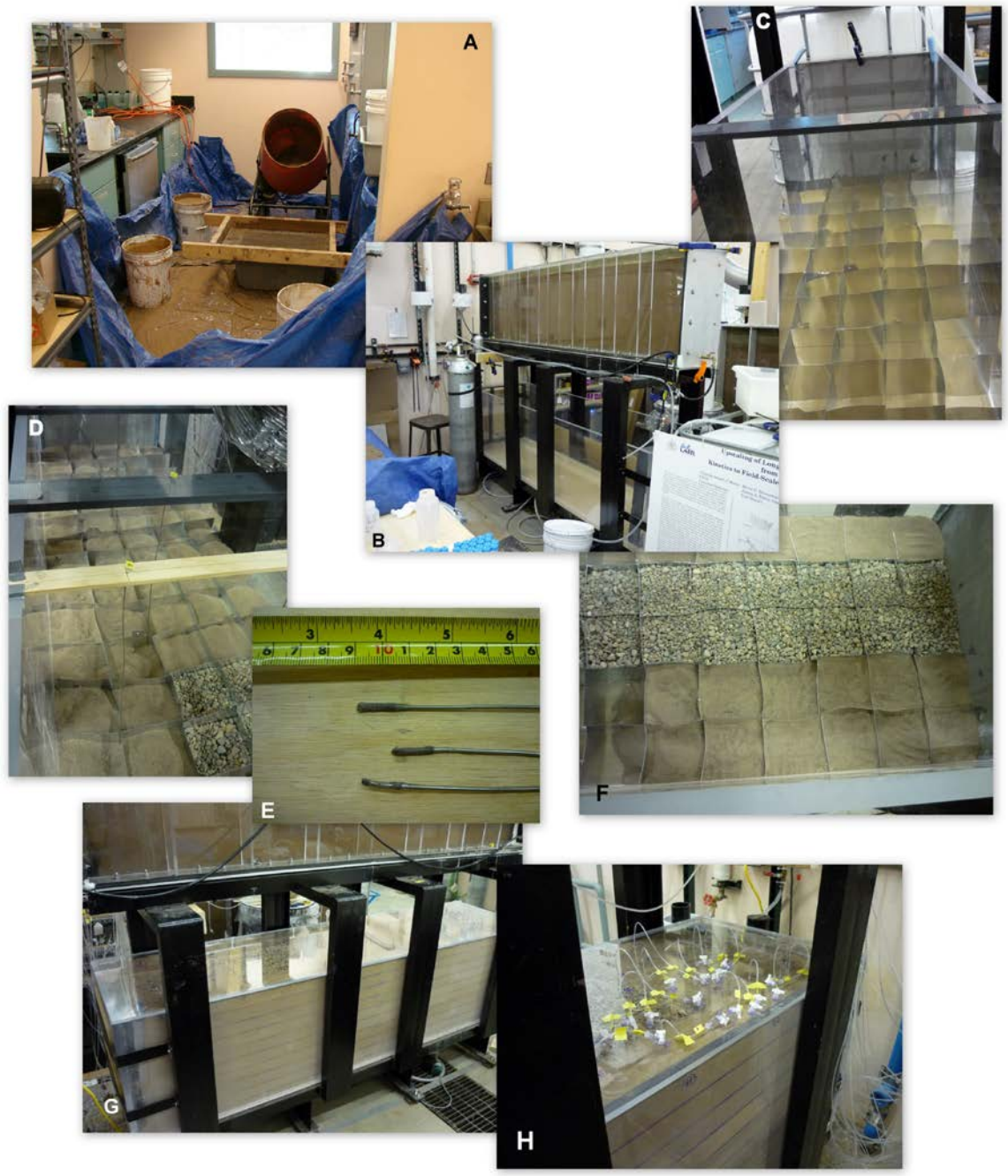

Figure 2.6 Tank construction and packing of tank #3, A- Wet sieving of 4-12mm size fraction, B- Tank #3 fully constructed underneath tank #2, C- Aluminum grid in place creating ~11cm cubes, D- Packing of the various size fraction in the aluminum grid with several sampling wells in place, E- The screened end of the sampling wells, F- Packing of the various size fractions, G- The tank is fully packed, and the lid is in place and caulked, H- Sample tubing and three way valves connected to the sampling wells.

Figure 2.7 Vertical cross section of tank #3 packing, upgradient end on the left, downgradient end on the right, y-dimension (into plane of page) ~5.6cm (~11.2cm thick)

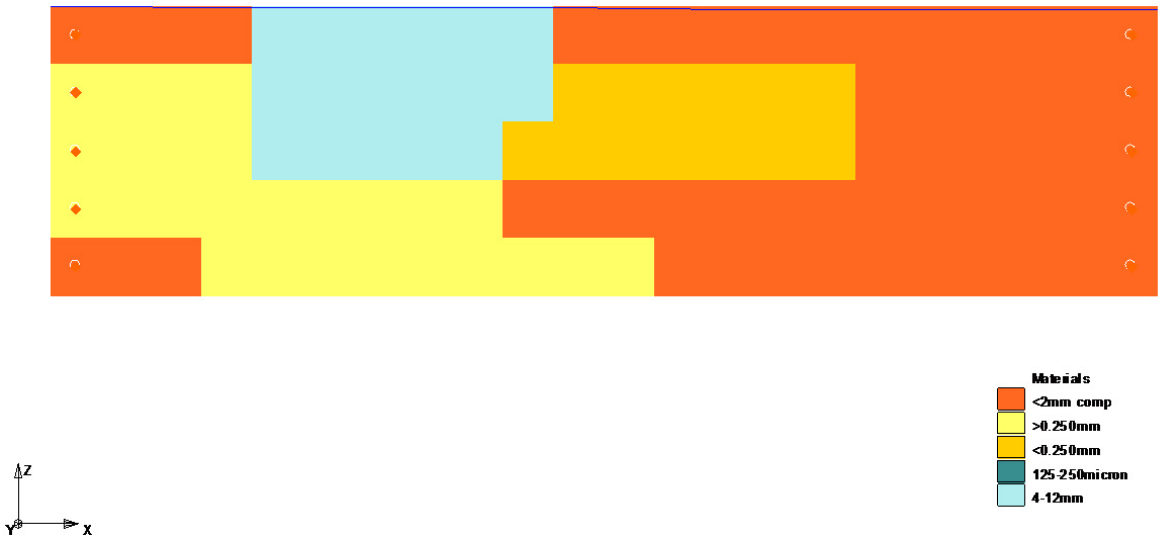

Figure 2.8 Vertical cross section of tank #3 packing, upgradient end on the left, downgradient end on the right, y-dimension (into the plane of the page) ~16.8cm (~11.2cm thick)

Figure 2.9 Vertical cross section of tank #3, upgradient end on the left, downgradient end on the right, y-dimension (into the plane of the page) ~28.0cm (~11.2cm thick)

Figure 2.10 Vertical cross section of tank #3, upgradient end on the left, downgradient end on the right, y-dimension (into the plane of the page) ~39.1cm (~11.2cm thick)

Figure 2.11 Vertical cross section of tank #3, upgradient end on the left, downgradient end on the right, y-dimension (into the place of the page) ~50.3cm (~11.2cm thick)

laid on top of the packed layer. The next layer was packed with the prescribed size fractions, and compacted with the vibrator. When the same particle size was packed in subsequent layers, the vibrator was used to compact both layers of sediments. When a different particle size was placed above another, the vibrator was only used to compact one layer. This process was repeated until all five layers of the tank were packed and compacted. At certain points in the tank where the 125-250µm fraction was juxtaposed with the 4-12mm material, removal of the aluminum grid caused the 125-250µm fraction to fill the pore space in the 4-12mm material. To counteract this, pieces of the same screen material used for the end filters were placed in between these two size fractions. The screen has much higher hydraulic conductivity than the surrounding sediments.

As the tank was being packed, spatial samplers were also put in place. These spatial samplers are akin to ground water sampling wells, just on a reduced scale. Placement of the wells was determined from the pre-modeling. Spatial density of the wells was higher in the zones of predicted higher flow; in the areas of lower flow, the density was much lower. A total of 46 wells were installed in the tank. They were constructed out of the 1/16 in. (0.16cm) OD tubing. The tubing was cut to the required

depth of the well,adding 1.5 in. (3.8cm) to allow for the protrusion of the well through the lid and the connection of sampling tubing. The bottom end of the tube was crimped shut, and a hole was drilled perpendicular to the length 0.5cm from the bottom of the well. The same screen material used for the end filters was cut into small rectangles, and wrapped around the well, covering the hole, and epoxied in place. The screened interval was $\leq$1cm. In packing the wells, the bottom of the well was placed in the sediment at the prescribed depth, and a pre-drilled board was placed across the top of the tank to substitute for what would eventually be the lid (see Figure 2.6). Thus, both ends of the well were held in place while the sediment was packed and compacted around the well. As the sediment got deeper, the board across the top became less necessary, and was removed while packing proceeded. Once the lid had been put in place, three way valves were again used to connect the tank to the pressure head array, and to allow for withdrawal of aqueous samples.

2.4.3 Tank Sampling/Water Flow

AGW-atmospheric tank #3 was used exclusively in this tank. This water is identical to the AGW-atmospheric used in tank #1, but with the addition of silicon in the form of sodium silicate (see Table 2.2). To make this solution, 68mls of sodium silicate solution (93.69g, [SiO_2] = 26.5%, 40-42°Be) was added to the 1000L basin where all other ground water salts had been dissolved. Because of the high pH of the sodium silicate, the 1000L basin was titrated with concentrated HCl to a final pH between 7.75-7.85. Air was continuously bubbled through the water to force equilibrium with atmospheric CO_2. The titration occurred over a period of several days, and was determined to be complete when the pH was stable for at least two days.

Sampling procedures in tank #3 were different due to the nature of the tank and sampling wells. The major difference is that the wells needed to be purged before sample was withdrawn. To complete this, 5ml of solution were withdrawn from each well immediately before sampling. This 5ml was discarded, and another 7-8mls of solution

were withdrawn using a clean syringe. This solution was then treated as before, being filtered followed by an immediate pH measurement, then being split for metals and alkalinity analysis, as well as for bromide. Influent/effluent samples were taken as in previous tanks. Outflow was directed to a tared 5-gallon bucket, and flow rate was determined by mass difference.

2.4.4 Tracer Test

The tracer test was conducted much as before, with the use of bromide (2.02×10^{-3} M) as tracer and a parallel head boundary for injection. The total length of time for the injection was 25.5 hours, and a total of 774.4mg (9.69×10^{-3} mols) of Br^- was injected. Monitoring continued until effluent values were non-detectable.

2.5 Uranium Desorption Experiments

In order to determine rate constants for uranium desorption, uranium release experiments were completed over a period of about 11 months. These experiments were completed on 6 different size fractions: <2mm composite, <0.250mm, >0.250mm, 500-1000μm, 250-500μm, and 125-250μm. The size fractions were created by dry-sieving using a standard sieve tower and a Ro-tap shaker. Approximately 500g of sediment was added to the coarsest sieve, and the tower was shaken for 15 minutes. This process was repeated until sufficient mass of each fraction was obtained. Forty grams of sediment were added to 500ml polyethylene bottles and 200mls of AGW-atmospheric was added to the bottles giving a soil:solution ratio of 200g/L. The bottles were placed on a shaker table and were constantly mixed. Triplicate reactors were created for each size fraction. Two blanks were created by spiking 200mls of AGW-atmospheric to 1μM total uranium.

Sampling occurred frequently at early points in time and became less frequent as the experiment continued. To sample the bottles the shaker table was shut off and the sediments were briefly allowed to gravity settle. pH was measured directly in the bottle. For most events, 0.3ml of sample were removed which allowed for uranium analysis only. At three events spread out over the 11 month time span 1.2-1.5ml of sample were taken which allowed for bulk cation analysis as well. The total change in soil:solution ratio over the 11 month period was 4.7%. Once the sample was removed, it was filtered through a 0.45μm PVDF filter into a liquid scintillation vial. From the scintillation vial, a measured amount was removed and added to a 1% nitric acid solution to give a final dilution of either 1:10 (for bulk metal analysis) or 1:100 (for uranium analysis only). This same procedure was followed for the blanks to quantify wall sorption.

Generally, no attempt was made to control pH or temperature of the bottles. The reactions between the sediments and the AGW controlled the pH. It is assumed that the water is in equilibrium with atmospheric CO_2 concentrations, as water removal for titrations would have caused a much more significant change in soil:solution ratios. pH in the blanks was adjusted to be near the values found in the reactors with sediments. However, these adjustments were slight (generally <0.1 pH units) and not always required. Temperature in the lab varied both diurnally and seasonally, and ranged from 18.9-28.3°C. The temperature was monitored with a thermometer attached to a laptop where measurements were made automatically on an hourly basis.

2.6 Analytical/Instrumental Methods

Major cation analysis (Na^+, K^+, Ca^{2+}, Mg^{2+}, Fe tot, Mn^{2+}, Sr^{2+}, Si tot, S tot) was completed on a Perkin Elmer Optima 3000 Inductively coupled plasma atomic emission spectrometer (ICP-AES). The samples were diluted 1:10 before analysis. A two point calibration curve was created for each element analyzed in an analytical run, and check standards were analyzed every twenty samples and varied ≤10%. An inline internal standard addition was used to correct for sample viscosity and instrument drift.

Uranium was measured using a Perkin Elmer Sciex Elan 6100 Inductively coupled plasma mass spectrometer (ICP-MS). The samples were diluted 1:100 before analysis. A five point calibration curve was created for each analytical run; r^2 values were typically >0.999. Two separate check standards were analyzed, one that was simply a uranium standard spiked into dilute nitric acid, and one that was a uranium standard spiked into AGW-atmospheric and diluted 1:100; these standards were analyzed every twenty samples, and varied ≤20%. An inline internal standard was used to account for instrument drift and sample viscosity variation. The concentration of the samples, once diluted, were rarely outside of the calibration range.

Bromide was measured using a Dionex Ion chromatograph (IC). The following instrumental components were used: CD25 conductivity detector, GP50 gradient pump, AS50 autosampler, AS50 chromatography compartment with an AS14A column. A carbonate based eluent was used. A five point calibration curve was created for each analytical run, and a check standard was analyzed at the beginning and end of each analytical run to check for instrument drift.

Solid phase total carbon (TC) and total inorganic carbon (TIC) on a UIC Inc. 5014 solid phase carbon analyzer. Prior to determining either TC or TIC samples were ground to <150μm with a mortar and pestle. For TC analysis, a massed sample (~20-30mg) was placed in a small crucible, and placed in an oven at 935°C. Oxygen gas carried the produced CO_2 to the detector. The detector performs a coulometric titration on the gas in solution. For TIC, a 2M sulfuric acid solution was added to a massed amount of sample. The evolved CO_2 gas was directed to the same titration detector.

Besides the pressure readings in the tank, independent estimates of hydraulic conductivity were made using ASTM method D 2434-68. This method uses a permeameter packed with the sediment of interest. A constant hydraulic gradient (constant head) was applied across the soil column, and water flow was measured as s function of time. Once steady state flow was achieved (~30minutes to two hours) flow measurements were taken, and hydraulic conductivity was calculated through Darcy's Law. Falling head determinations were also completed. Here, the permeameter was packed with the sediment, and the manometer was filled to the highest graduation. The

inlet and outlet to the chamber were opened, and head as a function of time was measured.

2.7 References

Barth, Gilbert R., Tissa H. Illangasekare, Mary C. Hill, and Harihar Rajaram. 2001b. A new tracer-density criterion for heterogeneous porous media. *Water Resources Research* 37 (1):21-31.

Davis, J.A., and Gary P. Curtis. 2003. Application of Surface Complexation Modeling to Describe Uranium(VI) Adsorption and Retardation at the Uranium Mill Tailings Site at Naturita, Colorado. Washington D.C.: U.S. Nuclear Regulatory Commission.

Kohler, Matthias, Gary P. Curtis, David E. Meece, and James A. Davis. 2004. Methods for Estimating Adsorbed Uranium(VI) and Distribution Coefficients of Contaminated Sediments. *Environmental Science and Technology* 38:240-247.

CHAPTER 3

EFFECTS OF PHYSICAL AND CHEMICAL HETEROGENEITY ON OBSERVED 2-D URANIUM TRANSPORT AT THE DECIMETER SCALE

3.1 Introduction

The use of mathematical models to describe complex environmental systems pervades the environmental sciences. From models for relatively small, simple systems, such as a batch reactor in the lab, to models involving whole earth processes, such as climate modeling, mathematical models derived from system specific conceptual models have led to a deeper understanding of the physical and chemical processes that occur in the natural world. However, scaling mathematical models from system to system, as well as scaling a single system through time to make system predictions remains problematic. The source of these extrapolation problems is often caused by 1) system heterogeneities (both physical and chemical), and 2) mathematical model discretization.

In contaminated ground water systems, these two problems are often exhibited by 'non-ideal' transport behavior which is typified by early breakthrough of a contaminant as well as long tailing periods. Furthermore, physical and chemical heterogeneities often exist at scales much smaller than an average discretization. Focusing on metal and radionuclide transport, there have been many attempts, both experimental and through modeling studies, to understand and overcome the limitations caused by heterogeneity. To help consider scaling and heterogeneity, Figure 3.1 shows three different lines. The top most line is a classification of experimental technique into four different methods of inquiry. The second line is a representation of relative heterogeneity differences between the experimental methods, and also breaks down each method into relative levels of heterogeneity. The bottom line is the length scale that corresponds most closely

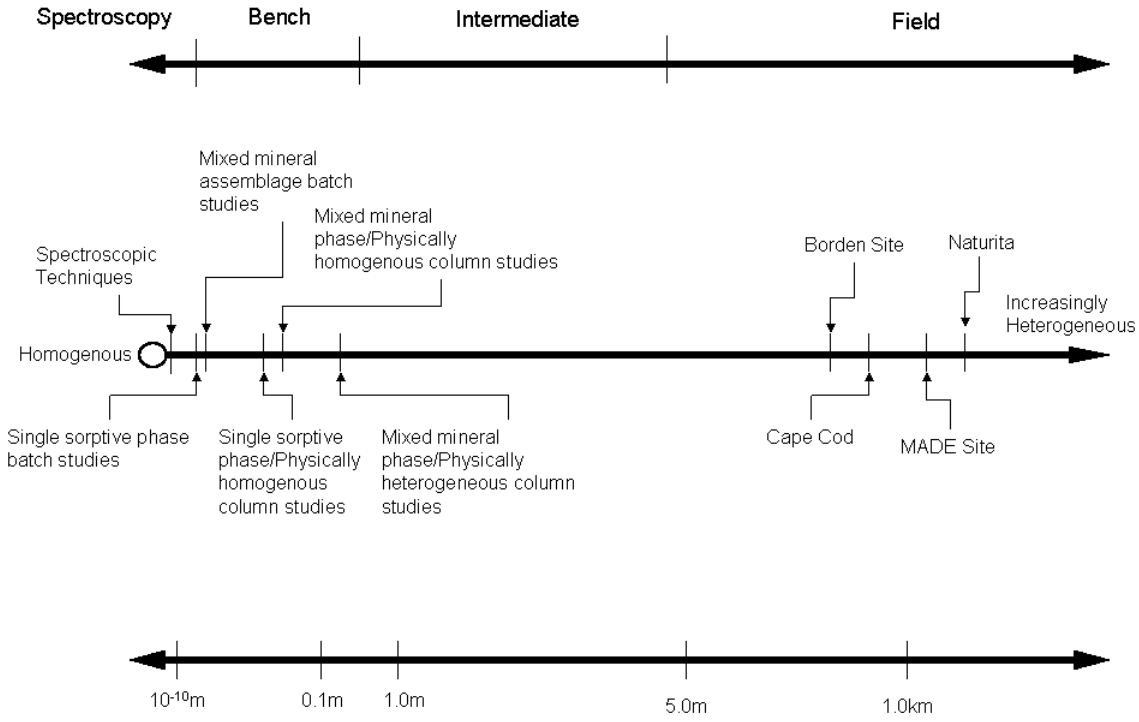

Figure 3.1 Relative heterogeneities of experimental systems, Top line: Experimental Methods, Middle line: Scale of increasing heterogeneity of different experimental methods in the literature, Bottom line: Characteristic length scales.

with the related experimental method. The length scales are not to scale; they are defined and aligned to approximate the length scale associated with each experimental method.

The first point to be made from this figure is that there is no experimental technique with a small enough sampling scale to be considered absolutely homogenous. The closest approximation to homogeneity is represented by the high energy spectroscopic techniques. These techniques are deemed to be the most homogeneous due to the fact that they are measurements of small numbers of atoms and are designed to get a structural information of a specific surface complex (e.g. *Sylwester et al.* [2000], *Bargar et al.* [2000], *Chisolm-Brause et al.* [2001], *Waychunas et al.* [2002], *Towle et al.* [1997], *Wersin et al.* [1994]).

Moving up on the heterogeneity scale, the next most homogenous system is that of the batch reactor, more specifically, batch reactors with a single sorbent and single sorbate. Batch reactors fall firmly in the bench scale experimental methods and due to their relative ease to perform and lack of special equipment required, this technique is widely used to probe metal/radionuclide sorption. There is no real associated length scale with batch reactors as they are truly point measurements. However, they are considerably higher on the heterogeneity scale compared to the spectroscopic techniques because even with a single mineral phase, there is often measurable surface site reactive heterogeneity; this heterogeneity is often modeled using surface sites of varying strength. Slightly higher on the heterogeneity scale are batch reactors with mixed mineral assemblages. These fall slightly higher as the mixed mineral assemblages allow for even higher surface heterogeneity relative to reactors with a single phase.

Above the batch reactors, in increasing order of heterogeneity, are column experiments with a single phase that have been physically homogenized (e.g., sieved), mixed mineral columns that have been physically homogenized, and mixed reactivity with macroscopic heterogeneities. These techniques are characterized as being more heterogeneous as there is not only surface site heterogeneity, but the nature of flow and reactions that occur through the columns can induce aqueous phase chemical gradients as well. This includes chemical gradients moving from the aqueous phase toward the mineral surface as well as chemical gradients moving from inlet to outlet of the column.

The next level of experimental inquiry is intermediate methods. As can be seen there are no experiments in this range for metal/radionuclide transport, which is a central point to this paper. The intermediate scale represents a level of heterogeneity between that possible in columns and that found in the field. It also falls between bench and field scale techniques in terms of length scale. Beyond the intermediate scale are the field scale methods. Even through many of the field scale sites specified are of the same order of magnitude in length (10^2-10^3m), they still do not plot in the same spot on the heterogeneity scale. This is due to natural variations in physical heterogeneity as well as chemical reactivity. The ordering of the sites listed is arbitrary as not all of these sites had metal transport studies, so chemical reactivity variation is largely unknown, and other sites do not have tracer studies, so physical heterogeneities are unknown.

There are four major steps in scaling relationships on the heterogeneity scale: from atomistic interaction to batch behavior, from single mineral batch data to mixed mineral phase batch data, from batch to column, and from batch to field. Studies with column to field scaling are exceedingly rare and will only be addressed in passing. The first step in scaling is from spectroscopically determined interactions at the atomistic level to the batch scale. In two separate papers this was completed with two different surface complexation models (SCM, *Ponthieu et al.* [2006], *Arai et al.* [2006]). Both of these papers use the spectroscopic data and surface species stoichiometry as an anchor point, and then fit their respective SCM constants from experimental results found in batch systems. Thus, the scaling method invoked was really ad-hoc data fitting around a known surface species. The major distinction between these and previous batch studies are that in other studies the surface stoichiometries are simply assumed. So, although these studies are anchored in a measurable reality, and they transcend experimental methods as shown in Figure 3.1, they are still limited in the amount of quantitative reactive scaling that was completed. Furthermore, as the developed SCM are not used in transport studies, scaling sorption reactions from the atomistic scale to beyond the batch scale has yet to be attempted.

The second major step in scaling behavior is from single mineral batch data to mixed mineral batch data. On the heterogeneity scale in Figure 3.1, this is an increase in surface heterogeneity without changing either the length scale or the experimental

methods scale. When performing experiments with a single class of minerals (e.g. clays), variations in sorption behavior are attributable to surface area variations of the different minerals (*Prikryl et al.* [2001], *Bertetti et al.* [1998]). Thus when sorption behavior is normalized to surface area sorption response is identical independent of mineral phase. In more complex systems where the mineral phases are not related, the generalized composite and component additivity modeling approaches have been developed (see *Davis et al.* [1998], *Payne et al.* [2006], and *Waite et al.* [2000] for full discussions). In general the GC approach is easier to apply and thus more widely used, and it can describe sorption behavior at a variety of experimental scales. As a scaling method, the GC approach is an engineered technique that ignores many fundamental relationships in favor of applicability and heterogeneity scale independence.

The next major step in scaling research is the extension of batch data to column transport studies. As can be seen in Figure 3.1, column studies are far more heterogeneous, have a definite associated length scale, and are within the same experimental methods realm as batch studies. Because of the fact that batch studies and column studies can be completed at the bench scale, these two types of experiments are commonly completed in tandem; the SCM is fit to batch data and then applied to the transport data of a column. *Barnett et al.* [2000], *Brusseau and Zachara* [1993] and *Gabriel et al.* [1998] all use sorption isotherms to describe ion-surface interactions. Thus, the conceptual models that they have chosen to describe ion-surface interactions are less capable to explicitly describe variations in sorption behavior as a function of chemical heterogeneity. This is reflected by the relatively narrow range of chemical conditions that are used in their column experiments. The authors find rather poor agreement between the column data and the modeled data when the isotherm values are used directly. To improve the fits, kinetic terms are included either for the chemical reactions themselves (*Barnett et al.* [2000], *Gabriel et al.* [1998]), or for physical mass transfer limitations (*Brusseau and Zachara* [1993]). *Szecsody et al.* [1998], *Kohler et al.* [1996], and *Stollenwerk* [1995] all use a SCM to describe ion-surface interactions. These more complex descriptions between ions and the mineral surfaces should be able to account for more chemical heterogeneity associated with moving from the batch to the column scale, and these descriptions can be linked to a transport code directly in reactive

transport modeling (RTM). However, in using the batch derived models to describe column data, the same discrepancies are seen as with the isotherm based studies. *Szecsody et al.* [1995] fit kinetic terms to fill discrepancies; both *Kohler et al.* [1996] and *Stollenwerk* [1998] re-fit SCM parameters to column data. Interestingly, in *Kohler et al.* [1996] the column derived SCM parameters were able to describe both batch behavior and data from subsequent column experiments without adjustment (i.e. heterogeneity scale independent). Similar results were found by *Zachara et al.* [2002] and *Steefel et al.* [2003] where an ion exchange model fit from more heterogeneous columns was able to describe batch data without adjustment, but not vice versa.

The final scaling steps which have been completed are to extrapolate batch data to field simulations. This has been completed in two ways, the first is to create a SCM from batch data, perform field characterization and then use the SCM directly in a RTM (*Curtis et al.* [2006], *Stollenwerk* [1998], *Kent et al.* [2000] and [1995], *Davis et al.* [2000]). *Curtis et al.* [2006] use the SCM as derived from batch conditions, and much of the data fitting comes in the form of fitting hydrologic variables. However, the observed uranium distribution and the modeled uranium distribution for their field site are in relatively good agreement. When the same RTM was used to describe column data, the fits were less accurate (*Davis and Curtis* 2003). In *Stollenwerk* [1998] and *Kent et al.* [2000] multiple surface site reactions were added to describe field data that were not necessary at smaller scales. These reactions are based on 'strong' surface sites whose affinity for the binding metal is much higher than average. In both cases the addition of this site type decreased the amount of lateral dispersion and gave better fits to observed data over long periods of time. The second method that has been used to compare bench and field scale reactivity is to determine *in-situ* K_D values and compare them to SCM predictions. This was completed by *Payne et al.* [2001] and *Curtis et al.* [2004]. In both of these studies favorable comparisons were made between measured and calculated values, implying that chemical reactivity is the same in the field as in the lab. Thus, it would appear that the discrepancies between model and observed data must be due to hydrologic fitting methods, or physical and chemical heterogeneity at field scales which exist at a different scale than that used to determine *in-situ* K_D values.

In all of these studies the total surface area is used as the scaling method. The assumption inherent in this approach is that the chemical reactivity observed at one scale is identical to that at another. There is certainly evidence for (*Payne et al.* [2001], *Curtis et al.* [2004], *Stollenwerk* [1998], *Kent et al.* [2000], *Turner et al.* [2006]) and against (*Szecsody et al.* [1998], *Kohler et al.* [1996], *Stollenwerk* [1995], and *Arnold et al.* [1998] and [2001], *Fuller et al.* [1996]) this assumption. Direct testing of this assumption from the studies presented is complicated by the available data and fitting procedures taken by the respective authors. It is also complicated by the fact that the data only exists at two scales. As can be seen in Figure 3.1 there is a large jump in heterogeneity and length scales moving between bench and field experimental techniques.

To help transcend this gap, uranium transport experiments have been performed at the intermediate scale. These experiments are preformed within a well defined flow domain with a known packing heterogeneity. The construction of the tanks allows for a high degree of spatial characterization that is impossible in field settings. The results of this experiment will allow for the testing of scaling methods including the assumption that chemical reactivity is constant as a function of scale.

3.2 Methods

Complete methods and lists of materials are presented elsewhere (see CHAPTER 2). A truncated version of the methods relevant to the conclusions made are presented here.

3.2.1 Tank Construction

Two intermediate scale tanks were constructed. Tank #1 had internal dimensions of 2.44m x 1.22m x 7.62cm (LxHxW); tank #2 had internal dimensions of 2.44m x 0.61m

x 7.62cm (LxHxW). Because of the different heights of the tanks, and the different masses of water and sediment required to fill the tanks, slightly different tank constructions were required. Tank #1 had aluminum plates along the bottom and two ends perpendicular to water flow. The walls parallel to flow were made of Plexiglas. The Plexiglas walls were screwed to an exterior frame made of welded aluminum for support (see Figure 3.2). Small sampling ports were drilled through the Plexiglas walls at regular intervals throughout the tank. These ports were created by drilling a 0.64cm hole half way through the thickness of the Plexiglas. In the center of that hole a 0.16cm hole was drilled all the way through the wall. A 0.64cm septa was placed in the hole, and held in place by use of a 0.64cm jam screw. This created a leak proof hole through which a needle could be placed to withdraw samples for porewater analysis; 56 ports were installed in Tank #1. The tank walls were bolted together, and were separated by a 1.25cm rubber gasket material to create a water tight seal.

End filters were constructed out of aluminum channeling, aluminum screen, and common household air filter material. Several 1.22m lengths of channeling were screwed together to a width of approximately 7.6cm. Several hundred 0.64cm holes were drilled through this channeling to allow for free water flow. The aluminum screen was screwed to the channeling, and wrapped around the air filter material which had been cut to size. Two of these end filters were made and placed in the up and down gradient end of the tanks. The screen and air filter material was molded so that it fit the internal dimensions of the tank exactly. The end filters allow for a well defined flow domain by keeping the sediments in place, and also maintained constant head boundaries within the tank.

Constant head boundaries were constructed from 8.9cm OD and 7.6cm ID pipe that was glued to a 17.8cm PVC end cap. The end cap was sealed with caulking, and two holes were drilled, one inside of the 7.6cm pipe, and one in the space between the 7.6cm pipe and the 17.8cm PVC end cap. Brass nipples were screwed into these holes to allow for connection of the tubing. Hose clamps were used to keep the tubing in place and free of leaks. Holes were drilled through the endplates of the aluminum plating and holes were punctured through the gasket material. The head boundaries were connected to these holes with 0.95cm tubing using brass nipples and valves which had been threaded into the aluminum end plates. The valves allowed for instantaneous starts and stops to

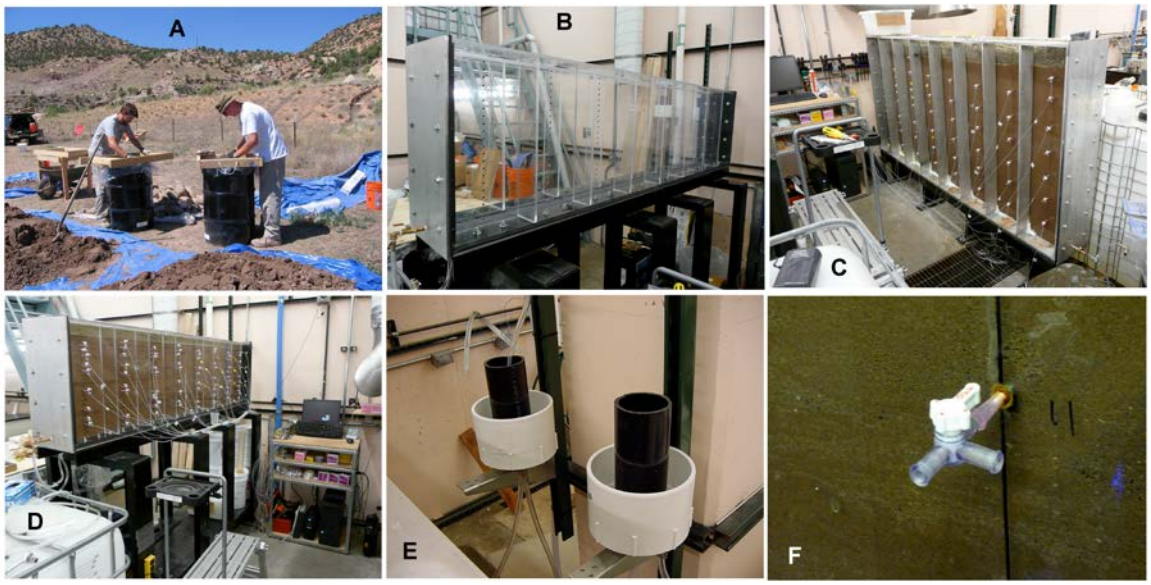

Figure 3.2 Field sieving and tank construction photos, A- Sieving sediments in the field, B- Tank #2 constructed but prior to packing, C- Tank #1 packed and connected to the pressure system, D- Tank #2 packed and connected to the pressure system, E- Head boundaries used to control flow through the tanks, F- Three way valve for sampling and pressure measurements.

flow. Prior to filling the tank with sediments, the tank was leak tested for about two weeks.

The major difference between tanks #1 and #2 is the height. Because tank #2 is relatively smaller, the exterior welded aluminum frame used in tank #1 was not needed. A similar Plexiglas frame was used instead (see Figure 3.2). This Plexiglas frame was epoxied to the exterior of the walls parallel to flow. Other than that the construction proceeded as in tank #1. A total of 176 sampling ports were installed in the wall of tank #2. Only a fraction of these were used in the experiments; the excessive number was installed to allow for sampling flexibility and for potential future experiments. Similar end filters were constructed, the only difference that they were half as tall as in tank #1. Identical head boundaries were constructed, and connected to the tank in a similar manner.

3.2.2 Tank Packing

Besides the constructed height of the tanks, the major difference between them is how they were packed. Tank #1 is considered to be physically homogenous, and tank #2 is considered to be physically heterogeneous. All of the sediments used in these experiments originated from a former uranium mill in southwestern Colorado, U.S.A. This site has been used as a research site for nearly a decade, and site specific details can be found in *Davis and Curtis* [2003]. In the summer of 2006, a collaborative effort between researchers at the USGS, Lawrence Berkeley National Lab (LBNL), and the Colorado School of Mines (CSM) was undertaken to collect enough sediments to fill the planned tank experiments. It was estimated that 12- 55 gallon drums would be required (~3300kg). Using a backhoe and a dump truck, sediment was removed down to the water table. The hole was placed in a location where there is still significant groundwater contamination, and where the sediments were known to have considerable amounts of sorbed uranium. Once the water table was reached another ~1m of depth was removed from an area of approximately $15m^2$. These sediments were roughly drained using the

dump truck, and laid on tarps for sieving. Three different size fractions were created in the field. Those size fractions are: <2mm, 2-4mm, and 4-12mm. The >12mm fraction was discarded. The vast majority of the sediment (11 drums) was composed of the <2mm material, which is the sediment that were used in both tanks #1 and #2.

Tank #1 was packed solely with the field created <2mm composite material. Prior to packing, the sediments were air dried in the laboratory in 50-100kg batches. The sediment was stirred about twice a day to expedite drying and to create as homogenous of a mixture as possible. As the sediments dried the color got lighter. When the sediments had achieved a uniform light color, they were considered to be dry. Tank #1 was packed in approximately 10cm lifts. Enough sediment to create about 10cm of depth was added to the tank. The sediment was then compacted by hand with a 1.25cm diameter aluminum rod. Once the sediment felt compacted, another 10cm worth of material was added. The compaction procedure also allowed for some vertical mixing between lifts. This procedure was repeated until the sediment depth was 10cm from the top of the tank. A layer of parafilm was put on top of the sediment, and the remainder of the tank was filled with a hydrated bentonite clay. The clay acted as both an evaporative barrier as well as a barrier to mixing with atmospheric CO_2. The hydraulic conductivity of the sediment was determined to be 4.09×10^{-4} cm/sec by ASTM method D 2434-68. As the tank was saturated, the sediments did subside about 7cm. The clay was pushed down by hand to maintain contact with the parafilm and to maintain the seal to the atmosphere. The exact mass of sediment was not measured, but using a bulk density of 1.5g/mL and the internal dimensions of the tank, a good estimate is 286kg. The labile uranium concentration (*Kohler et al.* [2004]) on the sediment is 1.8×10^{-2} μmol U/g sediment. Thus approximately 5.15mmols of uranium were added to the tank.

Tank #2 was packed with two different particle sizes created from the <2mm composite material. Approximately 200kg of <2mm composite material was air-dried as before. This material was re-sieved using a 0.250mm screen. This created the <0.250mm and >0.250mm size fractions. The sieving distribution was 43.1% <0.250mm, and 56.9% >0.250mm. The packing distribution can be seen in Figure 3.3. Because of the soil subsidence observed in tank #1, a concrete vibrator was used to compact the sediments in tank #2. Because of this, each layer was packed all at once as

opposed to in lifts as in tank #1. Thus, the first layer of >0.250mm material was added, and compacted with the concrete vibrator. The layer was topped off, re-compacted and the next layer was added. To create the 'block' of <0.250mm material at the upgradient end, a narrow (~0.5cm) aluminum slat was used. Both sides of the slat were simultaneously packed with the required size fractions. Each time a new layer was in place, the layer was compacted; great care was taken to compact only one layer at a time with the concrete vibrator. Before the final >0.250mm layer was packed, the aluminum slat was removed. As in tank #1, a layer of parafilm was placed on the uppermost layer of sediments, and a layer of hydrated clay was put on top of the parafilm to act as a barrier to the atmosphere. A total of 163.2kg of sediment were placed in tank #2 consisting of 69.8kg of <0.250mm and 93.4kg of >0.250mm material. This gives a packing distribution was 42.8% <0.250mm, and 57.2% >0.250mm. The hydraulic conductivities of the sediments were determined to be 1.16×10^{-3} cm/sec and 1.55×10^{-4} cm/sec for the >0.250mm and <0.250mm material, respectively. The labile uranium concentrations for the <0.250mm and >0.250mm size fractions was found to 1.8×10^{-2} μmol U/g sediment and 1.7×10^{-2} μmol U/g sediment, respectively. Thus a total of 2.87mmols U were added to the tank.

3.2.3 Experimental Procedures

Both tanks were saturated by allowing the influent to flow through the influent head boundary. Influent water compositions for the two experiments can be seen in Table 3.1. AGW-atmospheric was used exclusively in tank #1, while both AGW-atmospheric and AGW-2% were used in tank #2. To maintain equilibrium with either atmospheric CO_2 or the 2% CO_2, the AGW's were constantly sparged with the respective gases. Tank #1 took approximately 10 hours for the effluent head boundary to overflow, and the void volume was 80L. Tank #2 took approximately 48 hours to saturate and had a void volume of 48L. The relatively long saturation time was caused by the formation of a bubble in the effluent line impeding flow. Once the bubble was cleared the tank

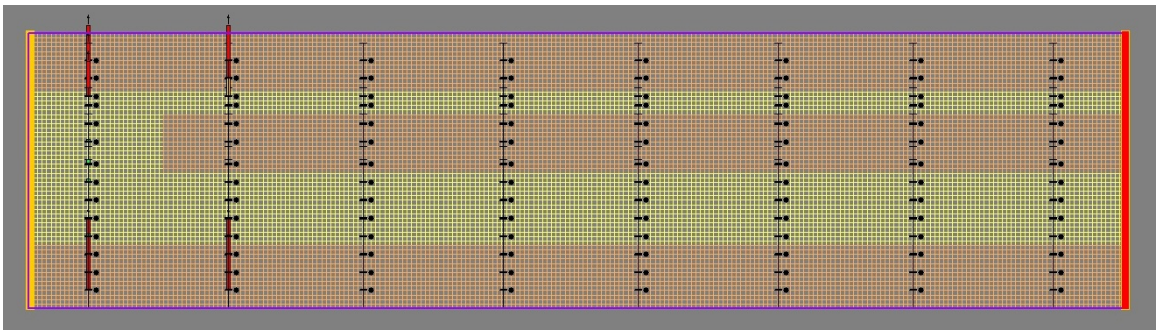

Figure 3.3 Tank #2 packing orientation, red cross hatch is the >0.250mm size fraction; the yellow cross-hatch is the <0.250mm size fraction; upgradient end is on the left, downgradient end is on the right.

Table 3.1 Artificial ground water compositions used in tanks #1 and #2. Ion concentrations are in molar, pH in standard pH units, and alkalinity is in meq/L.

Constituent	AGW-atmospheric	AGW-2%
Na^+	$2.43x10^{-2}$	$2.11x10^{-2}$
K^+	$2.50x10^{-4}$	$2.50x10^{-4}$
Mg^{2+}	$2.67x10^{-3}$	$2.67x10^{-3}$
Ca^{2+}	$5.73x10^{-3}$	$7.30x10^{-3}$
Cl^-	$1.65x10^{-2}$	$1.33x10^{-2}$
SO_4^{2-}	$1.21x10^{-2}$	$1.21x10^{-2}$
Ionic Strength	$5.11x10^{-2}$	$6.54x10^{-2}$
pH	7.85	7.15
Alkalinity	0.61	3.85
Equilibrium Gas	Atmospheric	2%CO_2, 20%O_2, 78%N_2
Calcite Saturation Index (calculated)	0.09	0.08

flowed naturally. AGW-atmospheric was used for the initial stages of tank #2; after 2.4 pore volumes (PV) were injected a 1.3 PV injection of AGW-2% occurred. After the injection, the influent was returned to AGW-atmospheric. For both tanks, the effluent was directed to a 5-gallon bucket and was measured periodically either volumetrically (tank #1) or by mass difference (tank #2) to determine flow rates.

Sampling procedures for both tanks were identical. A needle was placed through the septa for most of the sampling ports in tank #1, some of the ports were rendered unusable due to the soil subsidence and clay layers. In tank #2, needles were only installed in 26 total ports spaced throughout the tank. The sampling density was slightly higher at the upgradient end of the tank to allow for better characterization of chemical distributions around the block. Attached to the needles was a three way valve; this allowed for turning off and on the sampling ports, and also allowed for the connection of a of a digital sensor array (DSA 3207, Scanivalve Corp.) to measure local pressure head. To withdraw water samples, a syringe was connected to the third port on the three way valve. The three way valve was turned until the syringe was hydraulically connected to the water in the tank. Approximately 5-7mLs of solution were removed. The valve was turned so that the pressure array was again in hydraulic connectivity with the pore water. The syringe was removed and the sample was immediately filtered (0.45μm PVDF syringe filter) into a 15mL centrifuge tube. pH was immediately measured using a standard pH meter and probe calibrated with pH 4, 7, and 10 buffer. The sample was then split for analysis; 2mL of sample was acidified with 1.0M nitric acid for bulk ions (Ca, Na, K, Mg, Si, S_{tot}, Fe, Mn, Al) as well as uranium, 3mLs were refrigerated before being sent to LBNL for alkalinity titrations using an automatic titrator. When tracer tests were occurring, an additional 1-2mLs was refrigerated for bromide analysis. Bulk ions were analyzed on a Perkin Elmer Optima 3000 Inductively coupled plasma atomic emission spectrometer (ICP-AES). Uranium was analyzed on a Perkin Elmer Sciex Elan 6100 inductively coupled plasma mass spectrometer (ICP-MS). Bromide was determined with a Dionex Ion chromatograph (IC). In tank #1 every other port (horizontally and vertically) was sampled for a single sampling event giving a total of 24-25 spatial samples. For the next event, the ports that had not been sampled previously were sampled. Sampling events occurred every 4-5 days. In tank #2, the ports used for spatial

sampling were mostly static, although there was some variation in the down gradient end. Spatial samples (24-25) were taken weekly.

Effluent samples in both tanks were removed from t-joints installed in the effluent line emanating from each tank. For each effluent sample, the tubing was purged with 25-50mLs of water from the tank. Then 7mLs of solution was allowed to flow into a syringe with a filter already in place. Influent samples were taken directly from the influent head boundary. Once taken, the influent/effluent samples were split and analyzed just as the spatial samples. Influent/effluent samples were taken approximately weekly for tank #1 and every 2-3 days for tank #2.

Stop flow events were completed in both tanks to examine kinetic hindrances to uranium desorption. These were completed by simultaneously closing the valves on the influent and effluent ends of the tank. In tank #1 three were completed at 4.0, 4.5, and 6.0 PV and lasted for 97 hours, 354.5 hours, and 500.5 hours, respectively. In tank #2 only one was completed occurring at 1.3 PV and lasting 650 hours. All sampling was suspended during stop flow events.

Pulse bromide tracer tests were completed in both tanks to determine major water flow paths and for fitting of hydrologic parameters. In both tanks a bromide concentration of 2.02×10^{-3}M KBr spiked into AGW-atmospheric was used which has been shown to avoid density induced sinking relative to tritiated water (*Barth et al.* [2002]). Also in both tanks the bromide tracer was injected through a parallel head boundary connected to t-joint in the influent line. Because of the relative size and flow rate differences between the two tanks the injection times and total mass of bromide injected was slightly different for each tank. In tank #1 the injection occurred over 13.25 hours and a total of 201mg (2.52×10^{-3} mols) of Br^- were injected. In tank #2, the injection required 18.25 hours and a total of 153mg (1.91×10^{-3} mols) Br^- were injected.

3.3 Results

First the results relating to uranium behavior within both of the tanks is presented. This is followed by the bromide results from both tanks.

3.3.1 Uranium Data

Uranium breakthrough curves for both tanks #1 and #2 can be seen in Figure 3.4. It can be seen that tank #1 reached tailing behavior in two PV, while tank #2 reaches tailing behavior in about one PV. Also, in both tanks, when AGW-atmospheric is being used the tailing concentration is about 1.5μM. However, the tailing concentration in tank #2 almost doubles during the time of the AGW-2% injection. This is consistent with known uranium chemistry where increased alkalinity increases the rate and extent of uranium desorption. These two results together imply that chemical controls dominate the desorption and migration of uranium as opposed to physical heterogeneity controls induced by the different packing orientations. It is difficult to discern the reactions to the stop flow events in Figure 3.4. The same data is plotted in Figure 3.5 after normalizing the uranium concentration to the amount of sediment added as well as to the flow rates in each tank. The black arrows in the figure denote each stop flow event with the elapsed time of the event next to the arrow. It can be seen that for each of the stop flow events the normalized uranium flux increases. In tank #2 however, there is no re-bound in uranium concentrations. Also, the tank #2 normalized uranium flux increases slightly during the time of AGW-2% injection (area between the red arrows).

In addition to the effluent values, the spatial sampling allows for a well-characterized view of the processes occurring in the tanks. Figure 3.6 shows three different plots of uranium distribution within tank #1, while Figure 3.7 shows four different plots for tank #2. In Figure 3.6, the three plots chosen represent time points from the beginning, middle and end of the experimental time frame, a period of 164 days.

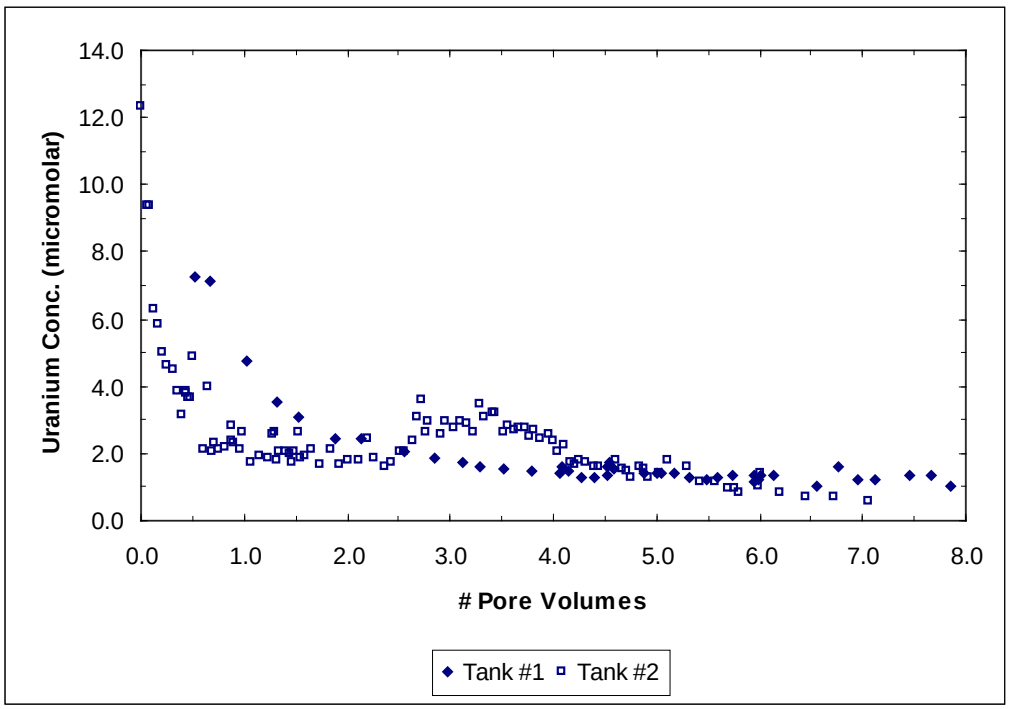

Figure 3.4 Uranium breakthrough curves for both tank #1 (solid symbols) and tank #2 (open symbols). Total uranium determined from tank effluent samples.

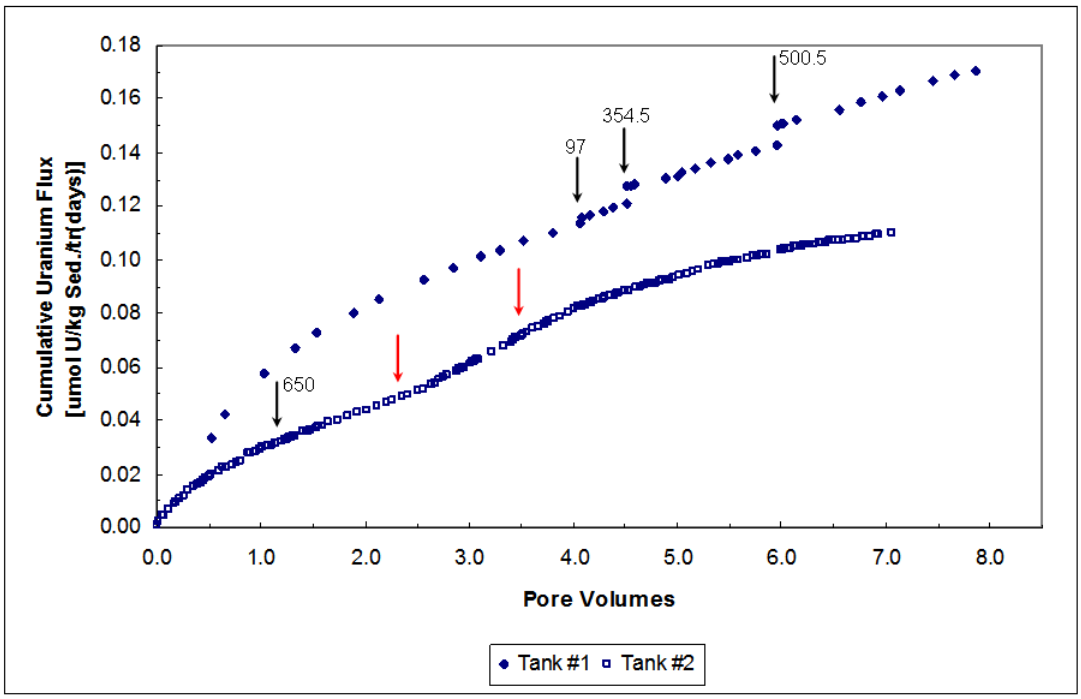

Figure 3.5 Normalized uranium flux as a function of pore volume in both tanks. Tank #1 is the closed symbols, tank #2 is the open symbols. Black arrows are stop flow events with the elapsed time (in hours) labeled next to the arrow. The area between the red arrows for tank #2 is the time of the AGW-2% injection.

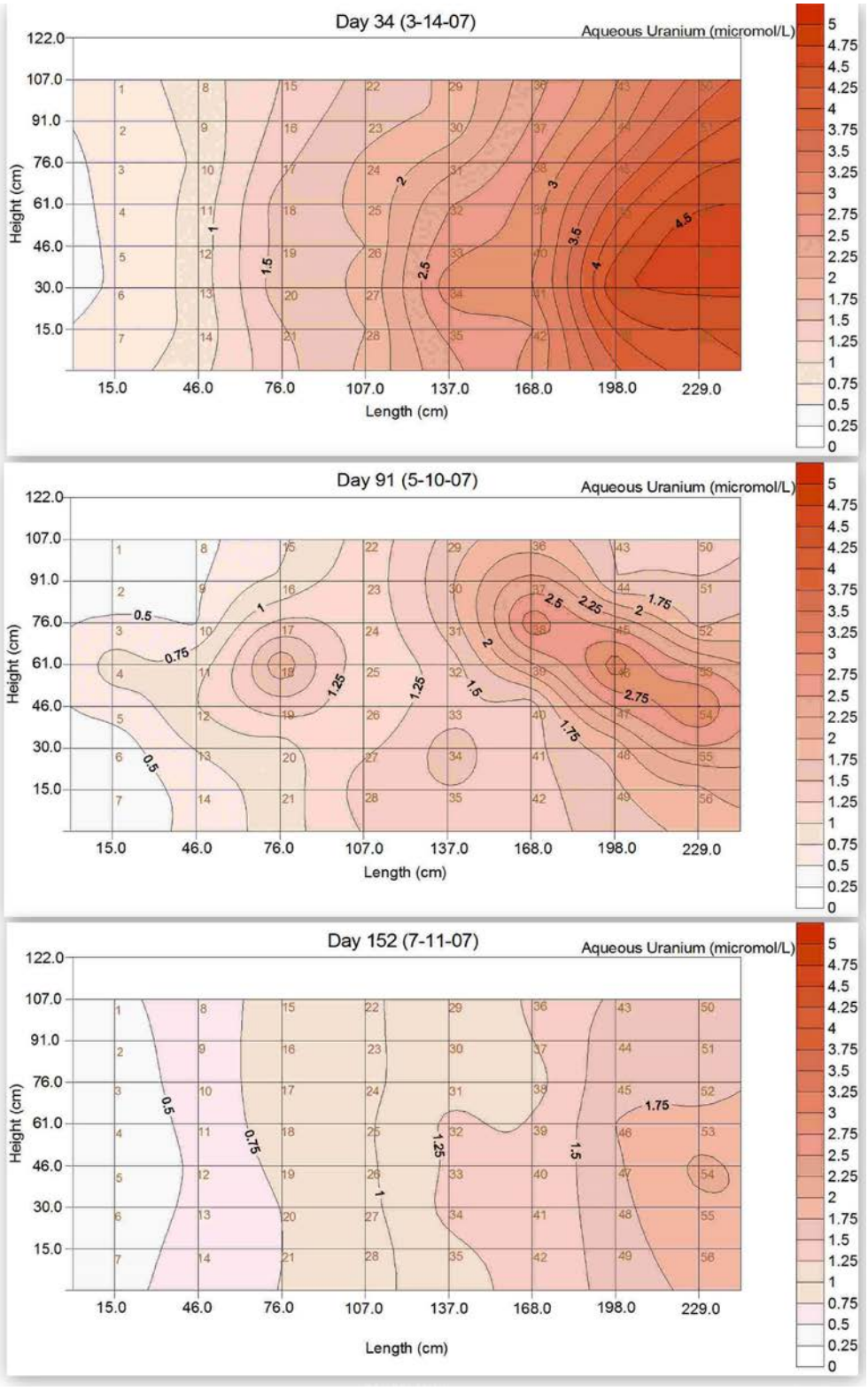

Figure 3.6 Kriged uranium spatial distributions from three different time points representing the beginning, middle and end of the experimental timeframe. Upgradient end is on the left, down gradient end is on the right.

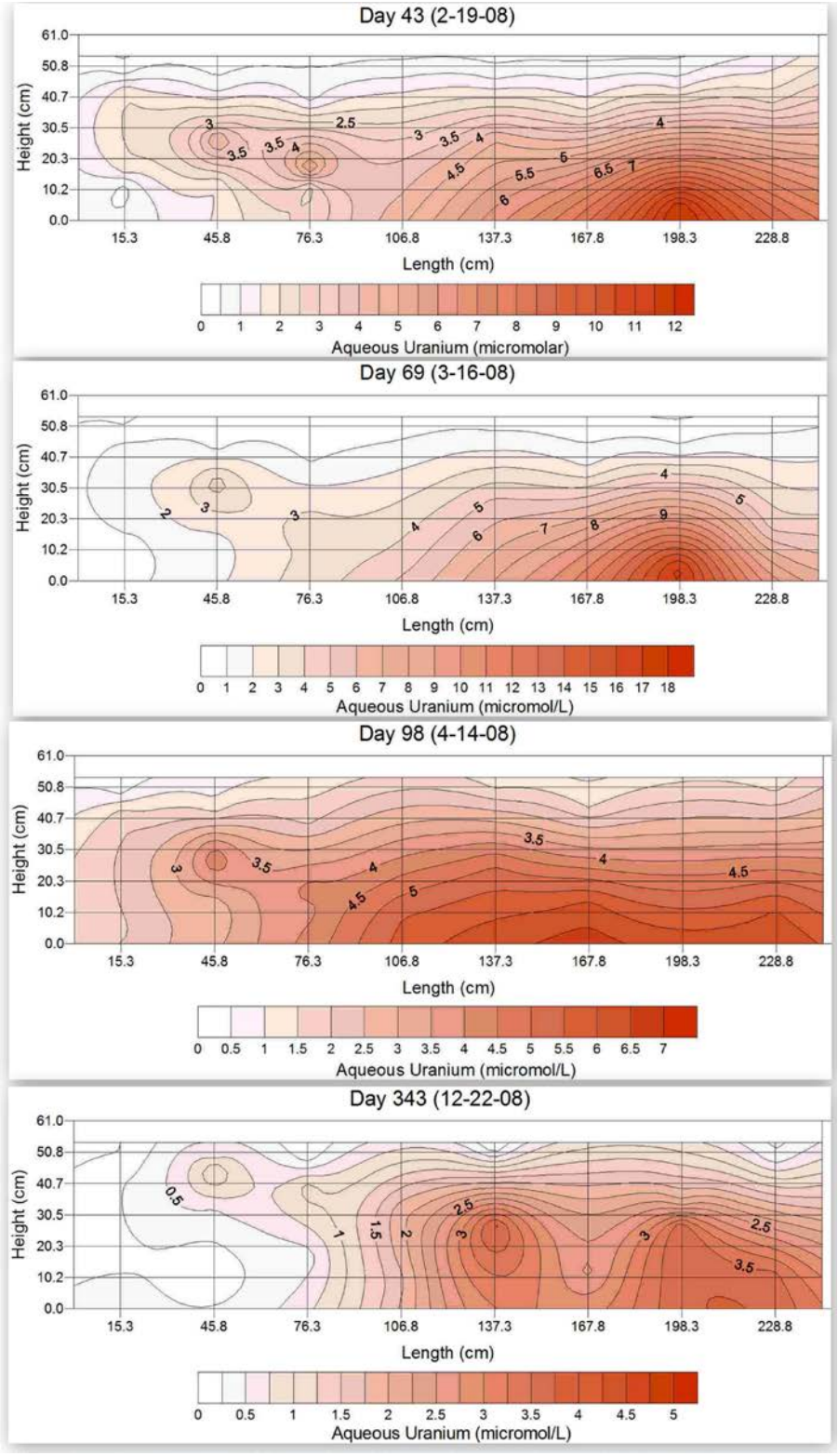

Figure 3.7 Kriged uranium spatial distributions for tank #2. Note the changing uranium scales. Upgradient end is on the left, downgradient end is on the right.

As can be seen from these plots, the uranium distribution is fairly regular, increasing in concentration as the water flows downgradient. The vertical concentrations gradients in the upgradient half of the tank are fairly flat, consistent with laminar flow. However, on the downgradient half this is not the case. Over time, Figure 3.6 shows that the general orientation of the concentration gradients is invariant; however the magnitude changes with earlier time points showing larger increases in uranium concentration as a function of assumed flowpath. In comparing the spatial sampling plots from before and after stop flow events, there is no appreciable change in uranium concentrations (data in APPENDIX B). Figure 3.7 shows similar plots but for tank #2; the total elapsed experimental time was 437 days. The effect of the block on the spatial distribution of uranium is clearly evident. The uranium concentrations in the block itself are often higher than in the higher flow zones immediately surrounding the block. On the downgradient half however, the effects of the macroscopic physical heterogeneities are less evident. Figures from days 69 and 98 in Figure 3.7 show the uranium spatial distributions immediately before and immediately after the 650 hour stop flow event. These two plots show that the uranium spatial gradients become less severe through the stop flow event. Discretization and visual summation of the uranium in each plot showed that the total uranium in solution was within 20% moving from before to after the stop flow event. All of the uranium spatial plots as well as kriged plots for pH, alkalinity, and calcium are in Appendices B and C. Generally, moving from up to down gradient the pH decreases, Ca^{2+} increases, and alkalinity increases for both tanks.

3.3.2 Uranium and Alkalinity Relationships

Figure 3.8 shows the relationship between uranium and alkalinity in tank #1 as a function of time. Each point represents the analysis from a single spatial sample for the given day. The lines are linear fits for each sampling point in time. It is interesting to note that the relationship is largely linear for any given sampling date, and that the slope changes as a function of time. Despite this change in slope, speciation calculations for

each sampling point in time show that the $Ca_2UO_2(CO_3)_3^0$ species dominate uranium aqueous speciation (>98%) over time and space. Figure 3.9 shows a similar plot for tank #2. In tank #2, the change in slope as a function of time is largely not present. Again though, the $Ca_2UO_2(CO_3)_3^0$ species dominates uranium aqueous chemistry over time and space. This species has been shown to be much less surface active relative to uranyl-carbonate species (*Dong et al.* [2005], *Fox et al.* [2006]). It should also be pointed out that the data from the AGW-2% injection is also included in this plot.

3.3.3 Bromide Data

Figure 3.10 shows the bromide breakthrough curves for both tank #1 and #2. Tank #1 exhibited more ideal behavior than tank #2 as expected for the relative differences in packing orientation. Tank #2 was traditionally non-ideal in that the bromide breaks through earlier, and tails much longer relative to the more homogenous tank #1. The mass recoveries for tank #1 and #2 were 79% and 85%, respectively. It is assumed that the <100% recoveries were caused by dilution of the bromide below quantitation limits in the effluent and variation in flow rates leading to integration errors. Results from the spatial analyses for bromide are shown in Figures 3.11 and 3.12. Figure 3.11 shows the distributions for tank #1 at the beginning, middle and end of the tracer test. The total elapsed real time for the tracer test was 46 days. Figure 3.12 shows similar distributions for tank #2. The total elapsed time for this tracer test was 180 days.

3.4 Discussion

It is well known that uranium chemistry is heavily dependent on dissolved carbon dioxide species. As seen in the previous plots, there is also a strong relationship between

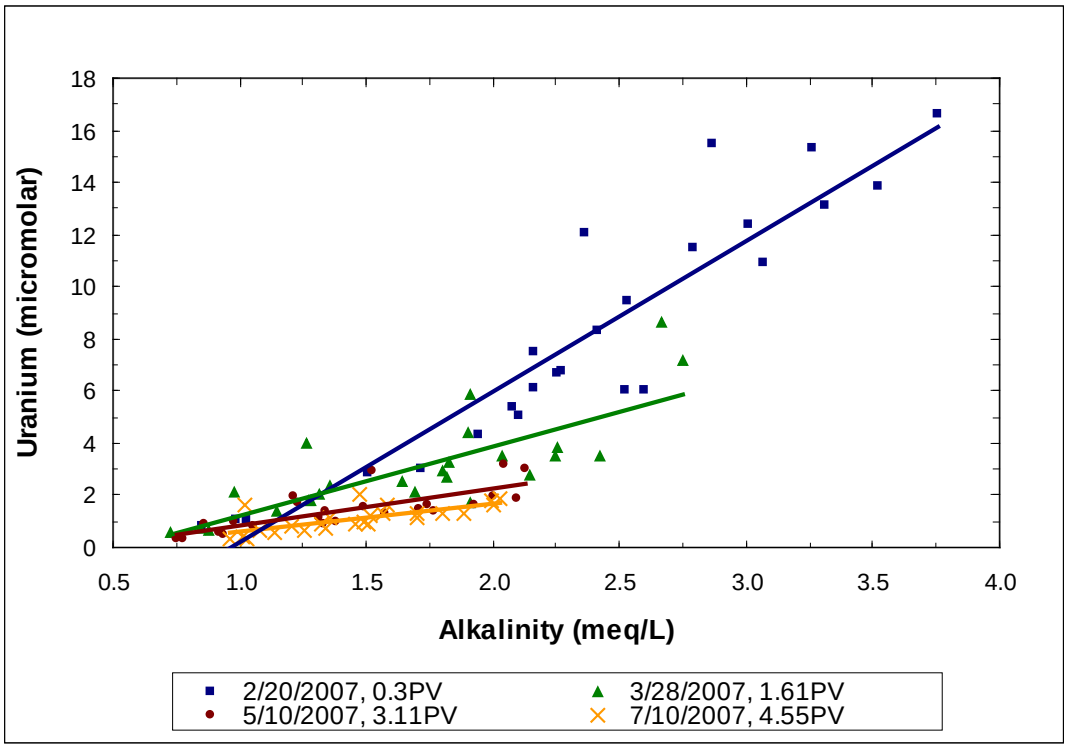

Figure 3.8 Uranium vs. alkalinity concentrations over time in tank #1. Each point represents the analysis from a single spatial sample. Lines of best fit are shown for each sampling point in time.

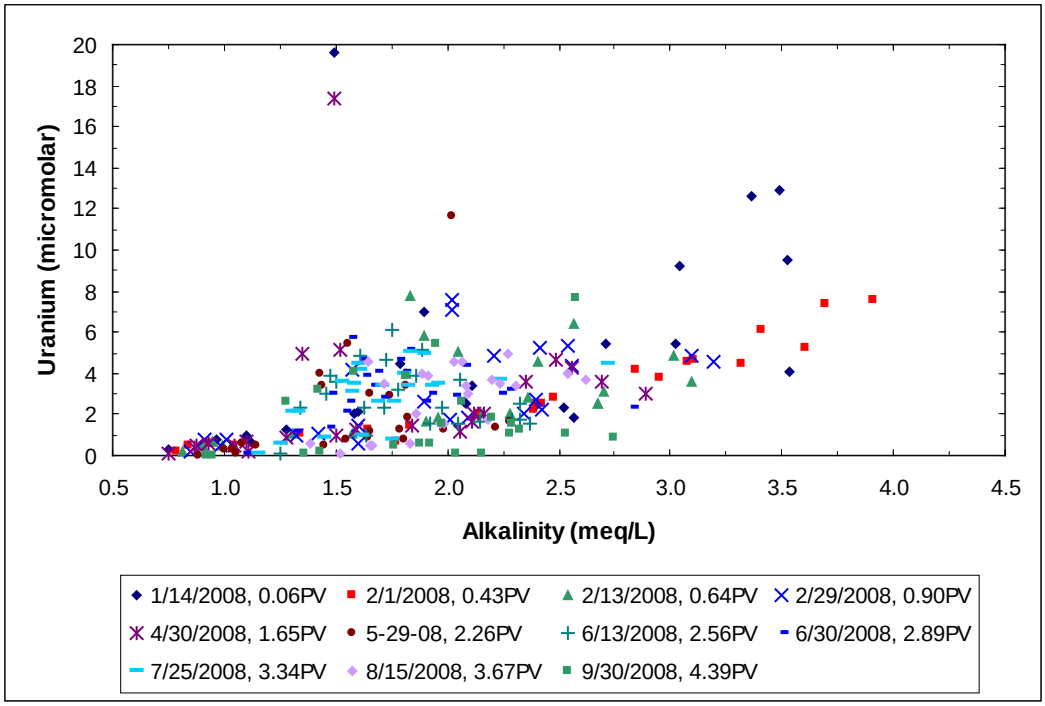

Figure 3.9 Uranium vs. alkalinity concentrations over time in tank #2. Each point represents the analysis from a single spatial sample.

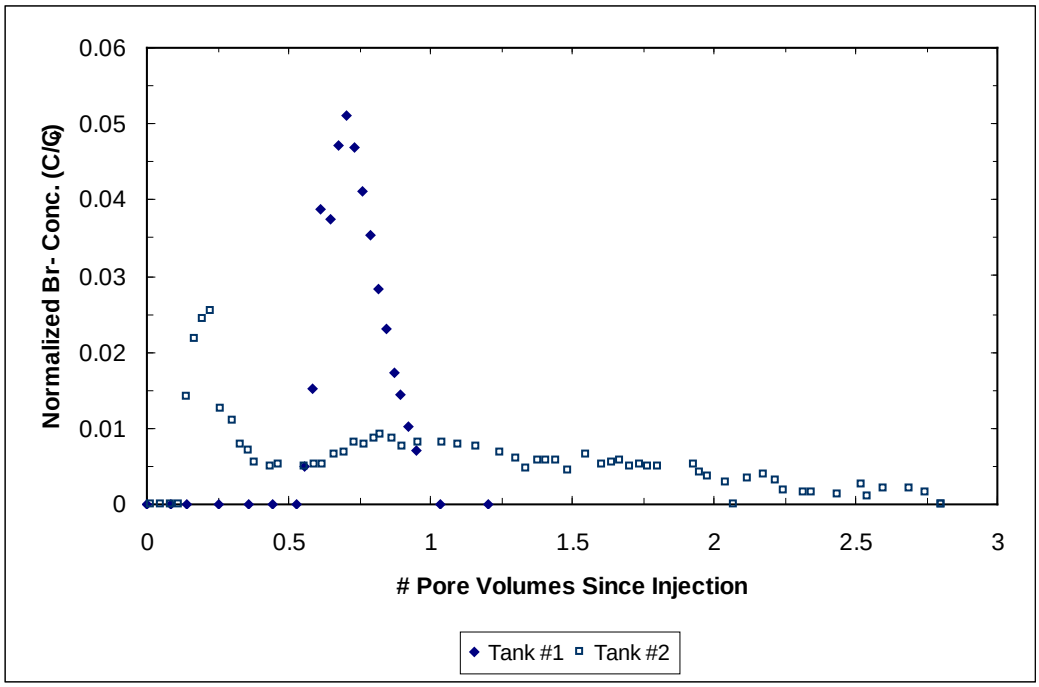

Figure 3.10 Normalized bromide breakthrough curves for tank #1 (closed symbols) and tank #2 (open symbols).

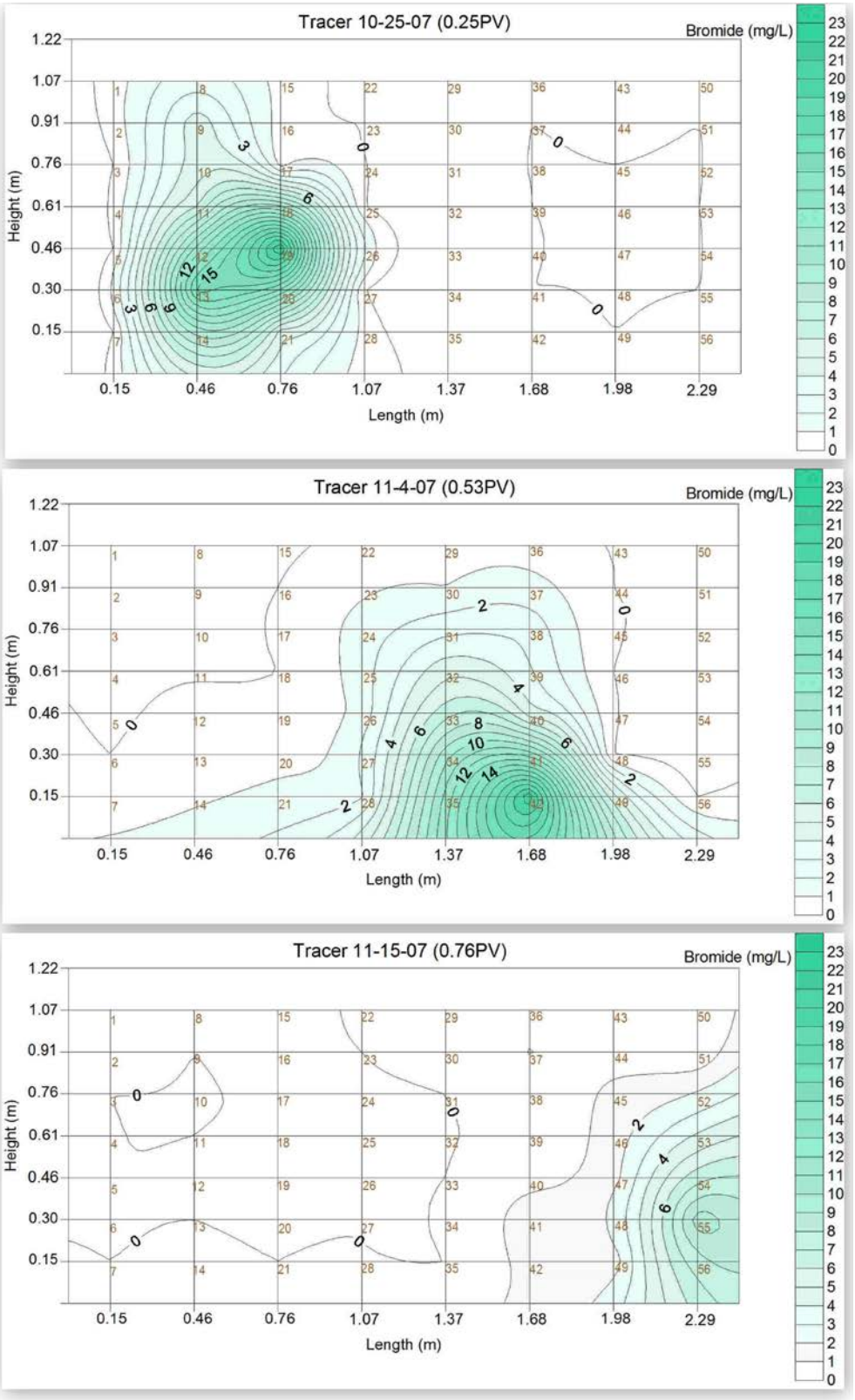

Figure 3.11 Kriged plots of bromide spatial distributions as a function of time in tank #1. Upgradient end on the left, downgradient end on the right.

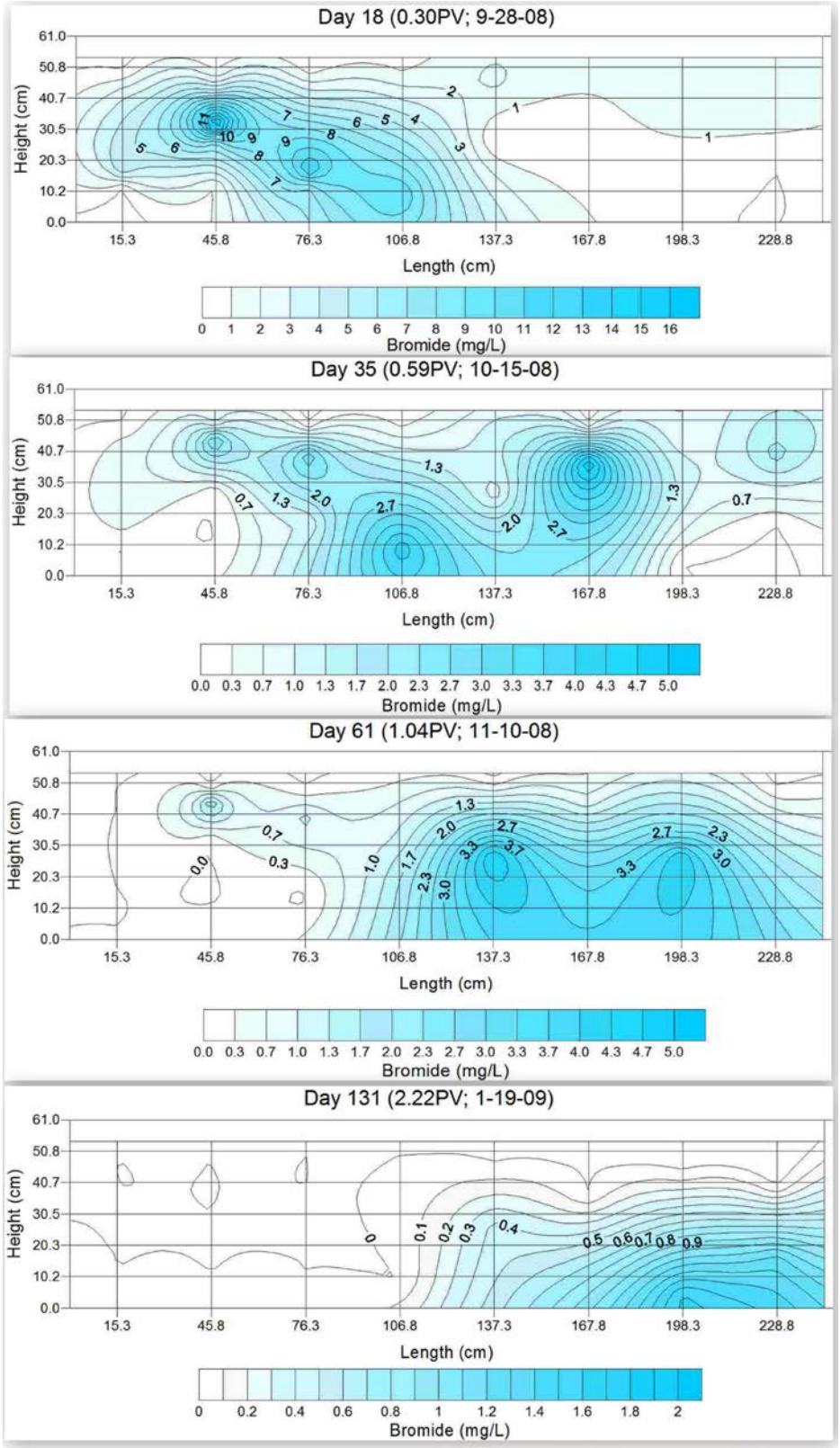

Figure 3.12 Kriged bromide plots as a function of time for tank #2. Upgradient end is on the left, downgradient end is on the right. Note the changing concentration scales.

uranium and alkalinity in both tanks. Further understanding of this relationship is necessary to be able to determine scaling methodologies for uranium transport.

3.4.1 Major Ion Solubility Controls

The field sediment composition was determined by XRD to be of a mixture of clay minerals (chlorite, smectite, illite, mica, kaolinite, and plagioclase) as well as quartz and calcite. For calcium, alkalinity, and pH the major sources of the concentration gradients within the tank are from the weathering of these minerals. Figure 3.13 shows the calcium concentrations from spatial sampling events for several time points within the experimental time frame for both tank #1 and tank #2 in pC/pH space. Also on the plot are the solubility limits for calcite for the range of PCO_2 that was found in the tanks, and gypsum solubility curves for the range of sulfate measured in the tank experiments. Tank #1 is supersaturated with respect to both calcite and gypsum for most of the experimental timeframe. Tank #2 falls into the range of possible equilibrium with calcite (SI = -0.75 – 0.36), however, the slope is parallel to that of gypsum equilibrium. In both tanks weaker correlations were found between calcium and PCO_2 implying that calcite is not the only source of either calcium or alkalinity; there may also be significant calcium associated with the clays via ion exchange reactions. It is also interesting to note the difference in behavior between the two tanks. Tank #2 has a broader pH range and a narrower calcium range than that seen in tank #1. The differences in observed reactivity are caused by the physical heterogeneity differences between the two tanks. The difference is extreme enough that different minerals may be controlling calcium solubility depending on the physical heterogeneity orientation. Variability in calcite reactivity based on physical orientation of the reactive and non-reactive zones has been described by *Li et al.* [2006] and [2007]. However, this behavior was modeled at pore scale levels of heterogeneity. This work is the first instance of observed chemical reactivity variation based on physical orientation of the sediments at the intermediate scale.

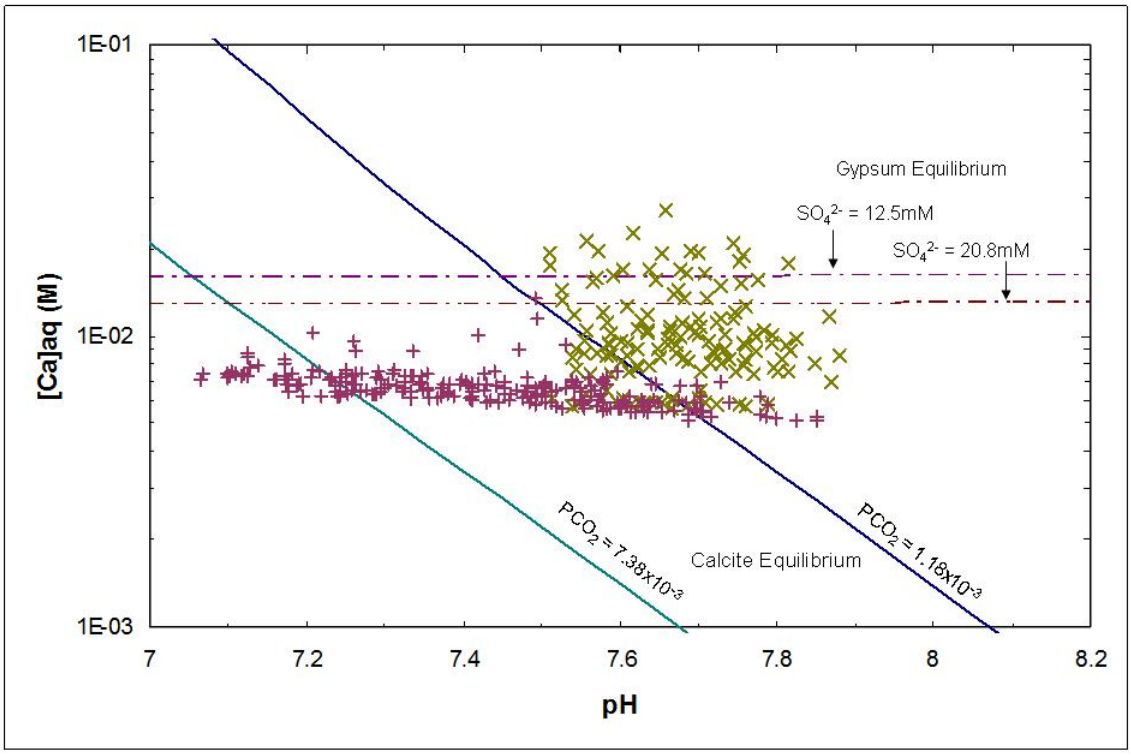

Figure 3.13 Calcium concentrations as a function of pH. Calcite solubility curves are the solid lines shown for the range of PCO_2 found in tanks #1 and #2. Gypsum equilibrium is shown by the dashed lines for the range of SO_4^{2-} found in tanks #1 and #2. x's are data from tank #1, while + symbols are data from tank #2.

Initial speciation calculations for uranium show that uranophane is the most likely U^{+6} phase to be controlling uranium solubility. Figure 3.14 shows the uranium concentrations for the same points in time as Figure 3.13, and also the uranium concentration assuming uranophane equilibrium for the pH and PCO_2 range found in both tanks. Because of the complex stoichiometry of uranophane, $(Ca(H_3O)_2(UO_2)_2(SiO_4)_2(H_2O)_3)$, the solubility curves are also sensitive to local silicon and calcium concentrations. For the lower end of the pH range, silicon variation over the range found experimentally in the tanks changes the solubility by a factor of about five, whereas at the higher end of the pH range silicon concentration causes no variation in uranophane solubility. Calcium concentrations change the solubility limits by a factor of approximately two over the entire pH range shown. The mean values from tank data (Ca^{2+}= 7.5mM, Si = 0.18mM) were used to create the solubility curves in Figure 3.14. It can be seen that for the majority of the time, the uranium concentrations are considerably lower than the amount that would be caused by uranophane equilibrium (Tank #1 SI range: -7.3 - -0.9, Tank #2 SI range: -8.1 – 0.6). Also there is a negative correlation between pH and PCO_2 (See Appendices B and C) in both tanks, so as the pH decreases, the upper solubility curve becomes more relevant. The undersaturation of the uranium solid phases implies desorption or other non-solubility controlled mechanisms (i.e. physical mass transfer) as a source for the uranium. As with calcium, the behavior was markedly different between the two tanks. Tank #2 had a broader range of uranium concentrations and pH than tank #1. For both uranium concentrations and pH, the points in Figure 3.14 are fairly evenly distributed with respect to time. There are decreases in uranium concentration as experimental time elapsed (see Figures 3.4, 3.6, and 3.7), but the pH spatial distribution, once established, is quite static.

3.4.2 Mineral-Uranium Surface Interactions

As was seen in Figure 3.14, a bulk uranium bearing solid phase is not controlling uranium concentrations. Thus it would appear that the source of the uranium is most

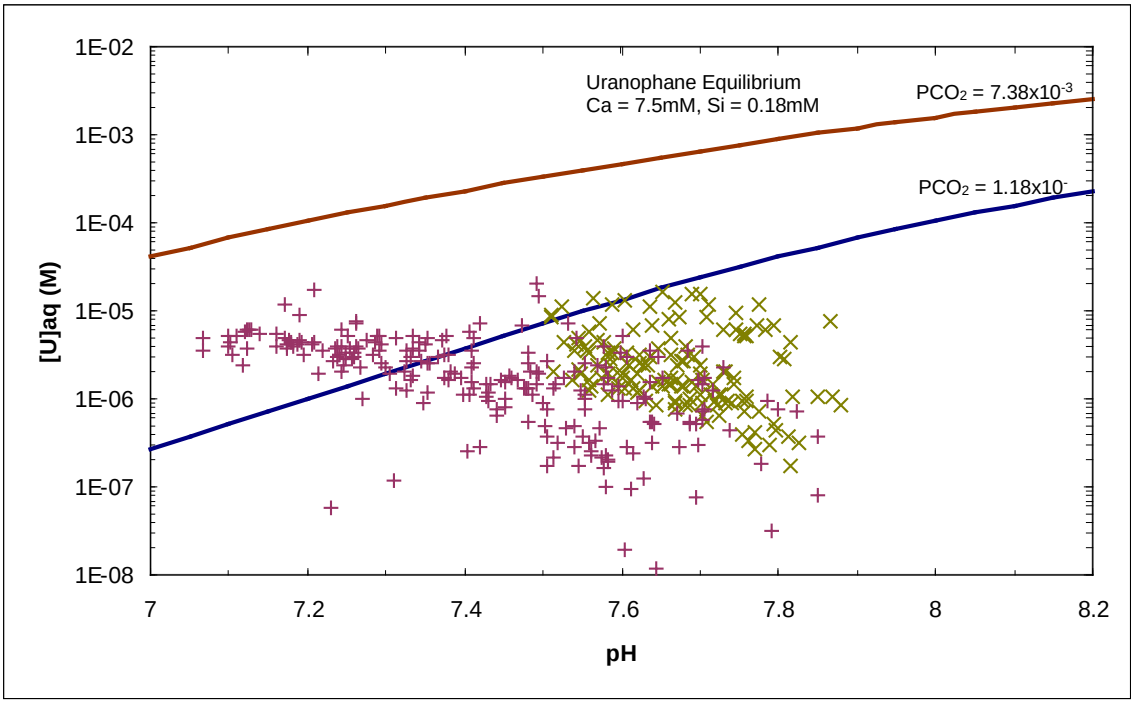

Figure 3.14 Uranium concentration as a function of pH. Uranophane equilibrium is shown by the two solid lines for the range of PCO_2 found in tanks #1 and #2 while holding calcium and silicon constant. x's are results from spatial samples for tank #1, while the + symbols are data for tank #2.

likely desorption from the sediments. Previous work at the Naturita site has led to the development of a surface complexation model (SCM, *Davis et al.* [2004]) which can describe uranium partitioning to the surface over a range of chemical conditions. This model was created from batch scale experiments, and has been applied to both column and field transport data. Here it will also be applied to the tank data to help explore the relationship between chemical reactivity and scale.

These calculations were completed using the PHREEQC speciation program. Uranium complexation reactions for both aqueous reactions (Table 3.2) as well as surface reactions were entered (Table 3.3). For consistency, many of the assumptions used in model development are also used here. The SCM consists of three site types: very strong, strong, and weak; these site types comprise 0.01%, 0.1% and 99.89% of the total sites, respectively. The site density was assumed to 1.92μmol/m^2. The surface area of the different size fractions were determined to be 7.12m^2/g, 7.88m^2/g, and 7.07m^2/g for the <2mm composite, the <0.250mm, and >0.250mm fractions, respectively. Further assumptions, unique to this application, also had to be made. First, since the model was being applied to spatial samples, the soil:solution ratio for a given sample had to be calculated. For all samples, it was assumed that the liquid volume came from a sphere centered on the end of the sampling needle within the tank. Using the sample volume (7mLs) and the local porosity a total volume which was affected by sampling was calculated. Using the bulk density, the sediment mass was calculated for the total volume. These calculations are summarized in Table 3.4. Second, the same SCM was assumed to be equally valid for all of the particle sizes. It was originally determined on the <3mm size fraction from the Naturita field site. *Davis and Curtis* [2003] commented that there was only a small amount of variation in the surface areas as a function of particle size. They attribute this to inefficient separation of the various particle sizes during dry sieving, and using various types of microscopy there appears to be fines adhering to the larger grains of sediment. This same behavior is evident in the surface areas reported in Table 3.4. There is little change in the measured surface area as the particle size decreases. This observation gives credence to the assumption that the SCM determined from the <3mm fraction will also be valid independent of the particle sizes used here. Because the same SCM was used, the only variations in the speciation

Table 3.2 Aqueous uranium reactions and constants used in the speciation modeling. Unless otherwise specified all values are from the NEA thermodynamic database (*Guillamont et al.* [2003]).

Reaction	Log β
$UO_2^{+2} + H_2O = UO_2OH^+ + H^+$	-5.25
$UO_2^{+2} + 2H_2O = UO_2(OH)_2 + 2H^+$	-12.15
$UO_2^{+2} + 3H_2O = UO_2(OH)_3^{-1} + 3H^+$	-20.250
$UO_2^{+2} + 4H_2O = UO_2(OH)_4^{-2} + 4H^+$	-32.4
$2UO_2^{+2} + H_2O = (UO_2)_2(OH)^{+3} + 1H^+$	-2.70
$2UO_2^{+2} + 2H_2O = (UO_2)_2(OH)_2^{+2} + 2H^+$	-5.62
$3UO_2^{+2} + 4H_2O = (UO_2)_3(OH)_4^{+2} + 4H^+$	-11.90
$3UO_2^{+2} + 5H_2O = (UO_2)_3(OH)_5^{+} + 5H^+$	-15.55
$3UO_2^{+2} + 7H_2O = (UO_2)_3(OH)_7^{-} + 7H^+$	-32.20
$4UO_2^{+2} + 7H_2O = (UO_2)_4(OH)_7^{+} + 7H^+$	-21.9
$UO_2^{+2} + Cl^- = UO_2Cl^+$	0.170
$UO_2^{+2} + 2Cl^- = UO_2(Cl)_2$	-1.100
$UO_2^{+2} + CO_3^{-2} = UO_2CO_3$	9.94
$UO_2^{+2} + 2CO_3^{-2} = UO_2(CO_3)_2^{-2}$	16.61
$UO_2^{+2} + 3CO_3^{-2} = UO_2(CO_3)_3^{-4}$	21.84
$3UO_2^{+2} + 6CO_3^{-2} = (UO_2)_3(CO_3)_6^{-6}$	54.0
$2UO_2^{+2} + CO_3^{-2} + 3H_2O = (UO_2)_2(CO_3)(OH)_3^{-1} + 3H^+$	-0.86
$3UO_2^{+2} + CO_3^{-2} + 3H_2O = (UO_2)_3(CO_3)(OH)_3^{+1} + 3H^+$	0.66
$11UO_2^{+2} + 6CO_3^{-2} + 12H_2O = (UO_2)_{11}(CO_3)_6(OH)_{12}^{-2} + 12H^+$	36.43
$UO_2^{+2} + SO_4^{-2} = UO_2SO_4$	3.15
$UO_2^{+2} + 2SO_4^{-2} = UO_2(SO_4)2^{-2}$	4.14
$UO_2^{+2} + 3SO_4^{-2} = UO_2(SO_4)_3^{-4}$	3.02
$2Ca^{+2} + UO_2^{+2} + 3CO_3^{-2} = Ca_2UO_2(CO_3)_3$	30.70[a]
$Ca^{+2} + UO_2^{+2} + 3CO_3^{-2} = CaUO_2(CO_3)_3^{-2}$	27.18[a]

a) *Dong and Brooks* [2006]

Table 3.3 Surface reactions used in the speciation calculations. All reactions were determined by *Davis et al.* [2004]. SS is a very strong surface site, S is a strong surface site, and W is a weak surface site.

Reaction	Log K
$SSOH + UO_2^{+2} = SSOUO_2^{+} + H^{+}$	6.798
$SOH + UO_2^{+2} = SOUO_2^{+} + H^{+}$	5.817
$WOH + UO_2^{+2} = WOUO_2^{+} + H^{+}$	2.570
$SSOH + UO_2^{+2} + H_2O = SSOUO_2OH + 2H^{+}$	-0.671
$SOH + UO_2^{+2} + H_2O = SOUO_2OH + 2H^{+}$	-2.082
$WOH + UO_2^{+2} + H_2O = WOUO_2OH + 2H^{+}$	-5.318

Table 3.4 Summary of calculations for chemical conditions around a single sampling point.

Size Fraction	Surface Area (m^2/g sediment)	Mass Sediment Affected by Sampling	Porosity	Bulk Density (g/mL)	Soil: Solution Ratio (g/L)	Uranium Surface conc. (μmol/g)
<2mm comp.	7.12	30.0	0.35	1.5	4286	$1.8x10^{-2}$
<0.250mm	7.88	28.6	0.42	1.71	4080	$1.8x10^{-2}$
>0.250mm	7.07	27.2	0.42	1.63	3889	$1.7x10^{-2}$

calculations are slight differences in the total amount of surface sites (~15%) caused by the small variation in surface area, porosity, and bulk density, and the aqueous concentration variations measured in the pore fluid. And finally, the uranium surface concentration was assumed to be constant over time and space. This was largely done as there was no way to know how the surface concentration was changing as a function of time and space. However, only 30% of the total uranium added to tank #1 and 25% of the total added to tank #2 had eluted over the experimental timeframe. The desorption calculations (described below) were repeated assuming that the eluted uranium had been removed from the tank in a spatially uniform manner. Using these values as the error in the desorption calculations, it equates to a total calculated error of ±37% in tank #1 and ±31% in tank #2.

The desorption calculations themselves took place in two stages. First the surface was defined with the mass, surface area, and reactions found in Tables 3.3 and 3.4. The initial surface consisted of only protonated sites. This surface was allowed to react with a 'loading solution' which loaded the surface with uranium; the loading solution had a bulk ion composition which approximated mean values from within the tank. The uranium concentration was varied until the calculated surface concentration matched the measured labile uranium concentration. Second, the loaded surface was then allowed to equilibrate with solutions defined to have the same ionic composition of those measured in the spatial sampling but with the uranium removed. Thus the desorption calculations are calculating the amount of uranium that would desorb into solution for the measured solution compositions. These results are presented in Figure 3.15. Error bars are only shown for selected data points for simplicity; the same ranges of errors apply to all the points shown. Data from the same sampling events as presented in Figures 3.13 and 3.14 was used. These data represent sampling time points that are evenly distributed over the entire experimental timeframe. Also, for tank #2, data points are shown from times when AGW-atmospheric as well as from when AGW-2% were being injected.

From Figure 3.15 it can be seen that the calculated model values for tank #1 are almost always higher than the measured values. This type of analysis has been completed by others, and discrepancies between measured and calculated values are most often attributed to the invalidity of the local equilibrium assumption. The same

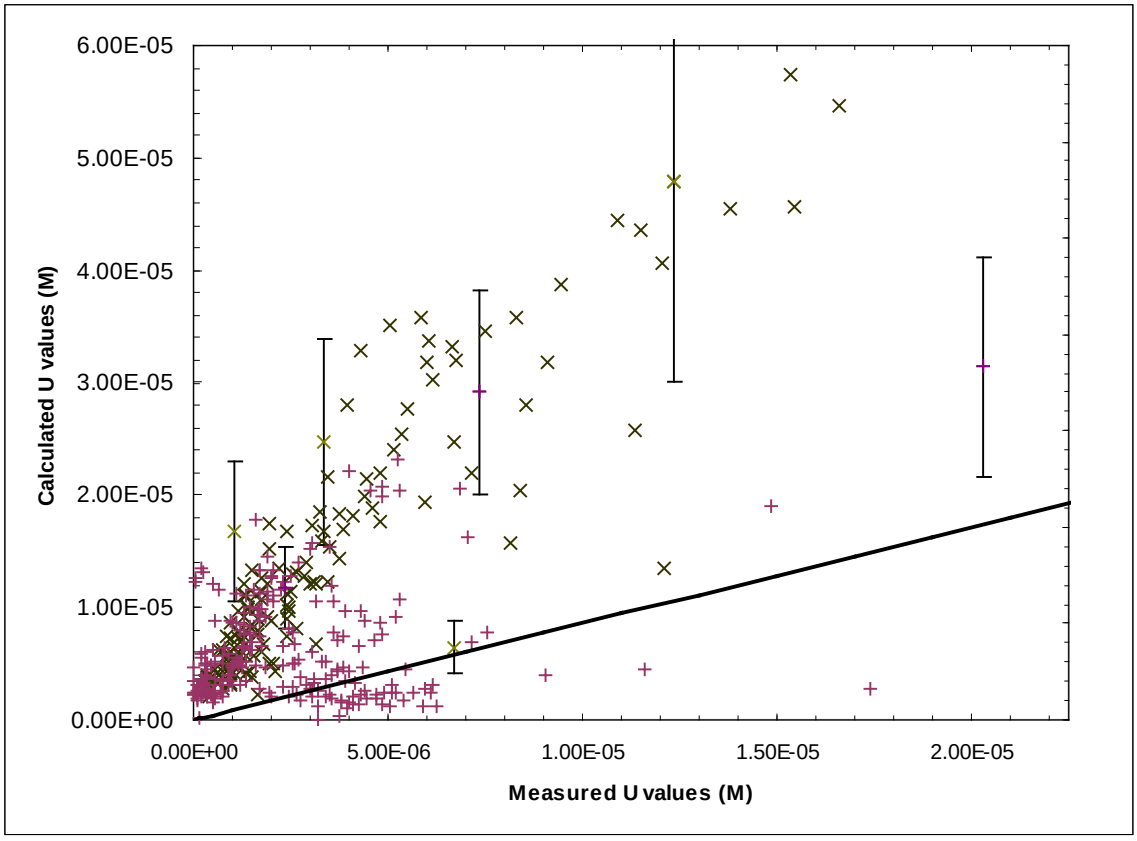

Figure 3.15 Calculated vs. measured uranium values for tanks #1 and #2. The x symbols are for tank #1 and the + symbols are for tank #2. The heavy black line is the 1:1 line which represents perfect agreement between the model and data. The error bars represent 37% error for tank #1 points, and 31% error for tank #2 points. Although they are not shown, they apply to all the plotted points.

interpretation can be applied to the majority of the points here. In tank #1 there appears to be a kinetic hindrance to uranium desorption causing the measured values to be consistently lower than those calculated from an equilibrium based model. Indeed, this is corroborated by the uranium BTC where stop flow events led to a re-bound in uranium concentrations. However, in tank #2 the SCM is slightly bi-modal in predictive capability. At low uranium concentrations (<~$2.5x10^{-6}$M) the SCM tends to over simulate uranium values; above that level the model either simulates the data fairly well, or slightly under simulates uranium values. For the sample points where uranium is over simulated in tank #2, the disparity between calculated values and data is identical to that seen in tank #1. When the model error is plotted as a function of pH, the points where the SCM accurately or under simulates uranium data occurs at the low end of the pH range (~7.1-7.4). The lowest pH in tank #1 is 7.51. It would appear that an alternative explanation to the discrepancies between calculated and measured values is that the accuracy of the SCM is dependent on chemical conditions. However, the SCM was developed from batch reactions that encompassed the chemical range found in the tank. This alternative explanation makes the interpretations of the stop flow event more complicated for tank #2.

In tank #2 the stop-flow event did not cause a re-bound in uranium concentrations, which would suggest that the local equilibrium assumption would apply. However, in looking at the uranium distributions before and after the stop flow event (Day 69 and 98 in Figure 3.7), there is a smoothing of spatial uranium concentration gradients. This smoothing of uranium distributions can either be caused by diffusion or by local desorption and re-adsorption reactions. For the time scale of the stop flow event diffusion of uranium over meter length scales is unlikely. This leaves local surface reactions to explain the difference between the spatial gradients. Since the surface reactions are continuing to occur in the absence of flow, it would appear that local equilibrium is not valid, and thus the SCM should not be able to describe the data. In the sampling event immediately after Day 98 (Day 106, see APPENDIX C), the uranium distribution seen in Day 69 is already re-established.

3.5 Conclusions

Two experiments were completed at the intermediate scale. The first was a physically homogenous packing of a field sediment that had been sieved to <2mm. The second used the same field sediment fraction, but further separated the sediment into <0.250mm and >0.250mm fractions. These two size fractions were packed in a spatially heterogeneous fashion at the decimeter scale to induce local water flow variations and chemical gradients. Samples were taken from the effluent as well as from ports installed spatially within the tanks. Stop-flow events were completed to test for the presence of kinetic hindrances to uranium desorption, and different influent water chemistries were used in tank #2 to test for the effects of temporal chemical heterogeneities. The inert tracer bromide was injected into both tanks to determine major water flow paths.

Several observations from the intermediate scale are consistent with uranium behavior that has been observed at other scales. Uranium spatial concentrations correlate well with alkalinity concentrations. Speciation calculations show that the dominant uranium species in both tanks over all time and space is the $Ca_2UO_2(CO_3)_3^0$ species. However, the uranium and alkalinity relationship varied as a function of time in tank #1 and was independent of time in tank #2. In general, uranium behavior was consistent with sorption behavior observed at the batch scale; increasing alkalinity correlates with increasing uranium concentrations, and decreasing pH correlates with increasing uranium concentrations. Effluent uranium values appear similar in behavior to breakthrough curves obtained from column experiments. In tank #1 uranium values increased during three separate stop flow events consistent with what has been observed in column studies.

Several other observations are either inconsistent with uranium behavior at other scales, or are unique to working at the intermediate scale. Uranium, pH, alkalinity, and calcium spatial distributions varied as a function of particle size distribution and induced flow regime. In tank #2, during a 650 hour stop flow event there was no re-bound in uranium concentrations. It appeared that local desorption and re-adsorption reactions off set each other leading to no net change in the uranium breakthrough curve. Bromide behavior between the two tanks differed considerably, in that, tank #1 showed fairly ideal transport behavior and tank #2 showed markedly non-ideal transport behavior. The

spatial samples in tank #2 show that the non-ideal behavior is caused by the slowing of the tracer as it passes through the block formation at the upgradient end of the tank.

Both a previously determined SCM as well as solubility calculations were used to describe the spatial reactivity from both tanks. In general the SCM calculations over calculate uranium behavior in tank #1, and either over or under calculate uranium behavior in tank #2 based on local pH values. From this analysis it would appear that local equilibrium assumptions are invalid for tank behavior. Solubility calculations show that the local reactivity of mineral phases between the tanks is considerably different. Thus physical orientation of the different particle sizes leads to different observed reactivity of the minerals within the tanks. Specifically with calcite, this spatial variability in reactivity can lead to variations in observed uranium behavior by controlling local alkalinity concentrations.

3.6 References

Arai, Y., M. McBeath, J. R. Bargar, J. Joye, and J. A. Davis. 2006. Uranyl adsorption and surface speciation at the imogolite-water interface: Self-consistent spectroscopic and surface complexation models. *Geochimica et Cosmochimica Acta* 70:2492-2509.

Arnold, T., T. Zorn, G. Bernhard, and H. Nitsche. 1998. Sorption of uranium(VI) onto phyllite. *Chemical Geology* 151:129-141.

Arnold, T., T. Zorn, H. Zanker, G. Bernhard, and H. Nitsche. 2001. Sorption behavior of U(VI) of phyllite: experiments and modeling. *Journal of Contaminant Hydrology* 47:219-231.

Bargar, J. R., R. Reitmeyer, J. J. Lenhart, and J. A. Davis. 2000. Characterization of U(VI)-carbonate ternary complexes on hematite: EXAFS and electrophoretic mobility measurements. *Geochimica et Cosmochimica Acta* 64:2737-2749.

Barnett, M. O., P. M. Jardine, S. C. Brooks, and H. M. Selim. 2000. Adsorption and Transport of Uranium(VI) in Subsurface Media. *Soil Science Society of America Journal* 64:908-917.

Barth, G. R., T. H. Illangasekare, M. C. Hill, and H. Rajaram. 2001. A new tracer-density criterion for heterogeneous porous media. *Water Resources Research* 37:21-31.

Bertetti, F.P., Roberto T. Pabalan, and Michael G. Almendarez. 1998. Studies of Neptunium(V) Sorption on Quartz, Clinoptilolite, Montmorillonite, and alpha-Alumina. In *Adsorption of Metals by Geomedia*, edited by E. A. Jenne. San Diego: Academic Press.

Brusseau, M. L., and J. M. Zachara. 1993. Tranport of Co2+ in a Physically and Chemically Heterogeneous Porous Medium. *Environmental Science and Technology* 27:1937-1939.

Chisolm-Brause, C. J., J. M. Berg, R. A. Matzner, and D. E. Morris. 2001. Uranium(VI) Sorption Complexes on Motmorillonite as a Function of Solution Chemistry. *Journal of Colloid and Interface Science* 233:38-49.

Curtis, G. P., P. Fox, M. Kohler, and J. A. Davis. 2004. Comparison of in situ KD values with a laboratory determined surface complexation model. *Applied Geochemistry* 19:1643-1653.

Curtis, Gary P., J.A. Davis, and David L. Naftz. 2006. Simulation of reactive transport of uranium(VI) in groundwater with variable chemical conditions. *Water Resources Research* 42: W04404, doi:10.1029/2005WR003979

Davis, J. A., J. A. Coston, D. B. Kent, and C. C. Fuller. 1998. Application of the Surface Complexation Concept to Complex Mineral Assemblages. *Environmental Science and Technology* 32:2820-2828.

Davis, J. A., D. B. Kent, J. A. Coston, K. M. Hess, and J. L. Joye. 2000. Multispecies reactive tracer test in an aquifer with spatially variable chemical conditions. *Water Resources Research* 36:119-134.

Davis, J.A., and Gary P. Curtis. 2003. Application of Surface Complexation Modeling to Describe Uranium(VI) Adsorption and Retardation at the Uranium Mill Tailings Site at Naturita, Colorado. Washington D.C.: U.S. Nuclear Regulatory Commission.

Davis, J.A., David E. Meece, Matthias Kohler, and Gary P. Curtis. 2004. Approaches to surface complexation modeling of uranium(VI) adsorption on aquifer sediments. *Geochimica et Cosmochimica Acta* 68(18):3621-3641.

Dong, W., W. P. Ball, C. Liu, Z. Wang, A. T. Stone, J. Bai, and J. M. Zachara. 2005. Influence of Calcite and Dissolved Calcium on Uranium(VI) Sorption to a Hanford Subsurface Sediment. *Environmental Science and Technology* 39:7949-7955.

Dong, W., and Scott C. Brooks. 2006. Determination of the Formation Constants of Uranyl and Carbonate with Alkaline Earth Metals (Mg^{2+}, Ca^{2+}, Sr^{2+}, and Ba^{2+}) Using Anion Exchange Method. *Environmental Science and Technology* 40:4689-4695.

Fox, P., J. A. Davis, and J. M. Zachara. 2006. The effect of calcium on aqueous uranium(VI) speciation and adsorption to ferrihydrite and quartz. *Geochimica et Cosmochimica Acta* 70:1379-1387.

Fuller, C. C., J. A. Davis, J. A. Coston, and E. Dixon. 1996. Characterization of metal adsorption variability in a sand and gravel aquifer, Cape Cod, Massachusetts, U.S.A. *Journal of Contaminant Hydrology* 22:165-187.

Gabriel, U., J.-P. Gaudet, L. Spadini, and L. Charlet. 1998. Reactive transport of uranyl in a goethite column: an experimental and modeling study. *Chemical Geology* 151:107-128.

Guillaumont, R., Fanghanel, T., Fuger, J., Grenthe, I., Neck, V., Palmer, D.A., and M.H. Rand. *Update on the Chemical Thermodynamics of Uranium, Neptunium, Plutonium, Americium, and Technetium.* Eds. Mompean, F.J., Illemassene, M., Domenech-Orti, C., and K. Ben Said. Nuclear Energy Agency. Elsevier Ltd. Amsterdam. 2003.

Kent, D. B., J. A. Davis, C. D. Anderson, and B. A. Rea. 1995. Transport of chromium and selenium in a pristine sand and gravel aquifer: Role of adsorption processes. *Water Resources Research* 31:1041-1050.

Kent, D. B., R. H. Abrams, J. A. Davis, J. A. Coston, and D. R. LeBlanc. 2000. Modeling the influence of variable pH on the transport of zinc in a contaminated aquifer using semiempirical surface complexation models. *Water Resources Research* 36:3411-3425.

Kohler, M., G. P. Curtis, D. B. Kent, and J. A. Davis. 1996. Experimental investigation and modeling of uranium(VI) transport under variable chemical conditions. *Water Resources Research* 32:3539-3551.

Kohler, M., G. P. Curtis, D. E. Meece, and J. A. Davis. 2004. Methods for Estimating Adsorbed Uranium(VI) and Distribution Coefficients of Contaminated Sediments. *Environmental Science and Technology* 38:240-247.

Li, L., C.A. Peters, and M.A. Celia. 2006. Upscaling geochemical reaction rates using pore-scale network modeling. *Advances in Water Resources* 29:1351-1370.

Li, L., C. A. Peters, and M. A. Celia. 2007. Effects of mineral spatial distribution on reaction rates in porous media. *Water Resources Research* 43:17.

Payne, T. E., R. Edis, B. R. Fenton, and T. D. Waite. 2001. Comparison of laboratory uranium sorption data with 'in situ distribution coefficients' at the Koongarra uranium deposit, Northern Australia. *Journal of Environmental Radioactivity* 57:35-55.

Payne, T. E., and P. L. Airey. 2006. Radionuclide migration at the Koongarra uranium deposit, Northern Australia- Lessons from the Alligator Rivers analogue project. *Physics and Chemistry of the Earth* 31:572-286.

Ponthieu, M., F. Juillot, T. Hiemstra, W. H. van Riemsdijk, and M. F. Benedetti. 2006. Metal ion binding to iron oxides. *Geochimica et Cosmochimica Acta* 70:2679-2698.

Prikryl, J. D., A. Jain, D. R. Turner, and R. T. Pabalan. 2001. UraniumVI sorption behavior on silicate mineral mixtures. *Journal of Contaminant Hydrology* 47:241-253.

Steefel, C. I., S. Carroll, P. Zhao, and S. Roberts. 2003. Cesium migration in Hanford sediment: a mulitsite cation exchange model based on laboratory experiments. *Journal of Contaminant Hydrology* 67:219-246.

Stollenwerk, K. G. 1995. Modeling the effects of variable groundwater chemistry in adsorption of molybdate. *Water Resources Research* 31:347-357.

Stollenwerk, K. G. 1998. Molybdate transport in a chemically complex aquifer: Field measurements compared with solute-transport model predictions. Water Resources Research 34:2727-2740.

Sylwester, E. R., E. A. Hudson, and P. G. Allen. 2000. The structure of uranium(VI) sorption complexes on silica, alumina and montmorillonite. *Geochimica et Cosmochimica Acta* 64:2431-2438.

Szecsody, James E., John M. Zachara, Ashokkumar Chilakapati, P.M. Jardine, and Alan S. Ferrency. 1998. Importance of flow and particle-scale heterogeneity on Co(II/III) EDTA reactive transport. *Journal of Hydrology* 209:112-136.

Towle, S. N., J. R. Bargar, G. E. Brown Jr., and G. A. Parks. 1997. Surface Precipitation of Co(II)(aq) on Al2O3. *Journal of Colloid and Interface Science* 187:62-82.

Turner, David R., F.P. Bertetti, and Roberto T. Pabalan. 2006. Applying Surface Complexation Modeling to Radionuclide Sorption. In *Surface Complexation Modeling*, edited by J. Lutzenkirchen. Amsterdam: Elsevier Ltd.

Waite, T. D., J. A. Davis, B. R. Fenton, and T. E. Payne. 2000. Approaches to modelling uranium(VI) adsorption on natural mineral assemblages. *Radiochimica Acta* 88:687-693.

Waychunas, G. A., C. C. Fuller, and J. A. Davis. 2002. Surface complexation and precipitate geometry for aqueous Zn(II) sorption on ferrihydrite I. X-ray absorption extended fine structure spectroscopy analysis. *Geochimica et Cosmochimica Acta* 66:1119-1137.

Wersin, P., M. F. Hochella Jr., P. Perrson, G. Redden, J. O. Leckie, and D. W. Harris. 1994. Interaction between aqueous uranium(VI) and sulfide minerals: Spectroscopic evidence for sorption and reduction. *Geochimica et Cosmochimica Acta* 58:2829-2843.

Zachara, John M., Steven C. Smith, Chongxuan Liu, James P. McKinley, R. Jeffrey Serne, and Paul L. Gassman. 2002. Sorption of Cs^{+} to micaceous subsurface sediments from the Hanford site, USA. *Geochimica et Cosmochimica Acta* 66 (2):193-211.
52:85-108.

CHAPTER 4

UPSCALING URANIUM(VI) TRANSPORT IN 3-D: CHEMICAL RESULTS OF TRANSPORT EXPERIMENTS AT THE DECIMETER SCALE

4.1 Introduction

After site characterization, one of the first steps in stochastic hydrology is to create a hydraulic conductivity field. This field, for a single realization, is spatially heterogeneous but static in time and space. The individual realization represents one possibility for water flow and inert transport within an aquifer with the ensemble average of realizations representing the most likely representation of inert fate and transport. Concomitantly, there is a reactivity field that controls the chemical reactions which can ultimately control the fate and transport of a given contaminant. These two fields are similar in nature; both are spatially heterogeneous but relatively static in time and space and they co-occur in a given aquifer, but for metal and radionuclide transport they are unrelated. Despite their lack of spatial relationship the physical flow domain interacts with the chemical reactivity domain to create non-ideal metal/radionuclide transport behavior.

In many studies chemical reactivity is explored in batch reactors to create a surface complexation model (SCM) to describe metal/mineral interactions. This SCM is then applied to transport data at the column scale (*Barnett et al.* [2000], *Gabriel et al.* [1998], *Szecsody et al.* [1998], *Brusseau and Zachara* [1993], *Stollenwerk* [1995], *Kohler et al.* [1996], *Zachara et al.* [2002], *Steefel et al.* [2003]). In most of these studies the SCM as directly applied to column scale transport data does not satisfactorily describe the observed transport behavior. This observation has been attributed to a lack of understanding of chemical kinetic behavior (*Barnett et al.* [2000], *Gabriel et al.* [1998], *Szecsody et al.* [1998]), chemical kinetics as well as mass transfer limitations (*Brusseau and Zachara* [1993]), and to an unexplained but observed change in chemical reactivity

as a function of scale which requires an alteration of the SCM (*Stollenwerk* [1995], *Kohler et al.* [1996], *Zachara et al.* [2002], *Steefel et al.* [2003]). In each of these studies when moving from a non-flow to an induced flow domain, there is an apparent change in reactivity as the reactivity and flow fields interact. This occurs despite the fact that in most of these studies at least one variable is often idealized (i.e. for field sediments only a very small particle size range is used, or a model sediment, quartz sand, is used). Thus many heterogeneities that would be present in a field setting have been specifically excluded.

These discrepancies in observed chemical behavior have been further investigated with pore scale modeling techniques. In one study, *Zhang et al.* [2008] found that local pore water velocity does not change the observed reaction rate; however, this is contrary to other experimental studies (*Pang et al.* [2002]). It has also been suggested that reaction rates in soils are not best described by a single value, but instead by a distributed set of reaction rates (*Haggerty et al.* [2004], *Chen and Wagenet* [1995]). These distributed rates may be a macroscopic summation of smaller scale chemical processes such as: pore scale reaction rates dependence on spatial orientations of reactive species (*Li et al.* [2006] and [2007]), varied sorption mechanisms (*Weber et al.* [1992]), coupled chemical reactions (*Maher et al.* [2006]), or local chemical concentration gradients near a reactive surface (*Li et al.* [2008], *Meile and Tuncay* [2006]). They may also be a combination of physical/chemical interactions such as dissolution and intragranular diffusion (*Liu et al.* [2004] and [2006]). In considering up-scaling of these small scale reaction rate variations *Liu et al.* [2008] combine a distributed rate model with a surface complexation model to quasi-mechanistically describe kinetically hindered uranium desorption, and couple it with a dual domain transport model. The model captures observed uranium behavior exceedingly well in 1-D experiments using <2mm sediments in a 10cm column, as well as in an 80cm column using un-sorted field sediments.

Most of the studies listed above use batch and column scale experiments. Thus it is relatively simple to make a detailed characterization of the sediment, and at least macroscopic heterogeneities are known. In field systems however, it becomes increasingly difficult to determine underlying causes of metal/radionuclide transport as characterization becomes less exacting. In response to this many assumptions are often

made such as simplifying the flow field (assumed spatially uniform hydraulic conductivity and dispersivity, *Curtis et al.* [2006]), or the role of the flow field is unclear, and one of many chemistry dependent mechanisms are the potential controlling factors in transport (kinetically hindered desorption (*Kent et al.* [1995]), pH dependent sorption (*Kent et al.* [2000]), or variable strength surface complexes (*Stollenwerk* [1998])). Furthermore, different conceptual models can often give the same output. For example, contaminant dispersion in an aquifer can be limited by lowering the dispersion coefficient or by adding a strong surface binding site for the metal of interest (*Stollenwerk* [1998], *Kent et al.* [2000]). These field studies all simplify the flow domain into 2-D, but the same phenomenon has been observed in three dimensional modeling studies. *Burr et al.* [1994] used a stochastic approach to hydraulic conductivity and sorption behavior (linear equilibrium adsorption described with K_D values). They describe 'pseudo-kinetic' behavior where the retardation factor varies with time and space (see also *Rajaram* [1997]). In *Burr et al.* [1994], pore scale processes cannot be controlling contaminant behavior as they have been simplified through the use of the K_D value. In contrast *Espinoza and Valocchi* [1997] use a physically uniform but chemically heterogeneous aquifer, and also observe 'pseudo-kinetic' behavior. In this case pore scale chemical processes and not physical processes are the cause of the aberrant behavior.

Often, upscaling from bench to field scale heterogeneity has focused on flow and transport coefficients and numerical methods (*Vogel and Roth* [2003], *Gasda and Celia* [2005], *Renard and de Marsily* [1997], *Schiebe and Yabusaki* [1998], *Levy and Berkowitz* [2003]). As has been noted however, for reactive contaminants, such as metals and radionuclides, upscaling techniques must also be studied to scale chemical reactivity from the bench to the field scale. This cannot be done with the current body of experimental knowledge. Field scale experiments are fundamentally limited in the level of characterization that can be completed to accurately describe the chemical reactivity field. Batch and column techniques are limited in the size and heterogeneity that can be introduced. Therefore, we have completed 3-D decimeter scale experiments to bridge the knowledge gap in scaling related experimental knowledge. Tank experiments are much more heterogeneous than bench scale techniques, and are larger by several orders of magnitude. Furthermore, they allow for known distributions of macroscopic physical

heterogeneities as well as a much higher degree of spatial and temporal characterization relative to field sites. Uranium contaminated sediment was used due to its high degree of aqueous and surface chemical reactivity. The outcome of these experiments is a comprehensive database against which reactive upscaling of transport models can be completed.

4.2 Methods

A full description of the experimental methods used can be found elsewhere (see Chapter 2). The methods presented here are a truncated version relevant to the conclusions of the study.

4.2.1 Tank Construction

The outer walls and bottom of the tank were constructed from 2.5cm thick Plexiglas. The walls were supported by an exterior frame made of welded steel supports. The bottom of the tank was first placed along the bottom of the frame. The longest walls (parallel to flow) were then put in place using industrial strength epoxy to form a water tight seal between the bottom and the walls. The end plates (walls perpendicular to flow) were then put in place. The endplates were epoxied to both the bottom and walls already in place. Once the walls were together, a bead of caulk was run along the interior of all the seams. The walls were clamped in place to dry, and the epoxy and caulk was allowed to cure for several days before proceeding. A hole was drilled in the middle of both endplates 8.3cm from the bottom. Into this hole, a small length of copper pipe was epoxied in place. The protruding end of the pipe was threaded and a brass valve was screwed on to the pipe. To the other end of the valve, a brass nipple was put in place to which the hosing was connected with a screw clamp. On the inside of the tank, two

endfilters were constructed to hold the sediment in place as well as to maintain the constant head boundaries. These endfilters were constructed of 7.6cm plastic slats which were screwed together to create a frame equal to the inside dimensions of the tank. A perforated aluminum plate was screwed to the plastic frame. Aluminum #750 mesh screening was spot-epoxied to the aluminum plate. These endfilters were placed in the up and down gradient ends adjacent to the endplates. Once packed (described below), a Plexiglas lid was placed on the top of the tank. Holes had been pre-drilled to allow the wells to protrude. A bead of caulk was run around each well hole, as well as along the entire wall/lid boundary to ensure an air-tight seal. Constant head boundaries were used to control the flow and were connected to the tank using 0.95cm tubing.

Small ground water wells were constructed to allow for porewater withdrawal throughout the spatial domain of the flow field. These wells were constructed from 0.16cm OD, 0.08cm ID aluminum tubing. The end of each well was clamped shut, and a small (~0.05cm) hole was drilled perpendicular to the length of well 0.5cm from the bottom. Each hole was screened over a depth of about 1cm with the #750 mesh described above; the mesh was held in place with epoxy. 46 total wells were made with lengths ranging from 5.8cm up to 52.6cm. The void volume of the deepest wells was <5mL.

4.2.2 Sediment Separation

Uranium contaminated sediment from the Naturita field site (*Davis and Curtis* [2003]) was used in this experiment. All of the sediment originated from ~3-5m below ground surface from the saturated zone. The wet sediment was brought up to the surface and roughly allowed to drain. This sediment was placed on large tarps where further drying occurred. Over the course of several days the sediment was sieved into 4-12mm, 2-4mm, and <2mm sizes using sieving tables. This sediment was further split in the lab into five different particle sizes: <2mm composite, <0.250mm, >0.250mm, 0.125-0.250mm, and 4-12mm. Each of these sediment sizes were treated in a slightly different

manner. The <2mm composite and 4-12mm fractions were created in the field. Large amounts (~1100kg) of the <2mm was brought back to the lab and allowed to air dry. The majority of this dried sediment was used directly as <2mm composite material in the tank. The remainder was dry sieved using a 0.250mm screen. This created the <0.250mm and >0.250mm size fractions. Approximately half of the <0.250mm fraction was re-sieved using a 0.125mm screen. What remained on the screen became the 0.125-0.250mm fraction; the fines (<0.125mm) were not used in this experiment.

The 4-12mm material had a high degree of fines adhering to the larger particles, and it was also contaminated with large, dried balls of clay which were not separated in the field. It is for these reasons that the 4-12mm fraction was wet-sieved. Because of the large masses involved (~300kg raw material), a portable cement mixer was used to mix the sediments with the water. A small portion (~30kg) of sediment was placed in the cement mixer with approximately 12-20L of DI water. The cement mixer was turned on, and the water and sediment was allowed to mix for several minutes. Immediately upon shutting off the mixer, the water and sediment was dumped onto a 4mm screen. What remained on the screen was washed with 0.25-0.5L of DI water to remove the remaining fines. The water was captured for re-use. The sediments were allowed to air dry before packing.

The total mass of each sediment used is: <2mm composite- 602kg, <0.250mm- 83kg, >0.250mm- 231kg, 0.125-0.250- 62kg, and 4-12mm- 179kg. This gives a total of 1157kg of sediment and an average bulk density of 1.59g/cm^3.

4.2.3 Sediment Packing

The placement of the sampling wells and the placement of the different particle sizes were determined through pre-modeling of several different orientations using an inert tracer. The flow domain was discretized into 500 cells with dimensions of 11.2cm x 11.7cm x 11.2cm (LxHxW, see Figures 4.1 through 4.5). The packing orientation with the most non-ideal flow and transport was used (for details see APPENDIX E). The

packing of the tank was completed in five 11.2cm layers. An aluminum frame was constructed to divide each level of the tank into 100 cells. From the pre-modeling, a map of particle size and well location was created, and the cells were filled according to the map. Size separated sediment was poured into each cell until it was nearly full. Juxtaposed cells with two different particle sizes were filled simultaneously to minimize leakage through the aluminum frame. Compaction of the sediment was completed using a concrete vibrator. After compaction, the cell was filled completely, and re-compacted. When an entire layer was packed, the aluminum frame was pulled out of the packed sediment and set on top of the packed layer to allow for the packing of the next layer. This process continued through all five layers. When adjacent layers had the same particle size, the concrete vibrator was extended through the layers to allow for compaction and to minimize packing density variation between the layers which may have led to preferential flow paths. When the 0.125-0.250mm fraction was immediately adjacent to the 4-12mm fraction, the smaller particle size flowed into the pore space of the larger sized material. To stop this, the 0.125-0.250mm cells were surrounded with the same #750 mesh used for the endfilters. This same behavior was not observed for any other particle size pairings.

The wells were packed into place during the packing of the sediments. The location of each well was known from the pre-modeling. Wells were placed at 9 different depths, with each depth corresponding to the middle of a single layer or to the boundary between two layers. As the sediment was added and the desired well depth was reached, a wooden slat with a pre-drilled hole was laid across the top of the tank at the location of the well. The well was extended through the hole, and the bottom of the well was placed based on measurements from the inside walls of the tank. Once the bottom of the well was in place, sediment was poured around it to hold it in place through the compaction process. The stabilizing wooden slat was left in place until enough sediment had been added to support the well (about a layer and a half); the wooden slat was then removed. This process was repeated for all of the wells.

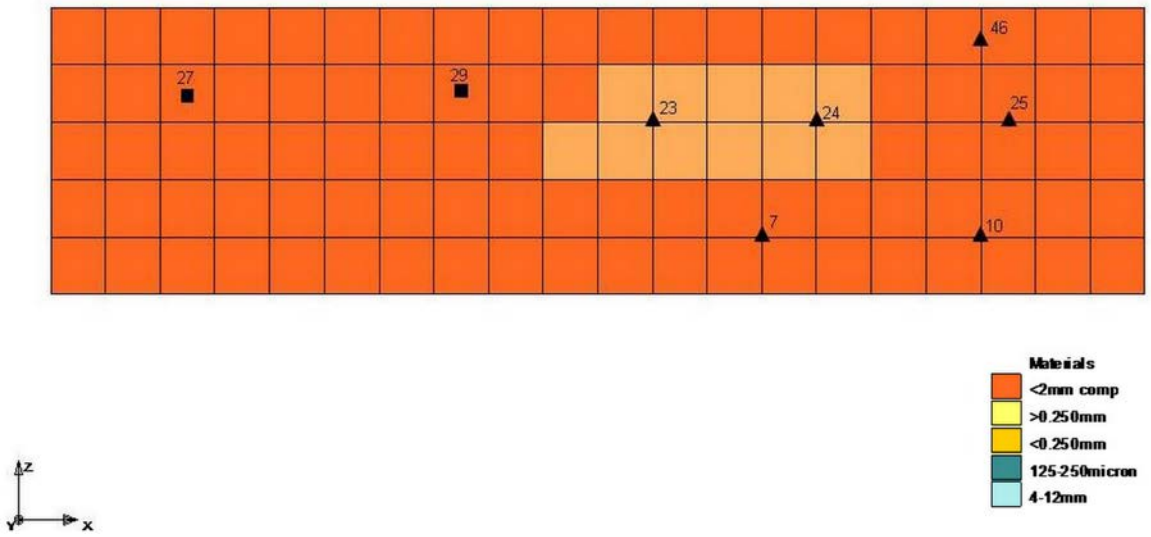

Figure 4.1 Vertical cross section (y = 0-11.7cm) through the tank showing packing orientation of the size fractions as well as the location of the sampling wells; upgradient end is on the left, downgradient end is on the right. The dimensions of each cell are 11.2cm x 11.7cm x 11.2cm (x, y, z). Square symbols are wells present in the middle of this cross section; triangles are wells which are on the boundary between cross sections. The number next to the well is the well number.

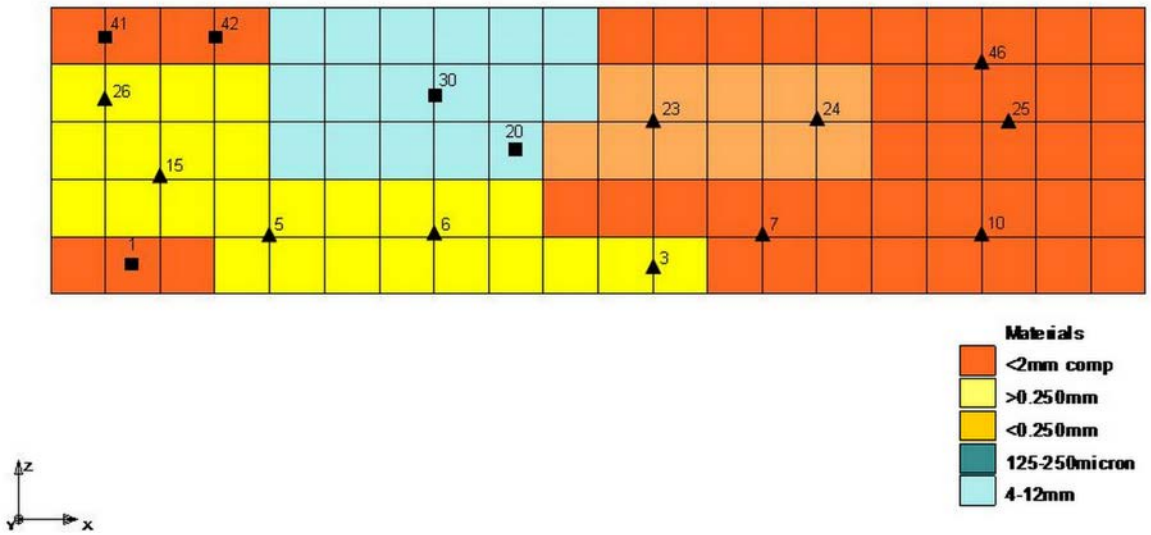

Figure 4.2 Vertical cross section (y = 11.7-23.4cm) through the tank showing packing orientation of the size fractions as well as the location of the sampling wells; upgradient end is on the left, downgradient end is on the right. The dimensions of each cell are 11.2cm x 11.7cm x 11.2cm (x, y, z). Square symbols are wells present in the middle of this cross section; triangles are wells which are on the boundary between cross sections. The number next to the well is the well number.

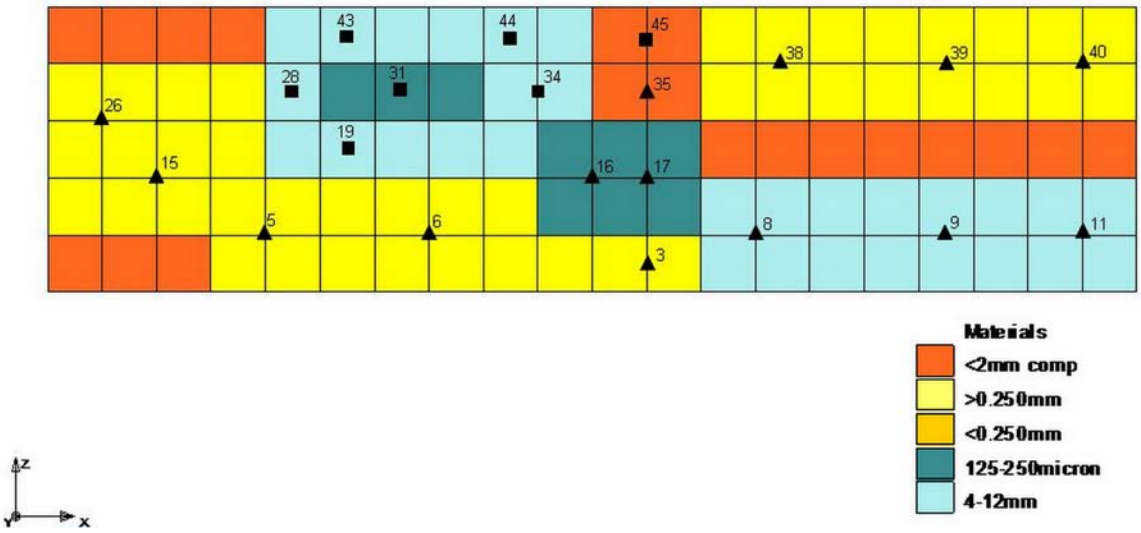

Figure 4.3 Vertical cross section (y = 23.4-35.1cm) through the tank showing packing orientation of the size fractions as well as the location of the sampling wells; upgradient end is on the left, downgradient end is on the right. The dimensions of each cell are 11.2cm x 11.7cm x 11.2cm (x, y, z). Square symbols are wells present in the middle of this cross section; triangles are wells which are on the boundary between cross sections. The number next to the well is the well number**.**

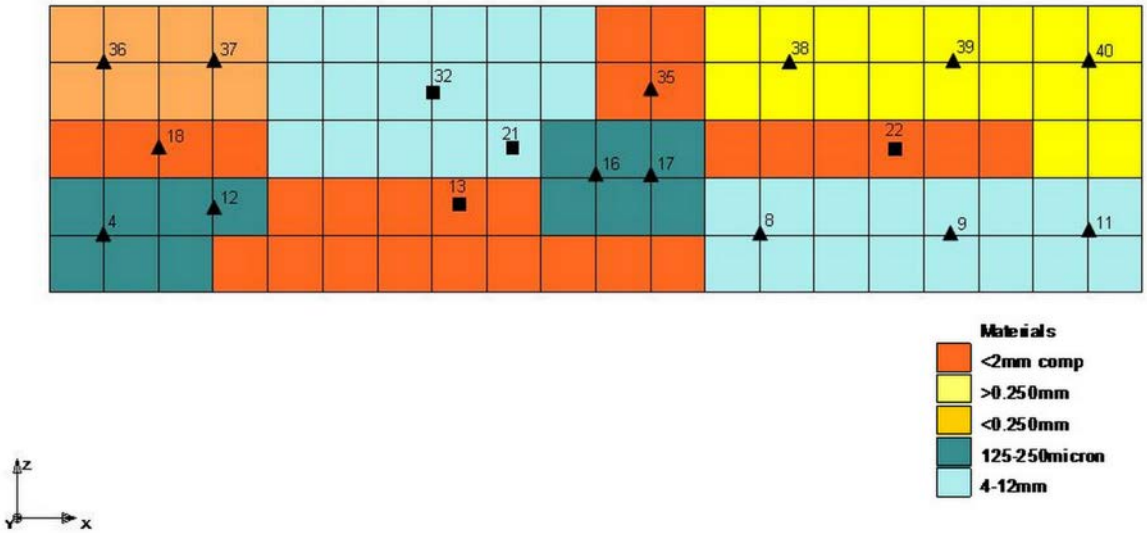

Figure 4.4 Vertical cross section (y = 35.1- 46.8cm) through the tank showing packing orientation of the size fractions as well as the location of the sampling wells; upgradient end is on the left, downgradient end is on the right. The dimensions of each cell are 11.2cm x 11.7cm x 11.2cm (x, y, z). Square symbols are wells present in the middle of this cross section; triangles are wells which are on the boundary between cross sections. The number next to the well is the well number.

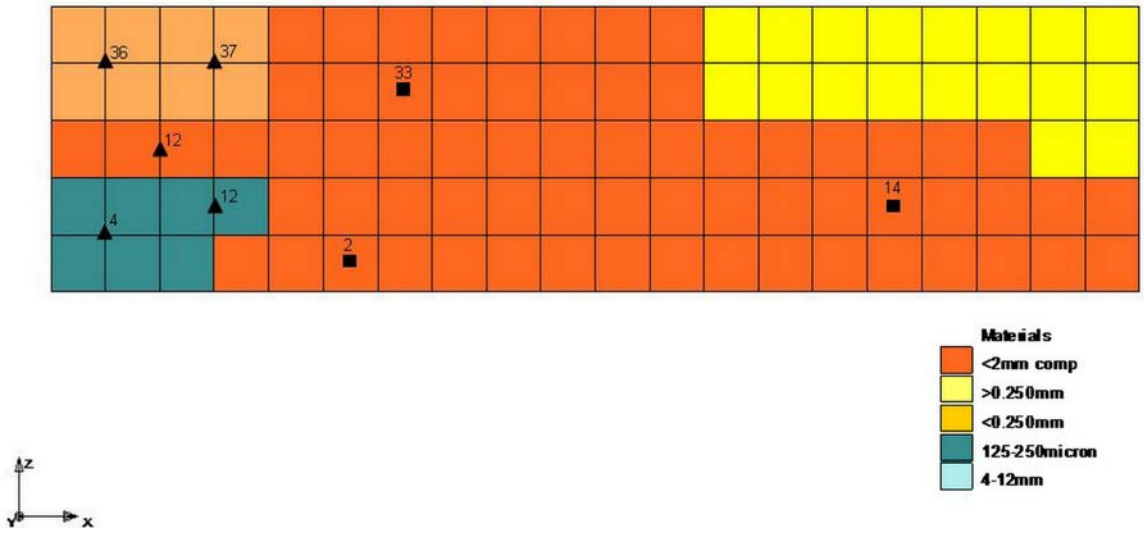

Figure 4.5 Vertical cross section (y = 0-11.7cm) through the tank showing packing orientation of the size fractions as well as the location of the sampling wells; upgradient end is on the left, downgradient end is on the right. The dimensions of each cell are 11.2cm x 11.7cm x 11.2cm (x, y, z). Square symbols are wells present in the middle of this cross section; triangles are wells which are on the boundary between cross sections. The number next to the well is the well number.

4.2.4 Water flow, Tracer Injection, Sampling and Analysis

An artificial groundwater (AGW) was used in the tank experiment. The composition, seen in Table 4.1, was intended to mimic that found at the Naturita field site. Average flow rates through the tank were 3.95 L/day (±0.75), and the time and spatially averaged Darcy flux was 3.34cm/day. Again, the goal was to mimic field relevant groundwater flow rates. AGW flowed through the tank for 9 months (~3.9PV). After 1.0PV had flowed through the tank, a pulse of bromide was injected into the tank as an inert tracer. The injection occurred by switching flow to an identical parallel head boundary. A total of 774mg (9.69×10^{-3}mols) of bromide was injected over a period of 25.5 hours. Bromide results are presented in Chapter 5.

Over the entire time of water flow through the tank, spatial samples were removed on a weekly basis from all of the groundwater wells, and effluent samples were taken twice a week. Effluent samples were removed from a T-joint in the effluent line. This

Table 4.1 Composition of the artificial groundwater; concentrations for ions are in molar, pH is in standard pH units, and saturation index is unitless.

Constituent	AGW Tank #3
Na^+	$2.47x10^{-2}$
K^+	$2.42x10^{-4}$
Mg^{2+}	$2.46x10^{-3}$
Ca^{2+}	$5.65x10^{-3}$
SiO_2	$4.72x10^{-4}/7.35x10^{-4}$
	(before/after 4-20-09)
Cl^-	$1.44x10^{-2}$
SO_4^{2-}	$1.34x10^{-2}$
Ionic Strength	$5.13x10^{-2}$
pH	7.85
Alkalinity (meq/L)	0.61
Equilibrium Gas	Atmospheric
Calcite Saturation Index (calculated)	0.06

line was purged with ~25-50mls of solution before taking a sample. At the top of each ground water well, a three way valve was put in place to allow for pore water removal, and for connection to a digital sensor array (DSA 3207, Scanivalve Corp.) to measure local pressure head. Sampling these wells was completed by connecting a syringe to the three way valve. Each well was purged with 5mls of volume, which was discarded. Then, using a clean syringe, ~7mls were removed for analysis. Once the effluent and spatial samples were taken, they were treated in an identical manner.

The pH of all samples was measured immediately using a standard pH probe and meter calibrated with pH 4, 7, and 10 buffers. The sample was then split into sub-samples depending on which analytes were being analyzed. Approximately 2ml were taken and refrigerated for bromide analysis. Another 2mls were taken and acidified with 50µl of 1M HNO_3 (pH<2) for uranium and bulk ion analysis (Na^+, K^+, Ca^{2+}, Mg^{2+}, Si_{TOT}, S_{TOT}). Uranium was measured using a Perkin Elmer Sciex Elan 6100 Inductively coupled plasma mass spectrometer (ICP-MS). Bulk ions were analyzed with a Perkin Elmer Optima 3000 Inductively coupled plasma atomic emission spectrometer (ICP-AES). The remaining fraction was refrigerated and shipped to collaborators at Lawrence Berkeley National Lab for alkalinity titrations using an automatic titrator.

4.3 Results

Results are divided between water chemistry characterization, and flow characterization.

4.3.1 Water Chemistry Results

Figures 4.6 through 4.8 show the spatial relationships for pH and uranium for three different, roughly equidistant, time points in the tank (note the changing uranium

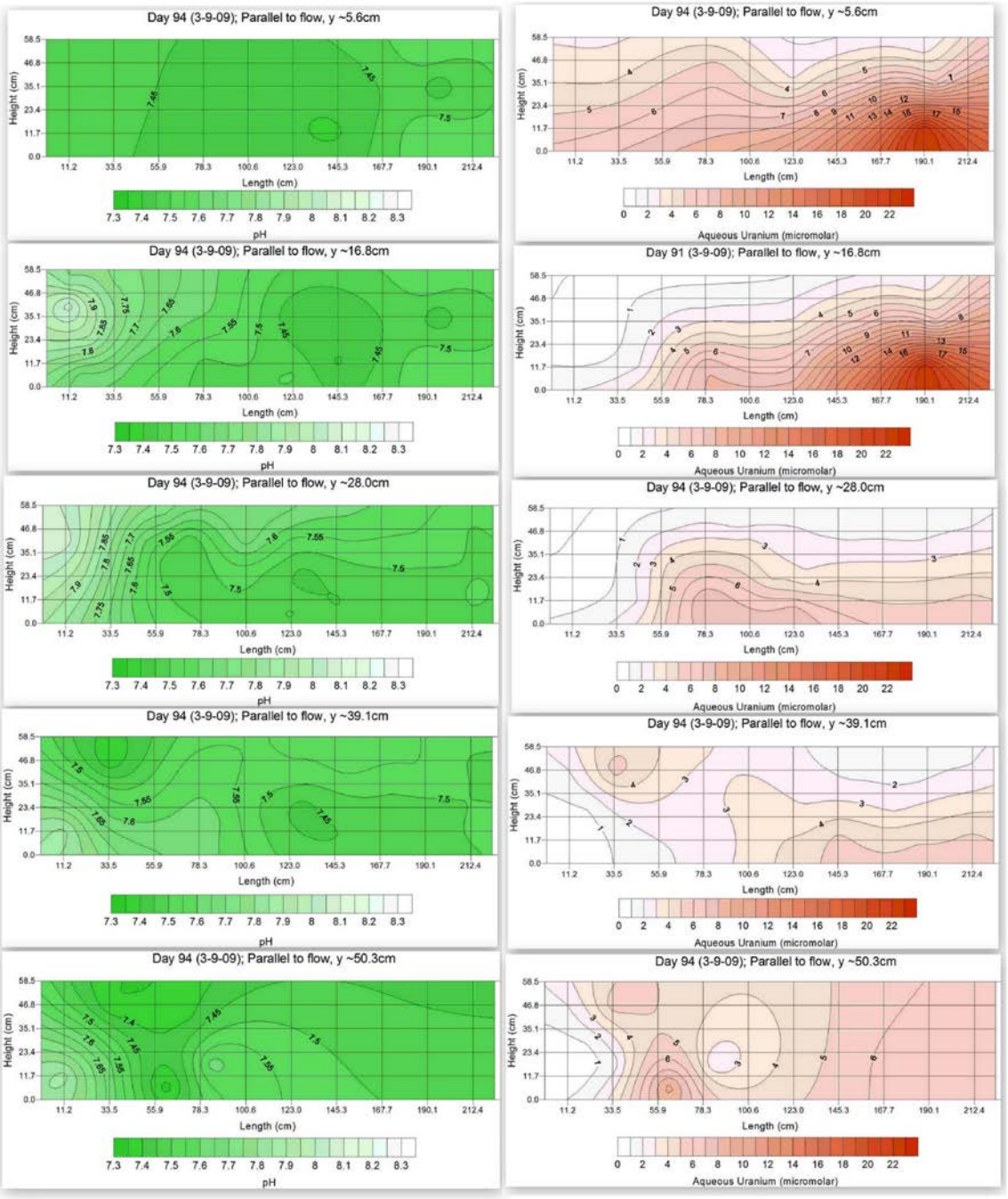

Figure 4.6 Spatial profiles for pH and uranium after 94 days of water flow. Each plot corresponds to the vertical cross sections in Figures 4.1 through 4.5.

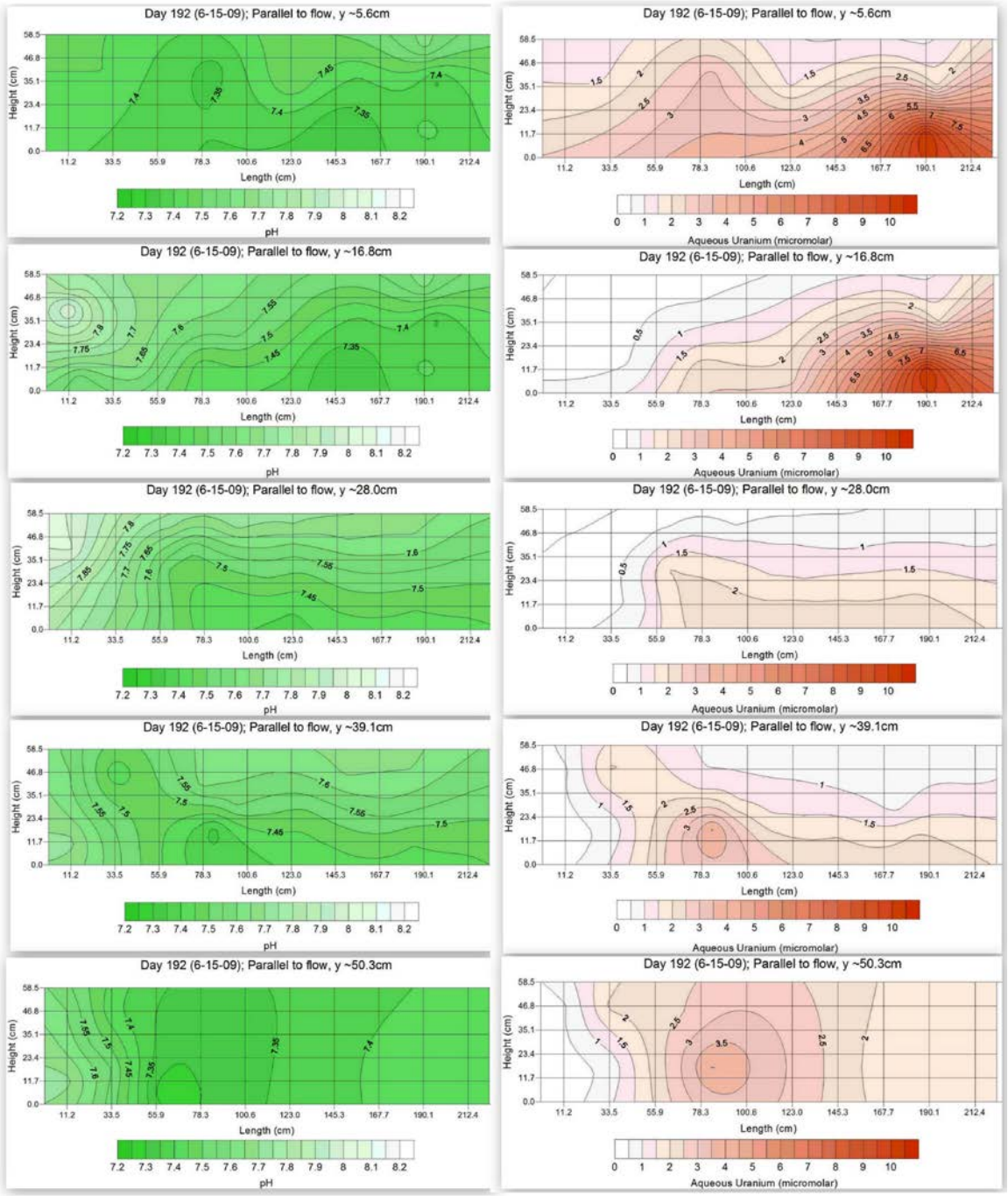

Figure 4.7 Spatial profiles for pH and uranium after 192 days of water flow. Each plot corresponds to the vertical cross sections in Figures 4.1 through 4.5.

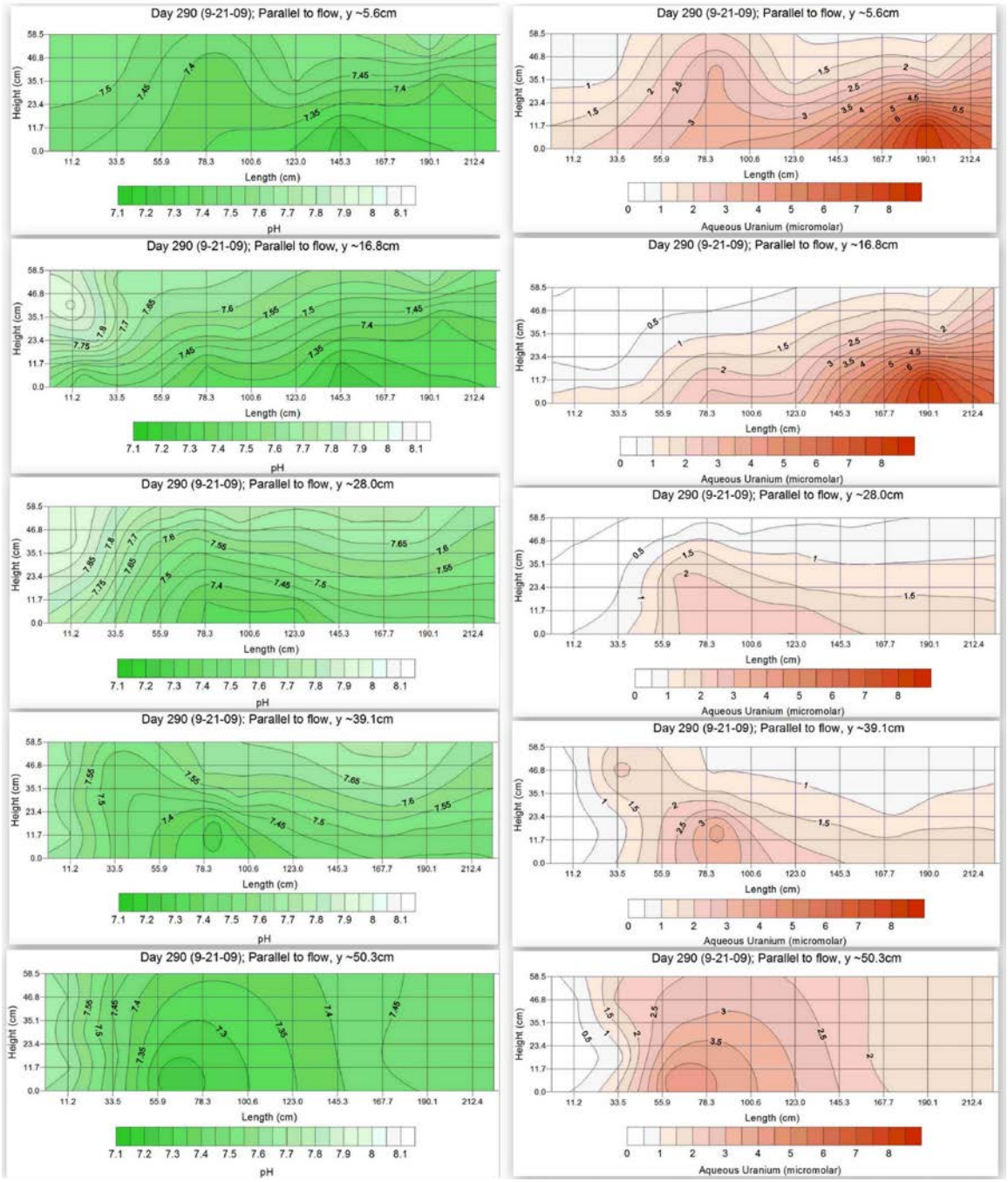

Figure 4.8 Spatial profiles for pH and uranium after 290 days of water flow. Each plot corresponds to the vertical cross sections in Figures 4.1 through 4.5.

concentration scales between the plots). In each plot it can be seen that pH values tend to drop rather precipitously in the up-gradient half of the tank, and maintain lower values throughout the flow domain. Also, the pH range is fairly small and similar for the different time points shown. Uranium concentrations tend to increase as the water moves down gradient. Concentration gradients for uranium were generally smooth, but well #10 tends to have much higher uranium concentrations than the surrounding areas. However, pH around well #10 is consistent with other local values. Uranium values through time generally decreased locally although the spatial gradients ranging from high to low were spatially static. In comparing the pH and uranium plots there is a visual relationship between pH and uranium where lower pH correlates with higher uranium values. This is shown explicitly with a correlation plot in Figure 4.9.

Each point in Figure 4.9 represents the analysis of a single sampling well for the date shown. The dates presented cover the entire experimental range. At early time points, 1-12-09 and 3-9-09, the correlation is quite weak, but at later time points, the relationship becomes much stronger. A notable exception to the trend is well #10, whose uranium concentrations were always much higher than other wells for a similar pH. Wells #2 and #7 are also anomalously high, but not as high as well #10 (wells #2 and #7 are 1-2 σ above the mean uranium value for a given sampling day, and well #10 is 4-5 σ above the mean). A similar plot is shown for calcium in Figure 4.10. A similar time dependence on the Ca-pH relationship is seen with the correlation getting better as a function of time. Figure 4.11 shows the uranium plotted as a function of calcium concentration. Here there is a time invariant relationship between all the data points.

Speciation calculations show that the $Ca_2UO_2(CO_3)^0$ dominates uranium chemistry over time and space. The trend in Figure 4.11 is consistent with these calculations. Also seen in Figure 4.11 is the behavior of well #10. At early time points well #10 plots above the linear relationship of all the other points. However, as experimental time progresses, the relationship falls on the same line as the other data points, just at higher concentrations. In Figures 4.9 and 4.10, the general trend is that upgradient wells tend to have larger x-ordinate values and downgradient wells have smaller values. In Figure 4.11, this relationship is reversed with the upgradient wells tending to have smaller x-ordinate values and downgradient wells have larger values.

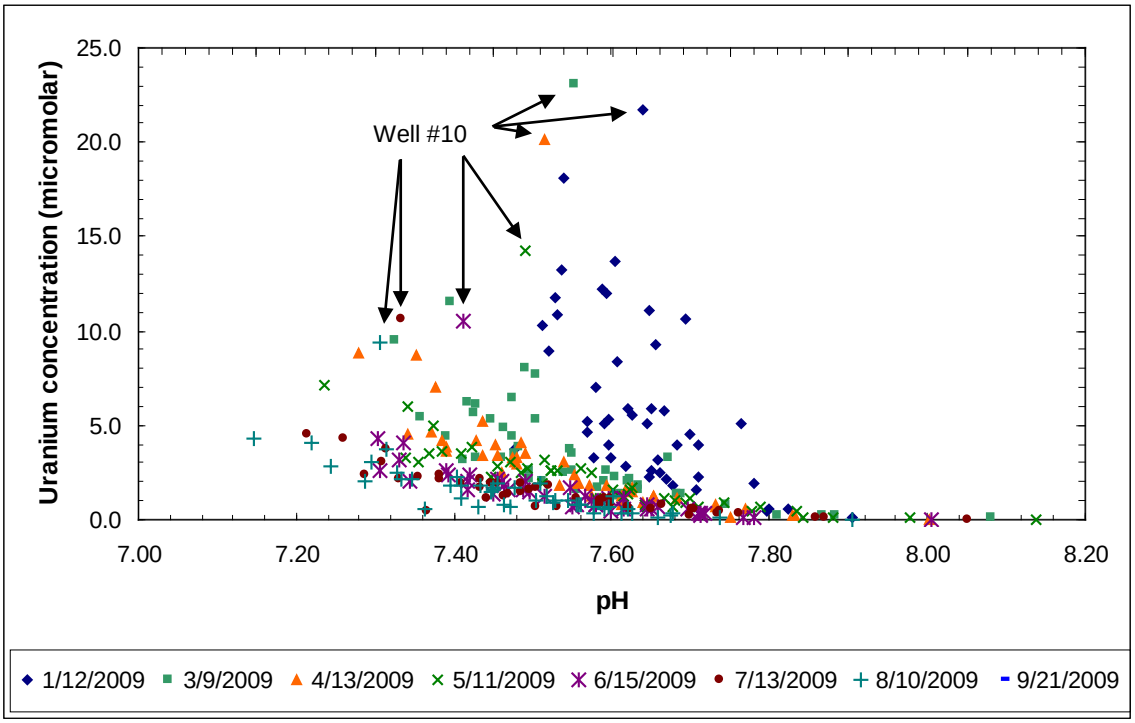

Figure 4.9 Correlation plot between uranium and pH. Each point represents the analysis from a single sampling well for the date shown. The dates shown encompass the majority of the experimental timeframe.

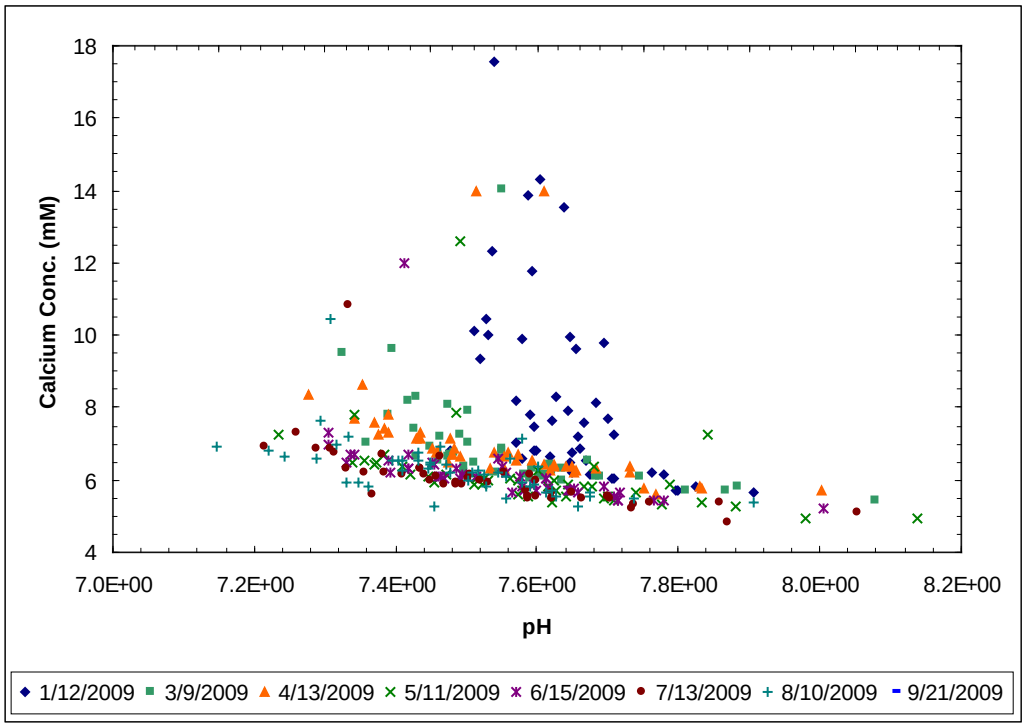

Figure 4.10 Correlation plot between calcium and pH. Each point represents the analysis from a single sampling well for the date shown. The dates shown encompass the majority of the experimental timeframe. Influent calcium concentration is 5.65mM.

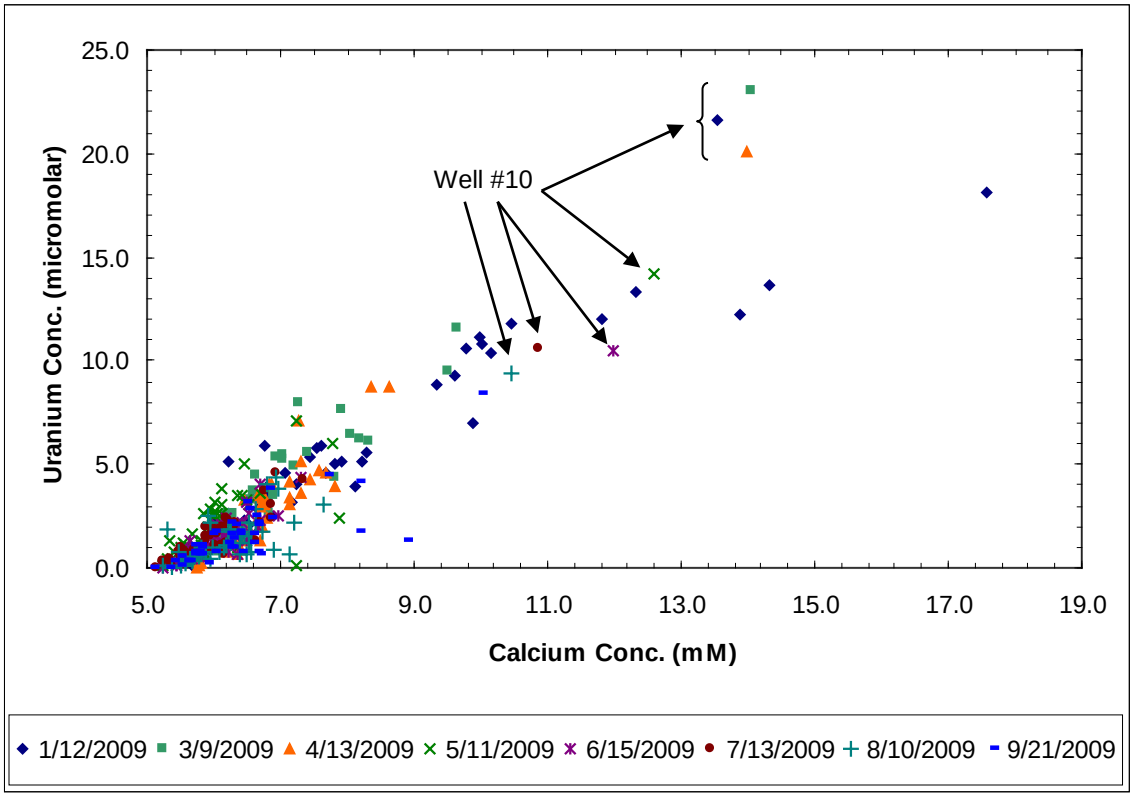

Figure 4.11 Correlation plot between uranium and calcium. Each point represents the analysis from a single sampling well for the date shown. The dates shown encompass the majority of the experimental timeframe.

Figure 4.12 is a correlation plot of silicon with pH showing a time independent relationship between them. Silicon is different from both calcium and uranium in that the net flux of silicon is from the solution phase to the solid phase; silicon concentrations generally decrease as a function of length downgradient. In the figure, upgradient wells tend to plot at higher pH and higher silicon values, while downgradient wells tend to plot at lower pH and silicon values. There is an apparent equilibrium relationship between pH and silicon, although it does not appear to be any well characterized silicon bearing mineral phase. Silicon concentrations assuming equilibrium with chlorite are shown on the plot. In general the shape of the line is parallel to the data but offset by about 30%. At all points in the tank, aqueous chemistry is supersaturated with respect to all major silicon bearing phases (kaolinite, albite, anorthite, K-feldspar, K-mica, Ca-montmorillonite, illite, chlorite, chalcedony, and quartz) with the exception of amorphous silica. The equilibrium concentration for amorphous silica for the entire pH range shown is 1.92-1.96mM.

4.3.2 Flow Calibrated Results

A calibrated ground water flow model was created in using Groundwater Modeling System 4.0. A model tank was created with particle size distributions identical to that in the real tank, but with a grid cell size of 2.796cm x 2.925cm x 2.794cm (x, y, z). Each particle size was assigned measured physical characteristics. Porosity was assumed to be spatially uniform at 0.37 based on packing densities. Hydraulic conductivities of the <2mm composite, <0.250mm, and >0.250mm fractions were measured from previous tank experiments (Chapter 3). Hydraulic conductivities of the 0.125-0.250mm fraction and the 4-12mm were estimated from particle size considerations. The values used are in the table on page 146. The calibrated values were created by changing the measured values to match the average flow through the tank (3.954L/day). Except for the values used for the 4-12mm fraction, all the other values were changed proportionately. Once

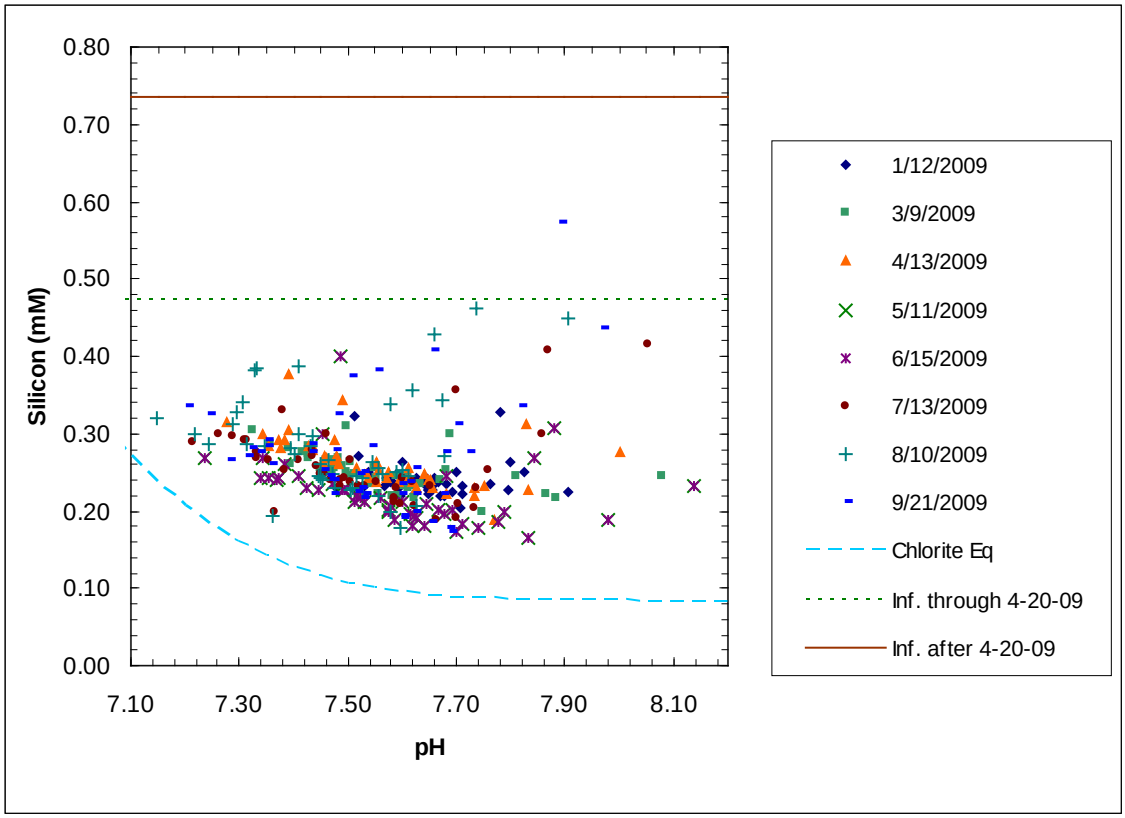

Figure 4.12 Correlation plot of silicon as a function of pH. Each point represents the results from a single well for the day indicated. Also shown are the influent concentrations before and after 4-20-09, as well as the solubility limit for silicon assuming equilibrium with chlorite ($Mg_5Al_2Si_3O_{10}(OH)_8$).

Sediment size	Hydraulic conductivity-measured (cm/sec)	Hydraulic conductivity-calibrated (cm/sec)
<2mm composite	4.09×10^{-4}	2.11×10^{-3}
<0.250mm	1.20×10^{-4}	5.97×10^{-4}
>0.250mm	6.40×10^{-3}	3.30×10^{-2}
0.125-0.250mm	NA	6.20×10^{-4}
4-12mm	NA	64.0

the flow balance was met, local flow velocities could be obtained from the magnitude of the flow vectors. The flow velocity in the cell closest to the screened section of the well was used to create the following plots. Note that flow direction is ignored.

Figure 4.13 shows the pH in all wells plotted as a function of local groundwater velocity. Each individual column of points is the results from a single well. Generally, pH decreased in a single well over time. At very low and very high groundwater velocities, a narrower pH range is observed, while at the intermediate range, a broader range is observed. Figure 4.14 shows the uranium data as a function of ground water velocity. A similar relationship is observed, however the wider range of uranium values is largely due to two wells (well #10 and 14). These wells are spatially related in that they are both down gradient wells, and they are both surrounded by <2mm composite material. Also note that the broad pH range occurs between ~1-10cm/day, while the broad uranium range occurs at ~0.1-1cm/day. Uranium is also plotted as a function of the number of local pore volumes to elute from the discretization cell in Figure 4.15. In Figure 4.15 the range of variables was restricted by choosing only wells that were surrounded by <2mm composite material and had local ground water velocities that were between 0.21 and 1.2cm/day. The data shown encompasses the entire experimental range. Smaller numbers of total eluted pore volumes on the graph represent smaller groundwater velocities and the wells are listed in order of increasing groundwater velocity.

Finally, Figure 4.16 shows the flux averaged uranium breakthrough curve from

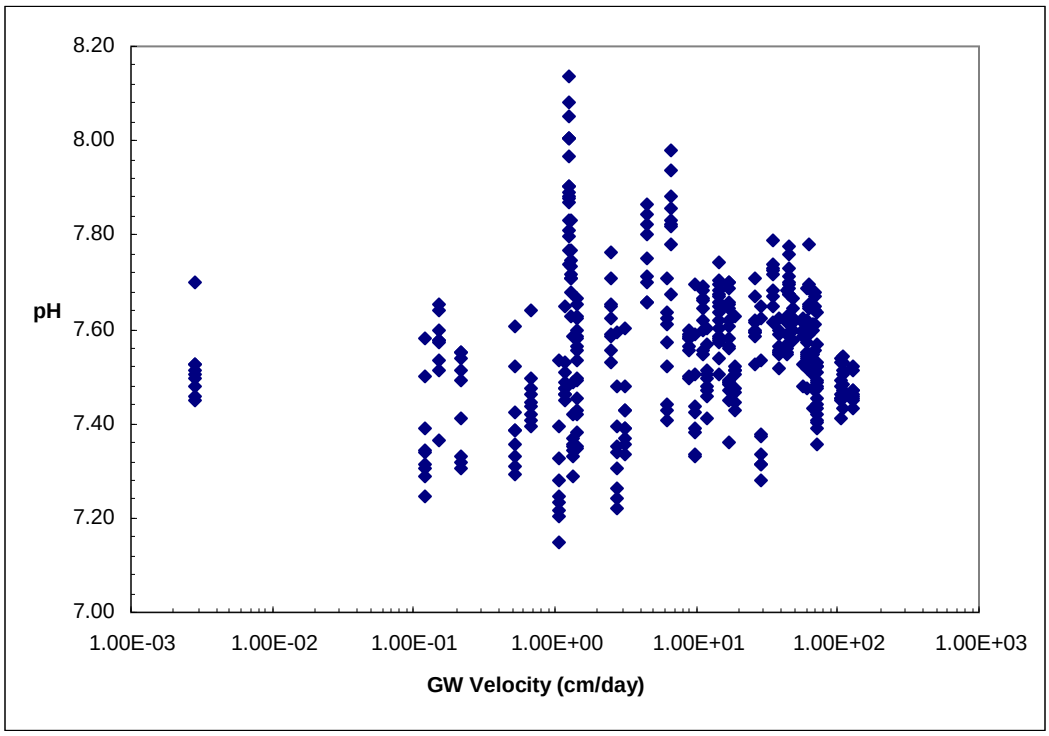

Figure 4.13 pH as a function of local ground water velocity. Each individual column of points represents the analysis from a single well.

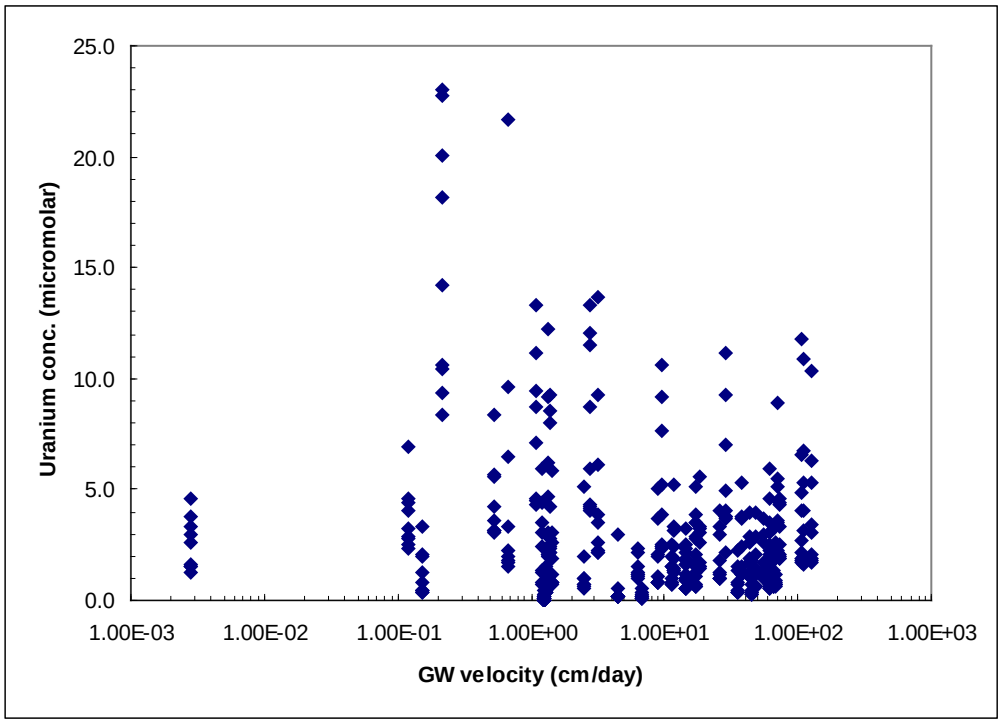

Figure 4.14 Uranium concentration as a function of ground water velocity. Each individual column of points represents the analysis from a single well.

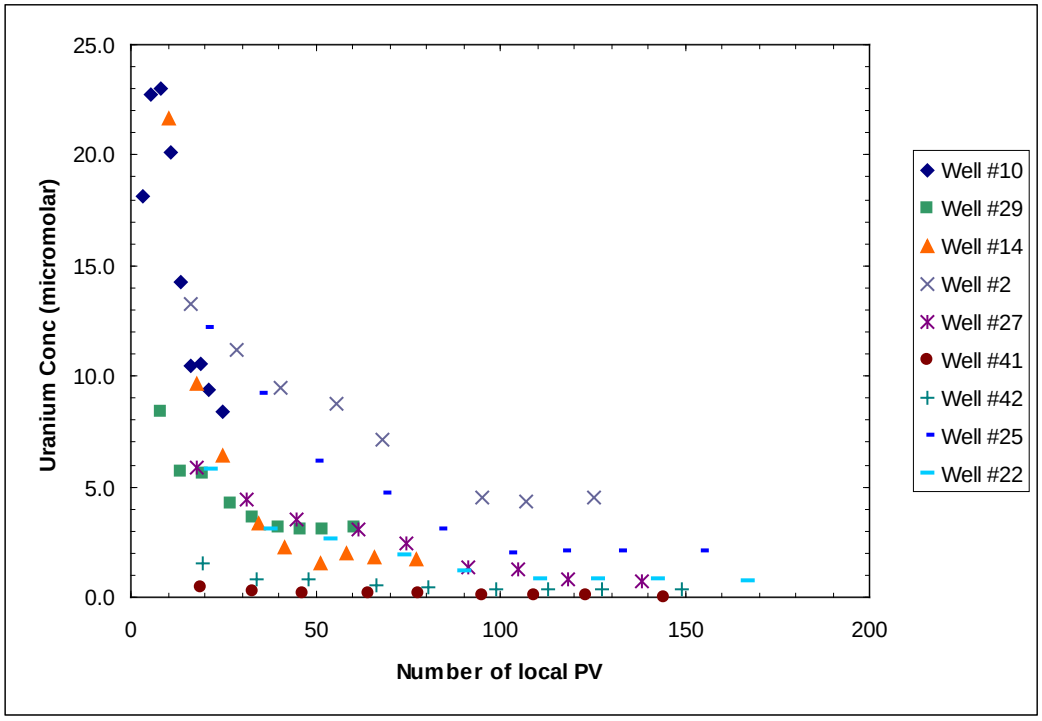

Figure 4.15 Uranium concentration as a function of local pore volumes eluted for a selected set of wells. The wells selected are all surrounded by <2mm composite material, and have local ground water velocities between 0.21-1.2cm/day.

the tank as a whole. One pore volume is approximately two months of real time. Assuming that the 4-12mm fraction had negligible sorbed uranium, and that the other size fractions all had $1.8x10^{-2}$μmol/g sediment (see Chapters 2 and 3), $1.76x10^{4}$μmols uranium were added, and only $4.80x10^{3}$ eluted, giving a mass recovery of 27%.

4.4 Discussion

There are two ways to interpret the results from the tank experiment: as a very large column, or as a very small field site. Depending on what the focus is, the tank has characteristics of both. For example, Figure 4.16 appears to be a fairly straightforward breakthrough curve. For much of the time, uranium elution is linear with a high rate of change (0-2 PV); then the mass elution slows considerably into a tailing phase where the behavior is still linear, but at a much smaller rate of change. This behavior is consistent with data reported at the column scale. When surface concentrations of uranium are high, and the uranium is located on the sediment near areas of mobile pore water, desorption is high and the so is the elution rate. As easily accessible surface uranium is depleted, and less accessible uranium constitutes the majority of the mass in solution, the elution rate slows and continues for a considerable period of time. Phenomenologically, the entire curve could be described with a first order decay type function. Other major ions in the tank (Ca^{2+}, Na^{+}, Mg^{2+}, S_{TOT}) also show behavior where the ion concentration at early time points is elevated relative to the influent concentrations, but the concentration slowly declines to influent levels (see APPENDIX D). Despite this apparent simplicity, considering the tank as a small field site complicates the analysis considerably.

A common technique with field sites is to krig the spatial data to allow for a visual representation of plume location. Indeed that was done here in Figures 4.6 through 4.8. In examining these plots the first observation is that even though there is a water flowpath of about 2m, there are still considerable fluctuations in local pH values and uranium concentrations both spatially and temporally. Some of these fluctuations are

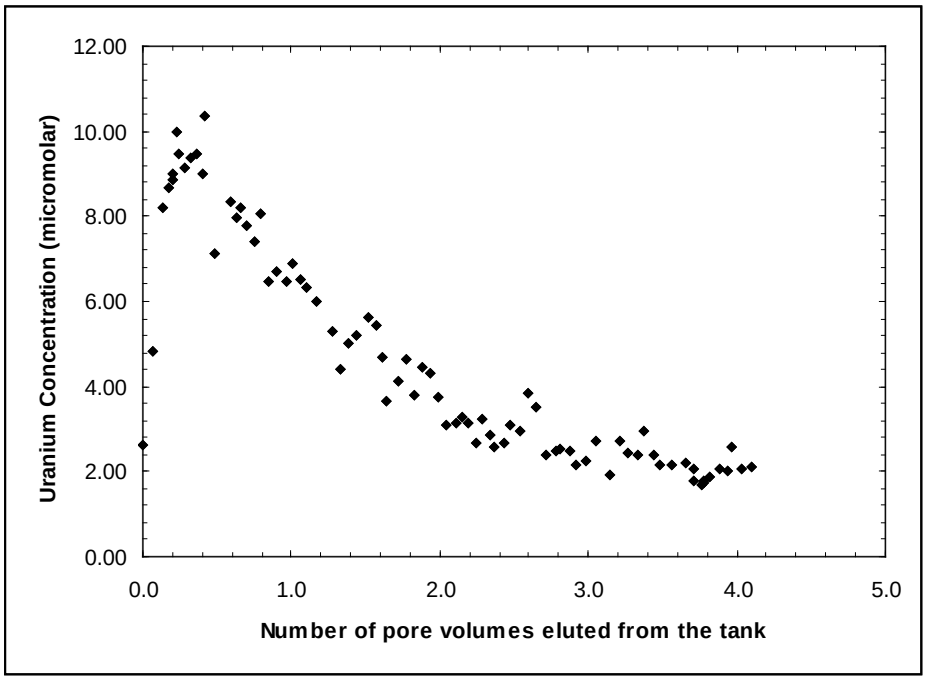

Figure 4.16 Uranium breakthrough curve as a function of pore volumes.

clearly linked to the physical heterogeneity induced in the tank by the placement of the particle sizes. This is the most pronounced in comparing spatial plots for both uranium and pH where y~28.0cm with Figure 4.3. A sharp vertical (perpendicular to flow) gradient occurs in both pH and uranium where the 4-12mm material is placed. It also appears that the source of the uranium is most likely from adjacent slices where the uranium concentrations are much higher, as the uranium concentration directly upgradient is <0.5μM. Thus local to these sharp gradients both uranium diffusion/advection from lower to higher flow zones, as well as a significant amount of advective mixing within the 4-12mm material appears to be occurring. There is also a clear correlation between uranium and physical heterogeneity in the slice where y~39.1cm. In this slice (compared to Figure 4.4), the uranium concentrations are higher in areas with larger flow velocities as determined from the flow calibrated simulations. Specifically the flow moves through the upgradient 4-12mm section, down through the <2mm composite and under the 0.125-0.250mm fraction into the downgradient 4-12mm section and then out of the tank. This is where the uranium concentrations tend to be higher in the y~39.1cm kriged plots. However, the physics of water flow is not the only variable in this small field site consideration.

Uranium desorption is known to be sensitive to many chemical variables including uranium concentration, pH, alkalinity, and mineral type. These variables also play a role in the observed distribution of uranium. The importance of this role is seen clearly in the correlation plots, Figures 4.9 through 4.11. For many cations, sorption onto a mineral surface decreases as pH decreases through both competition for binding sites as well as charge repulsion. This same behavior was seen throughout the tank. In areas where the pH is low, uranium concentrations were relatively high. When lines were fit through the data for days when the data was well described by a line ($r^2 \geq 0.7$, 4-13-09 through 9-21-09) and omitting the data from well #10, the x-intercept of all the lines ranged from 7.70-7.86; above this pH there should be near 100% uranium sorption. For samples with a pH above this range, the measured uranium values were among the lowest measured (0.033-0.122μM, n = 9). In the literature uranium sorption behavior in this pH range is mixed depending on the minerals involved and other experimental conditions. For many iron based mineral phases, as the pH increases from 7 to 8 there is a general

decrease in the amount of sorption when CO_2 is present (*Hsi and Langmuir* [1985], *Ho and Miller* [1986], *Waite et al.* [1994]) and also when Ca and CO_2 is present (*Fox et al.* [2006]). In certain iron mineral cases uranium sorption remains at 100% sorbed for this pH range (*Lenhart and Honeyman* [1999]). For many silicon based minerals in single mineral systems there is also a general decrease in uranium sorption from pH 7 to 8 when CO_2 is present (quartz, *Fox et al.* [2006], quartz, chlorite, muscovite, and albite, *Arnold et al.* [1998] and [2001] and *Schmeide et al.* [2000], quartz and clinoptilolite, *Prikryl et al.* [2001]). In mixed mineral and field based mineral systems the data is mixed ranging from a marked decrease in uranium sorption over this pH range (*Barnett et al.* [2002]), to no changes or a slight decrease in uranium sorption (*Zheng et al.* [2003]), to a marked increase in uranium sorption (*Dong et al.* [2005], *Benes et al.* [1998]). The degree that the sorption behavior changes is often dependent on specific conditions such as Ca concentrations, partial pressures of CO_2, and soil:solution ratios. However, interpreting the data from the tank in terms of equilibrium, pH based desorption edge the data is most in agreement with that of *Dong et al.* [2005]. This may be due to the presence of dissolved calcium and inorganic carbon species. Both *Dong et al.* [2005] and *Barnett et al.* [2002] use silty-clayey sediments similar to those used in the tank. However, *Barnett et al.* [2002] use sediments largely devoid of calcite while *Dong et al.* [2005] use sediments with and without added calcite. Since there is calcite in the sediments used in the tank, and there is evidence of calcite dissolution (Figure 4.11) it appears that the tank data is consistent with the batch data given in *Dong et al.* [2005].

Another hypothesis to explain the tank data is that there is a pH dependant, kinetic hindrance to desorption. This is corroborated by the fact that as the water-sediment contact time increases, as the water moves from up to down gradient, the uranium concentration also increases. This may also help to explain the time variable relationship between pH and uranium observed in Figure 4.10. However, if there is a kinetic hindrance to uranium desorption, it would appear that the effect is slight. In Figure 4.14, the relationship between uranium concentration and local groundwater velocity is relatively flat. Thus the supporting evidence for the kinetic response is somewhat mixed.

Figure 4.11 shows the pH-silicon relationship as a function of time. As opposed to the pH-U and pH-Ca relationships, the pH-Si relationship is fairly constant over the

entire time span studied. The influent concentrations changed as the AGW needed to be replenished halfway through the experiment, and it was difficult to get an exact silicon concentration. The measured values in the tank however, were always less than that in the AGW. Thus silicon is being removed from solution. On the plot, points that fall off the main line are generally from the most up-gradient wells (wells #1, 4, 26, 36, 41). Points that are on the line are from other areas in the tank. It appears that the reaction path in Figure 4.11 is from upper right to lower left in terms of silicon removal and pH suppression. The abrupt halt in the reaction path denotes a solubility control; however, as previously mentioned, there is no well characterized silicon bearing mineral phase whose silicon concentrations match the observed silicon-pH measurements. The reason for this relationship remains unclear, but it would appear that: 1. either silicon reactions are the overall control on pH in the tank or pH is forcing silicon removal from solution, 2. there is some sort of kinetic hindrance to this removal as the relationship becomes more linear as the water-sediment contact time increases, 3. this relationship is constant over the experimental timeframe.

For both silicon and uranium the observed behavior appears to be beyond what could be described using only thermodynamic considerations. Kinetic relationships appear to be influencing uranium desorption and silicon removal. Plotting the chemical constituents as a function of local groundwater velocity should elucidate the point further. Figure 4.13 plots pH as a function of groundwater velocity. Generally, the overall pH range is the highest at groundwater velocities between 1-10cm/day. At velocities both above and below this range, the pH range is much smaller. One possible explanation for this behavior is that at groundwater velocities <1cm/day the local equilibrium assumption may be valid and pH controlling reactions can approach a single value. At groundwater velocities higher than 10cm/day, the local equilibrium assumption is the most invalid, but instead physical and chemical interactions create an approach to a chemical steady state. In the 1-10cm/day range neither local equilibrium nor chemical steady state is being reached, so the local pH variation is controlled by the extent to which local chemical reactions can proceed given local reactivity and groundwater flow. This causes an observed increase in the overall range of observed pH values. For uranium (Figure 4.14), the largest uranium range is located between 0.1-1cm/day. However, this larger range is

dominated by two wells, #10 and #14. If those two wells are ignored, the general trend is toward larger ranges of uranium concentrations as a function of increasing groundwater velocity. For uranium then, it appears that for the range studied there is no discernible approach to a local equilibrium or chemical steady state. In transport studies with comparable groundwater velocities kinetic formulations limiting the amount of desorption have been necessary to describe the uranium data (*Kohler et al.* [1996], *Qafoku et al.* [2005]).

Understanding and quantifying uranium release rates as a function of scale is paramount to the description of uranium transport behavior at the field scale. In Figure 4.15 local uranium breakthrough curves are shown for wells surrounded only with <2mm composite material and with a specific groundwater velocity. Thus, this plot normalizes the data to groundwater velocity and surface reactivity, but not to aqueous phase heterogeneity. Despite these simplifications there is still a broad range of uranium behavior. The uranium response sometimes groups as a function of location within the tank. Wells #41 and 42 are very close in the tank and have similar uranium responses; the same is true for wells #27 and 29. However, well #22 has a similar uranium breakthrough curve to wells #27 and 29, but it is located at the downgradient end while wells #27 and 29 are at the upgradient end (see Figures 4.1 through 4.5). Also wells #2 and 25 are at opposite ends of the tank, yet have similar uranium responses. These similarities/dissimilarities do not correspond with local pH variations. Looking at only this data, it would appear that despite the fact that these wells are physically/chemically similar (same particle size, narrow groundwater velocity range) there is still spatial variation in the observed rate and extent of uranium desorption. This type of behavior has been used as a conceptual model at smaller scales (*Szecsody et al.* [1998]) but has not been observed from samples within an experimental flow domain where the physical and chemical heterogeneities are known.

Several wells exhibit this aberrant behavior to the extreme. Specifically wells #2, 7, and 10. Each of these wells has considerably higher concentrations of uranium and the other major ground water ions compared to the mean values for a given day, while pH and silicon values are not particularly different. It would appear that around these wells the sediments are especially reactive, although the reason for this is entirely unknown.

One possibility is that random packing variations put highly soluble salts near these wells, and the relatively low groundwater velocities did not carry away the dissolution by-products. However, well #10 does have an observed impact on uranium breakthrough behavior. The zones of highest flow within the tank are the areas around wells #8, 9, and 11 (see Figure 4.3 and 4.4). This means that the majority of the flow out of the tank is coming from this region. When uranium concentrations in that area are compared to the breakthrough curve (Figure 4.16), wells 8, 9, and 11 always have slightly lower concentrations. Thus there needs to be another relatively concentrated source of uranium to make up the mass balance in the effluent. In examining the spatial plots, the most likely candidate is the area around well #10. Enough uranium must be leaving that zone either by diffusion or advective flux to cause an increase in effluent uranium concentrations.

4.5 Conclusions

An intermediate scale 3-D experiment using uranium contaminated sediment has been completed. The sediment was divided into five different size fractions and packed in a heterogeneous fashion. An artificial ground water flowed through the tank for approximately ten months. Over that time period the aqueous phase was characterized through sampling 46 small scale ground water sampling wells. The flow field was simulated using GMS 4.0 to obtain local groundwater velocities near the wells. The observed data was analyzed as a function of chemical behaviors due to dissolution, weathering, and uranium desorption as well as through comparing chemical characteristics related to the physical characteristics associated with water flow velocities.

When considering the tank as a small field experiment, large spatial and temporal variations in pH and uranium were observed. The uranium concentration profiles are clearly dependant on the physical orientation of the sediment packing as abrupt changes in uranium concentration gradients were observed at certain particle size boundaries.

Local uranium concentrations correlate well with both pH and calcium but the specific nature of the relationship varied with time. Local silicon and pH are also strongly correlated, and the relationship appears to be dependant on the water-sediment interaction time, and does not change as a function of elapsed experimental time. One possible reaction path that leads to uranium desorption and transport within the tank is that the precipitation of a silicon bearing phase controls the pH, local pH controls the extent and dissolution rate of calcite, and the produced carbonate species control the rate and extent of uranium desorption. Any of these could be a rate limiting step, as there was clear indicators of spatially variable uranium release rates.

When the tank was considered as a large column experiment the uranium behavior was much more predictable. The uranium breakthrough curve out of the tank was smooth, and in the general shape of first order decay. Other major ions showed similar smooth behavior where the concentration starts quite high and slowly approaches influent concentrations. Thus, despite small scale complexity and a myriad of chemical and physical interactions, the macroscopic observed uranium behavior is quite simple. Generally when upscaling is discussed in the literature the assumption is that the need is for mathematical relationships that relate small scale complexity up to some equivalent scale for field application. However, the results from this experiment demonstrate that describing small scale, local complexity may not be necessary to describe larger scale behavior. These experiments demonstrate that there may be an inverse correlation between system size and required model complexity; there is a homogenization of uranium behavior caused by the increased heterogeneity associated with the scale of experiment. The scale at which measurements are made, and how measurements are interpreted may indeed relate quite strongly to the appropriate scaling response (*Cushman* [1986]). More experiments at the intermediate scale need to completed using different packing orientations, more geologically relevant orientations, and with a wider range of chemical heterogeneities to explore this hypothesis further.

4.6 References

Arnold, T., T. Zorn, G. Bernhard, and H. Nitsche. 1998. Sorption of uranium(VI) onto phyllite. *Chemical Geology* 151:129-141.

Arnold, T., T. Zorn, H. Zanker, G. Bernhard, and H. Nitsche. 2001. Sorption behavior of U(VI) of phyllite: experiments and modeling. *Journal of Contaminant Hydrology* 47:219-231.

Barnett, M.O., P.M. Jardine, S.C. Brooks, and H.M. Selim. 2000. Adsorption and Transport of Uranium(VI) in Subsurface Media. *Soil Science Society of America Journal* 64:908-917.

Barnett, M.O., P.M. Jardine, and S.C. Brooks. 2002. U(VI) Adsorption to Heterogeneous Subsurface Media: Application of a Surface Complexation Model. *Environmental Science and Technology* 36 (5):937-942.

Benes, P., K. Kratzer, S. Vlvkova, and E. Sebestova. 1998. Adsorption of Uranium on Clay and the Effect of Humic Substances. *Radiochimica Acta* 82:367-373.

Brusseau, Mark L., and John M. Zachara. 1993. Transport of Co^{2+} in a Physically and Chemically Heterogeneous Porous Medium. *Environmental Science and Technology* 27 (9):1937-1939.

Burr, D.T., Edward A. Sudicky, and R.L. Naff. 1994. Nonreactive and reactive solute transport in three-dimensional heterogeneous porous media: Mean displacement, plume spreading, and uncertainty. *Water Resources Research* 30 (3):791-815.

Chen, Wenlin, and Robert J. Wagenet. 1995. Solute Transport in Porous Media with Sorption-Site Heterogeneity. *Environmental Science and Technology* 29 (11):2725-2734.

Curtis, Gary P., J.A. Davis, and David L. Naftz. 2006. Simulation of reactive transport of uranium(VI) in groundwater with variable chemical conditions. *Water Resources Research* 42: W04404, doi:10.1029/2005WR003979.

Cushman, John H. 1986. On Measurement, Scale, and Scaling. *Water Resources Research.* 22(2):129-134.

Dong, Wenming, William P. Ball, Chongxuan Liu, Zheming Wang, Alan T. Stone, Jing Bai, and John M. Zachara. 2005. Influence of Calcite and Dissolved Calcium on Uranium(VI) Sorption to a Hanford Subsurface Sediment. *Environmental Science and Technology* 39 (20):7949-7955.

Espinoza, Carlos, and Albert J. Valocchi. 1997. Stochastic analysis of one-dimensional transport of kinetically adsobing solutes in chemically heterogeneous aquifers. *Water Resources Research* 33 (11):2429-2445.

Fox, Patricia, J.A. Davis, and John M. Zachara. 2006. The effect of calcium on aqueous uranium(VI) speciation and adsorption to ferrihydrite and quartz. *Geochimica et Cosmochimica Acta* 70:1379-1387.

Gabriel, U., J.-P. Gaudet, L. Spadini, and Laurent Charlet. 1998. Reactive transport of uranyl in a goethite column: an experimental and modeling study. *Chemical Geology* 151:107-128.

Gasda, S.E., and M.A. Celia. 2005. Upscaling relative permeabilities in a structured porous medium. *Advances in Water Resources* 28:493-506.

Haggerty, Roy, Charles Harvey, Claudius Freiherr von Schwerin, and Lucy C. Meigs. 2004. What controls the apparent time-scale of solute mass transfer in aquifers and soils? A comparison of experimental results. *Water Resources Research* 40.

Ho, C.H., and N.H. Miller. 1986. Adsorption of Uranyl Species from Bicarbonate Solution onto Hematite Particles. *Journal of Colloid and Interface Science* 110 (1):162-171.

Hsi, Ching-Kuo Daniel, and Donald Langmuir. 1985. Adsorption of uranyl onto ferric oxyhydroxides: Application of the surface complexation site-binding model. *Geochimica et Cosmochimica Acta* 49:1931-1941.

Kent, D.B., J.A. Davis, C.D. Anderson, and B.A. Rea. 1995. Transport of chromium and selenium in a pristine sand and gravel aquifer: Role of adsorption processes. *Water Resources Research* 31 (4):1041-1050.

Kent, D.B., R.H. Abrams, J.A. Davis, Jennifer A. Coston, and D.R LeBlanc. 2000. Modeling the influence of variable pH on the transport of zinc in a contaminated aquifer using semiempirical surface complexation models. *Water Resources Research* 36 (12):3411-3425.

Kohler, Matthias, Gary P. Curtis, D.B. Kent, and J.A. Davis. 1996. Experimental investigation and modeling of uranium(VI) transport under variable chemical conditions. *Water Resources Research* 32 (12):3539-3551.

Lenhart, John J., and Bruce D. Honeyman. 1999. Uranium(VI) sorption to hematite in the presence of humic acid. *Geochimica et Cosmochimica Acta* 63 (19/20):2891-2901.

Levy, Melissa, and Brian Berkowitz. 2003. Measurement and analysis of non-Fickian dispersion in heterogeneous porous media. *Journal of Contaminant Hydrology* 64:203-226.

Li, L., C.A. Peters, and M.A. Celia. 2006. Upscaling geochemical reaction rates using pore-scale network modeling. *Advances in Water Resources* 29:1351-1370.

Li, L., C.A. Peters, and M.A. Celia. 2007. Effects of mineral spatial distribution on reaction rates in porous media. *Water Resources Research* 43 W01419, doi:10.1029/2005WR004848.

Li, L., Carl I. Steefel, and Li Yang. 2008. Scale dependence of mineral dissolution rates within single pores and fractures. *Geochimica et Cosmochimica Acta* 72:360-377.

Liu, Chongxuan, John M. Zachara, Odeta S. Qafoku, James P. McKinley, Steve M. Heald, and Zheming Wang. 2004. Dissolution of uranyl microprecipitates in subsurface sediments at Hanford Site, USA. *Geochimica et Cosmochimica Acta* 68 (22):4519-4537.

Liu, Chongxuan, John M. Zachara, Wassana Yantasee, Paul D. Majors, and James P. McKinley. 2006. Microscopic reactive diffusion of uranium in the contaminated sediments at Hanford, United States. *Water Resources Research* 42.

Liu, Chongxuan, John M. Zachara, Nikolla Qafoku, P., and Zheming Wang. 2008. Scale-dependent desorption of uranium from contaminated subsurface environments. *Water Resources Research* 44 (W08413):10.1029/2007WR006478.

Maher, Kate, Carl I. Steefel, Donald J. DePaolo, and Brian E. Viani. 2006. The mineral dissolution rate conundrum: Insights from reactive transport modeling of U isotopes and pore fluid chemistry in marine sediments. *Geochimica et Cosmochimica Acta* 70:337-363.

Meile, Christof, and Kagan Tuncay. 2006. Scale dependence of reaction rates in porous media. *Advances in Water Resources* 29:62-71.

Pang, Lipang, Murray Close, Daniela Schneider, and Greg Stanton. 2002. Effect of pore-water velocity on chemical nonequilibrium transport of Cd, Zn, and Pb. *Journal of Contaminant Hydrology* 57:241-258.

Prikryl, James D., Alka Jain, David R. Turner, and Roberto T. Pabalan. 2001. Uranium(VI) sorption behavior on silicate mineral mixtures. *Journal of Contaminant Hydrology* 47:241-253.

Qafoku, Nikolla, P., John M. Zachara, Chongxuan Liu, Paul L. Gassman, Odeta S. Qafoku, and Steven C. Smith. 2005. Kinetic Desorption and Sorption of U(VI)

during Reactive Transport in a Contaminated Hanford Sediment. *Environmental Science and Technology* 39 (9):3157-3165.

Rajaram, Harihar. 1997. Time and scale dependent effective retardation factors in heterogeneous systems. *Advances in Water Resources* 20 (4):217-230.

Renard, Ph., and G. de Marsily. 1997. Calculating equivalent permeability: a review. *Advances in Water Resources* 20 (5-6):253-278.

Scheibe, Timothy D., and Steven Yabusaki. 1998. Scaling of flow and transport behavior in heterogeneous groundwater systems. *Advances in Water Resources* 22 (3):223-238.

Schmeide, K., S. Pompe, M. Bubner, K.H. Heise, G. Bernhard, and H. Nitsche. 2000. Uranium(VI) sorption onto phyllite and selected minerals in the presence of humic acid. *Radiochimica Acta* 88:723-728.

Steefel, Carl I., Susan Carroll, Pihong Zhao, and Sarah Roberts. 2003. Cesium migration in Hanford sediment: a multisite cation exchange model based on laboratory experiments. *Journal of Contaminant Hydrology* 67:219-246.

Stollenwerk, Kenneth G. 1995. Modeling the effects of variable groundwater chemistry in adsorption of molybdate. *Water Resources Research* 31 (2):347-357.

Stollenwerk, Kenneth G. 1998. Molybdate transport in a chemically complex aquifer: Field measurements compared with solute-transport model predictions. *Water Resources Research* 34 (10):2727-2740.

Szecsody, James E., John M. Zachara, Ashokkumar Chilakapati, P.M. Jardine, and Alan S. Ferrency. 1998. Importance of flow and particle-scale heterogeneity on Co(II/III) EDTA reactive transport. *Journal of Hydrology* 209:112-136.

Vogel, H.-J., and K. Roth. 2003. Moving through scales of flow and transport in soil. *Journal of Hydrology* 272:95-106.

Waite, T.D., J.A. Davis, T.E. Payne, G.A. Waychunas, and N. Xu. 1994. Uranium(VI) adsorption to ferrihydrite: Application of a surface complexation model. *Geochimica et Cosmochimica Acta* 58 (24):5465-5478.

Weber Jr., Walter J., Paul M. McGinley, and Lynn E. Katz. 1992. A Distributed Reactivity Model for Sorption by Soils and Sediments 1. Conceptual Basis and Equilibrium Assessments. *Environmental Science and Technology* 26 (10):1955-1962.

Zachara, John M., Steven C. Smith, Chongxuan Liu, James P. McKinley, R. Jeffrey Serne, and Paul L. Gassman. 2002. Sorption of Cs+ to micaceous subsurface

sediments from the Hanford site, USA. *Geochimica et Cosmochimica Acta* 66 (2):193-211.

Zhang, Xiaoxian, John W. Crawford, and Iain M. Young. 2008. Does pore water velocity affect the reaction rates of adsorptive solute transport in soils? Demonstration with pore-scale modeling. *Advances in Water Resources* 31:425-437.

Zheng, Zuoping, Tetsu K. Tokunaga, and Jiamin Wan. 2003. Influence of Calcium Carbonate on U(VI) Sorption to Soils. *Environmental Science and Technology* 37 (24):5603-5608.

CHAPTER 5

URANIUM EXPERIMENTS AT THE INTERMEDIATE SCALE: INERT TRANSPORT RELATIVE TO REACTIVE TRANSPORT

5.1 Introduction

The upscaling of reactive transport in groundwater systems is plagued by heterogeneity. Small and large scale physical heterogeneities can cause perturbations in the flow field, and these alterations in the flow field can change observed reaction paths (*Pang et al.* [2002], *Meile and Tuncay* [2006], *Brusseau and Zachara* [1993]). Conversely, reactive chemistry, which is also spatially and temporally variable, can cause perturbations of the flow field through local flow path alterations caused by mineral dissolution/precipitation (see *White and Brantley* [1995]). Thus physical and chemical heterogeneities interact with each other to cause deviations from ideal flow and transport. A large number of conceptual and mathematical models have been created to incorporate both large and small scale complexity (e.g. *Lichtner and Tartakovsky* [2003], *Liu et al.* [2008], *Li et al.* [2006], *Seeboonruang and Ginn* [2006]). However, these methods for upscaling reactive transport models remain theoretical with the absence of transport data at a range of heterogeneities.

Typically transport studies occur at two main levels of heterogeneity: bench and field. Within these two levels of heterogeneity there is some small variation in the total amount of heterogeneity based on experimental conditions. At the bench scale the overall length of an experimental column, the mass of sediment used, the use of an idealized vs. actual field sediment, and any sort of separation of particle sizes causing the introduction of physical heterogeneities can all contribute to the total heterogeneity in a system. At the field scale, different aquifers have different characteristics based on local geologic stratigraphy and mineralogy. For example the Borden site is often considered to be fairly physically homogenous (*Sudicky* [1986]), while the MADE site is considered to

be relatively heterogeneous (*Boggs et al.* [1992]). These variations in heterogeneity are often based on characterization of the hydraulic conductivity field and the assumption that deviations in tracer behavior from 'ideal transport' are positively correlated with site heterogeneity. Experimental inquiry at these two scales allows for different hypotheses to be tested; the bench scale work allows for delineation of fundamental interactions, while the field scale represents the scale of application.

A far less used scale of inquiry is intermediate between the bench and field scales. Often these experiments are performed in very long 1-D columns or in large constructed tanks, which can be either two or three dimensional. These types of experiments are critical to resolving issues surrounding upscaling based on the heterogeneity of a system. Although they are rarer, many intermediate scale experiments have been completed. These experiments most often focus on flow and inert transport. For example in some early tank work, *Silliman and Simpson* [1987] examine the effect of packing heterogeneities on the dispersivity of an ionic strength based tracer. They found that the structure of the packing heterogeneity can cause variations in tracer dispersivity and what would be the required upscaling response. In far more recent work *Levy and Berkowitz* [2003] performed tank experiments using three different packing heterogeneities and compared continuous time random walk (CTRW) model formulations to more traditional advective-dispersive equation (ADE) formulations. In general the CTRW did a better job than ADE based formulations in describing tracer behavior as a function of heterogeneity. However, many intermediate scale experiments use lab sands to facilitate packing (*Barth et al.* [2001] and [2001]a, *Levy and Berkowitz* [2003], *Schincariol and Schwartz* [1994], *Silliman and Simpson* [1987]). The use of lab sands does simplify both sediment procurement and packing procedures, but on the scale of relative heterogeneities lab sands are far less heterogeneous than field sediments both in mineral composition and size range. There is no way to know how this simplification affects tracer behavior and conclusions made on tracer behavior.

Another concern of intermediate scale investigation is that the average groundwater velocity through many of these tank experiments is often orders of magnitude higher than that found at field sites under ambient conditions. For example, *Oostrom et al.* [1991] use groundwater velocities ranging from 0.09-15.14m/day with the

average of 35 experiments being 4.6m/day. Other experimentalists have used similar ranges (*Barth et al.* [2001] and [2001]a, *Levy and Berkowitz* [2003], *Schincariol and Schwartz* [1994], *Silliman and Simpson* [1987]), while many field sites have reported values in cm/day range (e.g. *LeBlanc et al.* [1991]: 420cm/day, *Sudicky* [1986]: 9cm/day, see also *Gelhar et al.* [1992] and references therein). Again, it is unclear how the differences between experimental velocities and field velocities affect tracer behavior, overall conclusions, and necessary scaling response.

And finally, intermediate scale experiments are often focused on flow and transport or on reactive chemistry and do not perform experiments which are designed to test hypotheses relating to specific interactions between chemistry and water flow. For example, *Heiderscheidt et al.* [2008] examine organic phase dissolution, transport and oxidation; however, this study uses an engineered approach to chemistry using overall mass depletion rates instead of specific chemical reactions. Also, a uranium and technetium bio-immobilization study was completed by *Michalsen et al.* [2006]. In this study reactive chemistry relating to bio-reduction was considered, but variables relating to transport were not investigated. A counter example to this general trend is *Istok et al.* [1999]. In this paper a field sediment from the Hanford site was used to fill a wedge shaped tank, and a bromide solution was flushed through the tank to determine flow paths while a dithionate solution was pumped through the tank to control redox conditions. Reactive chemistry was linked to the ADE using first order reaction kinetics to describe dithionate reaction with iron bearing minerals. However, the goal of this study was to simulate field pump and treat remediation, so the velocities were higher than that dictated by ambient hydraulic gradients.

The goal of this study is to partially close the heterogeneity gap between the bench and field scale. This was completed through filling an intermediate scale tank with a uranium contaminated field sediment from a former uranium mill. The sediment was divided into 5 distinct particle sizes, and the tank was packed in a physically heterogeneous manner. Ground water rates were similar to that found at the field site (average bulk velocity: 3.34cm/day). Bromide was used as an inert tracer, and was monitored through the placement of 46 ground water wells. Other chemical

characteristics relating to uranium fate and transport (uranium, calcium, pH, alkalinity, other bulk ions) were also measured from these wells.

5.2 Methods

Packing methods, orientations, sampling protocol, and other experimental methods were presented in Chapters 2 and 4. For clarity, however, critical points will be repeated here. The pulse injection of bromide occurred over a period of 25.5 hours through a parallel head boundary feeding into the tank. The bromide concentration was 1.95×10^{-3} M KBr (155.5mg Br^-/L); this concentration has been shown to avoid the effects of density induced sinking (*Barth et al*. [2001]a). The total amount of bromide added was 9.69×10^{-3}mols (774mg). Bromide was monitored over a course of about six months until effluent values were below detectable limits. Bromide was being measured concurrently with uranium and other general water quality parameters.

Flow and transport of bromide within the tank was modeled using Groundwater Modeling System 4.0 (GMS). This program is a graphical interface to many commonly used flow and transport models; in this work the MODFLOW (*Harbaugh et al.* [2000]) and MT3DMS (*Zheng and Wang* [1999]) packages were used to describe flow and transport, respectively. The first step in the modeling process was to create a flow domain. The packing orientation and other physical characteristics (i.e. porosity) were input from the packing procedures (Chapter 4). The flow field was discretized in two different ways. The first was to calibrate flow alone, and the calibrated groundwater velocities were used to plot breakthrough curves for specific wells as a function of the local number of pore volumes (Figure 5.5). The discretization for this process had dimensions of 2.8cm x 2.9cm x 2.8cm (x, y, z) for a total of 32,000 cells. A coarser discretization was used to describe tracer transport due to computational considerations (Figure 5.4). The dimensions of this grid were 5.6cm x 5.9cm x 5.6cm (x, y, z) cells for a total of 4,000 grid cells. In GMS the hydraulic conductivity is linked to particle size and the conductivities for three out of the five particle sizes (<2mm composite, <0.250mm,

and >0.250mm) had been both measured directly using ASTM method D2434-68, and had been fit to local pressure head data from previous tank experiments (Chapter 3). The estimates from tank data were the initial input to the model. Hydraulic conductivities of the remaining two sizes were estimated based on particle size considerations. Once these initial estimates were added, the numbers were adjusted to match the observed head difference (2mm) and average flow rate (3.95L/day) observed in the tank. This calibrated flow model was used as input into the transport code.

The bromide pulse was simulated using two stress periods, one for the injection of bromide, and one for the elution of bromide. The input for the stress periods was taken from the experimental injection described above. However, a model injection time of 1.0 days was used and the bromide spike concentration had to be adjusted to 2.45 $x10^{-3}$ M (196mg/L) to match the total injected mass into the tank. The diffusion coefficient of bromide was initially set to $20.8x10^{-10}$ m^2/s (*Liu et al.* [2008]). And a value of 3m was used as the dispersivity (*Curtis et al.* [2006]).

5.3 Results

The kriged bromide concentration is plotted as a function of space for three different time points in Figures 5.1 through 5.3. These plots clearly show the bromide reaching all parts of the tank, and for all of the monitoring wells bromide was detectable for at least one sampling point in time (Other kriged plots presented as slices through the tank, similar to Figures 4.6 through 4.8 are available in APPENDIX D).

The effluent bromide breakthrough curve is shown in Figure 5.4. In general the breakthrough curve showed many of the non-idealities that have been observed at other scales including a relatively early breakthrough, and a long tailing period. Integrating the area under the curve gives a bromide mass recovery of 85%. Less than 100% recovery is likely attributable to small, day to day variations in flow and the dilution of the tracer in the effluent. When the tracer test had ended and there was no detectable bromide in the

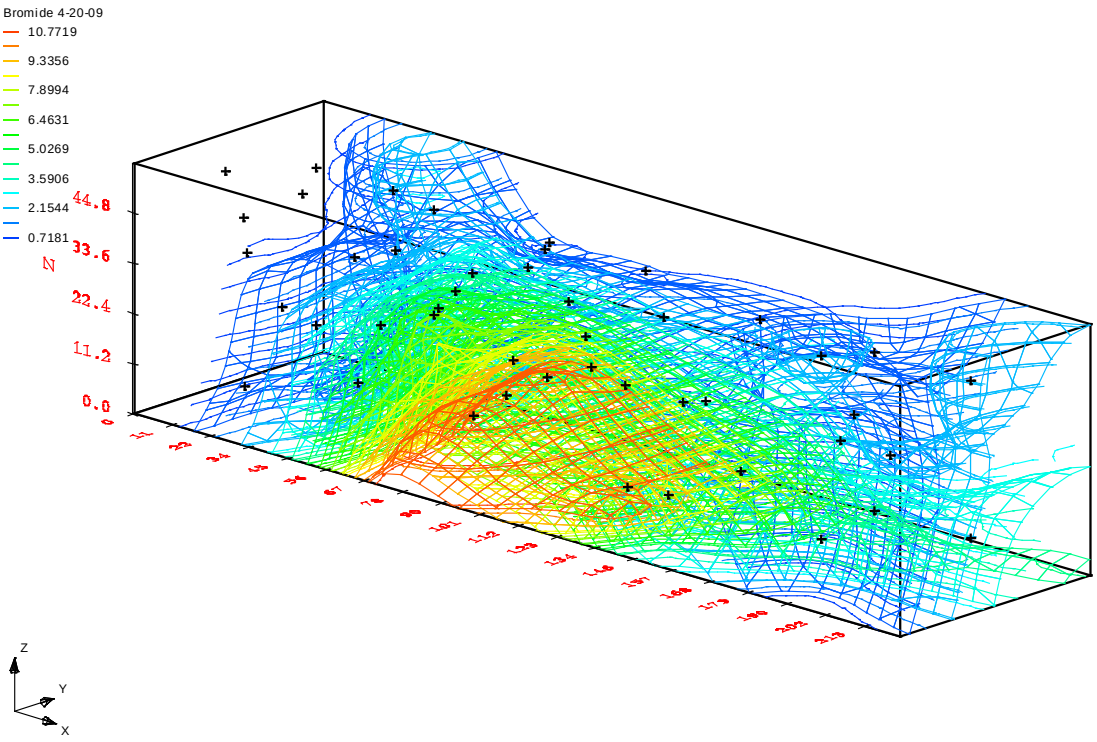

Figure 5.1 Bromide spatial distributions 46 days (0.73PV) after injection. The upgradient end is on the upper left, downgradient end is on the lower right. The number of wells with detectable bromide to create this plot is 38. Black points in plot represent well locations.

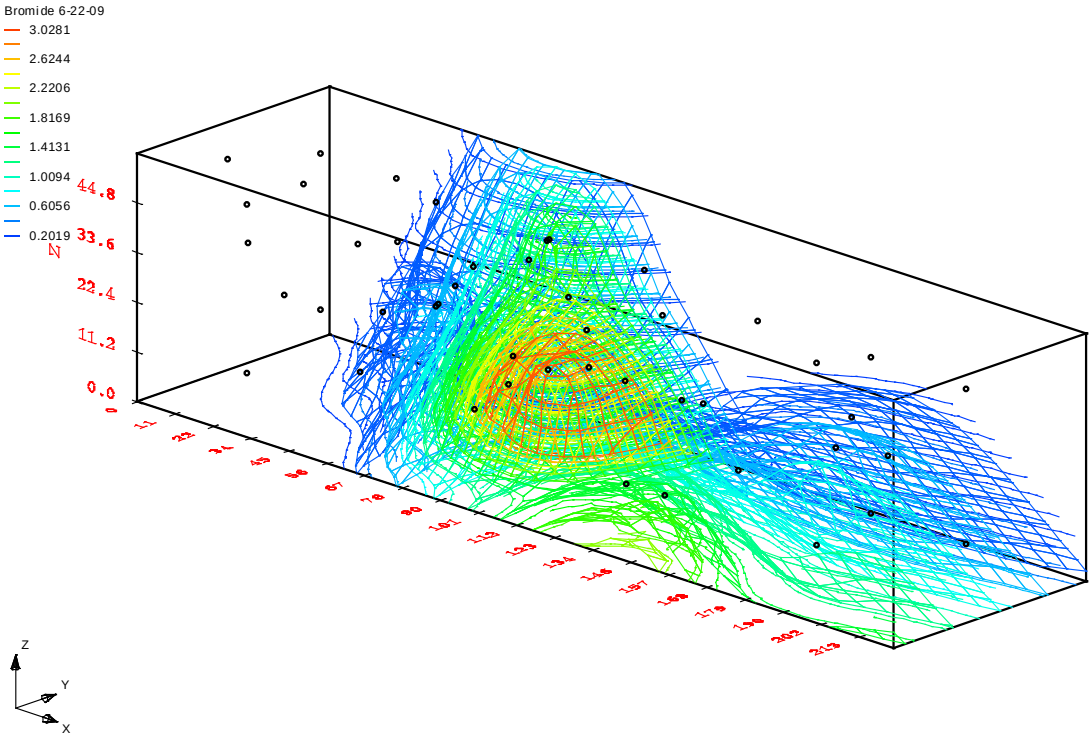

Figure 5.2 Bromide spatial distributions 109 days (1.65PV) since injection. Upgradient end is on the upper left, downgradient end is on the lower right. The number of wells with detectable bromide was 12.

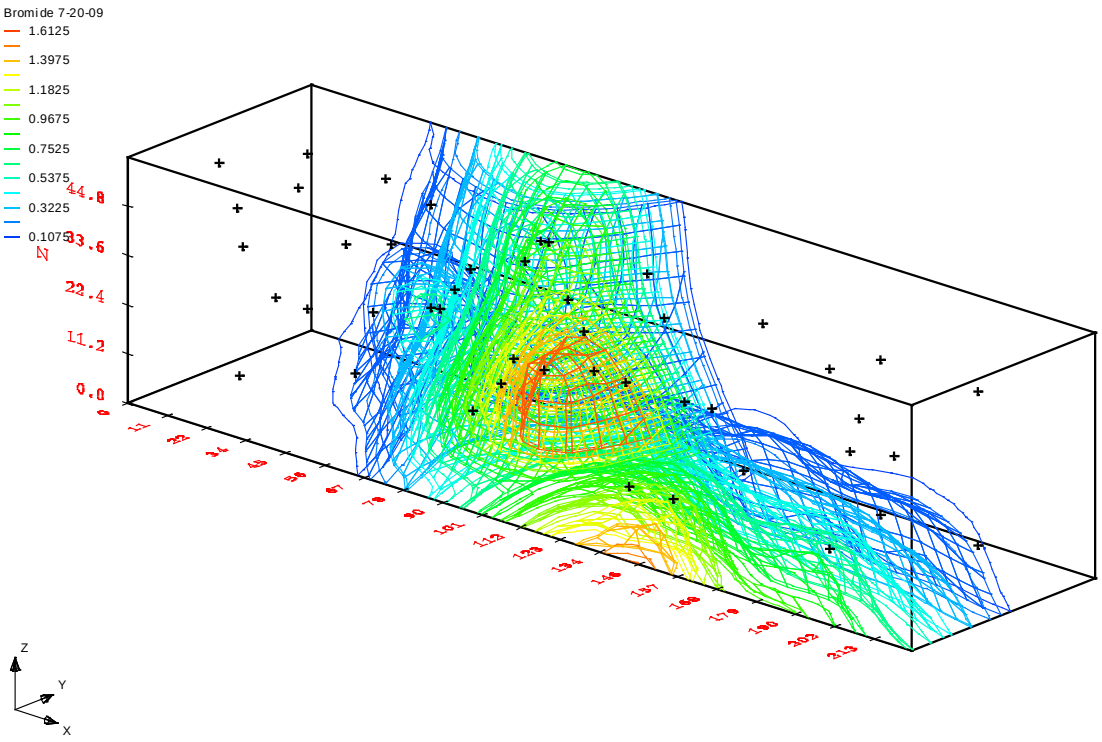

Figure 5.3 Bromide spatial distributions 137 days (2.10PV) after injection. Upgradient end is on the upper left, downgradient end is on the lower right. The number of wells with detectable bromide in this plots is 9.

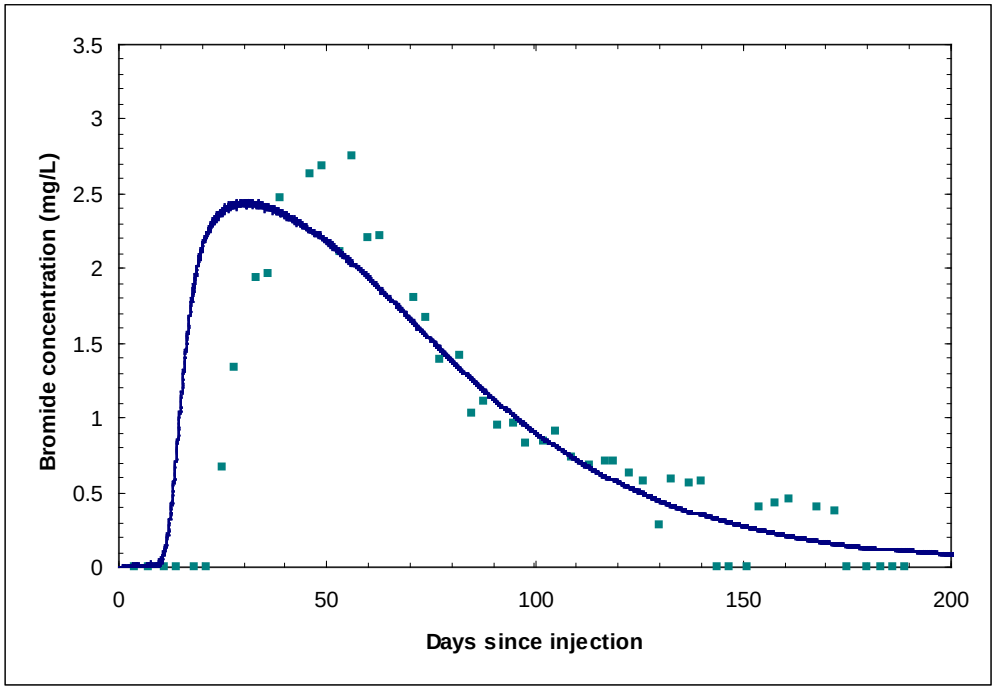

Figure 5.4 Bromide breakthrough curve and model fit, points are data from the tank, and the line is the model output. Model values are in Table 5.1.

effluent, there was still detectable bromide within the tank at wells #2, 3, 7, 10, 13, and 33. The model fits, also shown in Figure 5.4 are marginal. The only fitting parameter used was the diffusion coefficient of bromide (All model values listed in Table 5.1). A value of $1.1x10^{-8}$ m^2/sec captures the tailing behavior very well and the maximum concentration relatively well. However, the model curve is shifted to the left on the leading edge, thus predicting an earlier breakthrough than observed.

Several of the monitoring wells had detectable bromide for considerable periods of time (2 months or more). Using the calibrated flow model from above, breakthrough curves can be created for an individual well. An example of this type of plot is shown for wells #2 and 7 and 29 in Figure 5.5. Breakthrough curves for the other wells, 1, 3, 6, 13, 19, 31, 32, and 33 can be found in APPENDIX D. The three wells shown in Figure 5.5 encompass the overall range of responses for bromide migration in the tank. Well #7 is typically non-ideal, with a smaller peak concentration and longer tail that continues beyond the monitoring range. Well #19 is fairly ideal, with a sharp peak and a relatively short to non-existent tail. Well #32 defies classification as ideal or non-ideal; it is nearly sinusoidal in shape. Wells #29 and 33 also showed bizarre behavior, with well #29 having a very low concentration that persists for about two months and then returns to zero, while well #33 showed a linear increase to a maximum value of 1.59mg/L and then there was a linear decrease to 0.5mg/L at the end of the monitoring period. All of these wells can be classified into one of four categories based on their tracer response. This classification can be seen in Table 5.2. Also in the appendix are the model fits for each well. Only wells #3 and 7 were described with any sort of accuracy; no major features of the breakthrough curve for any of the other wells were captured by the model.

Uranium behavior within the tank was discussed in Chapter 4, but is summarized here to compare reactive uranium transport with non-reactive bromide transport. For the wells listed above with bromide concentrations that persisted for months, uranium behavior can be classified into six categories; these categories are shown in Table 5.3. The six categories are based on the amount of observed change in uranium concentration for a single well (small $<2.63\mu M$, $2.88\mu M \leq$medium$\leq 5.28\mu M$, high $>5.28\mu M$), and on the curvature of the breakthrough curve. For many of the wells, the curve is fairly

Table 5.1 Model values used to create breakthrough curve in Figure 5.4

	Particle Size	Value	Source
Hydraulic Conductivity (cm/sec)[1]	<2mm composite	2.1×10^{-3}	Chapter 3/Fitted
	<0.250mm	6.0×10^{-4}	Chapter 3/Fitted
	>0.250mm	3.3×10^{-2}	Chapter 3/Fitted
	0.125-0.250mm	3.3×10^{-3}	Estimated/Fitted
	4-12mm	6.4×10^{1}	Estimated/Fitted
Head Difference (mm)[1]		2	Measured
Porosity[1]		0.37	Measured
Dispersion Coefficient (m)[2]		3	*Curtis et al.* [2006]
Longitudinal:Transverse Dispersivity[2]		0.1	Assumed
Longitudinal:Vertical Dispersivity[2]		0.01	Assumed
Diffusion Coefficient (m^2/sec)[2]		1.1×10^{-8}	Fitted

1- Flow calibration

2-Transport calibration

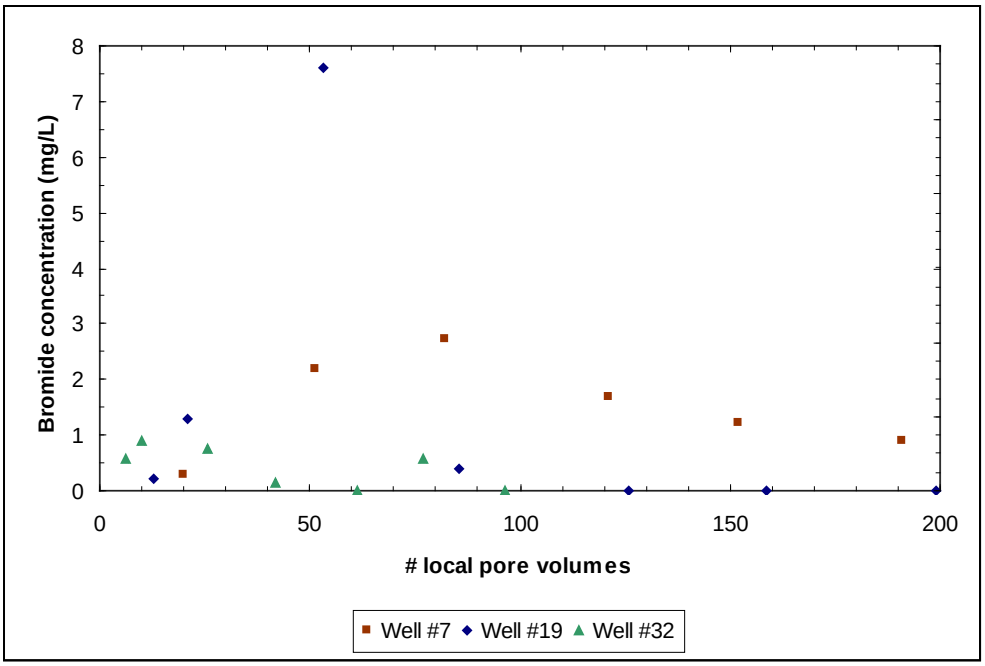

Figure 5.5 Bromide breakthrough curves for three wells, plotted as a function of local pore volumes eluted. The number of pore volumes for well #19 has been scaled down by a factor of 25; the number of pore volumes for well #32 has been scaled down by a factor of 40.

Table 5.2 Well classifications based on tracer response. The numbers in the table denote well ID numbers.

	Sharp Br^- peak	No sharp peak
Significant tailing	2, 3, 6, 13	7
No real significant tailing	1, 19, 31	29, 32, 33

Table 5.3 Well classifications based on uranium response. The numbers in the table denote well ID numbers. The small, medium, large change refer to uranium concentration changes, while 1 and 2-stage refer to the breakthrough curve. See text for details.

	Small Change	Medium Change	Large Change
2-stage	1, 32	29, 31	2, 3, 6, 7, 13
1-stage	19, 32	33	

smooth and follows that of exponential decay. For others, there appears instead to be a two stage breakthrough curve that would be best described by two linear functions, the first having a negative slope and the second being nearly horizontal (see Figure 4.14). The difference between these two types of curves is slight and often dictated by the placement of a single point. However, in looking at all of the uranium breakthrough curves (APPENDIX D) this behavior appears to be quite common (23 wells have one stage curves, 16 have two stage curves, and 5 are somewhat ambiguous). In Table 5.3, well #32 is ambiguous, and therefore listed twice.

5.4 Discussion

The initial motivation for this work was to create inert tracer transport data using a field sediment and ambient groundwater velocities. Comparing these results to other intermediate scale tracer tests is difficult due to the lack of 3-D field sediment based experiments. However, there are a few pulse injections in intermediate scale systems which allow for some comparison. With the use of variously sized lab sands, *Barth et al.* [2001a] packed a 2-D heterogeneous system. In this system, the breakthrough curve of bromide was fairly ideal, with no tailing but a pronounced shoulder. This is notable as the breakthrough curve was constructed from a vertical transect within the flow domain. *Istok et al.* [1999] used a homogenous packing of field sediment, and also observed ideal bromide behavior within the flow domain of the tank. Contrasting with what was seen in this work, at many of the points within the flow domain, the tracer response ranged from fairly ideal to untraditionally non-ideal (well #32). These effects are potentially attributable to boundary effects (*Berkowitz et al.* [2009]) or to multi-process non-equilibrium behavior (*Liu et al.* [2008], *Qafoku et al.* [2005], *Haggerty and Gorelick* [1995], *Brusseau et al.* [1992]). The other major difference between this study and others is the amount of time elapsed for a single tracer test. In this work the elapsed time from bromide injection to non-detect values in the effluent was approximately six months. In other intermediate scale work the total elapsed time of a single replicate ranges from 5

hours (*Levy and Berkowitz* [2003]) to 7 days (*Barth et al.* [2001], *Levy and Berkowitz* [2003]). Column and field scale work ranges from days to years (See Chapter 1). It has been suggested that groundwater model parameters may dependant on the time scale over which they are measured (*Rajaram* [1997], *Haggerty et al.* [2004]). Results from this experiment can also fill the timing gap that exists between the various scales of experiments.

Because of the dense characterization of pore fluids within the domain, part of the non-ideality can be attributed directly to the physical heterogeneity packed into the tank. Comparing the breakthrough curve for the entire tank (Figure 5.4) with the spatial plots of bromide distribution (Figures 5.1 through 5.3), it can be seen that tracer breakthrough at early time points is dominated by fast transport through the 4-12mm material. Velocity vectors determined in GMS indicate a stream tube through the middle of the tank flowing through both areas of 4-12mm material. Late time tailing is attributable to small pockets of lower velocities with still significant bromide concentrations acting as secondary sources for bromide in the effluent. A major conclusion from this experiment, however, is that despite the local complexities in tracer response, the breakthrough curve for the tank is smooth, and relatively unremarkable. Thus, despite the fact that small scale complexities lead to a large range of tracer behavior within the flow domain of the tank, the overall mass outflux from the tank is phenomenologically similar to those seen from much smaller scale column experiments. Much of the effects of increased heterogeneity are being smoothed as inert transport proceeds.

However, a traditional ADE-based modeling approach was incapable of accurately capturing tracer behavior. On a macroscopic scale, the model does a fair job of capturing late term tailing behavior, but did not predict the initial time of arrival. Even this level of model fit is unconvincing, as the model only describes tracer behavior in the effluent and not as a function of space. At all but two wells, the model predicts much earlier breakthrough, much shorter tails, and usually much higher maximum concentrations than observed. Thus, the model is incapable of describing small scale complexity, but does a marginal job of describing effluent behavior. The model itself is lacking a scalable 'instrument' (*Cushman* [1986]), and is only valid for certain levels of measurement (*Dagan* [1986]); specifically it is valid at the scale which it was calibrated.

Tables 5.2 and 5.3 were created to allow a comparison between inert and reactive transport. The assumption underlying this analysis is that the bromide is chemically inert and that its transport is dominated by mass transfer and advective flux alone. Uranium behavior is assumed to be affected by these same processes, as well as the chemical processes related to desorption, aqueous complexation and mineral weathering. One of the first points of interest in comparing these two tables is the cluster of wells 2, 3, 6, and 13. For bromide behavior these wells exhibited sharp bromide peaks and prolonged tailing. This can be interpreted with a dual domain type conceptual model where the initial peak is dominated by advective flux at which point the non-mobile zone is being loaded with bromide, and tailing can be attributed to transfer from the immobile zone back into the mobile zone as the diffusive gradient is reversed. This correlates well with the uranium behavior where these same wells had a large change in uranium concentrations and two stage breakthrough curves. The initial high uranium concentrations can be interpreted as uranium that is easily accessible to the mobile domain, and desorbs without kinetic hindrance until the source is exhausted. The second stage can represent the uranium that is only in contact with the immobile zone, and thus the long-term evolution of uranium is controlled by both mass transfer and chemical kinetics. However, this conceptual model does not explain why the second stage is linear and largely unchanging. Also, the range of values for this second stage has a range of 1-4.5μM. This may indicate a chemical as well as physical control.

Wells #2, 3, 6, and 13 are physically close within the tank, which may explain some of their similar behaviors. Well #7 which has similar uranium behavior and slightly different bromide behavior is located further downgradient. This alone may explain the different tracer behavior as the tracer solution is diluted with bromide free water. Several other wells are located near the space referred to here as the jelly do-nut. Located in the upper half of the upgradient half of the tank, the jelly do-nut is a 4-12mm do-nut filled with 0.125-0.250mm jelly (see Figures 4.1 through 4.5). Wells #19 and 32 are in the do-nut section, well #31 is in the jelly, and wells #29 and 33 are in the <2mm composite material on either side of the do-nut. Well #33 has the least smooth of all the uranium breakthrough curves, and also exhibits very strange (sinusoidal) bromide behavior. Well #32 also shows odd bromide behavior and is physically next to well #33 (11.2cm

between them). Well #29 also shows aberrant bromide behavior, but more consistent uranium behavior. Of these wells, well #19 is the most upgradient, and also has ideal tracer behavior. Well #31, in the jelly section, also exhibits surprisingly ideal behavior despite having the lowest calculated water velocity by two orders of magnitude. Thus within what is most likely a diffusion based domain, tracer behavior is still ideal. All of this is indicative of a highly heterogeneous flow field surrounding and passing through the jelly do-nut with advective mixing, diffusive mass transfer, as well as other physical and chemical processes co-occurring. Again, however, it is difficult to discern any of this complexity from the breakthrough curves for the tank.

The complexity above connotes that several possible conceptual models may be accurate for different wells and locations in the tank. As previously mentioned, wells #2, 3, 6, and 13 appear to be describable by a dual domain conceptual model. Since they are so physically close in the tank this can define a zone where the dual domain is valid. It is important to note that this area transcends areas of different particle sizes. Well #19, however, has fairly ideal tracer behavior and relatively smooth uranium behavior that may be describable by the advective dispersive equation. Other wells, 29, 32, and 33, do not appear to have behavior consistent with any single published conceptual model. Thus, locally within the tank there is a possibility of three or more different valid conceptual models. None of this variability in behavior is attributable to observable heterogeneity such as packing orientation of particle sizes or calculated ground water velocity. It can be assumed that much of this observed behavior is due to small local variations caused by unquantified, pore scale heterogeneities. Again, however, despite these local small scale variations the breakthrough curve for the tank is smooth and comparable to column scale breakthrough curves. This information may help delineate confusing contaminant behavior in modeling studies where pore scale effects have dominated (*Espinoza and Valocchi* [1997]) versus where they have found to be negligible (*Burr et al.* [1994]).

If the tank is considered as being near the scale of an individual discretization for a field scale simulation, the results of this experiment show that explicit incorporation of pore scale behavior in field scale simulations is probably not necessary. Indeed, for models to be used as heuristic devices or as a pragmatic tools, simplifications are

required (*Konikow and Bredehoeft* [1992], *Oreskes et al.* [1994], *Steefel et al.* [2005]) and deciding which simplifications to make will be dictated by examining transport data at a range of heterogeneities. More experimental evidence at this length scale, but with varying amounts of heterogeneity will be necessary to test this hypothesis. This would include tank packings with geologic relevance. Besides increasing physical heterogeneities, chemical heterogeneities will also need to be studied through the use of varied mineralogies and a wider range of influent compositions to mimic those found at sites with radionuclide releases.

5.5 References

Barth, Gilbert R., Mary C. Hill, Tissa H. Illangasekare, and Harihar Rajaram. 2001. Predictive modeling of flow and transport in a two-dimensional intermediate-scale, heterogeneous porous medium. *Water Resources Research* 37 (10):2503-2512.

Barth, Gilbert R., Tissa H. Illangasekare, Mary C. Hill, and Harihar Rajaram. 2001a. A new tracer-density criterion for heterogeneous porous media. *Water Resources Research* 37 (1):21-31.

Berkowitz, Brian, Andrea Cortis, Ishai Dror, and Harvey Scher. 2009. Laboratory experiments on dispersive transport across interfaces: The role of flow direction. *Water Resources Research* 45:W02201, doi:10.1029/2008WR007342.

Boggs, J. Mark, Steven C. Young, Lisa M. Beard, Lynn W. Gelhar, Kenneth R. Rehfeldt, and E. Eric Adams. 1992. Field Study of Dispersion in a Heterogeneous Aquifer 1. Overview and Site Description. *Water Resources Research* 28 (12):3281-3291.

Brusseau, Mark L. 1992. Transport of Rate-Limited Sorbing Solutes in Heterogeneous Porous Media: Application of a One-Dimensional Multifactor Nonideality Model to Field Data. *Water Resources Research* 28 (9):2485-2497.

Brusseau, Mark L., and John M. Zachara. 1993. Tranport of Co2+ in a Physically and Chemically Heterogeneous Porous Medium. *Environmental Science and Technology* 27 (9):1937-1939.

Burr, D.T., Edward A. Sudicky, and R.L. Naff. 1994. Nonreactive and reactive solute transport in three-dimensional heterogeneous porous media: Mean displacement, plume spreading, and uncertainty. *Water Resources Research* 30 (3):791-815.

Curtis, Gary P., J.A. Davis, and David L. Naftz. 2006. Simulation of reactive transport of uranium(VI) in groundwater with variable chemical conditions. *Water Resources Research* 42:W04404, doi:10.1029/2005WR003979.

Cushman, John H. 1986. On Measurement, Scale, and Scaling. *Water Resources Research* 22 (2):129-134.

Dagan, Gedeon. 1986. Statistical Theory of Groundwater Flow and Transport: Pore to Laboratory, Laboratory to Formation, Formation to Regional Scale. *Water Resources Research* 22 (9):120S-134S.

Espinoza, Carlos, and Albert J. Valocchi. 1997. Stochastic analysis of one-dimensional transport of kinetically adsorbing solutes in chemically heterogeneous aquifers. *Water Resources Research* 33 (11):2429-2445.

Gelhar, Lynn W., Claire Welty, and Kenneth R. Rehfeldt. 1992. A Critical Review of Data on Field-Scale Dispersion in Aquifers. *Water Resources Research* 28 (7):1955-1974.

Haggerty, Roy, and Steven M. Gorelick. 1995. Multiple-rate mass transfer for modeling diffusion and surface reactions in media with pore-scale heterogeneity. *Water Resources Research* 31 (10):2383-2400.

Haggerty, Roy, Charles Harvey, Claudius Freiherr von Schwerin, and Lucy C. Meigs. 2004. What controls the apparent time-scale of solute mass transfer in aquifers and soils? A comparison of experimental results. *Water Resources Research* 40 doi: 10.1029/2002WR001716.

Harbaugh, A.W., E.R. Banta, Mary C. Hill, and M.G. McDonald. 2000. MODFLOW-2000, the U.S. Geological Survey modular ground-water model-- User guide to modularization concepts and the Ground-Water Flow Process: USGS.

Heiderscheidt, J.L., R.L. Siegrist, and Tissa H. Illangasekare. 2008. Intermediate-scale 2D experimental investigation of in situ chemical oxidation using potassium permanganate for remediation of complex DNAPL sources. *Journal of Contaminant Hydrology* 102:3-16.

Istok, Jonathan D., J.E. Amonette, C.R. Cole, J.S. Fruchter, M.D. Humphrey, James E. Szecsody, S.S. Teel, V.R. Vermeul, M.D. Williams, and Steven Yabusaki. 1999. In Situ Redox Manipulation by Dithionite Injection: Intermediate-Scale Laboratory Experiments. *Ground Water* 37 (6).

Konikow, Leonard F., and John D. Bredehoeft. 1992. Ground-water models cannot be validated. *Advances in Water Resources* 15:75-83.

LeBlanc, D.R, Stephen P. Garabedian, K.M. Hess, Lynn W. Gelhar, Richard D. Quadry, Kenneth G. Stollenwerk, and Warren W. Wood. 1991. Large-Scale Natural Gradient Tracer Test in Sand and Gravel, Cape Cod, Massachusetts 1. Experimental Design and Observed Tracer Movement. *Water Resources Research* 27 (5):895-910.

Levy, Melissa, and Brian Berkowitz. 2003. Measurement and analysis of non-Fickian dispersion in heterogeneous porous media. *Journal of Contaminant Hydrology* 64:203-226.

Li, L., C.A. Peters, and M.A. Celia. 2006. Upscaling geochemical reaction rates using pore-scale network modeling. *Advances in Water Resources* 29:1351-1370.

Lichtner, Peter C., and D.M. Tartakovsky. 2003. Stochastic analysis of effective rate constant for heterogeneous reactions. *Stochastic Environmental Research and Risk Assessment* 17:419-429.

Liu, Chongxuan, John M. Zachara, Nikolla Qafoku, P., and Zheming Wang. 2008. Scale-dependent desorption of uranium from contaminated subsurface environments. *Water Resources Research* 44 (W08413):10.1029/2007WR006478.

Meile, Christof, and Kagan Tuncay. 2006. Scale dependence of reaction rates in porous media. *Advances in Water Resources* 29:62-71.

Michalsen, Mandy M., Bernard A. Goodman, Shelly D. Kelly, Kenneth M. Kemner, James P. McKinley, Joseph W. Stucki, and Jonathan D. Istok. 2006. Uranium Technetium Bio-Immobilization in Intermediate-Scale Physical Models of an In Situ Bio-Barrier. *Environmental Science and Technology* 40 (22):7048-7053.

Oostrom, M., J.S. Hayworth, J.H. Dane, and O. Guven. Behavior of Dense Aqueous Phase Leachate Plumes in Homogenous Porous Media. *Water Resources Research* 28 (8):2123-2134.

Oreskes, Naomi, Kristin Shrader-Frechette, and Kenneth Belitz. 1994. Verification, Validation, and Confirmation of Numerical Models in the Earth Sciences. *Science* 263:641-646.

Pang, Lipang, Murray Close, Daniela Schneider, and Greg Stanton. 2002. Effect of pore-water velocity on chemical nonequilibrium transport of Cd, Zn, and Pb. *Journal of Contaminant Hydrology* 57:241-258.

Qafoku, Nikolla, P., John M. Zachara, Chongxuan Liu, Paul L. Gassman, Odeta S. Qafoku, and Steven C. Smith. 2005. Kinetic Desorption and Sorption of U(VI) during Reactive Transport in a Contaminated Hanford Sediment. *Environmental Science and Technology* 39 (9):3157-3165.

Rajaram, Harihar. 1997. Time and scale dependent effective retardation factors in heterogeneous systems. *Advances in Water Resources* 20 (4):217-230.

Schincariol, Robert A., and Franklin W. Schwartz. 1990. An Experimental Investigation of Variable Density Flow and Mixing in Homogenous and Heterogeneous Media. *Water Resources Research* 26 (10):2317-2329.

Seeboonruang, Uma, and Timothy R. Ginn. 2006. Upscaling heterogeneity in aquifer reactivity via exposure-time concept: Forward model. *Journal of Contaminant Hydrology* 84:127-154.

Silliman, S.E., and E.S. Simpson. 1987. Laboratory Evidence of the Scale Effect in Dispersion of Solutes in Porous Media. *Water Resources Research* 23 (8):1667-1673.

Steefel, Carl I., Donald J. DePaolo, and Peter C. Lichtner. 2005. Reactive transport modeling: An essential tool and a new research approach for the Earth sciences. *Earth and Planetary Science Letters* 240:539-558.

Sudicky, E.A. 1986. A Natural Gradient Experiment on Solute Transport in a Sand Aquifer: Spatial Variability of Hydraulic Conductivity and Its Role in the Dispersion Process. *Water Resources Research* 22 (13):2069-2082.

White, A.F., and Susan L. Brantley. 1995. Chemical Weathering Rates of Silicate Minerals. Edited by P. H. Ribbe. Vol. 31, Reviews in Mineralogy. Washington D.C.: Mineralogical Society of America.

Zheng, C., and P.P. Wang. 1999. MT3DMS, A modular three-dimensional multi-species transport model for simulation of advection, dispersion, and chemical reactions of contaminants in groundwater systems; documentation and user's guide. Vicksburg: U.S. Army Engineer Research and Development Center.

CHAPTER 6

SUMMARY OF ION BEHAVIORS FROM ALL THREE TANKS

Throughout most of this document, the behavior of individual ions is considered on a tank by tank basis or as a change over time. This chapter will plot similar data from all three tanks to explicitly demonstrate the similarities and differences between behaviors in the tanks. This process ignores many subtleties of the data; many of these were discussed in previous chapters. The goal here is to compare the differences based on the known macroscopic heterogeneities placed in the tanks. In this sense, tank #1 is the most homogenous (1 particle size, uniformly packed), tank #2 is more heterogeneous (2 particle sizes, non-uniformly packed), and tank #3 is the most heterogeneous (5 particle sizes, non-uniformly packed). In terms of solid phase chemical heterogeneities, tanks #1 and #2 are similar (subsets of a single size fraction with identical mass ratios were used with different packing orientations), while tank #3 introduces more chemical heterogeneity related to the addition of two particle sizes that were not used in the previous tanks, and the fact that the mass ratios of three particle sizes which had been used in previous tanks was not the same as previous tanks.

Figure 6.1 shows uranium breakthrough curves for all three tanks. The largest differences appear to occur within the first two pore volumes of elution. Tank #1 starts at an intermediate concentration and declines along an exponential decay curve. Tank #2 has the highest initial concentration and declines the most sharply. Tank #3 starts at a very low value, increases to an intermediate value, and then declines nearly linearly when plotted on this scale. However, after two pore volumes, the differences in the tank behaviors approach a minimum. Tailing behavior for all three tanks occurs at a uranium concentration of about 2μM (for tank #2 the AGW-2% was being injected from about 2.5-4.0 PV) and this behavior continues until the end of monitoring. A likely interpretation of this behavior is that micro scale processes (e.g. intragranular diffusion,

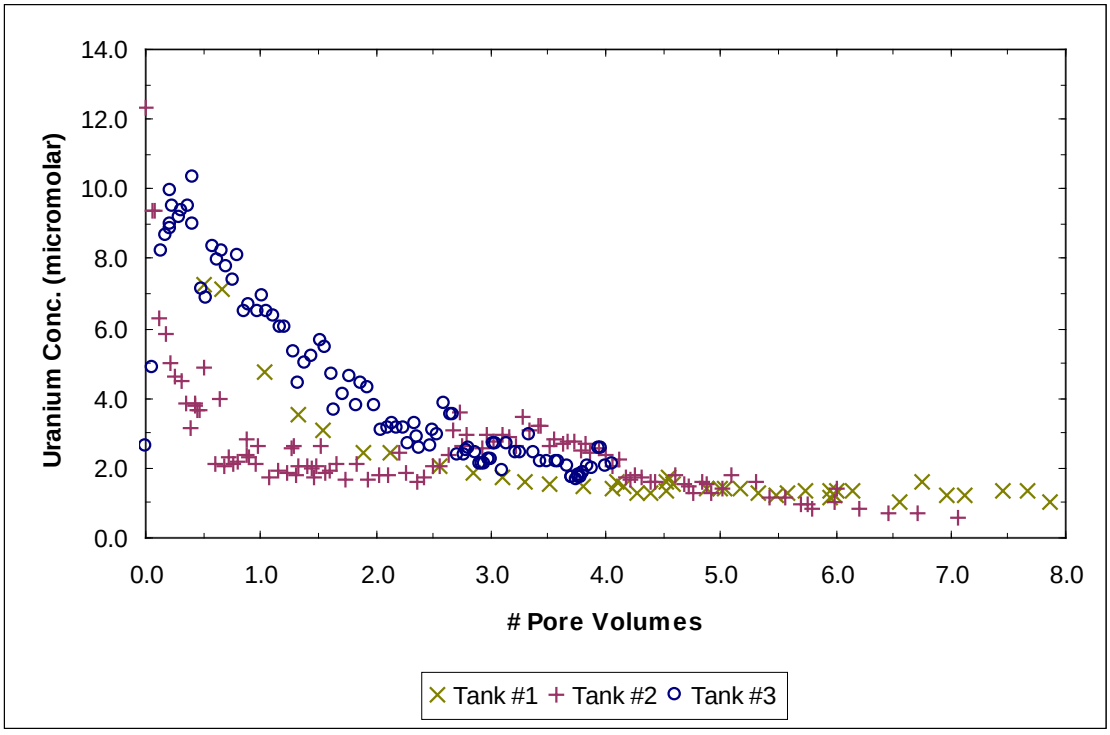

Figure 6.1 Uranium breakthrough curves for all three tanks. Samples removed from the effluent line of each individual tank.

kinetically hindered desorption) are controlling the ultimate release rates of uranium. Thus, because the tanks are at least comparable with respect to retention time (see Table 2.1), the uranium release and concentrations are being controlled by these much smaller scale processes and are at least semi-independent of macroscopic scale physical and chemical heterogeneities. Figure 6.2 plots the same data after being normalized to retention time and the amount of sediment added to the individual tanks. Here the rate of the normalized uranium flux (slope of the lines) is approximately equal, especially after 2PV when tailing behavior is seen in the breakthrough curves. In these curves it is noteworthy that the drastic differences in chemical and physical heterogeneities show uranium behavior that is not drastically different.

Figure 6.3 shows the normalized breakthrough curves for bromide for each of the tanks. Tank #1 is quite ideal with a large C_{max} and no tailing; this is the expected behavior for such a homogenous system. Tank #2 shows traditionally non-ideal behavior with an earlier breakthrough, lower C_{max}, and long tail. Tank #3 shows behavior between the first two with a slightly later breakthrough, a C_{max} that occurs at about the same number of pore volumes as tank #1, but a tail that matches the length and normalized concentration of tank #2. Since only physical heterogeneities need be considered, the increasing heterogeneity from tank #1 to tank #3 again leads to relatively simplified behavior. Tank #1 acts as a homogenous control. Tank #2 has slightly more physical heterogeneities and has a breakthrough curve consistent with what is seen at other experimental scales as heterogeneity is increased. But then, tank #3, the most heterogeneous system, exhibits breakthrough behavior between tanks #1 and #2. Thus the addition of more heterogeneity (size, number and orientation of size fractions, dimensionality) does not make for more complex tracer breakthrough behavior; instead, the homogenous tank #1 and slightly heterogeneous tank #2 act as end members, and the most heterogeneous system has attributes of both. From an up-scaling perspective this is consistent with the idea of an equivalent porous medium where small scale heterogeneities can be simplified/ignored and the output approaches that of an ideal system described with effective parameters.

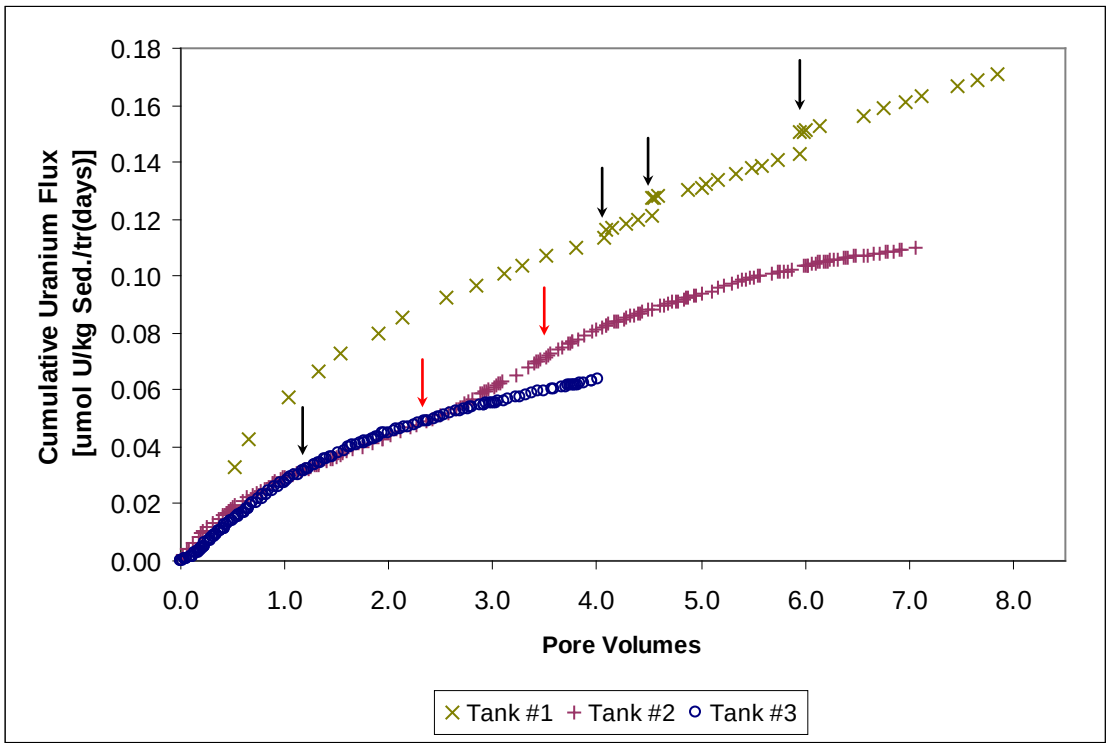

Figure 6.2 Normalized uranium fluxes from all three tanks. The black arrows denote stop flow events in tanks 1 and 2; there was no stop flow event in tank 3. The red arrows denote the time when AGW-2% was being injected into tank 2.

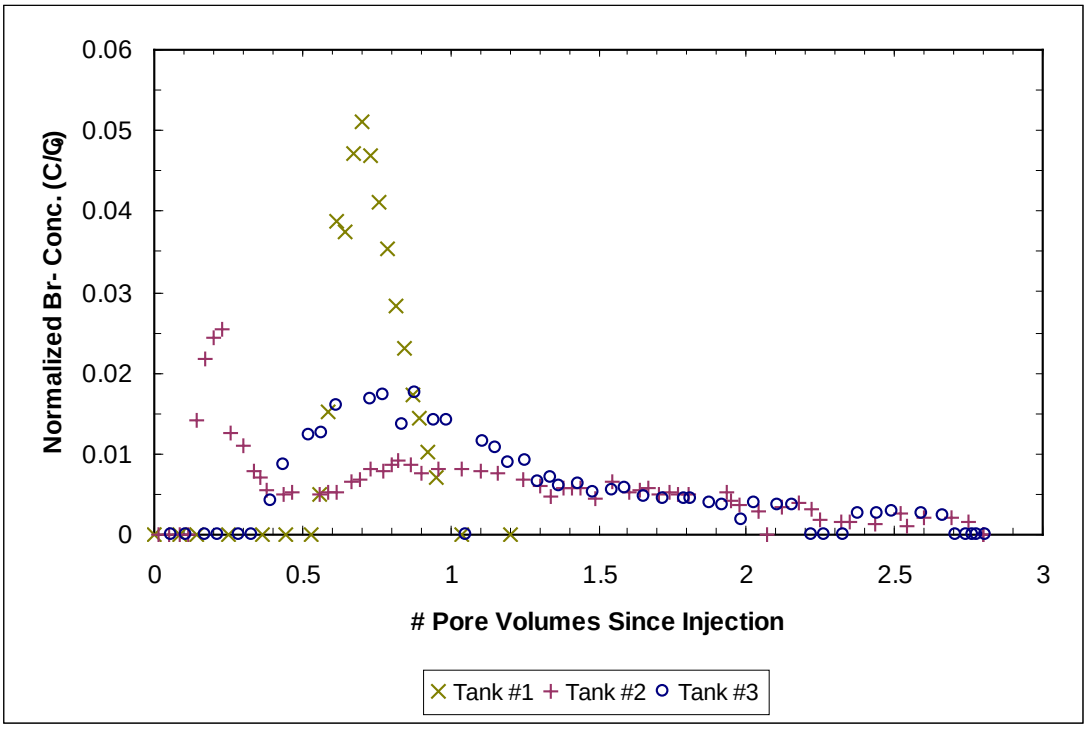

Figure 6.3 Normalized bromide breakthrough curves for all three tanks as a function of pore volumes since the bromide was injected. Samples removed from effluent line of the individual tanks.

Besides comparing effluent values, spatial sample analyses from within the flow domain of each tank can also be compared. Table 6.1 shows the range of values for a selected set of dates for all three tanks. The dates were selected to cover the majority of the experimental timeframe for each tank, but not all the data was used to simplify the figures. In table 6.1 it can be seen that the range of pH values changes with increasing heterogeneities (tank #1 is the smallest, tank #3 is the largest), the range of alkalinity values is not remarkably different between the tanks, while the range of ion concentrations in tank #1 are 2.4-7.5 greater than that in tanks #2 and #3. These relationships are shown as correlation plots in Figures 6.4 to 6.7. All of the constituents are plotted as a function of pH with uranium being shown in Figure 6.4, alkalinity in Figure 6.5, calcium in Figure 6.6 and silicon in Figure 6.7.

In Figure 6.4, it can be seen that the uranium-pH correlation is the strongest for tanks #2 and #3, and it is weaker for tank #1. Much of this is kinetically related (see Chapters 3 and 4), but if this data is only considered under macroscopic heterogeneities then other relationships emerge. Tank #1 has the widest range and weakest relationship between these two variables. Tank #2 has a narrower range and tighter correlation, and tank #3 again falls between these two end members. The reasons for this are unclear, but a major possibility includes advective mixing. From the bromide tracer tests, tank #1 has the least amount of vertical mixing. Thus the vertical mixing of reactants related to uranium desorption is also minimized. This lack of mixing relative to the other tanks may allow for the creation of chemical gradients not seen in the other tanks due to the vertical mixing which includes the broader uranium range of values. It is important enough to re-iterate that the pH-uranium relationship of tank #3 falls between that of tank #1 and tank #2.

That same relationship between the tanks is seen in Figure 6.5 correlating alkalinity and pH. Here, tank #3 has the tightest correlation, while tanks #1 and #2 have weaker correlations. And, much of tank #3 overlaps considerably with tank #1, but again tank #3 plots between the behaviors of tank #1 and tank #2. In stark contrast to this behavior is the calcium-pH relationship shown in Figure 6.6. In Figure 6.6, it can be seen that tank #2 and #3 are practically indistinguishable with exceedingly strong correlations, while tank #1 has no real correlation between these variables. This relationship implies a

Table 6.1 Minimum, maximum, and the range of values for master variables within all three tanks. Data from the following dates was used: Tank 1: 3-6-07, 4-28-07, 6-12-07, 7-11-07, Tank 2: 3-8-08, 5-8-08, 7-11-08, 9-2-08, 12-22-08, Tank 3: 3-9-09, 5-11-09, 7-13-09, 9-21-09. This table corresponds to the data shown in Figures 6.4 to 6.7.

		pH	Alkalinity (meq/L)	Uranium (μM)	Calcium (mM)	Silicon (mM)
Tank #1	Minimum	7.494	0.77	0.277	5.647	0.092
	Maximum	8.004	3.07	25.403	40.103	1.164
	Difference	0.510	2.30	25.126	34.455	1.071
Tank #2	Minimum	7.066	0.89	0.009	5.607	0.027
	Maximum	7.778	2.91	14.562	10.229	0.583
	Difference	0.712	2.02	14.554	4.622	0.556
Tank #3	Minimum	7.203	0.39	0.033	4.836	0.172
	Maximum	8.052	3.43	10.584	10.859	0.573
	Difference	0.849	3.04	10.550	6.023	0.401

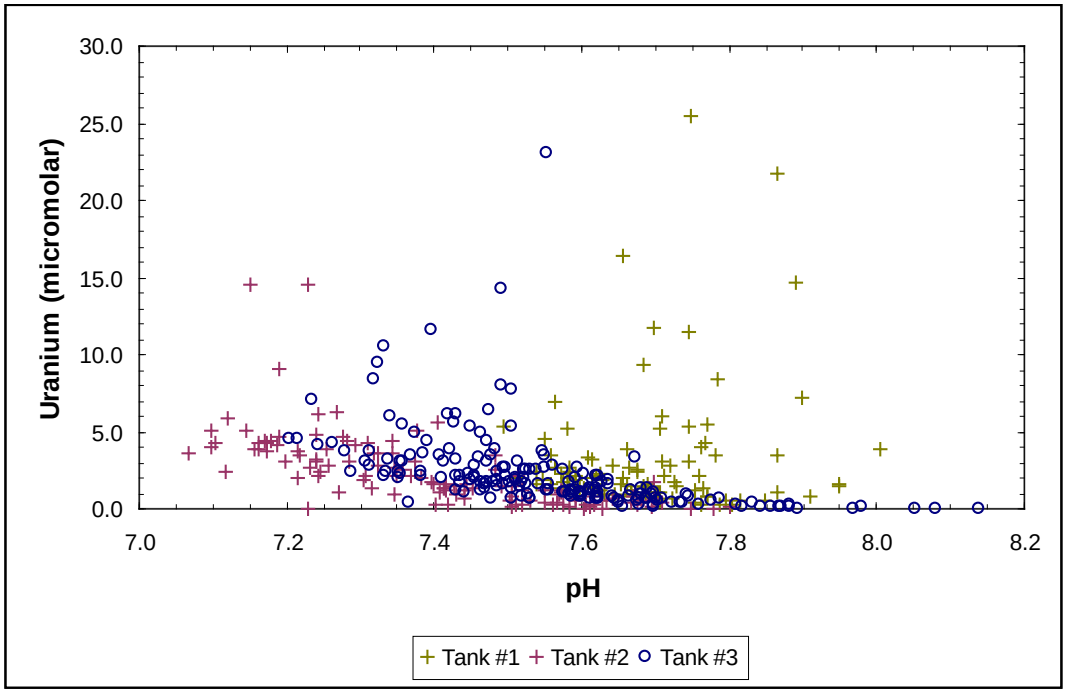

Figure 6.4 Uranium versus pH results from spatial samples for all three tanks. The samples were taken from within the flow domain. Dates shown include: Tank 1: 3-6-07, 4-28-07, 6-12-07, 7-11-07, Tank 2: 3-8-08, 5-8-08, 7-11-08, 9-2-08, 12-22-08, Tank 3: 3-9-09, 5-11-09, 7-13-09, 9-21-09.

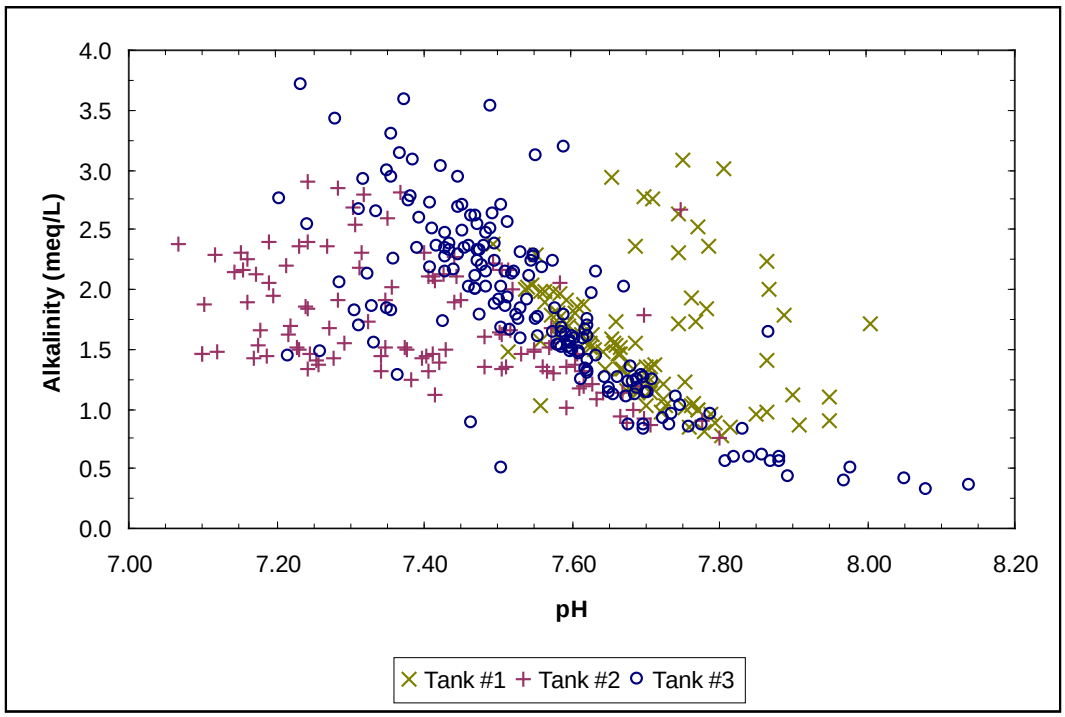

Figure 6.5 Alkalinity versus pH results from spatial samples for all three tanks. The samples were taken from within the flow domain. Dates shown include: Tank 1: 3-6-07, 4-28-07, 6-12-07, 7-11-07, Tank 2: 3-8-08, 5-8-08, 7-11-08, 9-2-08, 12-22-08, Tank 3: 3-9-09, 5-11-09, 7-13-09, 9-21-09.

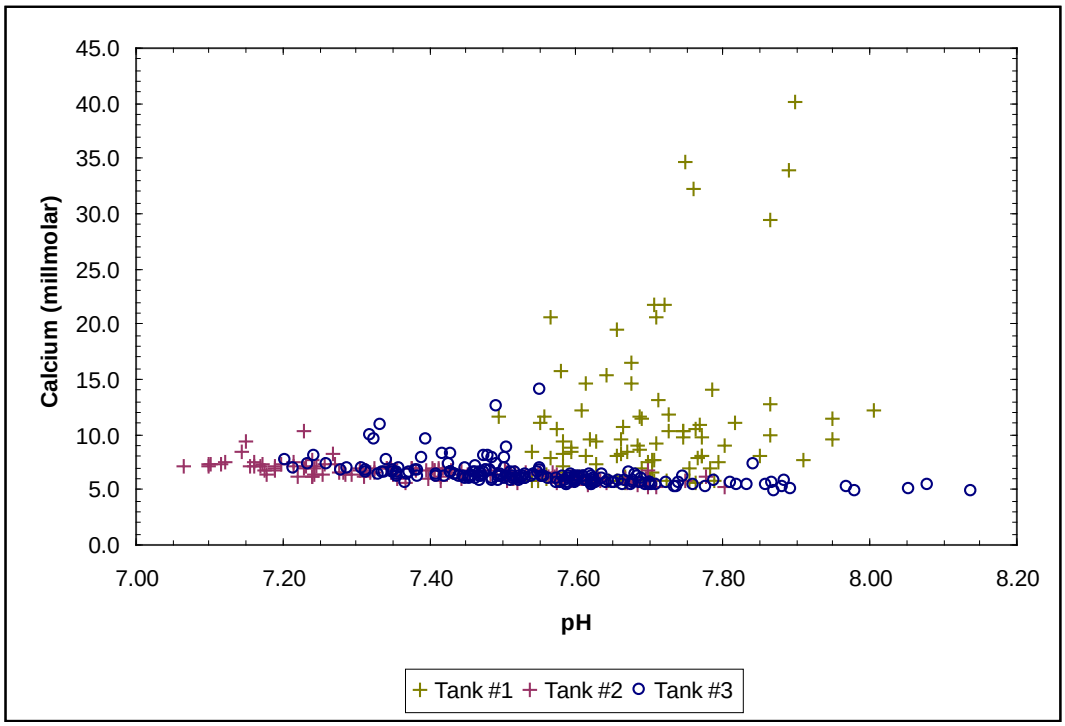

Figure 6.6 Calcium versus pH results from spatial samples for all three tanks. The samples were taken from within the flow domain. Dates shown include: Tank 1: 3-6-07, 4-28-07, 6-12-07, 7-11-07, Tank 2: 3-8-08, 5-8-08, 7-11-08, 9-2-08, 12-22-08, Tank 3: 3-9-09, 5-11-09, 7-13-09, 9-21-09.

solubility control on calcium in tanks #2 and #3 which is not occurring in tank #1. Again, this may be attributable to minimized advective mixing in tank #1, where reactants are not sufficiently mixed to cause the dissolution/precipitation of calcite to maintain equilibrium.

Figure 6.7 shows the silicon-pH relationship between the tanks. This is probably the most complex of all of these correlation plots. Just as with calcium, tanks #2 and #3 plot in very similar space with tight correlations, while tank #1 is distinctly different with no correlation. This plot even more interesting because of the fact that the steady-state relationship seen in tanks #2 and #3 are approached from both high and low silicon concentrations. In tank #2 there was no silicon in the influent, while in tank #3 the concentration was either 0.472mM or 0.735mM. Thus in tank #2 the net flux of silicon is from the solid phase to the aqueous phase, while in tank #3 the net flux of silicon is from the aqueous phase to the solid phase. This is indicative of a solubility control, but the mineral controlling solubility has yet to be identified (see Chapter 4). The reason that silicon appears to be a scatter plot in tank #1 is unknown, but possibilities include weathering rates of the clay minerals and advective mixing. The fact that the silicon-pH and calcium-pH relationships are similar between tanks may point to the fact that there is a significant amount of calcium associated with the clay minerals potentially in an ion exchange capacity. Data in previous chapters also indicated that calcite may not be the only calcium source. It is difficult, and beyond the scope of this document, to separate the contribution of these two possible sources on calcium distributions. However, unraveling this information may be critical to understanding uranium distributions as a function of heterogeneity.

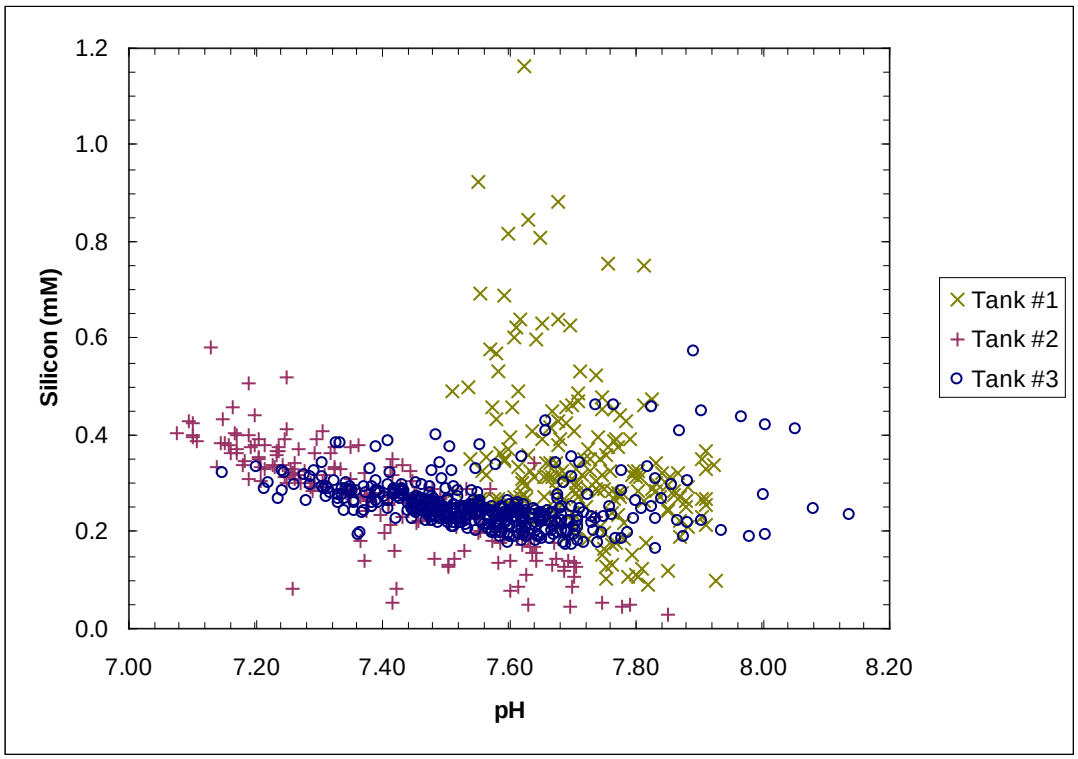

Figure 6.7 Silicon versus pH results from spatial samples for all three tanks. The samples were taken from within the flow domain. Dates shown include: Tank 1: 3-6-07, 4-28-07, 6-12-07, 7-11-07, Tank 2: 3-8-08, 5-8-08, 7-11-08, 9-2-08, 12-22-08, Tank 3: 3-9-09, 5-11-09, 7-13-09, 9-21-09.

CHAPTER 7

CONCLUSIONS

Three intermediate scale experiments were completed with a range of physical and chemical heterogeneities. These systems simulated saturated groundwater flow through a uranium contaminated sediment. In all three tanks chemical constituents were monitored as a function of space and time; physical characteristics were monitored by measuring local pressure head values. These three experiments have created a unique and extensive database against which scaling methodologies can be tested.

Tank #1 was a 2-D physically homogenous tank, while tank #2 was a 2-D physically heterogeneous tank. Tank #2 had additional chemical heterogeneity in that the influent composition was altered at two separate time points within the experiment. In comparing the results from these two tanks many conclusions can be drawn:

- The rate of uranium release from both tanks was similar as long as the influent composition was similar.
- After an initial elution of uranium rich water, the rates achieved a steady state that persisted throughout the experimental timeframe.
- Uranium distributions varied spatially with time and space, and correlated well with pH, alkalinity, and dissolved calcium concentrations.
- The inert tracer bromide showed significantly different behavior between the two tanks with tank #1 showing relatively ideal transport behavior and tank #2 showing non-ideal breakthrough behavior.
- A previously determined surface complexation model scaled through available surface area was incapable of describing uranium distributions as a function of space and time. This would indicate that the local equilibrium assumption is invalid, or that transport and surface complexation chemistry must be linked to describe uranium distributions.

Tank #3 was a 3-D physically heterogeneous tank. The results from this experiment are:

- Uranium distributions correlate well with pH, calcium, and dissolved alkalinity, but the nature of the relationship changes with time.
- Uranium spatial distributions are clearly dependant on macroscopic physical heterogeneities as there are sharp gradients near certain particle size boundaries.
- There were many anomalous wells that had consistently and persistently higher ion concentrations than the majority of wells.
- Bromide behavior through the tank showed traditionally non-ideal behavior with long tailing.
- The bromide transport behavior was modeled with relative success using an ADE based flow and transport model.
- Depending on whether effluent data or well data is considered, the data as a whole looks smooth or erratic, respectively.

There are also several unresolved issues within the tank. The first of which is the pH-Si relationship. This relationship is steady over time, space and heterogeneity. In all three tanks the relationship between these two variables is described fairly well by a single curve. This is even more impressive as in tanks #1 and #2 the approach to this relationship is approached through weathering and dissolution from the sediments, while in tank #3 it is approached from removal of silicon from solution, ostensibly through precipitation. If this silicon phase is controlling the pH, this may represent the 'first domino' in the chain controlling the chemistry of uranium desorption.

The 'second domino' is calcite dissolution. If the silicon phase is controlling pH, then it is inadvertently controlling alkalinity values as well, through both equilibrium and kinetic concerns surrounding calcite dissolution. The dissolved carbonate is known to effect uranium desorption and represents the 'third domino'. Thus, once the phase controlling the pH-Si relationship is known, how these two minerals interact to release the alkalinity will greatly help data interpretation from the tanks.

Dissolved carbonate effects both the rate and extent of uranium desorption. Further, there is evidence that the release rate from the different particle sizes is measurably different, ostensibly due to the different physical locations of various uranium pools. There is no obvious effect of these variable rates, but they may help to explain both the outlier wells and the overall shape of the breakthrough curve. Using these measured rates to describe uranium distribution within the flow domain will allow for method development relating to the scaling of kinetic desorption parameters.

And finally, much of the conclusions regarding smooth and regular behavior were based on the breakthrough curves from the tanks. In general RTM is used to describe transport to a specific receptor be it a groundwater well or a receiving body like a river. The breakthrough curve from the tank is analogous to a free release into a river, but does not make sense in considering prediction at a specific well. Thus how the seemingly chaotic behavior observed at the level of the well sums into the overall breakthrough curve is of paramount importance in determining risk to receptors. Indeed, this is the direct statement of the scaling problem.

The issue of scaling in environmental systems is critically linked to heterogeneity. A reasonable relationship is that as heterogeneity of a system increases the role of scaling effects will also increase. However, this does not mean that model complexity needs to increase, just that the scale effects as a function of heterogeneity need to be understood. In order to gain this understanding experiments must be completed at a range of heterogeneity and scale lengths ranging from column to the field scales. For reactive transport modeling, the nature of the heterogeneity needs to extend to both the physical and chemical realms.

Epilogue

"They say, *Here's the truth*,
and I say, *Is that all there is?*
And they say,
Kind of. Pretty much. As far as we know."

-Neil Gaiman
'*Goliath*', short story found in:
Fragile Things, William Morrows, New York, 2006.